

AD-A188 526

MICRODESIGNING OF LIGHTWEIGHT/HIGH STRENGTH CERAMIC
MATERIALS (U) WASHINGTON UNIV SEATTLE DEPT OF MATERIALS
SCIENCE AND ENGINEERING I A AKSAY 30 AUG 87

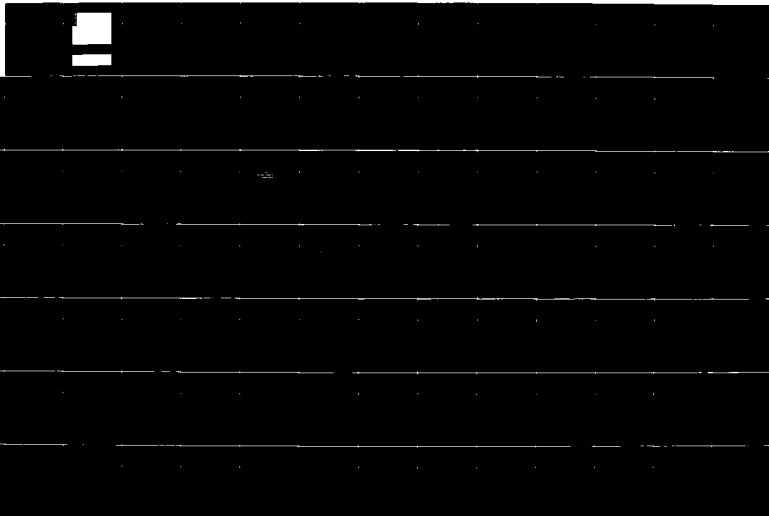
1/4

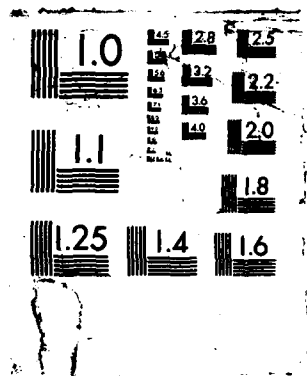
UNCLASSIFIED

AFOSR-TR-87-1595 AFOSR-83-0375

F/G 11/2

ML





AD-A188 526



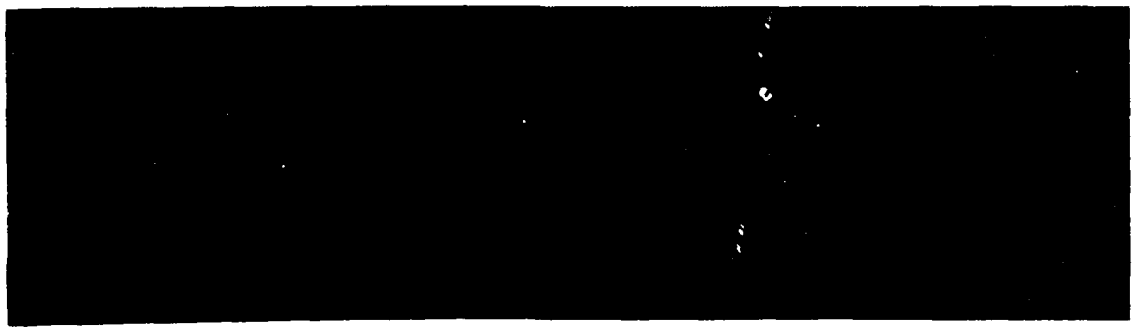
MICRODESIGNING OF LIGHTWEIGHT/HIGH STRENGTH
CERAMIC MATERIALS

Final Technical Report
Prepared for

Air Force Office of Scientific Research
Grant No. AFOSR-83-0375

I.A. Aksay, Principal Investigator

August 30, 1987



Unclassified
 SECURITY CLASSIFICATION OF THIS PAGE

REPORT DOCUMENTATION PAGE				
1a. REPORT SECURITY CLASSIFICATION Unclassified		1b. RESTRICTIVE MARKINGS		
2a. SECURITY CLASSIFICATION AUTHORITY		3. DISTRIBUTION / AVAILABILITY OF REPORT Approved for public release; Distribution unlimited		
2b. DECLASSIFICATION / DOWNGRADING SCHEDULE				
4. PERFORMING ORGANIZATION REPORT NUMBER(S)		5. MONITORING ORGANIZATION REPORT NUMBER(S) AFOSR-TR- 87-1595		
6a. NAME OF PERFORMING ORGANIZATION University of Washington	6b. OFFICE SYMBOL (if applicable)	7a. NAME OF MONITORING ORGANIZATION AFOSR/NC		
6c. ADDRESS (City, State, and ZIP Code) Seattle, WA 98195		7b. ADDRESS (City, State, and ZIP Code) Bldg. 410 Bolling AFB, DC 20332-6448		
8a. NAME OF FUNDING / SPONSORING ORGANIZATION AFOSR	8b. OFFICE SYMBOL (if applicable) NC	9. PROCUREMENT INSTRUMENT IDENTIFICATION NUMBER Grant No. AFOSR-83-0375		
8c. ADDRESS (City, State, and ZIP Code) Bldg. 410 Bolling AFB, DC 20332-6448		10. SOURCE OF FUNDING NUMBERS		
		PROGRAM ELEMENT NO. 61102F	PROJECT NO. 2303	TASK NO. A3
11. TITLE (Include Security Classification) Microdesigning of Lightweight/High Strength Ceramics				
12. PERSONAL AUTHOR(S) I.A. Aksay, G.C. Stangle, W.Y. Shih, M. Sarikaya				
13a. TYPE OF REPORT Final Technical	13b. TIME COVERED FROM 9/30/83 TO 11/30/86	14. DATE OF REPORT (Year, Month, Day)	15. PAGE COUNT	
16. SUPPLEMENTARY NOTATION				
17. COSATI CODES			18. SUBJECT TERMS (Continue on reverse if necessary and identify by block number)	
FIELD	GROUP	SUB-GROUP	Ceramics, Composite, Materials, Colloidal Processing	
19. ABSTRACT (Continue on reverse if necessary and identify by block number) This final technical report describes the results of research conducted under Grant No. AFOSR-83-0375, which deals primarily with the processing and characterization of low density and high strength ceramic matrix composites for structural applications. Experimental studies were conducted on phase transitions in colloidal systems and microstructure/nanostructure evolution during sintering. Additional studies were conducted on boron carbide-aluminum ceramic/metal composites. Finally, theoretical studies have been made to provide the foundation for developing a more fundamental understanding of colloidal systems.				
20. DISTRIBUTION / AVAILABILITY OF ABSTRACT <input checked="" type="checkbox"/> UNCLASSIFIED/UNLIMITED <input checked="" type="checkbox"/> SAME AS RPT <input type="checkbox"/> DTIC USERS		21. ABSTRACT SECURITY CLASSIFICATION Unclassified		
2a. NAME OF RESPONSIBLE INDIVIDUAL Donald R. Ulrich		22b. TELEPHONE (Include Area Code) (202) 767-4963	22c. OFFICE SYMBOL NC	

D FORM 1473, 84 MAR

83 APR edition may be used until exhausted.
 All other editions are obsolete.

SECURITY CLASSIFICATION OF THIS PAGE
 Unclassified

**MICRODESIGNING OF LIGHTWEIGHT/HIGH STRENGTH CERAMIC
MATERIALS**

*Air Force Office of Scientific Research
Final Technical Report Grant No. AFOSR-83-0375*

I.A. Aksay, Principal Investigator

August 30, 1987

Department of Materials Science & Engineering
Advanced Materials Technology Program, The Washington Technology Center
University of Washington
Seattle, Washington 98195

Approved for public release,
distribution unlimited

Contents

1. Introduction	1
2. Fundamental Studies in Processing	2
2.1 Novel Powder Synthesis Techniques	2
2.2 Dispersion, Stability, and Rheology	3
2.3 Consolidation of Colloidal Suspensions	4
2.4 Sintering and Microstructure Development	5
2.5 Post-Sintering Properties Characterization	6
3. Development of Light Weight Ceramic-Metal Composites	7
3.1 Capillarity and Reaction Thermodynamics	8
3.2 Densification	9
3.3 Microstructures	9
3.4 Mechanical Properties	10
3.5 Summary and Conclusions	11
4. Theoretical Studies	11
5. Personnel	15
6. Facilities	16
Description	16
7. Technical Communications	17
7.1 Presentations	17
7.2 Publications	21
7.3 Theses Granted	24
7.4 Patents	25
ACKNOWLEDGMENT	25
APPENDICES	26

Contents



Accession For	
NRIS OR&I	✓
DTIC TAB	[]
Unannounced	[]
Justification	
By	
Date	
Distribution	
Dist	
A-1	

List of Illustrations

Figure 1. Various processing paths followed in powder consolidation. 4

List of Illustrations

1. Introduction

This is a comprehensive final technical report for the Air Force Office of Scientific Research (AFOSR) research grant No. AFOSR-83-0375, entitled *Microdesigning of Lightweight/High Strength Ceramic Materials*. This report summarizes research accomplishments during the period 1 October 1983 to 30 June 1987 (including the no-cost extension period from 1 December 1986 to 30 June 1987). The overall objective of the program has been concerned primarily with the processing and characterization of low density (< 3.0 g/cc) and high strength (> 800 MPa) ceramic matrix composites for structural applications. In order to achieve this goal, three main task areas have been emphasized: (i) fundamental studies in processing, (ii) processing of ceramic/metal composites, and (iii) theoretical studies.

The work in the first task area consisted of experimental studies on phase transitions in colloidal systems and microstructure/nanostructure evolution during sintering. Our major accomplishments are described in Section 2 of this report. These studies dealt with the dispersion, consolidation, and sintering of ceramic powders and ceramic-forming gels, in an effort to provide a fundamental understanding of key processing parameters that affect the microstructure of the material. The key contribution of these studies has been the recognition of the fact that colloidal consolidated particle compacts display hierarchical clustering due to multiple-site nucleation and growth of particle clusters. Consequently, such hierarchically clustered structures display a multimodal void size distribution. Such inhomogeneities introduced during the pre-sintering stage generally remain in the finished product as defects, thus compromising the product's mechanical properties. Our success in the processing of these high performance materials derives from our fundamental understanding of the colloidal dispersion and consolidation techniques required for developing tailored microstructures.

The work in the second task area saw development of techniques for processing a new class of particulate-based and low density (2.6 g/cc) ceramic-metal composites composed of boron carbide-aluminum and aluminum diboride-aluminum composite materials. These materials exhibited high fracture toughness ($14.4 \text{ MPa}\cdot\text{m}^{1/2}$), high fracture strength (645 MPa), and high hardness (2400 KII (1000 g)). The primary focus of this study was the processing, mechanical testing, and microstructural analysis and characterization of these composite materials. Results are described in Section 3 of this report. These results can provide fundamental information regarding the interrelationship between mechanical properties and microstructural and compositional variations. This information should allow better identification of the key processing parameters that control the macroscopic properties of boron carbide-aluminum ceramic/metal composites.

Work in the third task area consisted of developing theoretical models in parallel with the experimental studies. The goal of the theoretical studies was to help understand colloidal systems (in the suspension state as well as in the consolidated state) from a more fundamental basis. Results are described in Section

4. Models of particle-particle interaction, particle-polymer interaction, and colloidal suspension stability were developed, based upon statistical mechanical and interparticle potential analysis techniques. Significant achievements include developing a general equilibrium phase diagram for monodisperse and bimodal particle systems and characterizing the uniformity of colloidal sediments. Initial models were modified to include electrosterically stabilized systems, non-equilibrium systems, and interfacial as well as bulk properties.

2. Fundamental Studies in Processing

The overall objective of this portion of the research program was to establish the guidelines for processing and microdesigning low density and high strength ceramic materials for structural applications. In particular, the work sought to develop a fundamental understanding of the important parameters involved in the dispersion, consolidation, and sintering of particles in the size range of 10^{-9} to 10^{-3} m. These particles may be spheroidal, plate-like, or rod-like, and may form a highly dispersed or an agglomerated suspension. Surfactants or polymers may be added to a suspension to improve the consolidation step, resulting in the tailored packing of the particles in the green microstructure. Densification may take place with the addition of heat and/or pressure. This program studied each of these areas in detail, in order to improve upon current processing methodology in designing and producing desired microstructural features.

In order to achieve this goal, five main task areas were emphasized: (i) novel powder synthesis techniques, (ii) fundamental studies in the dispersion and rheology of colloids, (iii) colloidal consolidation and characterization of the resulting microstructure, (iv) sintering and microstructure/nanostructure evolution, and (v) post-sintering properties characterization.

2.1 Novel Powder Synthesis Techniques

In an attempt to improve the purity of ceramic powders and to successfully achieve mixing of pre-ceramic components on a molecular scale, experimental work has been performed on the synthesis of ceramic precursor materials. The precursors, prepared by T. Yogo in our laboratory, include oxy-alkoxides for the production of mullite and B_4C powders. Extremely fine powders can be produced by using techniques of polymeric condensation with the monomers synthesized in our laboratory. Alternatively, these pre-ceramic polymers (or copolymers) could be used directly in shape-forming processes, with conversion to ceramic taking place subsequently. T. Yogo has successfully synthesized the monomeric units for the B_4C precursors. Ongoing studies of the polymerization of the B_4C precursor, as well as

commercially available aluminum- and silicon-containing oxy-alkoxides indicate that polymerization is possible. Preliminary evidence shows that some ceramic material is produced upon densification.

2.2 Dispersion, Stability, and Rheology

The powder dispersion, consolidation, and sintering scheme for forming ceramic bodies from colloidal powders is shown in Figure 1. The interest in such a process is due mainly to the realization that unwanted inhomogeneities introduced into a powder compact during the presintering stages generally remain in the finished product as defects. A significant difficulty which arises in employing colloidal particles is their tendency to agglomerate due to interparticle (particularly van der Waals) attractive forces. Such clustering leads to undesirable micro- and nano-structures and to highly viscous suspensions. The following paragraphs describe the fundamental experimental work performed on the dispersion and stability of submicron ceramic particles in suspension. Such information can be used to improve techniques for obtaining higher packing densities and microstructural uniformity, and for fabricating complex geometries not otherwise obtainable by alternative processing methods.

A study of interparticle interaction and clustering dynamics of attractive particles was conducted on an aqueous suspension of monosized, nanosized particles with a well-characterized surface chemistry. Gold particles with a diameter of 150 Å were used as a model system in order to study collision and aggregation rates in cluster formation. Specifically, the effects of crystallographic orientation and surface characteristics on the formation of particle clusters were investigated. Hierarchically clustered structures displaying a multimodal void size distribution were produced.

The adsorption of surfactants and polymers on the surface of dispersed colloidal particles and the stability of colloidal suspensions was investigated more fully (see Appendices I - V). The model systems of polymethacrylic acid (PMAA) and polyacrylic acid (PAA) adsorbed on α -Al₂O₃ were chosen. The adsorption behavior of polyelectrolyte on the particle surface and on the transition boundary between stable and flocculated suspensions were determined for a variety of concentrations and molecular weights of polyelectrolyte added to the suspension. A stability map was created, which can be a useful processing tool for tailor-making suspensions by varying the polyelectrolyte concentration and the solution pH to obtain the desired properties.

Suspension rheology is intimately connected with dispersion and suspension stability. Particle-particle interaction energies affect viscosity primarily by altering aggregation behavior and hence suspension structure. Important results (see Appendices III and IV) indicate that it is possible to prepare 70 v/o aqueous suspensions of α -Al₂O₃ with sufficient fluidity for ceramic processing by electrosteric stabilization of the colloidal suspension.

PROCESSING BY POWDER CONSOLIDATION

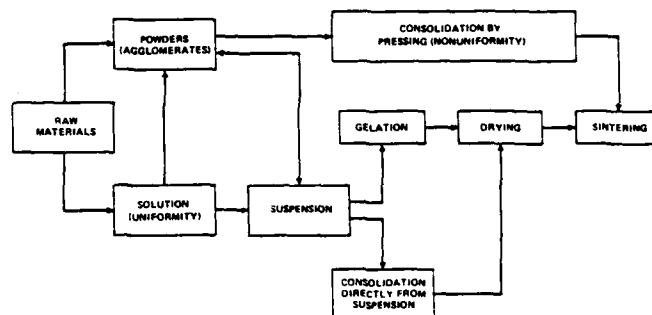


Fig. 1: Various processing paths followed in powder consolidation. Suspension route is used to eliminate unwanted particle clusters (agglomerates). Gelation route is for particles smaller than $\sim 75\text{nm}$.

Figure 1: Various processing paths followed in powder consolidation.

Suspension route is used to eliminate unwanted particle clusters (agglomerates). Gelation route is for particles smaller than $\sim 75\text{ nm}$.

2.3 Consolidation of Colloidal Suspensions

Colloidal consolidation is, in the usual sense, simply the nucleation and growth of particle clusters. It is, then, the transition of a colloidal suspension from a dispersed to a flocculated state. It may also be considered as a transition from a fluid-like to a solid-like state. The applications for ceramics processing are certainly clear. Extensive theoretical work (see Chapter 4) and a review (Appendix VI) have been completed by our group on this topic. In addition, AFOSR/DARPA funding has also supported the following experimental work.

A bimodal or polydisperse particle size distribution can produce particle compacts that sinter to full density at significantly lower temperatures than systems composed of monosized particles (Appendix VII).

Consolidation of bimodal or polydispersed systems, however, is complicated by particle segregation due to different particle migration rates. This work (Appendix VIII) investigated long-range particle segregation of a suspension that contained particles with a bimodal size distribution, undergoing consolidation. Results showed that the consolidation mechanism is initially filtration and later sedimentation, resulting in a gradation of microstructural homogeneity. Particle segregation in the bimodal system was shown to be reduced by increasing particle concentration.

Additional studies of the consolidation of colloidal suspensions included a combined theoretical and experimental investigation on the behavior of fiber-containing suspensions in the presence of thermal and mechanical forces. The properties of these fiber suspensions are expected to resemble rod-like macromolecular polymer systems that form liquid crystals. As in liquid crystal systems, fiber alignment and fiber cluster formation are expected to occur in high fiber concentrations. The results of this work are expected to lead to improved processing techniques in the fabrication of useful ceramic fiber-reinforced ceramic materials. Preliminary observations of fiber suspensions under the influence of audio-frequency vibrations include the formation of cluster domains with roughly parallel alignment, the formation of separated columns of aligned whiskers, and the formation of other regular patterns including 60-degree branched structures.

2.4 Sintering and Microstructure Development

In the sintering of consolidated ceramic powder compacts, microstructural inhomogeneities introduced during consolidation lead to variations in sintering kinetics and subsequent microstructural evolution. Particles that are more densely packed sinter to full density at a higher rate and at lower temperatures than do less densely packed particles. Three conditions must be achieved in the consolidated powder compact in order to sinter successfully at lower temperatures: small particle size, narrow pore size distribution, and uniform spatial distribution of pores. The effects of these parameters on sintering kinetics and microstructure evolution were studied in detail and are described below.

A consolidated compact composed of smaller particles sinters more quickly and at lower temperatures than does compact composed of relatively larger particles; this is due to a larger chemical potential in the former as a result of its smaller radius of curvature. Sol-gel processing employs submicron-sized particles and has advantages for reducing the sintering temperature and for preparing materials with high uniformity and parity compared to conventional processing. Shinohara and Aksay investigated the sintering and microstructure evolution of alumina (Appendices XXVa and XXVb) and mullite-forming (Appendix XXVc) gels. Enhanced densification and lower sintering temperatures were achieved when the dense particle packing of nanosized particles resulted in a relatively small pore size. Slow drying of the gels was of course necessary to minimize anisotropic shrinkage of the gel prior to sintering.

The study of the effect of pore size distribution upon sintering and densification behavior naturally follows from the work described in the previous paragraph. A model system was thus devised (see Appendices VII and IX) to investigate microstructure evolution during sintering in a ceramic compact with a controlled pore structure. The approach was motivated by the space-filling concept, which suggests that the addition of fine particles in a coarse matrix results in the reduction of pore size and overall porosity. A colloidally consolidated ceramic compact was prepared from a suspension of particles with a bimodal particle size distribution. The packing density went through a maximum at an intermediate value for a volume fraction of fines (see Figure 1 in Appendix VII), thus suggesting an optimum amount of small particles that was required to occupy the void space between large particles. As a result, the pore size distribution was smaller, which led to lower sintering temperatures and times. Grain growth was consequently reduced. The evolution of pore size distribution during densification was studied by mercury porosimetry, showing that bimodal compacts retained open pores during sintering and thus reduced the sintering temperature and improved the degree of densification.

A novel approach to the fabrication of porous ceramics with controlled pore size, shape and spatial distribution was developed (Appendices X and XI) in our laboratory. The geometry and topology of the pore space in the ceramic body was precisely controlled by introducing solid organic material in the colloidal ceramic material by codispersion or lamination, followed by thermolytic decomposition of the organic solid. The space initially occupied by the organic inclusions forms the pore network in the body and thus results in the controlled formation of microstructure.

The effect of fibers and whiskers on the consolidation of ceramic fiber-ceramic matrix composites was investigated. The objective of this study has been to prepare fiber-reinforced mullite matrix composite materials in order to produce high-strength dense ceramic bodies at reduced ($< 1250^{\circ}\text{C}$) sintering temperatures. Fabrication of the mullite matrix was accomplished by sol-gel processing technology, whereby a monomeric silica-rich compound is polymerized in a suspension containing a fine alumina-rich powder. The gel thus formed was used in either the wet monolithic form or in the dried, powdered form. Chopped, short fibers of various aspect (i.e., length/diameter) ratios were incorporated into the mullite matrix-forming material prior to heat treatment. Fiber concentration, expressed as a volume fraction, altered both the degree and rate of densification: increased fiber concentration (up to 15%) required higher sintering temperatures and longer sintering times to achieve a given degree of densification. (See also Appendix XXVII).

2.5 Post-Sintering Properties Characterization

The goal of these studies in the processing of high performance materials has been to improve the properties of the resulting ceramic bodies. Microstructural features inherited from earlier processing steps certainly affect structural properties, as do chemical and grain size changes occurring during sintering and

densification. The microstructure/nanostructure considerations have been described in earlier sections. Characterization of the latter properties, as well as the optical properties of mullite, will be discussed below.

The chemical identity of various phases in polycrystalline ceramic materials and interphase regions at grain boundaries was studied by a variety of analytical techniques, in particular the high resolution transmission electron microscopy (HREM) imaging technique. First, the reaction series during the sintering of kaolinite (Appendix XII) and metakaolinite (Appendix XIII) to mullite was studied, in order to characterize the reaction and reaction products responsible for the 980°C exotherm observed during sintering. The exotherm was found to exist due to the formation of a nearly pure $\gamma\text{-Al}_2\text{O}_3$ -type spinel phase as a result of a phase separation in the amorphous dehydroxylated kaolinite matrix. Second, an evaluation of the use of the HREM technique for the detection of grain boundary amorphous phases was prepared (Appendix XIV). The technique was then employed to provide a detailed characterization of the interphase regions of polycrystalline mullite prepared from kaolinite and alpha-alumina (Appendix XV); identification of crystalline and amorphous phases were made by the HREM technique, as was the growth direction of crystallites during mullite formation.

Additional post-sintering characterization included developing a quantitative method for relating infrared transparency to post-densification microstructure of mullite. In another study, the transparency of mullite to infrared radiation was shown to be dependent primarily on the purity and post-sintering microstructure (Appendix XVI). Mullite-forming gels were used to prepare monolithic ceramic bodies, which densified to nearly (98%) theoretical density at 1250°C. Infrared transparency depended upon 'pore-filling' (i.e., microstructure evolution) by viscous phase deformation of silica and subsequent crystallization of mullite during sintering. Infrared absorption analysis can thus in this case be used to characterize the completeness of chemical reaction, the nature of pore size distribution, and the degree of densification.

3. Development of Light Weight Ceramic-Metal Composites

Ceramic-metal composites, when properly processed, combine the useful properties of ceramic and metal materials into one system. The synthetically processed group of refractory carbide-metal composites have traditionally been processed by liquid phase sintering, an effective lower cost fabrication process. However, its applicability to ceramic-metal composites has only been illustrated in thermodynamically compatible systems. The WC-Co and TiC-Ni systems are the best studied examples of these thermodynamically compatible systems. Most ceramic-metal composite systems of interest, however, are thermodynamically incompatible at elevated temperatures. Therefore, when the liquid phase sintering approach is attempted, chemical reactions may result in the depletion of either the metal or the ceramic phase prior to full densification. Consequently, a number of difficulties have been encountered in the development of

many ceramic-metal composite systems. Low temperature, solid-state densification methods provide a solution to the phase depletion problems encountered at elevated temperatures. However, the main disadvantage of low temperature processing methods is that in the absence of chemical reactions, wetting of the ceramic by the metal phase is not always achieved. In such cases, even with high pressure forming techniques, porosity is not completely eliminated.

The preliminary studies performed under a Lawrence Livermore National Laboratory (LLNL) contract have shown that B_4C -Al and B_4C -Cu-Si composite systems can be processed to nearly full densities in lightweight cermets at temperatures below $1200^\circ C$ only by hot isostatic pressing techniques. The new work, outlined below, describes the main accomplishments which were undertaken between 1983-86. The main emphasis at this phase of the effort was given to the development of B_4C -Al and SiC-Al cermets by an infiltration technique. During this period, a methodology was formulated to circumvent the problems encountered in the microdesigning of thermodynamically incompatible ceramic-metal composites in terms of the wetting characteristics of the ceramic phase by the metal, the rate of chemical reactions at the interfaces, the resultant microstructures, and the mechanical properties achieved. This methodology will be illustrated here. The most successful results during this phase of the program were achieved in B_4C -Al cermets. Therefore, the main emphasis below will be given to the processing, microstructures, and properties of B_4C -Al cermets.

3.1 Capillarity and Reaction Thermodynamics

In order to achieve intimately mixed multiphase combinations, the first requirement is to control the wetting characteristics of the solid phases by the liquid metal. At high temperatures, chemical reactions at the interfaces result in a change in the interfacial free energies and thus in the contact angle. Therefore, non-wetting systems (i.e., thermodynamically incompatible) can be turned into wetting systems by taking advantage of these chemical reactions. In the B_4C -Al system, contrary to the earlier studies, it was found that Al can be turned to wetting at temperatures above $1000^\circ C$. However, mass transport across the interface that initially results in wetting may result in the formation of new phases in excessive amounts. The control of these chemical reactions in the formation of new phases in the B-C-Al ternary, as described below, is the key factor in the processing of B_4C -Al alloys. It is these chemical reactions which take place uncontrollably fast in SiC-Al and AlB, respectively, at the interfaces between the major ceramic and metal phases in these cermets.

The formation of seven binary and ternary phases have been established between $680^\circ C$ (T_m of Al) and $1400^\circ C$ (Appendices XVII and XVIII). The major phases are AlB_2 and Al_4BC (a newly discovered phase), (Appendix XIX) AlB_4C_2 and Al_4C_3 above $1200^\circ C$. The reaction thermodynamic studies determined that local equilibrium conditions between 800 and $1200^\circ C$ must be established so that Al_4BC (the so-called

X-Phase) will evolve and tie-up most of the free carbon required to form Al_4C_3 . It is established that Al_4C_3 is undesirable (as in SiC-Al cermets) because of its hygroscopic nature and poor mechanical properties. Above 1200°C, local equilibrium conditions do not suppress Al_4C_3 formation. Therefore, to process B_4C -Al cermets it is necessary to rapidly heat the composite to a point near 1200°C to ensure wetting and then subsequently cool to temperatures much below 1200°C for the development of the desired microstructure.

3.2 Densification

B_4C -Al composites cannot undergo pressureless or pressure assisted densification unless wetting occurs. In ceramic-metal composites, it is established that phase rearrangement is the major densification mechanism during the liquid phase sintering. The extent of phase rearrangement depends on the degree of packing density and chemical inhomogeneities that exist in a powder compact after the initial consolidation. Due to phase rearrangement, these inhomogeneities are amplified during sintering. The formation of large voids due to the rearrangement of the liquid phase is of particular concern, especially in incompatible systems, such as B_4C -Al. Observations have shown that sintered, hot-pressed, and hot isostatically pressed B_4C -Al composites all possess large voids which are surrounded by rigid ceramic shells.

The problems associated with phase rearrangement during liquid phase sintering were used to our advantage when the fabrication process was modified, where liquid metal was infiltrated into the monolithic porous ceramic, in a manner similar to the densification of agglomerates (Appendix XX). This approach allows the densification of fully dense and uniform composites, as the optimized hydraulic resistance and the thickness of the porous substrates facilitate a rapid infiltration technique. To obtain porous B_4C substrates with modified surface characteristics, compacts were heat treated above 2000°C to obtain a ceramic skeleton. These B_4C substrates, with a predetermined amount of void percentage, were then infiltrated with molten Al at about 1200°C. As a result, two major types of B_4C -Al composites were formed. In the first case, the metal completely depleted to form a dense multi-ceramic microstructure. In the second case, a certain amount of Al was retained in the final microstructure. These two cases produced different microstructures with various interfacial characteristics resulting in wide variation in mechanical properties.

3.3 Microstructures

In contrast to liquid phase sintering where the development of microstructure depends mainly on the sintering temperature and time, the infiltration technique microstructures can be altered in several stages.

These stages are as follows: (i) The first is the dispersion and consolidation stage where colloidal dispersion and consolidation of B_4C powders control the B_4C/Al ratio of the final product. For high B_4C content (70%), highly dispersed aqueous suspensions (with pH at 10.5) were used, and for low B_4C contents, flocculated aqueous suspensions (with pH at 4) were used. (ii) The second stage is sintering, which is performed at 1800 to 2200°C and which results in the formation of B_4C "sponges." Depending on the sintering conditions, the total porosity, the grain and channel connectivity, and the chemical composition of the substrate can all be modified. (iii) The third stage is the infiltration stage, which is performed at about 1150°C. Depending on the time of infiltration and on the cooling schedule after the completion of infiltration, controlled microstructures with varying amounts of metal and reaction product phases can form. (iv) Lastly, there are post heat treatments which involve stress retraining procedures on the as-cooled composites. In addition, there is the modification of the microstructure of the metal phase, especially when alloying elements are also used.

3.4 Mechanical Properties

Samples of B_4C -Al composites prepared by the infiltration technique have been subjected to various mechanical property tests. Both the fracture strength (4-point bending) and fracture toughness (SENB) and Chevron Notch properties exhibit the best values for 35% initial Al content. These values are 645 MPa for the strength and $9.7 \text{ MPa}\cdot\text{m}^{1/2}$ for the toughness, 545 MPa for the strength and $14.4 \text{ MPa}\cdot\text{m}^{1/2}$ toughness, respectively.

Properties are not necessarily controlled by the total initial and retained Al phase alone, but also by the reaction products which especially form during the infiltration stage. It was also found that the porous B_4C skeleton itself cannot be responsible for the deviation of rule of mixtures seen in the property data. The maxima on the fracture strength and K_{Ic} data appear to be related to the continuity factor which is defined as the average number of connected grains.

Studies analyzing how alloying elements in Al affect the microstructures and the mechanical properties were also initiated during this period of the program. Both 2024 and 7075-Al alloys were used which are based mainly on Cu and Zn, respectively. As expected, the effect of alloying elements on the overall properties of the composites came from their tendency to form precipitates, thereby changing the properties of the metal phase. In addition, because of the high infiltration temperature ($> 1150^\circ\text{C}$), exceptionally high for metal processing, some desirable and undesirable formation of intermetallic compounds among the alloying elements and among B and C may take place. While there is a gradual decrease in hardness values as the metal content is increased, both in toughness and in strength there is a substantial initial increase before a gradual decrease takes place. This behavior was also observed in other classical ceramic-metal composites, such as WC-Co (Appendix XXVd). These changes in the mechanical properties of

B₄C-Al alloy composites that are affected by the microstructural variations as a result of processing variables will be one of the main focuses in the continuation of this program. These structural changes take place at nano-scale, especially at the ceramic-metal interfaces and in the metal phase, requiring high spatial resolution characterization techniques.

3.5 Summary and Conclusions

During this phase of the program, intrinsically hard and potentially tough lightweight cermets were developed by applying thermodynamical guidelines as processing principles. Composites of SiC-Al were shown to have a poor combination of mechanical properties and stability because of the uncontrollable reactions which take place during the infiltration stage. On the other hand, B₄C-Al cermets were successfully processed to yield excellent mechanical properties (fracture strength up to 645 MPa, fracture toughness up to 14.4 MPa.m^{1/2}). In this system, which is an incompatible ceramic metal composite, the wetting requirement of the ceramic phase by the metal was achieved by taking advantage of the chemical reactions between the ceramic and the metal phases. Since the retention of the metal phase in the final product is an essential requirement, the detrimental effect of the chemical reactions was minimized by using an infiltration technique. In this procedure, the molten metal is infiltrated into a partially sintered B₄C "sponge" having a predetermined amount of porosity which is filled by the metal phase to achieve a fully dense composite.

It has been illustrated that the unique properties associated with the individual phases which form in B₄C-Al cermets allow the formation of many "tailorable" microstructures with wide ranging mechanical properties. In addition, it has been shown that the introduction of alloying elements into the metal component has an added advantage in designing the composites now at the nano-scale, especially in controlling the interfacial characteristics between the ceramic and the metal. The next challenge will be in the understanding and controlling of these nanostructural features in the further development of the B₄C-Al cermets.

4. Theoretical Studies

The goal of the theoretical studies is to provide a fundamental understanding of various phenomena that occur in the various stages of colloidal processing, namely, dispersion, consolidation, and sintering, and as a result, to help design better procedures to process ceramic materials to meet specific needs. During the past few years, the theoretical program has grown significantly. We have been able to extend our studies from monodispersions to bimodal systems, from equilibrium calculations to non-equilibrium ones.

from electrostatically stabilized systems to sterically stabilized ones, from bulk properties to interfaces. The results are very fruitful.

The achievements are outlined as follows: (1) A general equilibrium phase diagram for monodisperse systems which summarizes the stability region of the colloidal solids, the colloidal liquids, and the colloidal gases in the parameter space (see Appendix XXI); (2) Phase diagrams of monodisperse and bimodal charged colloidal particles (see Appendices XXII and XXVe); (3) Non-equilibrium aggregation studies for monodisperse as well as binary colloidal suspensions (see Appendices XXIII, XXIV and XXVf); and (4) Polymer adsorption on colloidal particles and steric interactions between colloidal particles (see Appendix XXVg).

The work in (1) is concerned with the general equilibrium phase diagram of monodisperse colloidal systems. The essence of the work is that I. A. Aksay and R. Kikuchi were able to develop a lattice-gas model in which there exists three distinct phases. The ordered low-temperature phase is identified as the solid phase. The two disordered phases, one of which has a higher density than the other, are identified as the liquid phase and the gas phase, respectively. The use of the cluster variation method (CVM) enables the authors to obtain the phase diagram in the parameter space accurately. The phase diagram summarizes the stability regions of the solids, liquids, and gases when the interparticle attraction energy is varied. This work has served as a general guideline for much of the experimental work (for the details, see the review in Appendix XXI) and also has served as a nucleus for the rest of the theoretical effort.

The work in (2) is concerned with the crystallization of colloidal particles under repulsive conditions. The essence of this work is that the authors Shih et al. were able to calculate the free energies of *all* phases (the various crystalline phases as well as the liquid phase) with a variational principle. Because they treated all phases on equal footing, they were able to come up with very accurate theoretical phase diagrams. For the monodisperse systems, the theory predicted the body-centered-cubic (bcc) and the face-centered-cubic (fcc) crystalline structures for the colloidal solids. The bcc phase exists only when the particle charge is high and the particle density is low, while the fcc phase dominates in most of the solid phase regions (see Appendix XXII). These predictions are in very good agreement with experiments on various colloidal systems. In particular, in the ceramic suspensions where the particle charge is usually not too high, the fcc phase has been identified with monodisperse silica suspensions. As for bimodal systems, the theory predicts instability of the substitutional crystals against the formation of the liquid phase. Let γ denote the ratio of the diameter of the small particles to that of the large particles. When γ is close to 1, say, 0.8, although the system can freeze into a crystalline solid, the freezing density as a function of the small-particle concentration has a maximum at some intermediate concentration; when γ is farther from 1, say, 0.5, the crystalline phase *cannot* be formed in most of the phase space, except in the regions that are close to the pure cases. The implication of these predictions is that in most bimodal (or polydispersed) systems, one gets colloidal "glasses" rather than colloidal crystals and hence a narrower pore size distribution.

These predictions provide a fundamental understanding for the consolidation behavior in bimodal colloidal systems as described in Section 2.

The work in (3) is concerned with the agglomeration in monodisperse systems as well as in binary suspensions when the colloidal particles are under attractive conditions. Agglomeration is a *non-equilibrium* phenomenon and thus *cannot* be explained by an equilibrium theory. The essence of this work is that the authors were able to develop a *non-equilibrium* aggregation model in which they allow the interparticle attraction E to be finite so that binding and unbinding are both possible. It turned out that the colloidal aggregates can be either *fractal* or compact depending on the condition. The fractal dimension of the aggregates can vary with E and with time. We have also estimated the sedimentation density as a function of E , which closely resembles the experimental curve. In colloidal processes, as a rule, one has non-equilibrium situations rather than equilibrium ones. Therefore, the theory provides a better fundamental understanding as to how the structure of the agglomerated solids varies with experimental conditions and also provides a new way of characterizing the structure of the agglomerated solids, namely, the fractal dimension. A detailed comparison between the theory and the experiments is given in Appendix XXIV.

As for binary suspensions, experimentally, it is seen that an initially stable suspension of alumina particles can be induced to undergo flocculation when a less attractive species, e.g., organic microemulsion particles, is added to the suspension. Furthermore, when the organic microemulsion particle density reaches some critical value the whole suspension becomes free from flocculation again. The details of the experiments are contained in Section 2. This phenomenon is analogous to the so-called depletion flocculation and depletion stabilization in polymer-colloidal systems. To explain this phenomenon, we have performed both aggregation simulations as well as equilibrium calculations. The aggregation simulations show exactly the same behavior as seen in the experiments; i.e., the cluster size has a peak with respect to the density of the second-species particles while the equilibrium calculations show a monotonic increase in cluster size with respect to the second-species particle density. The discrepancy between the result of the simulations and that of the equilibrium calculations clearly indicates that the restabilization of the first-species particles at higher second-species-particle densities is due to kinetics. This work is especially important in interpreting the experimental results in sterically stabilized systems that contain excess polymer in solution.

The work in (4) is concerned with the polymer adsorption on colloidal particles and the steric interaction between colloidal particles. So far, most theoretical studies of polymer adsorption have dealt with *single-chain* adsorption behavior. In reality, this is rarely the case. It is therefore important to study the multi-chain adsorption. We have studied the multi-chain adsorption with equilibrium calculations as well as with computer simulations.

While most computer simulations deal with single-chain adsorption for neutral polymers, we have done simulations for *multichain* adsorption of neutral polymers as well as polyelectrolytes. The preliminary

results show that when the monomers have repulsion between themselves such as in the case of charged polyelectrolytes, the saturated adsorption amount is smaller than when there is no repulsion between monomers. This agrees with experiments described in Section 2. The simulation further indicates that in the repulsive condition, although the adsorption amount is smaller, the height of the adsorption layer is actually larger. The adsorption height determines the range of the steric interaction between two adsorbed layers and is therefore an important parameter in tailoring the interparticle interaction. Another advantage of the simulation is that it can give structural information which can be directly compared with neutron or x-ray scattering data.

In summary, the results of the theoretical studies are very encouraging. We have been able to extend the studies to various conditions ranging from monodispersions to binary suspensions, from electrostatic interactions to steric interactions, and from equilibrium calculations to non-equilibrium ones. In addition, we have provided more fundamental understanding for the experiments.

5. Personnel

1. Professors

- a. I.A. Aksay b. R. Kikuchi c. M. Sarikaya

2. Research Associates

- a. D.M. Dabbs b. A.J. Pyzik c. W.Y. Shih
d. B. Sonuparlak

3. Visiting Scientists

- a. T. Yogo b. M.E. Persson

4. Research Staff

- a. D.L. Milius

5. Graduate Students

- a. R.M. Allmann III h. T. Laoui
b. J. Cesarano III i. J. Liu
c. L.A. Chick j. D.L. Milius
d. S.K. Fukuda k. N. Shinohara
e. D.M. Gallagher l. R. Yamada
f. C. Han m. M. Yasrebi
g. G.H. Kim

6. Undergraduate Students

- a. A.M. Davis h. J.M. Kiehlbauch
b. J.M. Day i. C.B. Martin
c. M.J. Edwards j. E.C. Martin
d. M.B. Giuffre k. S.S. Pak
e. M.J. Gordon l. H.H.S. Ro
f. G.L. Jones m. S.C. Wong
g. S. Jones

6. Facilities

The following equipment was purchased for use by the research group with funding from grant no. AFOSR-83-0375.

Description

- ASEA Pressure System, spare parts, optional elect. hyd. C, molybdenum furnace, \$50.00.
- Perkin-Elmer-Thermal analysis system, Disc drive, professional computer, keyboard, TAC7-instrument controller, demo model AD2-Z, TGA-thermogravimetric analyzer, monitor: model 7500, \$5,000 + 2,000 dem.
- Leeds & Northrup, Pyrometer, heating elements, automatic pyrometer, objective lens, \$2,692.
- Nicolet, 5DXB FT-IR Spectrometer System, \$9,384.
- Water still, Mega Pure, cartridge demineralizer, cartridge organic removal, wall bracket, \$1,020.
- Richard Brew Furnace, element, Model 466, \$969.
- Allied Fisher, Scientific pH meter, \$718.
- Brookfield Engr. Lab equipment, Thermogel, extra sample chamber, extra spindle, \$1,553.
- Astro Industries, heating element for Astro Model 2570, \$1,295.
- Ili Temp. Graphite, tube furnace, \$60,274.
- Gatan Inc. - Cold, stage for Model 600, Dual Ion Mill, \$3,970.
- Brookhaven - light, scattering system, B1 - 200 SM Goniometer with options, B1 - 4 T multiple, sample time, B1 - CON stepping motor, controller fiber, \$34,735.
- Newport Optical Table, Vibration Isolation System, XK 4A-28, Air Filter, Ar-F, \$8,578.

- Spectra Physics - Laser, 15 mW HeNe Laser, model XK 124-B, \$3,337.
- Power Meter Newport, Model 820 AC, \$1,175.
- ONCTI 182509, IBM-AT computer wkstn, 80287 NDP, cable for printer model 339, Microsoft C Compiler Ver 3.0, Fortran Compiler Ver. 3.31, DOS Programmers Ref. Man., Macro assembler 4.0, Word Ver. 3.0, IBM-AT Technical Ref. Man., \$5,126.
- EGA & graphics card & Epson FX - 85 Printer, \$913.
- NEC - Multisync Hi - Res. Color Monitor, \$720.
- AST Rampage/Port with 512 K, \$793.

7. Technical Communications

7.1 Presentations

1. Aksay, I.A. and Sarikaya, M., "Mullitization of Kaolinite," presented at the 36th Pacific Coast Regional Meeting of the American Ceramic Society, San Diego, CA, October 3-5, 1983.
2. Pyzik, A. and Aksay, I.A., "Development of B₄C/Cu-Alloy Cermets," presented at the 36th Pacific Coast Regional Meeting of the American Ceramic Society, San Diego, CA, October 3-5, 1983.
3. Sonuparlak, B. and Aksay, I.A. "Kaolinite Reaction Series," presented at the 36th American Ceramic Society Annual Meeting, Pittsburgh, PA, April 29-May 3, 1984.
4. Pyzik, A.J. and Aksay, I.A., "Phase Rearrangement during Liquid Phase Sintering." presented at the 86th American Ceramic Society Annual Meeting, Pittsburgh, PA, April 29-May 3, 1984.
5. Aksay, I.A., Kikuchi, R., Allman, M. III, and Davutoglu, A. "Phase Transitions in Colloidal Systems," presented at the 58th Colloid and Surface Science Symposium of the American Chemical Society, Pittsburgh, PA, June 11-13, 1984.

6. Aksay, I.A., "Structure of Colloidal Phases," presented at the "Ceramic Films & Substrates," Aurora, NY, July 15-18, 1984.
7. Sonuparlak, B. and Aksay, I.A. "Mullite Formation with Molecularly Mixed $\text{SiO}_2\text{-Al}_2\text{O}_3$," presented at the 37th Pacific Coast Regional American Ceramic Society, San Francisco, CA, October 28-November 1, 1984.
8. Yasrebi, M. and Aksay, I.A., "Microstructural Uniformity in Ceramic-Organic Binder System," presented at the 37th Pacific Coast Regional of American Ceramic Society, San Francisco, CA, October 28-November 1, 1984.
9. Aksay, I.A., "Defects in Colloidal Crystals," presented at the 37th Pacific Coast Regional of the American Ceramic Society, San Francisco, CA, October 28-November 1, 1984.
10. Milius, D., Pyzik, A.J., and Aksay, I.A., "Sintering of SiC With Liquid Aluminum," presented at the 37th Pacific Coast Regional of the American Ceramic Society, San Francisco, CA, October 28-November 1, 1984.
11. Han, C. and Aksay, I.A., "Uniform Densification of Bimodal Particle Systems," presented at the 37th Pacific Coast Regional of the American Ceramic Society, San Francisco, CA, October 28-November 1, 1984.
12. Sonuparlak, B., Yasrebi, M., and Aksay, I.A., "Processing of High Strength Porous Alumina," presented at the American Ceramic Society 87th Annual Meeting, Cincinnati, OH, May 5-9, 1985.
13. Cesarano, J. and Aksay, I.A., "Polyelectrolyte Adsorption on $\alpha\text{-Al}_2\text{O}_3$ and Aqueous Suspension Stability," presented at the American Ceramic Society 87th Annual Meeting in Cincinnati, OH, May 5-9, 1985.
14. Aksay, I.A., "Structural Characteristics of Alumina-Rich Melts in the System $\text{Al}_2\text{O}_3\text{-SiO}_2$," presented at the American Ceramic Society 87th Annual Meeting in Cincinnati, OH, May 5-9, 1985.
15. Pyzik, A.J. and Aksay, I.A. "Processing of High Toughness Boron Carbide - Aluminum Composite," presented at the American Ceramic Society 87th Annual Meeting, Cincinnati, OH, May 5-9, 1985.
16. Cesarano, J. and Aksay, I.A., "Interaction of Polymethacrylic Acid with $\alpha\text{-Al}_2\text{O}_3$ in Aqueous Suspension," presented at the 59th International Conference on Surface and Colloid Science, Clarkson University, Potsdam, NY, June 24-28, 1985.

17. Sarikaya, M., Pyzik, A.J., and Aksay, I.A., "Effect of Secondary Phases on the Properties of B_4C -Al Composites," presented at the American Ceramic Society Pacific Coast Regional Meeting, Irvine, CA, October 27-30, 1985.
18. Pyzik, A.J. and Aksay, I.A., "Processing, Microstructure, and Mechanical Properties of Boron Carbide - Aluminum Alloy Composites," presented at the 38th Pacific Coast Regional Meeting of the American Ceramic Society, Irvine, CA, October 27-30, 1985.
19. Sonuparlak, B., Sakai, M., Yasrebi, M., and Aksay, I.A. "Processing Method to Retain the Strength of Fully Dense State in Porous Ceramics," presented at the 38th Pacific Coast Regional Meeting of the American Ceramic Society, Irvine, CA, October 27-30, 1985.
20. Milius, D., Pyzik, A.J., and Aksay, I.A., "Processing and Mechanical Properties of AlB_2 -Al Composites," presented at the 38th Pacific Coast Regional Meeting of the American Ceramic Society, Irvine, CA, October 27-30, 1985.
21. Aksay, I.A., "Forming of Ceramics with Submicron Size Powders," presented at the 13th Automotive Materials Conference, *Processing of Automotive Ceramics*, University of Michigan, Ann Arbor, Michigan, November 6-7, 1985.
22. Aksay, I.A., Shinohara, N., and Sonuparlak, B., "Processing of Mullite Ceramics," presented at the 88th Annual American Ceramic Society Meeting, Chicago, IL, April 27-May 1, 1986.
23. Yasrebi, M. and Aksay, I.A., "Processing of Dense Ceramic Bodies from Ceramic-Organic Binder Compacts," presented at the 88th American Ceramic Society Meeting, Chicago, IL, April 27-May 1, 1986.
24. Shinohara, N., Sonuparlak, B., and Aksay, I.A., "Processing of Mullite Ceramics," presented at the 88th Annual American Ceramic Society Meeting, Chicago, IL, April 27-May 1, 1986.
25. Gallagher, D. and Aksay, I.A., "Solvent and Surfactant Effects in Co-Dispersion," presented at the 88th Annual American Ceramic Society Meeting, Chicago, IL, April 27-May 1, 1986.
26. Sarikaya, M., Aksay, I.A., and Pyzik, A.J., "Microdesigning of Ceramic-Metal Composites," presented at the Ceramic Microstructures '86: Role of Interfaces Symposium, Berkeley, CA, July 28-31, 1986.

27. Sarikaya, M., "High-Resolution TEM Studies of Mullite Formation in Metakaolinite," presented at the 44th Annual Meeting of Electron Microscopy Society of America, Albuquerque, NM, August 10-15, 1986.
28. Dabbs, D.M. and Aksay, I.A., "Infrared Transparent Mullite for Use Above 1600°C," presented at the 30th Annual SPIE Technical Symposium on Infrared & Optical Transmitting Materials, San Diego, CA, August 18, 1986.
29. Dabbs, D.M. and I.A. Aksay, "FTIR Characterization of Mullite-Forming Gels," presented at American Ceramic Society 39th Pacific Coast Regional Meeting, Seattle, WA, October 22-24, 1986.
30. Gallagher, D. and I.A. Aksay, "Surfactant Adsorption on B₄C and Al Interfaces in Nonaqueous Solutions," presented at American Ceramic Society 39th Pacific Coast Regional Meeting, Seattle, WA, October 22-24, 1986.
31. Hirata, Y. and I.A. Aksay, "Long Range Particle Segregation in Colloidal Filtration," presented at American Ceramic Society 39th Pacific Coast Regional Meeting, Seattle, WA, October 22-24, 1986.
32. Shinohara, N. and I.A. Aksay, "Sintering and Cracking Behavior of Boehmite with α -Al₂O₃ Additive," presented at American Ceramic Society 39th Pacific Coast Regional Meeting, Seattle, WA, October 22-24, 1986.
33. Shinohara, N., I.A. Aksay, and B. Sonuparlak, "Sintering of Monolithic Mullite Gel from Boehmite and TEOS," presented at American Ceramic Society 39th Pacific Coast Regional Meeting, Seattle, WA, October 22-24, 1986.
34. Yamada, R. and I.A. Aksay, "Translucent Mullite Ceramics Fully Densified at 1250°C," presented at American Ceramic Society 39th Pacific Coast Regional Meeting, Seattle, WA, October 22-24, 1986.
35. Sonuparlak, B. and I.A. Aksay, "Processing of Mullite Matrix Composites," presented at American Ceramic Society 39th Pacific Coast Regional Meeting, Seattle, WA, October 22-24, 1986.
36. Cesarano III, J. and I.A. Aksay, "Aspects of Polyelectrolyte Stabilization and Aqueous Suspension Processing," presented at American Ceramic Society 39th Pacific Coast Regional Meeting, Seattle, WA, October 22-24, 1986.
37. Aksay, I.A. and D.L. Milius, "Impact Resistance of B₄C/Al Composites," presented at American Ceramic Society 39th Pacific Coast Regional Meeting, Seattle, WA, October 22-24, 1986.

38. Aksay, I.A. and D.L. Milius, "Input Resistance of B₄C/Al Composites," presented at American Ceramic Society 39th Pacific Coast Regional Meeting, Seattle, WA, October 22-24, 1986.
39. Laoui, T., M. Sarikaya and I.A. Aksay, "Characterization of a New Phase in Al-B-C Ternary System," presented at American Ceramic Society 39th Pacific Coast Regional Meeting, Seattle, WA, October 22-24, 1986.
40. Kim, G.H., M. Sarikaya and I.A. Aksay, "Characterization and Fractography of B₄C-Al Alloy Cermet," presented at American Ceramic Society 39th Pacific Coast Regional Meeting, Seattle, WA, October 22-24, 1986.
41. Sarikaya, M. and I.A. Aksay, "High Resolution Transmission Electron Microscopy Investigation of the Interfaces in Ceramic-Metal Composites," presented at American Ceramic Society 39th Pacific Coast Regional Meeting, Seattle, WA, October 22-24, 1986.

7.2 Publications

1. Sarikaya, M., I.A. Aksay, and G. Thomas, "High Resolution Microscope Characterization of Interfaces in Ceramics," *Advances in Materials Characterization, II*. Eds. R.L. Snyder, R.A. Condrate, Sr., and P.F. Johnson (New York: Plenum Publishing, 1985).
2. Han, C., I.A. Aksay, and O.J. Whittemore, "Characterization of Microstructural Evolution by Mercury Porosimetry," *Advances in Materials Characterization, II*. Eds. R.L. Snyder, R.A. Condrate, Sr., and P.F. Johnson (New York: Plenum Publishing, 1985).
3. Halverson, D., A.J. Pyzik, and I.A. Aksay, "Processing and Microstructural Characterization of B₄C-Al Cermet," *Ceramic Engineering & Science Proceedings*, Vol. 6, No. 7-8 (July and August, 1985).
4. Aksay, I.A., "Fundamentals of Powder Consolidation in Colloidal Systems," in *Ceramics Today and Tomorrow*, Eds. S. Haka, H. Soga, and S. Kuma, Ceramic Society of Japan, Tokyo, Japan, (1986), pp. 71-85.
5. Shinohara, N., D.M. Dabbs, and I.A. Aksay, "Infrared Transparent Mullite Through Densification of Monolithic Gels at 1250°C," *SPIE Infrared and Optical Transmitting Materials*, Vol. 683, 19-24 (1986).

6. Sarikaya, M. and I.A. Aksay, "High Resolution TEM Studies of Mullite Formation in Metakaolinite." *Proceedings of 45th Annual Meeting of the Electron Microscopy Society of America*, G.W. Bailey, ed., San Francisco Press (1987).
7. Sonuparlak, B., M. Sarikaya, and I.A. Aksay, "Spinel Phase Formation at the 980°C Exothermic Reaction in the Kaolinite to Mullite Reaction Series." *J. Am. Ceram. Soc.*, to be published, November (1987).
8. Shih, W., I.A. Aksay, and R. Kikuchi, "Phase Diagrams of Charged Colloidal Particles," *J. Chem. Phys.* **86**(9), 5127-32 (1987).
9. Sarikaya, M., T. Laoui, D.L. Milius, and I.A. Aksay, "Identification of a New Phase in the Al-C-B Ternary by High Resolution Transmission Microscopy," *Proceedings of the 45th Annual Meeting of the Electron Microscopy Society of America*, G.W. Bailey, ed., San Francisco Press (1987).
10. Cesarano, J. III, I.A. Aksay, and A. Bleir, "Stability of Aqueous α -Al₂O₃ Suspensions," Submitted to *J. Am. Ceram. Society*, accepted for publication (1987).
11. Cesarano, J. III, and I.A. Aksay, "Interactions Between Polyelectrolytes and Oxides in Aqueous Suspensions." In "Surface and Colloid Science in Computer Technology," K.L. Mittal, ed. (New York: Plenum Press, 1987).
12. Aksay, I.A., W.Y. Shih, and M. Sarikaya, "Colloidal Processing of Ceramics," *Proceedings of the Third International Conference on Ultrastructure Processing of Ceramics, Glasses, and Composites*, held in San Diego, CA, February 23-27, 1987.
13. Shih, W.Y., I.A. Aksay, and R. Kikuchi, "A Reversible Growth Model: Cluster-Cluster Aggregation with Finite Binding Energies." In press: *Phys. Rev. A*, (1987).
14. Cesarano, J. III, and I.A. Aksay, "Processing of α -Al₂O₃ with Highly Concentrated Aqueous Alumina Suspensions." Submitted to *Am. Cer. Soc. Bulletin* (1987).
15. Pyzik, A., I.A. Aksay, and M. Sarikaya, "Microdesigning of Ceramic-Metal Composites," in *Ceramic Microstructures, '86* J.A. Pask and A.G. Evans, eds., Plenum Press, NY (1987).
16. Aksay, I.A. and R. Kikuchi, "Structures of Colloidal Solids," in *Science of Ceramic Chemical Processing*, L.L. Hench and D.R. Ulrich (eds.), John Wiley and Sons, New York (1986), pp. 513-21.

17. Halverson, D., A.J. Pyzik, I.A. Aksay, and W.F. Snowden, "Processing of Boron Carbide Aluminum," *Adv. Ceram. Mat.*, in press (1987).
Papers in Preparation
18. Liu, J., W.Y. Shih, R. Kikuchi, and I.A. Aksay, "On the Clustering of Binary Colloidal Suspensions," to be submitted to *J. Colloid Interface Sci.* (1987).
19. Han, C., and I.A. Aksay, "Sintering of Bimodal α -Al₂O₃ Compacts" to be submitted to *J. Am. Ceram. Soc.* (1987)
20. Hirata, Y. and I.A. Aksay, "Long Range Particle Segregation in Colloidal Filtration" to be submitted to *J. Am. Ceram. Soc.* (1987)
21. Sonuparlak, B., and I.A. Aksay, "High Strength Porous Ceramics: I. Processing" to be submitted to *J. Am. Ceram. Soc.* (1987)
22. Sakai, M., B. Sonuparlak, and I.A. Aksay, "Porous Al₂O₃ with Controlled Pores: II. The Effects of Pores on Fracture Parameters" to be submitted to *J. Am. Ceram. Soc.* (1987)
23. Shinohara, N., and I.A. Aksay, "Processing of Dense Al₂O₃ Through Gelation: I. Cracking Problem." to be submitted to *J. Am. Ceram. Soc.* (1987)
24. Shinohara, N. and I.A. Aksay, "Processing of Dense Al₂O₃ Through Gelation: II. Densification Kinetics." to be submitted to *J. Am. Ceram. Soc.* (1987)
25. Shinohara, N., M. Sarikaya, and I.A. Aksay, "Low Temperature Sintering of Mullite Through Sol-Gel Processing from Boehmite-TEOS." to be submitted to *J. Am. Ceram. Soc.* (1987)
26. Sarikaya, M., and I.A. Aksay, "High Resolution Electron Microscopy Characterization of Ceramic-Metal Interfaces," to be submitted to *J. Am. Ceram. Soc.* (1987)
27. Pyzik, A.J. and I.A. Aksay, "Relations Between Microstructure and Some Mechanical Properties on the B₄C-Al Composites," to be submitted to *J. Am. Ceram. Soc.* (1987)
28. Shih, W.Y., J. Lui, and I.A. Aksay, "Polymer and Polyelectrolyte Adsorption on Colloidal Surfaces," to be submitted to *J. Colloid Interface Sci.* (1987)

29. Chick, L.A. and I.A. Aksay, "The Influences of Alignment and Clustering on the Packing of Whiskers and Fibers," in *Proc. Mat. Res. Soc.*, (to be published 1988).
30. Yogo, T. and I.A. Aksay, "Mullite Synthesis from Aluminosiloxane Polymer," *J. Am. Ceram. Soc.*, manuscript in preparation, (1987).
31. Schilling, C.H., M. Yasrebi, and I.A. Aksay, "Flocculation Kinetics in Colloidal α -Al₂O₃ Suspensions: Effects on Microstructural Development in Cast Bodies," *J. Am. Ceram. Soc.*, manuscript to be published (1987).
32. Yamada, R., and I.A. Aksay, "Densification of Mullite Matrix Composites," *Proc. Mat. Res. Soc.*, to be published (1988).
33. D.L. Milius and I.A. Aksay, "Processing and Mechanical Properties of AlB₂-Al Composites," *J. Am. Ceram. Soc.*, in preparation (1987).
34. M. Sarikaya, T. Laoui, and I.A. Aksay, "Phase Identification in Al-B-C Ternary System," *J. Am. Ceram. Soc.*, in preparation (1987).
35. M. Sarikaya, D.L. Milius, and I.A. Aksay, "Characterization of Interfaces in Ceramic-Metal Composites by High Resolution Transmission Electron Microscopy," in *Atomic and Molecular Processing of Electronic and Ceramic Materials*, Materials Research Society, Proceedings of 23rd University Conference in Ceramic Science, Seattle, Aug. 30-Sept. 2, 1982.

7.3 Theses Granted

1. Han, C., "Sintering of Bimodal Compact," M.S., University of California (Los Angeles), 1985.
2. Cesarano, J. III, "Polyelectrolyte Adsorption on α -Alumina and Aqueous Suspension Behavior," M.S., University of Washington, 1985.
3. Laoui, T., "Morphological and Crystallographic Characterization of B₄C-Al Composites," M.S., University of Washington, 1986.
4. Milius, D.L., "The Sintering of Silicon Carbide with Liquid Aluminum," M.S., University of Washington, 1986.

5. Yamada, R., "Pressureless Sintering of Short-Fiber Reinforced Mullite," M.S., University of Washington, 1987.
6. Kim, G.H., "Microstructural and Fractographic Characterization of B₄C-Al Cermets," M.S., University of Washington, 1987.

7.4 Patents

1. Pyzik, A.J. and Aksay, I.A., *A Multipurpose Boron Carbide-Aluminum Composite and Its Manufacture via the Control of the Microstructure.*
2. Sonparlak, B. and Aksay, I.A., *Processing of Porous Ceramics with Strength Equal to its Dense State.*

ACKNOWLEDGMENT

The principal investigator is grateful for the contributions of G.C. Stangle, M. Sarikaya, W.Y. Shih, and D.M. Dabbs for their contributions in compiling this report. H.L. Larson is similarly acknowledged for her helpful editorial comments during all stages of the report preparation.

APPENDICES

- I. Cesarano and Aksay (1987a).
- II. Cesarano, Aksay, and Bleier (1987).
- III. Cesarano and Aksay (1987b).
- IV. Yasrebi, Aksay, and Cesarano (1987).
- V. Yasrebi and Aksay (1987).
- VI. Aksay (1985).
- VII. Han and Aksay (1987).
- VIII. Hirata (1987).
- IX. Han, Aksay, and Whittemore (1985).
- X. Sonuparlak and Aksay (1987).
- XI. Sakai, Sonuparlak and Aksay (1987).
- XII. Sonuparlak, Sarikaya and Aksay (1987).
- XIII. Sarikaya and Aksay (1987).
- XIV. Sarikaya, Aksay and Thomas (1985).
- XV. Sarikaya and Aksay (1987).
- XVI. Shinohara, Dabbs, and Aksay (1986).
- XVII. Halverson, Pyzik and Aksay (1985).
- XVIII. Halverson, Pyzik, Aksay, and Snowden (1987).
- XIX. Sarikaya, Laoui, Milius and Aksay (1987).
- XX. Pyzik, Aksay, and Sarikaya (1987).
- XXI. Aksay and Kikuchi (1986).
- XXII. Shih, Aksay, and Kikuchi (1987a).
- XXIII. Shih, Aksay, and Kikuchi (1987).
- XXIV. Aksay, Shih, and Sarikaya (1987).
- XXV. Abstracts of Papers in Preparation.
- XXVI. Theses abstracts.

APPENDIX I
Interactions Between Polyelectrolytes and Oxides in
Aqueous Suspensions

(Cesarano and Aksay 1987a)

INTERACTIONS BETWEEN POLYELECTROLYTES AND OXIDES IN AQUEOUS SUSPENSIONS

Joseph Cesarano III and Ilhan A. Aksay

Department of Materials Science and Engineering
University of Washington
Seattle, Washington 98195

Colloidal stability of aqueous $\alpha\text{-Al}_2\text{O}_3$ suspensions with polymethacrylic acid (PMAA) was studied in the pH range of 3 to 10. Stability is related to the adsorption of PMAA on $\alpha\text{-Al}_2\text{O}_3$ as controlled by the chemistries of both the $\alpha\text{-Al}_2\text{O}_3$ surface and the PMAA. The adsorption behavior of PMAA on $\alpha\text{-Al}_2\text{O}_3$ is basically "high affinity" type near and below the zero point of charge of $\alpha\text{-Al}_2\text{O}_3$ (pH 8.7). A stability map was determined which outlines the critical amount of adsorbed PMAA required to achieve dispersion.

INTRODUCTION

Polyelectrolytes are widely used in industrial applications to prepare highly concentrated (> 50 v/o) ceramic suspensions which are subsequently fabricated into dense components by sintering. Although a variety of polyelectrolytes are commercially available and are used effectively in the preparation of suspensions, their role in colloidal stabilization is not clearly understood.

In this paper, we aim to provide a clearer understanding of particle dispersion with adsorbed polyelectrolytes and relate it to the surface chemistries of the suspended particles and the polyelectrolyte. Aqueous oxide suspensions will be considered as a general example. The particular emphasis will be on the dispersion of $\alpha\text{-Al}_2\text{O}_3$ suspensions with polymethacrylic acid (PMAA).

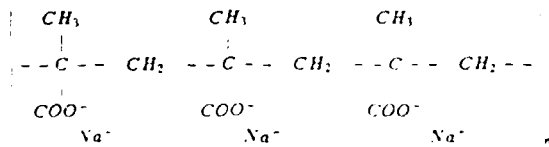
BACKGROUND INFORMATION

(1) Polyelectrolytes

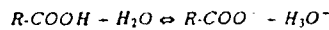
A polyelectrolyte is a polymer that contains ionizable functional groups which are capable of dissociating into ionized charged sites. A typical polyelectrolyte structure is shown in Fig. 1. In general, there are three types of polyelectrolytes. Anionic polyelectrolytes contain acid groups which can ionize to form negative sites, e.g., $-\text{COO}^-$ or $-\text{OSO}_3^-$. Cationic

polyelectrolytes contain basic groups that form positive sites, e.g., $-NH_2^+$. Polyelectrolytes which have both acid and basic groups are termed polyampholytes and can be negatively or positively charged. Since polyelectrolytes are ionic in nature they are generally water soluble.

In aqueous systems, the solution behavior and the extent to which the functional groups dissociate and the overall charge of the polymer are dependent on the surrounding pH and ionic strength. Using polymethacrylic acid (PMAA) as an example (Fig. 1), each acid group on the polymer chain will have its own effective dissociation constant (pQ); therefore, the fraction of the functional groups which are dissociated (α) will be dependent on the pQ values and the pH .



For each acid group:



$$Q = \frac{(R\text{-COO}^-)(H_3O^+)}{(R\text{-COOH})}$$

$$pQ = -\log Q = pH - \log \left(\frac{\alpha}{1-\alpha} \right)$$

Fig. 1: Structure and dissociation reaction for polymethacrylic acid - Na salt.

(2) Surface Charging of Oxides

When a metal oxide powder (i.e., Al_2O_3) is placed in an aqueous medium, surface reactions take place until equilibrium is established between the solid and the aqueous medium. This can be viewed as a two step process: formation of surface hydroxyls due to surface hydration, followed by ionization of these hydroxyl groups to yield a positively or negatively charged surface depending on the pH of the solution.¹

Many authors have modeled the dissociation of the hydroxide surface to yield a positively or negatively charged surface. The common explanation is that the surface sites ionize to form positive and negative sites and the resulting sites then react with counterions in solution.¹⁻⁶ In general, the dissociation of the surface hydroxyl groups is represented as:

$$MOH_2^+ = MOH^0 - H_3^+ \quad K_1 = \frac{MOH^0 \cdot H_3^+}{MOH_2^+} \quad \text{and} \quad (11)$$

$$MOH^0 = MO^- + H_3^+ \quad K_2 = \frac{MO^- \cdot H_3^+}{MOH^0} \quad (12)$$

where,

- M is a surface metal ion site
- MOH^0 is a neutral, hydroxylated surface site
- MOH_2^+ is a positive surface group
- MO^- is a negative surface group
- H_3^+ is a proton located at the surface, and
- $K_{1,2}$ are the respective equilibrium reactions constants.

The reactions above show that at low pH values the reactions will proceed to the left and the formation of positive MOH_2^+ surface sites will be dominant. Similarly, at high pH values (low concentration of H_3^+) the reactions will proceed to the right and the formation of negative MO^- surface sites will be dominant. It should be noted that at any given pH there are equilibrium concentrations of all of the surface species (i.e., MOH_2^+ , MOH^0 , MO^-). For example, at high pH values there are mostly MO^- sites, but depending on the reaction constants there can still be appreciable concentrations of MOH^0 and MOH_2^+ sites. At a characteristic pH , the concentrations of MOH_2^+ and MO^- sites will be equal and the overall net surface charge will be zero. This characteristic pH for a given material is termed the zero point of charge (zpc) for that material. For pH values below the zpc, the net surface charge is positive and above the zpc the net surface charge is negative.

In general, the characteristic pH for the zpc for a given oxide is strongly dependent on the relative basic and acidic properties of the solid. The crystalline form, material preparation, and the degree of surface hydroxylation will also affect the zpc. For example, the zpc for Al_2O_3 has been reported to be from 6.5 to 9.5.^{1,7,8}

(3) Polyelectrolyte Adsorption Behavior

When charged polymers are adsorbed onto oxides to cause flocculation or stabilization, it is generally true that electrostatic interaction is the primary adsorption mechanism. In other words, polyelectrolytes adsorb much more appreciably when oppositely charged to the solid adsorbent. When the polyelectrolyte and solid are similarly charged, some adsorption can still occur, but this adsorption is comparatively low.

Some typical examples of polyelectrolyte adsorption on oxides are given below. In the flotation industry, the percent recovery of a mineral is related to how efficiently the collector (anionic or cationic surfactant) is adsorbed. As shown in Fig. 2, the percent recovery (and adsorption of anionic and cationic surfactants) is mainly determined by the surface charge on goethite ($HFeO_2$). Therefore, pH is the most important variable. Below pH 6.7 goethite is positively charged and above pH 6.7, it is negatively charged. Therefore, it is clearly shown that the collector must be anionic when the solid is positively charged and cationic when the solid is negatively charged. Flotation ceases at pH 12.3 as a result of hydrolysis of the cationic surfactant at such a high pH .¹⁰ Therefore, it can be concluded that the basic adsorption is electrostatic in nature and involves the ionized form of the surfactant. Modi and Fuerstenau¹¹ have shown that these phenomena hold for corundum (Al_2O_3), and Iwasaki, Cooke, and Choi¹² have shown that the flotation of hematite (Fe_2O_3) can be explained by these principles.

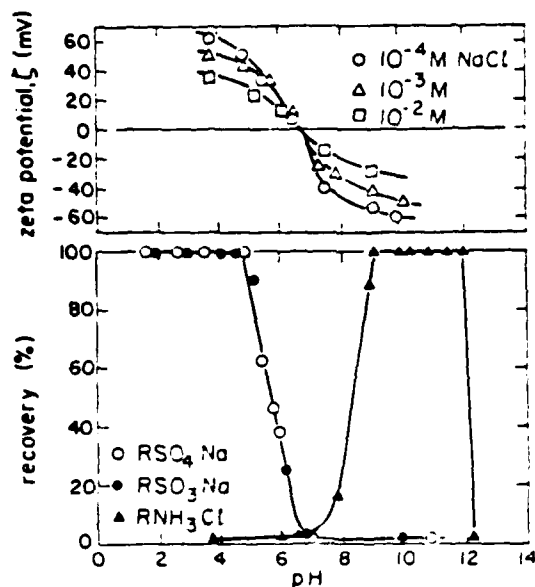


Fig. 2: The dependence of the flotation properties of goethite on surface charge. Upper curves are zeta potential as a function of pH at different concentrations of sodium chloride. Lower curves are the flotation recovery in 10⁻³ M solutions of dodecyl ammonium chloride, sodium dodecyl sulfate, or sodium dodecyl sulfonate. From ref. 9

Gebhardt and Fuerstenau¹³ studied the adsorption of anionic polyacrylic acid (PAA) on rutile (TiO₂), hematite, and silica as a function of pH. The amount of PAA adsorbed on Fe₂O₃ is shown in Fig. 3. The zpc of Fe₂O₃ occurs at pH 8.3 and the adsorption decreases to near-zero values at pH values above 8.3. Similar adsorption behavior was found for TiO₂ which has a zpc of 6.3. No adsorption in the pH range 3-9 was observed for silica which has a zpc at approximately pH 2.5. In conclusion, for PAA adsorption on oxides it was determined that the PAA adsorption plateau level decreases with increasing pH until near-zero values of adsorption occur near the zpc of the oxide but some specific adsorption still occurs at the zpc. It was also determined that positive zeta potentials are reversed to negative as PAA is adsorbed.

Lopatin¹⁴ found similar behavior when polymethacrylic acid (PMAA) was adsorbed onto anatase (TiO₂). It was suggested that the adsorbed molecules form a monolayer of interpenetrating coils and that electrostatic bonding to anatase, which is positively charged on the acid side of an isoelectric zone between pH 4 and 6, is the primary mechanism for adsorption at pH values from 2 to 4. Below pH 2, entropy effects and hydrogen bonding may be the dominant factors; above pH 4, adsorption falls rapidly to zero.

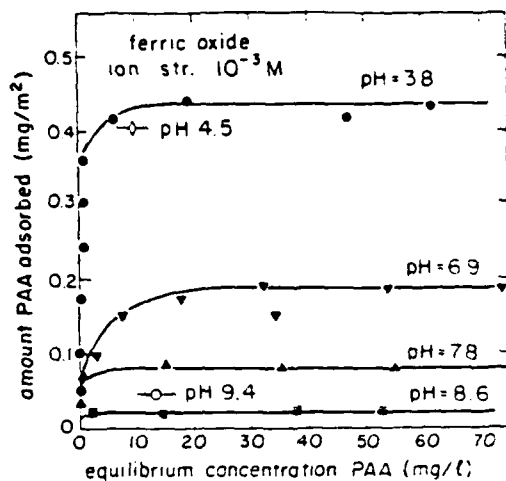


Fig. 3: Amount of PAA (MW 2×10^6) adsorbed on hematite as a function of equilibrium PAA concentration for various pH values. From ref. 13.

EXPERIMENTAL MATERIALS AND METHODS

In order to more clearly unify the concepts previously discussed for a working system, some experiments were conducted using polymethacrylic acid as the polyelectrolyte and $\alpha\text{-Al}_2\text{O}_3$ as the colloidal powder.

(1) Materials and Chemicals

The Na^+ salt of polymethacrylic acid (PMAA-Na)^{*} used had an average molecular weight of 15,000 (Fig. 1). The alumina powder used was a very high purity $\alpha\text{-Al}_2\text{O}_3$.[†] The average particle diameter was $0.37 \mu\text{m}$ and the surface area was $5.9 \text{ m}^2/\text{g}$.

The water used was distilled and deionized. Adjustments of pH were completed with analytical grade HCl and NaOH solutions and ionic strength was adjusted with NaCl as desired.

(2) Potentiometric Titrations

To measure the fraction of dissociated COOH groups (α) versus pH for PMAA-Na and the surface charge (σ) versus pH for Al_2O_3 , potentiometric titrations of the control electrolytes were compared to titrations of the samples.[‡]

^{*}Polysciences, Inc., Pittsburgh, PA.

[†]Sumitomo Chemical America, Inc., New York, NY (AKP-30; > 99.99% pure).

[‡]Radiometer TRS822 automatic titration unit, Radiometer, Copenhagen, Denmark.

This procedure of using potentiometric titrations to determine surface chemistries is clearly outlined by Hunter.¹⁵ Titrations are completed on a blank electrolyte solution and electrolyte solution with a known amount of sample. The difference between the amounts of titrant added to obtain a certain *pH* is the amount of titrant that reacted with the sample. With this information both the fraction of functional groups dissociated on polymers and the surface charge on ceramic powders can be easily calculated.

The titrations were completed in a nitrogen atmosphere and in each case 40 ml samples had known but small volumes of PMAA-Na (< 0.1 g) and Al_2O_3 (< 2 vol %) and when necessary NaCl solutions were used to adjust ionic strength. Prior to titration, the Al_2O_3 powder was cleaned to remove soluble ions using soxhlet extraction. With this technique the powder is continuously washed with freshly distilled water.

(3) Adsorption Isotherms

The adsorption of PMAA-Na on α -alumina was also determined using the titration unit. Suspensions of 20 vol % Al_2O_3 were prepared with various amounts of PMAA at various *pH* values. The samples were then put into a gentle mechanical shaker for approximately 24 hours and then centrifuged for 45 minutes at 2000 RPM. A known amount of supernatant was then analyzed by titration to determine the amount of PMAA left in solution.

(4) Settling and Zeta Potential Experiments

Settling experiments were completed with 2 vol % Al_2O_3 suspensions. Various amounts of PMAA-Na were added to the suspensions and were then ultrasonicated and magnetically stirred for at least 4 hours. Suspensions were then poured into graduated cylinders and after several days the final sedimentation cake heights were recorded.

Zeta potential measurements of each sample described above were completed with a Micro-Electrophoresis Apparatus.* These measurements can only be completed on very dilute suspensions. Therefore, it was very important that the 2 vol % Al_2O_3 samples were centrifuged and the supernatant carefully decanted into a beaker. Then a portion of the sediment was remixed with the supernatant. Prior to taking the measurements the new dilute suspensions were very briefly ultrasonicated and magnetically stirred for 15 minutes to ensure that only singlet particles were measured. At least ten measurements were completed for each sample to ensure accuracy.

(5) Viscosity Measurements

Viscosity measurements of the suspensions were done with a rotary viscometer.†

* Rank Brothers, Bottisham, Cambridge, England.

† Brookfield Engineering Laboratories, Inc., Stoughton, MA.

EXPERIMENTAL RESULTS AND DISCUSSION

(1) Surface Chemistry of PMAA-Na and α - Al_2O_3

The polyelectrolyte polymethacrylic acid- Na^+ salt (PMAA-Na) (Fig. 1), with an average molecular weight of 15,000, has approximately 138 available carboxylic acid sites or functional groups per molecule. Depending on the solvent conditions (i.e., pH and ionic strength), the fraction of functional groups which are dissociated (i.e., COO^-) and those which are non-dissociated (i.e., $COOH$) will vary. As the fraction dissociated (α) increases from ~ 0 to ~ 1.0 , the polymer surface charge varies from relatively neutral to highly negative. Therefore, the behavior of the polymer in solution is also dependent on the solvent conditions. Fig. 4 shows the fraction of dissociated acid groups as a function of pH and background $NaCl$ concentration. As the pH and salt concentration increase, the dissociation and negative charge characteristics of the polymer increases.

Fig. 4 shows that at pH values of ≥ 8.5 the PMAA is effectively totally negative with $\alpha \sim 1$. In this condition, experimental evidence shows that the PMAA molecules are in the form of relatively large expanded random coils in solution.¹⁶ This results from electrostatic repulsion between the negatively charged surface sites. As pH is decreased the number of negatively charged sites also continually decreases until the PMAA is effectively neutral near pH 3.4 and $\alpha \rightarrow 0$. In this condition the PMAA chains approach insolubility and form relatively small coils or clumps.¹⁶

A plausible explanation for the role of salt concentration on the degree of dissociation is that the presence of salt results in electrostatic shielding between negatively charged sites on the PMAA and this causes a decrease in the probability of having non-dissociated acid groups (i.e., $COOH$) as explained below. At a given pH , the system is in a dynamic equilibrium state where any given acid group is part of the time dissociated and part of the time non-dissociated but the overall fraction dissociated remains constant. Upon an increase in salt concentration, the probability of COO^- groups being stable with surrounding Na^+ ions in close proximity increases and therefore the probability of H_3O^+ ions reacting with available COO^- groups to reform $COOH$ decreases. Therefore, upon dissociation, it is more difficult for COO^- groups to reform to $COOH$ and the dynamic equilibrium is shifted to a higher fraction of dissociation. Similarly, salt decreases the activity of H_3O^+ which shifts the equilibrium towards more dissociation as shown in Fig. 1.

Fig. 5 shows a measure of the relative charge density (σ) on the surface of the Al_2O_3 particles as a function of pH . At every pH , there is a large number of positive, neutral, and negative sites. The σ value gives the overall net charge density. At the zpc, the number of positive sites equals the number of negative sites and the net charge equals zero. For α - Al_2O_3 , the zpc is at approximately pH 8.7. Both σ values and the zpc are in very close agreement to that of Hass.¹⁷

In Fig. 5 a comparison with Fig. 4 indicates that there should be a great deal of electrostatic attraction between the negatively charged polymer and the positively charged Al_2O_3 particularly in the pH range from 3.5 to 5.7. This will be related to adsorption below.

(2) Adsorption of PMAA-Na on α - Al_2O_3

Fig. 6 shows the resulting adsorption for various pH values plotted as mg PMAA adsorbed per m^2 surface area of Al_2O_3 versus the initial amount of PMAA-Na added (on a dry weight basis of Al_2O_3). The solid diagonal line represents the adsorption behavior that would occur

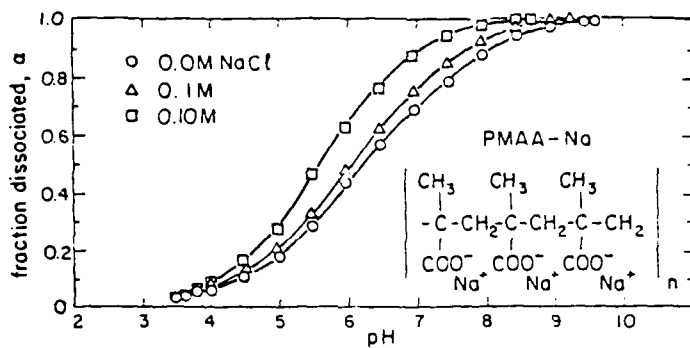


Fig. 4: Fraction of acid groups dissociated versus pH as a function of salt concentration for polymethacrylic acid-Na salt, MW 15000.

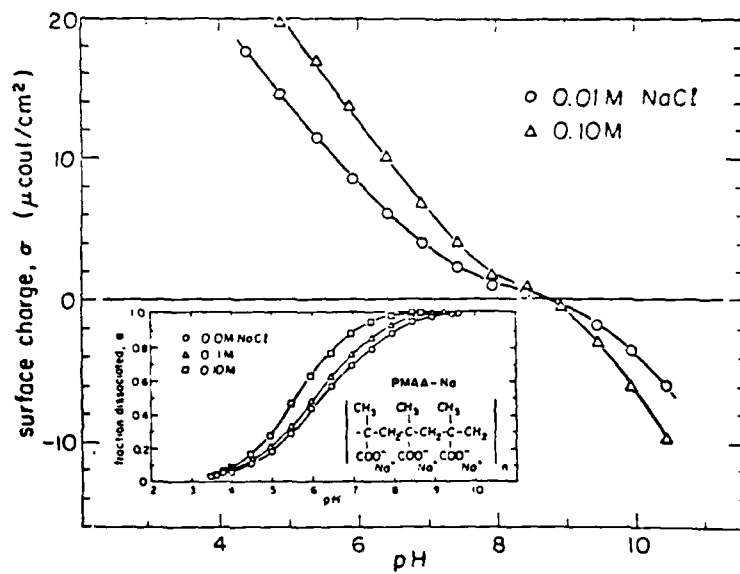


Fig. 5: The relative surface charge versus pH for Sumitomo AKP.30 $\alpha\text{-Al}_2\text{O}_3$ with an insert of Fig. 4.

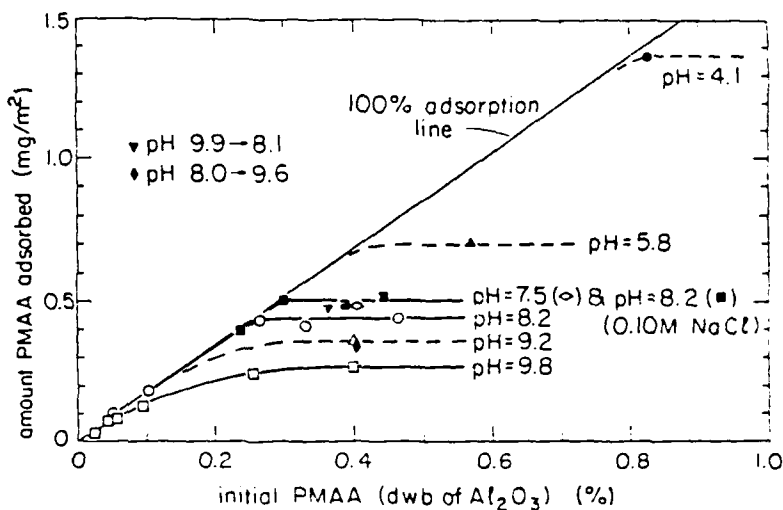


Fig. 6: The amount of polymethacrylic acid-Na salt adsorbed on Sumitomo AKP 30 α - Al_2O_3 as a function of initial PMAA-Na added.

if 100% of the PMAA added were to adsorb.

It is clearly shown that the amount adsorbed increases greatly with decreasing pH . This is in agreement with recent polyelectrolyte adsorption theory developed by Van der Schee et al.^{18,19} as explained below. For pH values above the zpc, α is approximately 1 and the negatively charged sites on the polyelectrolyte chains tend to repel each other. This repulsion suppresses the formation of loops in the adsorbed conformation. Consequently, the polyelectrolyte chains adsorb in a relatively flat conformation with each chain covering a relatively large amount of surface area. It should be noted that there still can be polyelectrolyte tails extending into solution even though the formation of loops is inhibited. The determined values for polyelectrolyte adsorption in this configuration were on the order of a few tenths of a mg/m^2 . As the pH is decreased and α approaches 0 (Fig. 4), the polyelectrolyte chains become uncharged and the formation of loops in the adsorbed configurations is enhanced. Thus, the covered surface area per adsorbed chain is relatively small, and it takes more adsorbed chains to form a saturated monolayer. Commonly measured values of this type of adsorption are a few mg/m^2 which is in agreement with the experimental results.²⁰

Fig. 6 also shows that there is a difference between the adsorption behavior above the zpc and below the zpc. For pH 9.8, there is a gradual attainment to the saturated adsorption plateau; but, at pH 8.2 and below plateau adsorption is reached without having any appreciable PMAA left in solution. Therefore, it is concluded that at pH values near and below the zpc, the adsorption behavior is basically "high affinity" type adsorption where practically all of the PMAA which is added adsorbs on the surface and follows the 100% line until a

saturation plateau level is reached. Only after that limit does non-adsorbed PMAA become appreciably present in solution. This also agrees with adsorption theory when there is an added electrostatic influence for adsorption and a negative or partly negative polyelectrolyte adsorbs on a positively charged surface.¹⁹ Above the zpc, due to similar net charges, a barrier for adsorption exists, so that in order to adsorb appreciable amounts of PMAA there has to be a corresponding equilibrium concentration of PMAA in solution. Adsorption in this region is due to the presence of positive surface sites even though the net surface charge is negative.

Fig. 6 also shows that the presence of background salt can slightly increase the adsorption. This occurs because the background salt has an electrostatic shielding effect between negatively charged sites on the PMAA thereby causing the chains to behave more like uncharged polymers and enhancing the development of loops. This type of behavior is commonly observed in many systems and is in agreement with adsorption theory.^{18,19} It should also be noted that even with 0.1 M NaCl concentrations stable suspensions are achieved after saturation adsorption occurred.

The degree of reversibility of this system is indicated by the ▼ and ♦ points in Fig. 6. At these points, the suspensions were made at the initial pH values indicated and shaken for 4 hours. The suspensions were then adjusted to the indicated pH values and shaken for 20 or more hours before an analysis was completed. The system which is initially at pH 9.9 and then adjusted to pH 8.1 adsorbs a final amount which is consistent with what is expected if the initial pH is already 8.1. This is expected since at pH 9.9 there is appreciable non-adsorbed PMAA in solution which could be easily adsorbed once the pH is lowered. A change in the configuration of the adsorbed PMAA may occur but there are no observable changes in the suspension behavior. On the other hand, when the initial pH is 8.0 and then adjusted to 9.6, total reversibility is not observed but only part of the expected PMAA desorbs. This shows that the PMAA is relatively strongly held on the Al_2O_3 surface. It also shows that with time most of the PMAA can desorb, at least for pH values near and above the zpc.

(3) Consolidated State

The effect of incomplete adsorption and flocculation on the consolidated state was determined by sedimentation and centrifugation experiments. Fig. 7(a) shows that trace amounts of PMAA-Na (< 0.25%) induces flocculation and large sedimentation volumes. This results because the binding energy between the particles is high and the particle clusters that form during consolidation behave as rigid flow units and do not pack densely.²¹ In contrast, at concentration levels of approximately 0.35-0.5% PMAA-Na, the binding energy between particles is low and the particle clusters display relatively denser packing structure.²¹

These data are also correlated with the zeta potential measurements for the same systems. Fig. 7(b) shows that with increasing polymer content, the zeta potential decreases to zero and then reverses sign. Above 0.5% polymer, the zeta potential approaches a nearly constant value. This is due to saturated monolayer adsorption of the anionic polyelectrolyte.

If one correlates the data from Figs. 7(a) and (b) it can be concluded that with small additions of PMAA-Na (i.e., < 0.1%) there is charge neutralization and subsequent flocculation. In this region flocculation is mainly due to electrostatic patch model flocculation whereby flocculation takes place because negatively charged patches due to the adsorbed polyelectrolyte are attracted to positively charged patches of surface on other particles. When the molecular weight is relatively low then maximum flocculation occurs when the zeta potential is approximately zero. This type of behavior is discussed by Bleier and Goddard²². In the

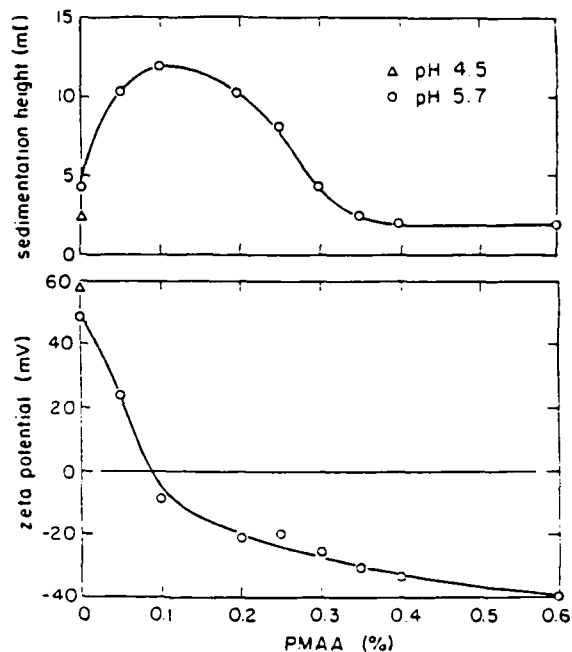


Fig. 7: (a) Sedimentation height and (b) zeta potential versus percent poly-methacrylic acid-Na (MW ~ 15,000) for 2 vol % suspensions of Sumitomo AKP 30 α - Al_2O_3 .

range 0.1 to 0.3% PMAA-Na, flocculation is due to a combination of two effects: (1) the zeta potential is relatively low in magnitude, and (2) incomplete adsorption results in polymer bridging where two or more particles can be mutually adsorbed by polymer chains.

It can also be concluded that the PMAA results in more efficient consolidation. Upon settling, the pure Al_2O_3 case (0% polymer) shows a larger sediment volume than the system with 0.4% polymer added even though the zeta potentials are -48 mV and -33 mV, respectively. The stability determined by settling rates and sedimentation heights do not appear to be equal until zeta potentials of ≥ 58 mV are reached for the pure Al_2O_3 suspensions. This means that the increased stability and dispersion of the 0.4% polymer system may be due to an enthalpic steric stabilization interaction in combination with the repulsion effect due to electrostatics. These mechanisms together can be termed electrosteric.

From these results some preliminary conclusions can be made: (1) only very minute amounts of PMAA-Na are necessary to flocculate Al_2O_3 suspensions, (2) a critical amount of PMAA-Na is needed before stabilization occurs, and (3) PMAA-Na does indeed provide an enhanced stabilization effect.

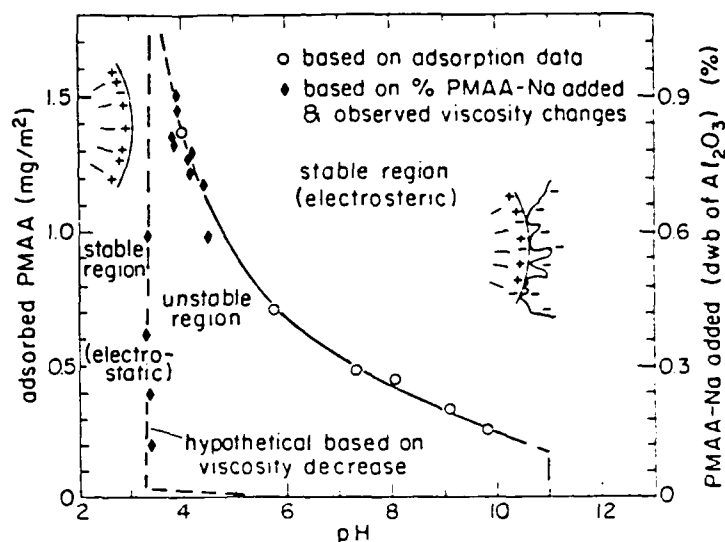


Fig. 8: A stability map showing the amount of adsorbed PMAA-Na required to form stable suspensions of Sumitomo AKP 30 α - Al_2O_3 as a function of pH.

(4) Stability Map for PMAA-Na/ Al_2O_3 System

With the above information and the adsorption data in Fig. 6 a stability map was constructed and is shown in Fig. 8.

Fig. 8 is a plot of the amount of PMAA adsorbed at the plateau levels versus pH. In other words, for any pH near and below the zpc, it is a measure of the amount of PMAA which must be adsorbed to achieve a stable suspension. Regions above the curve are stable and dispersed. Regions below the curve are unstable and show an onset to flocculation. The reason for the assumed steep decrease in adsorption at pH 3.3 is because of observed viscosity decreases. For example, as pH is decreased on samples which are initially stable, the viscosity noticeably increases when crossing the stability, instability boundary region. This is expected since at those lower pH values, it takes more PMAA to maintain a stable suspension and these suspensions are below that critical level. This is the same as moving to the left from a stable region on Fig. 8 and entering the unstable region. Once the pH is decreased further to pH 3.3, deflocculation reoccurs and viscosity sharply decreases and approaches that of a system stabilized at pH 3.3 without any PMAA present. Since at pH 3.3 Al_2O_3 is stable without the presence of PMAA due solely to electrostatic interactions, it is believed that there are a combination of two possible mechanisms for the observed restabilization of Al_2O_3 below pH 3.3 in the presence of PMAA. One explanation is that below pH 3.3 the PMAA sufficiently desorbs since this is also the pH at which the PMAA loses its negative charge and approaches that of a neutral polymer thereby losing a strong driving force for adsorption (Fig. 4) and losing its solubility. Concurrently, some PMAA may still be adsorbed but the effectively neutral polymer layer may be small enough so that the electric double layer

Table 1: Rheology data at various pH's for 20 v/o AKP-30 suspensions with 0.312% (dwb) of PMAA-Na MW 15,000.

pH	η (cp) at 10 RPM
5.2	1650
7.4	< 10
8.7	< 10
9.3	< 10
9.8	< 10
10.2	< 10

(formed by the highly positive Al_2O_3 surface) may extend past the polymer layer. In this way, electrostatic stabilization due to electric double layer interactions can still occur.

Table 1 illustrates the transition from stability to instability based on viscosity measurements. A series of samples with 0.312% PMAA were prepared at various pH values. Viscosities above pH 7 are < 10 cp while the viscosity at pH 5.2 is more than two orders of magnitude greater, indicating flocculation. This is in agreement with Fig. 8 which shows a stability instability transition at \sim pH 7 for 0.312% PMAA.

CONCLUSIONS

1. The adsorption behavior of polymethacrylic acid on alumina is very much dependent on solvent conditions and the surface charge characteristics of the PMAA and Al_2O_3 ; as pH is decreased the adsorption of PMAA increases until insolubility and charge neutralization of the PMAA is approached; for pH values near and below the zero point of charge for Al_2O_3 , there is an added electrostatic attractive potential for adsorption which results in a high affinity type adsorption behavior.
2. For pH values near and below the zpc, PMAA induces flocculation until an adsorption saturation limit is reached and the binding energy between particles is reduced below a critical level.
3. Once saturation adsorption occurs and stability is achieved, the PMAA induced stabilization shows an enhanced stability as compared to suspensions stabilized electrostatically without the presence of polyelectrolytes.
4. The stability map introduced here can be a useful processing tool for tailor-making suspensions with varying amounts of polymer from low to high pH's depending on the desired properties.

ACKNOWLEDGEMENTS

The authors gratefully acknowledge the contributions of Dr. Alan Bleier who directed part of the work at the Oak Ridge National Laboratory and Prof. Hans Lyklema whose insight and discussion were very helpful. This research was sponsored by the Advanced Research Projects Agency of the Department of Defense and was monitored by the Air Force Office of Scientific Research under Grant No. AFOSR-83-0375.

REFERENCES

1. P. L. de Bruyn and G. E. Agar, "Surface Chemistry of Flotation," in *Froth Flotation 50th Anniversary Volume*, D. W. Fuerstenau, ed., The American Institute of Mining Metallurgical, and Petroleum Engineers, Inc., (1962) p. 91.
2. S. Voyutsky, *Colloid Chemistry* (Translated from Russian by N. Bobrov), MIR Publishers, Moscow (1978).
3. W. J. Wnek and R. Davies, *J. Colloid Interface Sci.*, **60** 361 (1977).
4. R. J. Hunter, *J. Colloid Interface Sci.*, **37** 564 (1971).
5. D. E. Yates, S. Levine, and T. W. Healy, *Trans. Faraday Soc.*, **70** 1807 (1974).
6. G. A. Parks and P. L. de Bruyn, *J. Phys. Coll. Chem.*, **66** 967 (1962).
7. G. A. Parks, *Chem. Rev.*, **65** 177 (1965).
8. M. Robinson, J. A. Pask, and D. W. Fuerstenau, *J. Am. Ceram. Soc.*, **47** 516 (1964).
9. I. Awasaki, S. R. B. Cooke, and A. F. Colombo, "Flotation Characteristics of Goethite," U.S. Bur. Mines, Rep. Invest. 5593 (1960).
10. F. F. Aplan and D. W. Fuerstenau, "Principles of Nonmetallic Mineral Flotation," in *Froth Flotation 50th Anniversary Volume*, D.W. Fuerstenau, ed., The American Institute of Mining, Metallurgical, and Petroleum Engineers, Inc., (1962) p. 170.
11. H. J. Modi and D. W. Fuerstenau, *AIME Trans.*, **217** 281 (1960).
12. I. Iwasaki, S. R. B. Cooke, and H. S. Choi, *AIME Trans.*, **217** 227 (1960).
13. J. E. Gebhardt and D. W. Fuerstenau, "Adsorption of Polyacrylic Acid at Oxide/Water Interfaces," in *Colloids and Surfaces*, Elsevier Scientific Publishing Co., Amsterdam, (1983) p. 221.
14. G. Lopatin, "The Adsorption of Polymethacrylic Acid from Solution," Ph.D. Thesis, Polytechnic Institute of Brooklyn (1961).
15. R. J. Hunter, *Zeta Potential in Colloid Science - Principles and Applications*, Academic Press, New York (1981).
16. R. Arnold and J. Th. G. Overbeek, *Recueil*, **69** 192 (1950).
17. W. C. Hasz, "Surface Reactions and Electrical Double Layer Properties of Ceramic Oxides in Aqueous Solution," M.S. Thesis, Massachusetts Institute of Technology (1983).
18. H. A. Van der Schee and J. Lyklema, *J. Phys. Chem.*, **88** 6661 (1984).
19. J. Papenhuijzen, H. A. Van der Schee, and G. J. Fleer, *J. Colloid Interface Sci.*, **104** 540 (1985).
20. G. J. Fleer and J. Lyklema, in *Adsorption from Solution at the Solid/Liquid Interface* G. D. Parfitt and C. H. Rochester, eds., p. 153, Academic Press, New York (1983).
21. I. A. Aksay and R. Kikuchi, "Structures of Colloidal Solids," in *Ultrastructure Processing of Ceramics, Glasses, and Composites II*, L. L. Hench and D. R. Ulrich, eds., Wiley & Sons, New York (1986).
22. A. Bleier and E. D. Goddard, *Colloids and Surfaces*, **1** 407 (1980).

APPENDIX II
Stability of Aqueous α -Al₂O₃ Suspensions with
Polymethacrylic Acid Polyelectrolytes

(Cesarano, Aksay, and Bleier 1987)

STABILITY OF AQUEOUS α - Al_2O_3 SUSPENSIONS
WITH POLYMETHACRYLIC ACID (PMAA) POLYELECTROLYTE

Joseph Cesarano III and Ilhan A. Aksay

Department of Materials Science and Engineering
College of Engineering
University of Washington
Seattle, Washington 98195

Alan Bleier

Metals and Ceramics Division
Oak Ridge National Laboratory
Oak Ridge, Tennessee 37831

Submitted to

The Journal of the American Ceramic Society

March 25, 1987

STABILITY OF AQUEOUS α - Al_2O_3 SUSPENSIONS
WITH POLYMETHACRYLIC ACID (PMAA) POLYELECTROLYTE*

Joseph Cesarano III and Ilhan A. Aksay

Department of Materials Science and Engineering
College of Engineering
University of Washington
Seattle, Washington 98195

Alan Bleier

Metals and Ceramics Division
Oak Ridge National Laboratory**
Oak Ridge, Tennessee 37831

March 25, 1987

ABSTRACT

Stability of aqueous α - Al_2O_3 suspensions with Na^+ salt of polymethacrylic acid (PMAA- Na) polyelectrolyte was studied as a function of pH. At a given pH, the transition from flocculated to the dispersed state corresponded to the adsorption saturation limit of the powders by the PMAA. As pH was decreased, the adsorption saturation limit increased until insolubility and charge neutralization of the PMAA was approached. The critical amount of PMAA required to achieve stability is outlined in a stability map.

* Presented at the 87th Annual Meeting of the American Ceramic Society, Cincinnati, OH, May 7, 1985 (#95-B-85).

** Operated by Martin Marietta Energy Systems, Inc., for the U.S. Department of Energy.

I. INTRODUCTION

For many applications in ceramic processing it is desirable to sinter at relatively low temperatures and to obtain fully dense and fine grain microstructures. One method by which these goals can be accomplished is by using submicron size particles. In order to achieve a uniformly consolidated compact, it is also advantageous to use dispersed colloidal suspensions which contain upwards of 50 vol % solids while still maintaining relatively low viscosities of less than 1 Pa-s.

In general, suspensions can be dispersed by electrostatic, steric, or electrosteric stabilization mechanisms.¹ Electrostatic stabilization is accomplished by generating a common surface charge on the particles. Steric and electrosteric stabilization, on the other hand, are achieved by adsorption of polymeric additives which serve to form 'protective colloids'.

The main problems, related to ceramic processing, that were found to exist in electrostatically stabilized systems derive from aging effects and complications of processing multiphase systems.² The aging effects are commonly due to the solubility of particles in the suspending medium. For instance, in the case of suspensions prepared with H₂O under acidic or basic conditions, pH changes with time due to the solubility of the particles.² These pH changes can drastically influence rheology and suspension behavior, sometimes within a relatively short time frame of minutes to hours.² A second problem with electrostatically stabilizing suspensions which have more than one phase is that it is difficult, if not impossible, to find a pH range in which all of the particles have a substantial surface charge of the same sign so that irreversible agglomeration is prevented.³ In general, ceramic suspensions can be stabilized electrostatically; but, improvement of the suspensions to better meet the requirements necessary for ceramic processing is possible by incorporating polymeric additions.

Industrial experience shows, for instance, that by using polyelectrolytes as dispersants or deflocculants, in highly concentrated oxide suspensions, problems related to high viscosity, aging, and processing of multiphase systems can be drastically reduced and that suspensions with

adequate fluidity can be prepared.⁴ However, in spite of these advantages to using polyelectrolytes to stabilize suspensions, a great deal of misunderstanding exists in the general ceramic community as to the fundamental roles of these polymeric additives. Thus, this investigation was designed to elucidate the mechanisms of polyelectrolyte stabilization and to relate them to the chemistry of the powder surface and the polymer additive. An aqueous α - Al_2O_3 system with polymethacrylic acid (PMAA) was chosen as the model.

II. MATERIALS AND EXPERIMENTAL METHODS

1. Materials and Chemicals

The ceramic used in this study was of very high purity (> 99.995 %), submicron size, and relatively monodispersed (0.2-1.0 μm) α - Al_2O_3 powder.* The average diameter measured by an x-ray absorption/sedimentation technique† was 0.37 μm . The average surface area as measured by standard B.E.T. N_2 adsorption‡ was 5.9 m^2/g .

The polyelectrolyte studied was the Na^+ salt of polymethacrylic acid (PMAA-Na) with an average molecular weight of 15,000.¶ Figure 1 shows the PMAA-Na structure and that the functional groups are carboxylic acid (COOH) groups.

The water used was distilled and deionized. pH was adjusted with standardized analytical grade HCl and NaOH solutions (1.0 N and 0.1 N). Analytical grade NaCl was used to adjust the ionic strength as desired.

*Sumitomo Chemical America, Inc., New York, NY (AKP-30).

†Micromeritics, Norcross, GA (Sedigraph 5000).

‡Quantachrome Co., Syosset, NY (Quantasorb).

¶Polysciences, Inc., Pittsburgh, PA.

2. Experimental Methods

(A) **Potentiometric Titrations:** To measure the fraction of dissociated COOH groups (α) versus pH for PMAA-Na (Fig. 1) and the surface charge versus pH for Al_2O_3 , potentiometric titrations of the control electrolyte solutions were compared to titrations of the polymer solutions and oxide suspensions.*

This procedure of using potentiometric titrations to determine polymer behavior and surface chemistry of solid is clearly outlined by Arnold and Overbeek⁵ and by Hunter⁶ for oxides. Titrations were completed on a blank electrolyte solution and the polyelectrolyte solution or suspension with a known amount of sample. The difference between the amounts of titrant added to obtain a certain pH was the amount of titrant that reacted with the sample. With this information, both the fraction of functional groups dissociated on polymers and the surface charge on ceramic powders can be easily calculated.^{5,6}

The titrations were completed in a N_2 atmosphere and in each case 40 ml samples had known but small volumes of PMAA-Na (< 0.1 g) and Al_2O_3 (< 2 vol %); and, when desired, NaCl solutions were used to adjust the ionic strength. Prior to titration, the Al_2O_3 powder was cleaned to remove soluble ions using Soxhlet extraction.⁷ With this technique the powder is continuously washed with freshly distilled water.

(B) **Adsorption Isotherms:** The adsorption of PMAA-Na on the alumina was also evaluated using the automatic titration unit in the first derivative titration mode. Suspensions of 20 vol % Al_2O_3 were prepared with various amounts of PMAA-Na at various pH values. While the Al_2O_3 was being added, the pH was constantly monitored and adjusted so that it was always within 0.2 pH units from the desired pH value. After mixing, the samples were ultrasonicated for approximately 1 min. and the pH measured and adjusted again if necessary. The samples were then put into a gentle mechanical shaker for approximately 24 hours and then centrifuged for 45 min. at 2000 RPM. A portion of the supernatant was then analyzed by first derivative titration to determine the amount of PMAA left in solution. Fig. 2(a)

*Radiometer, Copenhagen, Denmark (Radiometer TRS822).

shows the shape of a typical PMAA-Na titration curve and its corresponding first derivative plot. The distance between peaks represents the amount of titrant to reach the endpoint and depends linearly on the amount of PMAA-Na titrated as shown in Fig. 2(b). This relationship was therefore used to determine the amount of PMAA-Na remaining in solution after adsorption: A known volume of the supernatant was diluted with water to approximately 40 ml. This solution was then sealed in the titration cell and the pH adjusted to 9.8, while the sample chamber was subjected to N₂ bubbling. The pH adjustment to 9.8 ensured that any PMAA-Na would be fully dissociated. This will be discussed fully below. The first derivative titrations were then conducted with 0.5 N HCl and the distance between peaks recorded. Standards were prepared to establish Fig. 2(b) and this calibration was used to determine adsorption behavior of PMAA. Background salt did not induce significant deviation in this calibration.

(C) Settling and Zeta Potential Experiments: Settling experiments were done using 2 vol % Al₂O₃ suspensions. Various amounts of PMAA-Na were added to the suspensions and were then ultrasonicated and stirred for at least 4 hours. Of each suspension, 70 ml was then poured into graduated cylinders and after several days the final sedimentation cake heights were recorded.

Electrophoretic mobility was measured* and used to calculate zeta potential according to Henry's equation.³ These measurements can only be completed on very dilute suspensions. Therefore, it was very important that the 2 vol % Al₂O₃ samples were centrifuged and the supernatant carefully decanted into a beaker, thereby ensuring that only a very minute amount of the sediment was remixed with the supernatant. Prior to the measurements, the samples were ultrasonicated and stirred for 15 minutes to ensure that only the mobility of the single particles was measured. At least ten measurements were completed for each sample to ensure accuracy.

*Rank Brothers, Bottisham, Cambridge, England (Micro-Particle Electrophoresis Apparatus Mark II).

(D) **Viscosity Measurements:** Viscosity of the suspensions was measured using a rotary viscometer* equipped with a recorder and a small sample chamber so that only 8 ml samples were necessary for each measurement.

III. RESULTS AND DISCUSSION

1. Chemistry of PMAA-Na and the Surface of α - Al_2O_3

The polyelectrolyte polymethacrylic acid- Na^+ salt (PMAA-Na, Fig. 1), with an average molecular weight of 15,000, has approximately 138 available carboxylic acid sites or functional groups per molecule. Depending on the solvent conditions (i.e., pH and ionic strength), the fraction of functional groups which are dissociated (i.e., COO^-) and those which are non-dissociated (i.e., COOH) will vary. As the fraction dissociated (α) increases from 0 to 1.0, the polymer charge varies from relatively neutral to highly negative. Therefore, the behavior of the polymer in solution also depends on the solvent conditions. Fig. 3 shows the fraction of dissociated acid groups as a function of pH and background NaCl concentration. As the pH and salt concentration increase, the dissociation and negative charge characteristics of the polymer increases.

Fig. 3 shows that at pH values ≥ 8.5 the PMAA is negative and saturated with $\alpha \sim 1$. In this condition, experimental evidence shows that the PMAA molecules are in the form of relatively large expanded random coils in solution.⁵ This configuration results from electrostatic repulsion between the negatively charged surface sites. As pH is decreased, the number of negatively charged sites also continually decreases until the PMAA is effectively neutral near pH 3.4 and $\alpha \rightarrow 0$. In this condition the PMAA chains approach insolubility and form relatively small coils or clumps.⁵

*Brookfield Engineering Laboratories, Inc., Stoughton, MA (Digital Viscometer, Model RVTD).

A plausible explanation for the role of salt concentration on the degree of dissociation is as follows. The probability of COO^- groups being stable surrounded by Na^+ counterions in close proximity increases with increasing $[\text{NaCl}]$ and therefore the probability of H_3O^+ ions reacting with available COO^- groups to form COOH decreases. Additionally, added salt decreases the thermodynamic activity of H_3O^+ , shifting the equilibrium towards more dissociation as depicted in Fig. 1.

Using similar reasoning, this behavior explains why pQ , defined in Fig. 1, increases with increasing α and decreasing background salt concentrations (Fig. 4). pQ is the effective dissociation reaction constant. For a polyacid such as PMAA, pQ varies for each acid site, depends on the local environment, and increases as each successive acid group dissociates. This situation occurs because increased electrostatic interactions between (-) sites on the polymer make dissociation of neighboring sites more difficult. Since increased salt concentration promotes electrostatic shielding and makes dissociation less difficult, pQ decreases. An interesting note is that extrapolation of pQ values to $\alpha = 0$ yields 4.86. This value is consistent with those for simple organic acids which only have one acid group. Both the pQ and α behavior are in agreement with the PMAA titration results of Arnold and Overbeek.⁵

Fig. 5 shows the charge density (σ) on the surface of the Al_2O_3 particles as a function of pH. At every pH, there is a large number of positive, neutral, and negative sites. The σ value gives the overall net charge density. At the zero point of charge (zpc), the number of positive sites equals the number of negative sites and the net charge equals zero. For our sample of $\alpha\text{-Al}_2\text{O}_3$, the zpc is at approximately pH 8.7. Both σ values and the zpc are in very close agreement to that of Hasz.⁹

Finally, a comparison of Fig. 5 with Fig. 3 indicates that there should be a great deal of electrostatic attraction between the negatively charged polymer and the positively charged Al_2O_3 particularly in the pH range from 3.5 to 8.7. This relationship will be discussed further in the next section.

2. Adsorption of PMAA-Na on α -Al₂O₃

Fig. 6 shows adsorption at various pH values, plotted as mg PMAA adsorbed per m² surface area of Al₂O₃, versus the initial amount of PMAA-Na added (on a dry weight of Al₂O₃ basis). The solid diagonal line represents the adsorption behavior that would occur if 100 % of the PMAA added were to adsorb. Though this plot is not of the usual form for adsorption data, its utility in ceramic processing will become evident.

It is clearly shown that the amount adsorbed increases greatly with decreasing pH. This behavior agrees with recent polyelectrolyte adsorption theory developed by Van der Schee et al.^{10,11} For pH values above the zpc, α is approximately 1 and the negatively charged sites on the polyelectrolyte chains tend to repel each other. This repulsion suppresses the formation of loops in adsorbed conformation. Consequently, the polyelectrolyte chains adsorb in a relatively flat conformation with each chain apparently covering a relatively large amount of surface area. Note that polyelectrolyte tails can still extend into solution even though the formation of loops is inhibited. The determined adsorption values for polyelectrolyte in this configuration are on the order of a few tenths of a mg/m². As the pH is decreased and α approaches 0 (Fig. 3), the polyelectrolyte chains become uncharged and the formation of loops in the adsorbed configurations is, in principle, enhanced. Thus, the projected surface area per adsorbed chain is relatively small, and more adsorbed chains are required to establish a saturated monolayer. Commonly measured values for this type of adsorption are a few mg/m² which is in agreement with the experimental results.¹²

Fig. 6 also shows a difference between the adsorption behavior above the zpc and below the zpc. For pH 9.8, there is a gradual attainment of the saturated adsorption plateau. In contrast, for systems at pH 8.2 and less, the plateau adsorption is reached without any appreciable PMAA remaining in solution. Therefore, it is concluded that for pH values near and more acidic than the zpc, the adsorption behavior is of the 'high affinity' type. Practically all of the PMAA which is added adsorbs on the surface and the data follow the 100 % line until a saturation plateau level is reached. Only beyond this limit does nonadsorbed PMAA become appreciably present in solution. This observation also agrees with the adsorption theory if an electrostatic influence on adsorption

and a negative or partly negative polyelectrolyte adsorption on a positively charged surface are considered.¹¹ Above the zpc, due to similar net charges, a barrier for adsorption increasingly develops, so that in order to adsorb PMAA, there has to exist a corresponding equilibrium concentration of PMAA in solution. Adsorption in this region is due to the minority of positive surface sites when the net surface charge is negative.

Fig. 6 also shows that the presence of background salt can slightly increase adsorption. This occurs because the background salt has an electrostatic shielding effect between negatively charged sites on the PMAA thereby causing the chains to behave more like uncharged polymers and enhancing the development of loops. This type of behavior is commonly observed in many systems and agrees with recent concepts on adsorption.¹¹ Even with 0.1 M NaCl concentrations, stable suspensions are achieved after saturation adsorption occurred.

Reversibility of adsorption is indicated by the ▼ and ♦ points on Fig. 6. Under these conditions, the suspensions were prepared at the initial pH values indicated and shaken for 4 hours. The suspensions were then adjusted to desired final pH values and shaken for 20 or more hours prior to analysis. The system which is initially at pH 9.9 and then adjusted to pH 8.1 adsorbs a final amount, consistent with that obtained when the initial pH is 8.1. This correspondence might be expected since at pH 9.9 there is appreciable nonadsorbed PMAA in solution which could be easily adsorbed once the pH is lowered. A change in the configuration of the adsorbed PMAA may occur; but, thus far no observable changes in the suspension behavior can be related to such changes. On the other hand, when the initial pH is 8.0 and then adjusted to 9.6, complete reversibility is not observed but only a fraction of PMAA desorbs. This behavior suggests that the PMAA is relatively strongly held on the Al_2O_3 surface. It also possibly indicates that with sufficiently extended times most of the PMAA might desorb, at least for pH values near and above the zpc.

3. Consolidated State

The effect of incomplete adsorption and flocculation on the consolidated state was determined by sedimentation and centrifugation experiments. Fig. 7(a) shows that trace amounts of PMAA-Na ($< 0.25\%$) induces flocculation and large sedimentation volumes. This results because the binding energy between the particles is high and the particle clusters that form during consolidation behave as rigid flow units and do not pack densely.¹³ In contrast, at concentrations of approximately $0.35-0.50\%$ PMAA-Na, the binding energy between particles is low and the particle clusters display relatively denser packing structure.¹³

These data also correlate with the zeta potential determinations. Fig. 7(b) shows that with increasing polymer concentration, the zeta potential decreases to zero and then reverses sign. Above 0.5% polymer, the zeta potential approaches a nearly constant value of -40 mV. This value reflects the saturated monolayer of polyelectrolyte on Al_2O_3 .

It can be further concluded from Figs. 7(a) and (b) that small additions of PMAA-Na (e.g., $< 0.1\%$) neutralize charge and induce subsequent flocculation. In this regime, flocculation is mainly due to electrostatic patch model flocculation whereby flocculation takes place because negatively charged patches due to the adsorbed polyelectrolyte are attracted to positively charged patches of surface on other particles. When the molecular weight is relatively low then maximum flocculation occurs when the zeta potential is approximately zero or even still slightly positive. This type of behavior is discussed by Bleier and Goddard.¹⁴ In the range from $0.1-0.3\%$ PMAA-Na, flocculation is due to a combination of two effects: (1) the zeta potential is relatively low in magnitude, and (2) incomplete adsorption results in polymer bridging where two or more particles can be mutually adsorbed by polymer chains.

It can also be concluded that the PMAA results in more efficient consolidation. Upon settling, pure Al_2O_3 (0% polymer) shows a larger sediment volume than the system with 0.4% polymer added even though the zeta potentials are $+48$ mV and -33 mV, respectively. The stability determined by settling rates and sedimentation heights do not appear to be equal until zeta potentials of ≥ 58 mV are reached for the pure Al_2O_3 suspensions. This trend means that the increased stability and dispersion of the 0.4% polymer system may be due to a steric stabilization

interaction in combination with the repulsion effect due to electrostatics. These mechanisms together can be termed electrosteric.

From these results some preliminary conclusions can be made: (1) only very minute amounts of PMAA-Na are necessary to flocculate Al_2O_3 suspensions, (2) a critical amount of PMAA-Na is needed before stabilization occurs, and (3) PMAA-Na does indeed provide an enhanced stabilization effect.

4. Stability Map for PMAA-Na/ α - Al_2O_3 System

With the above information and the adsorption data in Fig. 6, a stability map can be constructed. Fig. 8 is a plot of the amount of PMAA adsorbed at the plateau levels versus pH. In other words, for any pH near and below the zpc, it is a measure of the amount of PMAA which must be adsorbed to achieve a stable suspension. Regions above the curve are stable and dispersed. Regions below the curve are unstable and show an onset to flocculation. The reason for the assumed steep decrease in adsorption at pH 3.3 is because of observed viscosity decreases (Table I). For example, as pH is decreased on samples which are initially stable, the viscosity noticeably increases when crossing the stability/instability boundary region. This is expected since at those lower pH values, more PMAA is needed to maintain a stable suspension and the subject suspensions

Table I: Rheology data at various pH's for 20 vol % α - Al_2O_3 suspensions with 0.312 % (dwb) of PMAA-Na MW 15,000.

pH	$\eta(10^{-3} \text{ Pa-s})$ at 10 RPM
5.2	1650
7.4	< 10
8.7	< 10
9.3	< 10
9.8	< 10
10.2	< 10

are below that critical level. This process is the same as moving to the left from a stable region on Fig. 8 and entering the unstable region. Once the pH is decreased further to 3.3, deflocculation reoccurs and viscosity sharply decreases and approaches that of a system stabilized at pH 3.3 without any PMAA present. Since at pH 3.3 the suspension is stable without the presence of PMAA due solely to electrostatic interactions, it is believed that there is a combination of two possible mechanisms for the observed restabilization of Al_2O_3 below pH 3.3 in the presence of PMAA. One explanation is that below pH 3.3 the PMAA sufficiently desorbs since this is also the pH at which the PMAA loses its negative charge and its configuration and electrical state approach those of a neutral polymer with a greatly diminished driving force for adsorption (Fig. 3); it may even approach its solubility limit. Concurrently, some PMAA may still be adsorbed but the effectively neutral polymer layer may be small enough so that the electric double layer (formed by the highly positive Al_2O_3 surface) may extend past the polymer layer. In this way, electrostatic stabilization due to electric double layer interactions can still occur.

Table I illustrates the transition from stability to instability based on viscosity measurements. A series of samples with 0.312 % PMAA was prepared at various pH values. Viscosities above pH 7 were $< 10^{-2}$ Pa-s while the viscosity at pH 5.2 was more than two orders of magnitude greater, indicating flocculation. This is in agreement with Fig. 8 which shows a stability/instability transition at - pH 7 for 0.312 % PMAA.

IV. CONCLUSIONS

1. The adsorption behavior of polymethacrylic acid on alumina depends on solvent conditions and the charge characteristics of the PMAA and the Al_2O_3 surface: As pH is decreased, the adsorption of PMAA increases until insolubility and charge neutralization of the PMAA is approached; for pH values near and below the zero point of charge for Al_2O_3 , there is an added electrostatic attractive potential for adsorption which results in a high affinity type adsorption behavior.

2. For pH values near and below the zpc, PMAA adsorbs and may induce flocculation until an adsorption saturation limit is reached and the binding energy between particles is reduced below a critical level.
3. Once saturation adsorption occurs and stability is achieved, the PMAA induced stabilization exhibits an enhanced stability, compared to suspensions stabilized electrostatically without the polyelectrolyte.
4. The stability map introduced here is a useful processing tool for tailoring suspensions with varying amounts of polymer, depending on the desired properties. For instance, if higher concentrations of polymer are desired, perhaps for high mechanical strength in the consolidated state, acidic conditions would be recommended. However, if dispersion is ultimately important and the effects of the adsorbed polymer are not desired, basic conditions would be more suitable. The knowledge gained from the stability map is necessary to predict the amount of polymer necessary to stabilize aqueous alumina suspensions at various pH's for any known surface area and well-defined zpc.

Acknowledgements

This research was sponsored by the Air Force Office of Scientific Research (AFOSR) and the Defense Advanced Research Projects Agency of the Department of Defense, and was monitored by AFOSR under Grant No. AFOSR-83-0375, and by the Division of Materials Science, U.S. Department of Energy, under contract No. DE-AC05-84OR21400 with Martin Marietta Energy Systems, Inc. The authors gratefully acknowledge J. Lyklema whose insight and discussion were very helpful.

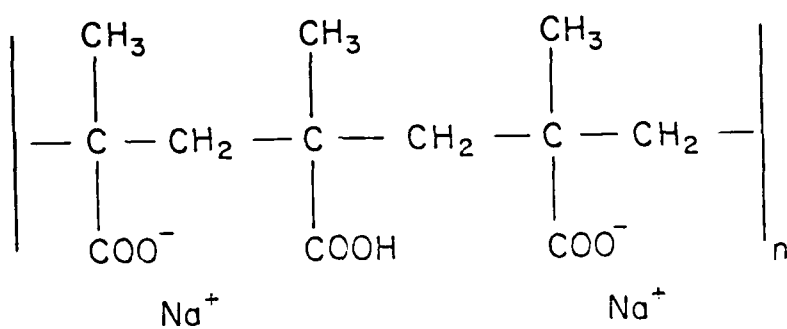
REFERENCES

1. D. H. Napper, *Polymeric Stabilization of Colloidal Dispersions*, Academic Press, London, 1983.
2. I. A. Aksay, F. F. Lange, and B. I. Davis, "Uniformity of $Al_2O_3-ZrO_2$ Composites by Colloidal Filtration," *J. Amer. Cer. Soc.* **66**, C190 (1983).
3. G. W. Phelps, S. G. Maguire, W. J. Kelly, and R. K. Wood, *Rheology and Rheometry of Clay-Water Systems*, Cyprus, Sandersville, GA, 1984, pp. 19-21.
4. Alcoa Technical Brochure, "Alcoa Reactive Aluminas," June 1972.
5. R. Arnold and J. Th. G. Overbeek, "The Dissociation and Specific Viscosity of Polymethacrylic Acid," *Recueil*, **69**, 192 (1950).
6. R. J. Hunter, *Zeta Potential in Colloid Science - Principles and Applications*, Academic Press, London, 1981.
7. R. M. Roberts, J. C. Gilbert, L. B. Rodewald, and A. S. Wingrove, *An Introduction to Modern Experimental Organic Chemistry*, 2nd Edition, Holt, Rinehart and Winston, Inc., New York, 1974, pp. 57-62.
8. D. C. Henry, "The Cataphoresis of Suspended Particles. Part I - The Equation of Cataphoresis," *Proc. Roy. Soc. (London)*, **A133**, 106 (1931).
9. W. C. Hasz, "Surface Reactions and Electrical Double Layer Properties of Ceramic Oxides in Aqueous Solution," M.S. Thesis, Massachusetts Institute of Technology (1983).
10. H. A. Van der Schee and J. Lyklema, "A Lattice Theory of Polyelectrolyte Adsorption," *J. Phys. Chem.* **88**, 6661 (1984).
11. J. Papenhuijzen, H. A. Van der Schee, and G. J. Fleer, "Polyelectrolyte Adsorption I. A New Lattice Theory," *J. Colloid Interface Sci.* **104**, 540 (1985).
12. G. J. Fleer and J. Lyklema, in *Adsorption from solution at the Solid/Liquid Interface*, G. D. Parfitt and C. H. Rochester, eds., Academic Press, New York, 1983, p. 153.
13. I. A. Aksay and R. Kikuchi, "Structures of Colloidal Solids," in *Science of Ceramic Chemical Processing*, L. L. Hench and D. R. Ulrich, eds., Wiley and Sons, New York, 1986, pp. 513-21.
14. A. Bleier and E. D. Goddard, "Flocculation of Aqueous Silica Suspensions Using Cationic Polyelectrolytes," in *Colloids and Surfaces*, Elsevier Scientific Publishing Co., Amsterdam, 1980, p. 407.

FIGURE CAPTIONS

- Figure 1: Schematic of a PMAA-Na segment and the dissociation reaction.
- Figure 2: (a) A typical titration curve for PMAA-Na and its corresponding first derivative plot; and (b) linear relationship between the amount of PMAA-Na titrated and the meq of titrant corresponding to the distance between the peaks in (a).
- Figure 3: Fraction of acid groups dissociated versus pH as a function of salt concentration for PMAA-Na salt, MW 15,000.
- Figure 4: pQ versus the fraction dissociated as a function of salt concentration for PMAA-Na salt, MW 15,000.
- Figure 5: The relative surface charge versus pH for the α -Al₂O₃ powder.
- Figure 6: The amount of PMAA-Na salt adsorbed on α -Al₂O₃ as a function of the initial amount of PMAA-Na added.
- Figure 7: (a) Sedimentation height; and (b) zeta potential versus % PMAA-Na for 2 vol % suspensions of α -Al₂O₃.
- Figure 8: Colloidal stability map of α -Al₂O₃ (20 vol %) suspensions as a function of adsorbed PMAA-Na salt and pH.

PMAA - Na



For each acid group:



$$Q = \frac{(\text{A} - \text{COO}^-) (\text{H}_3\text{O}^+)}{(\text{A} - \text{COOH})}$$

$$\text{p}Q = -\log Q = \text{pH} - \log \left(\frac{\alpha}{1-\alpha} \right)$$

Figure 1

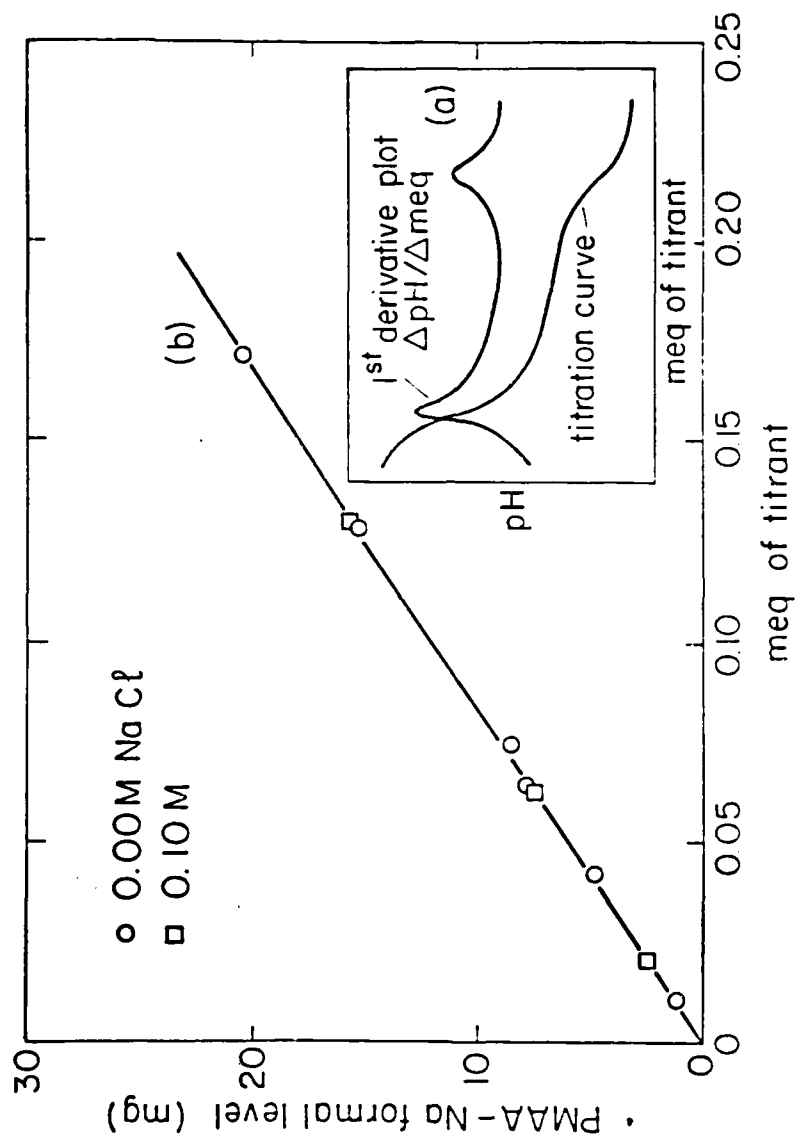


Figure 2

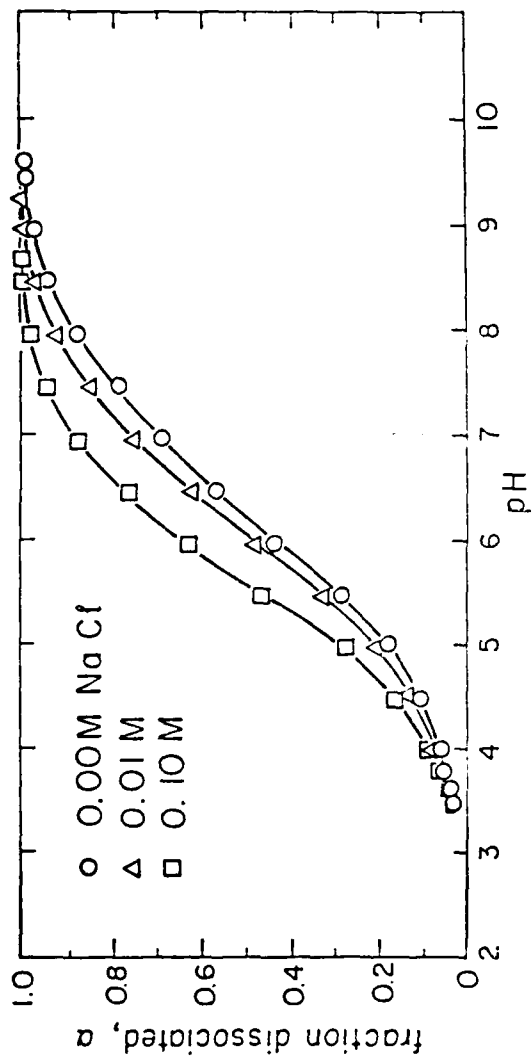


Figure 3

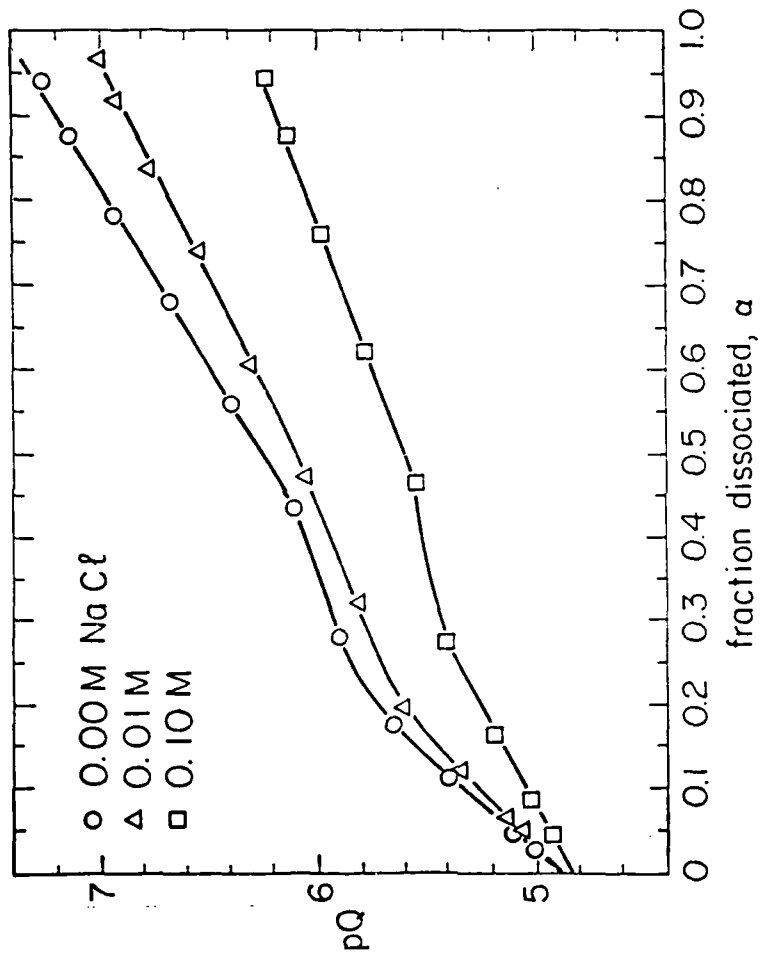


Figure 4

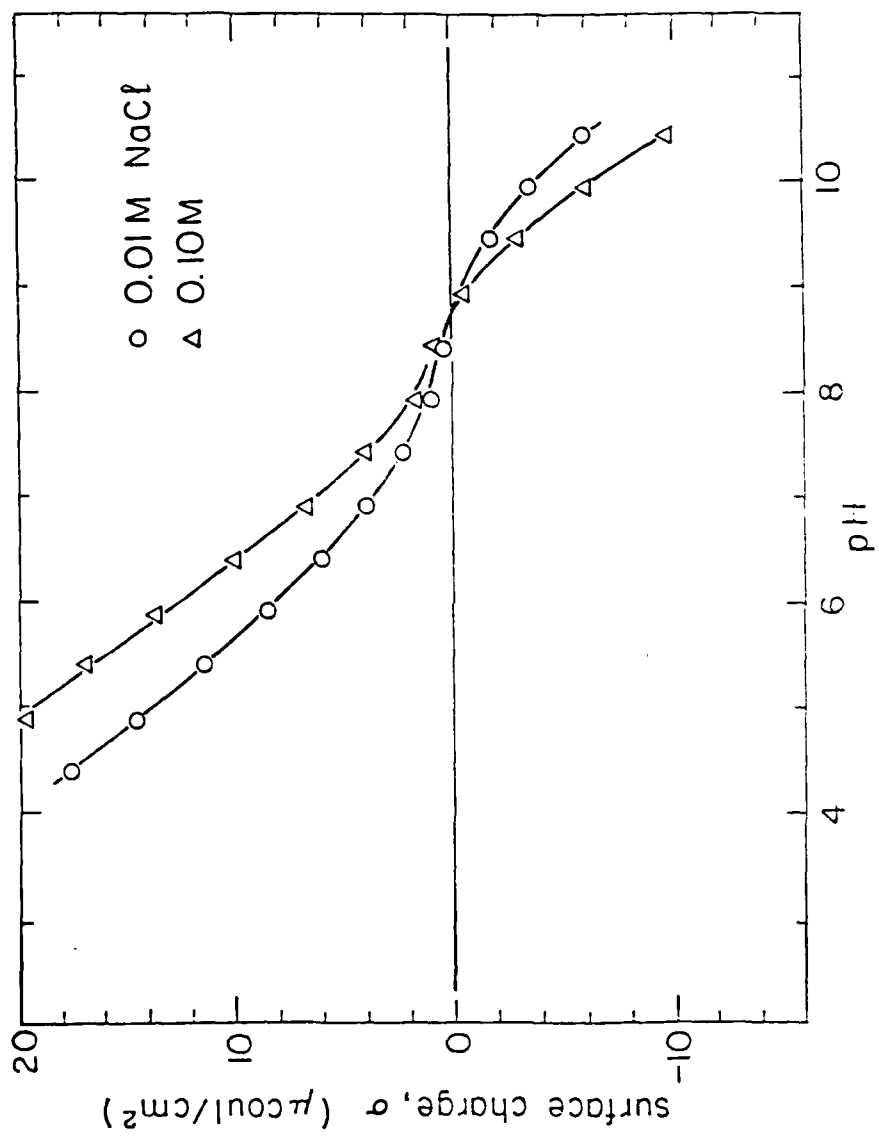


Figure 5

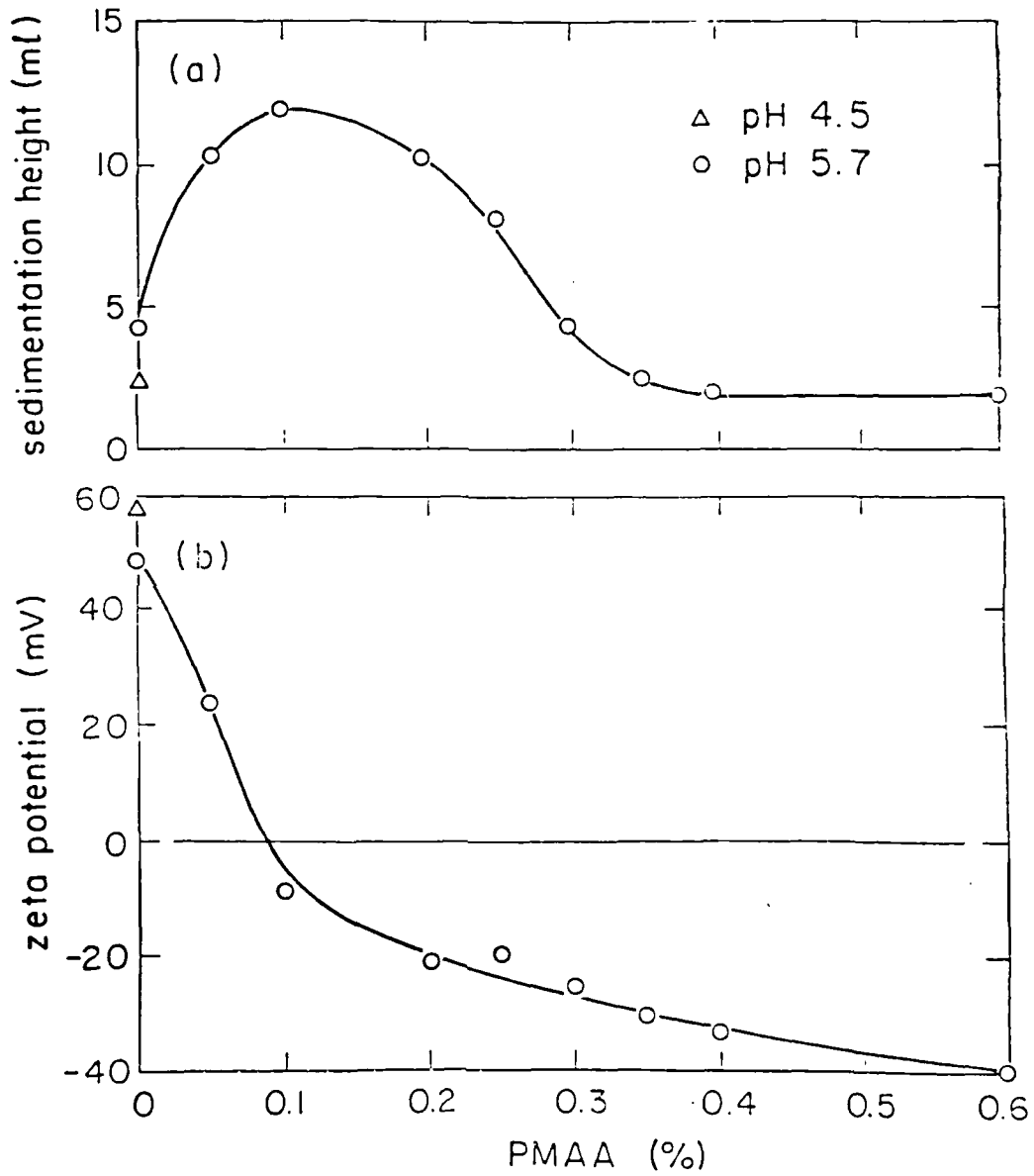


Figure 7

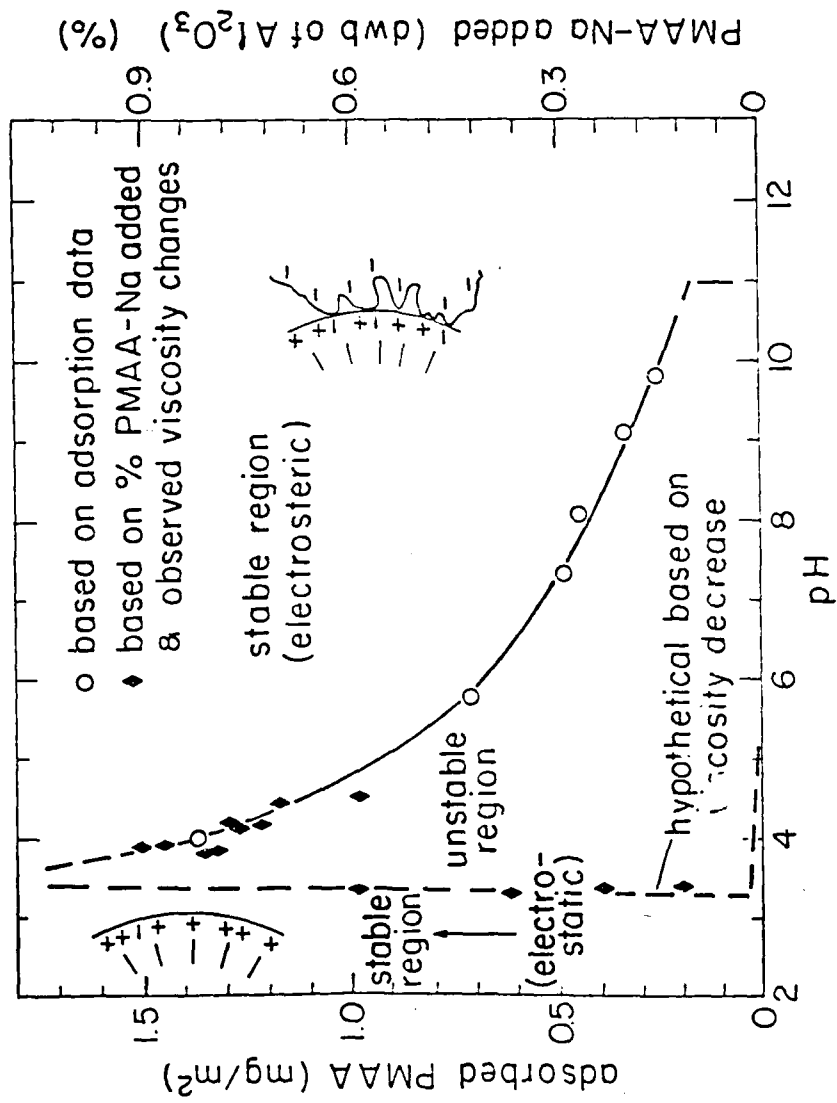


Figure 8

APPENDIX III
Processing of α -Al₂O₃ with Highly Concentrated
Aqueous Alumina Suspensions

(Cesarano and Aksay 1987b)

PROCESSING OF α -Al₂O₃ WITH HIGHLY CONCENTRATED
AQUEOUS ALUMINA SUSPENSIONS

Joseph Cesarano III and Ilhan A. Aksay

Department of Materials Science and Engineering
College of Engineering
University of Washington
Seattle, Washington 98195

Submitted to

The American Ceramic Society Bulletin

April 25, 1987

PROCESSING OF α - Al_2O_3 WITH HIGHLY CONCENTRATED
AQUEOUS ALUMINA SUSPENSIONS

Joseph Cesarano III and Ilhan A. Aksay

Department of Materials Science and Engineering
College of Engineering
University of Washington
Seattle, Washington 98195

April 25, 1987

ABSTRACT

Stability and rheology of aqueous α - Al_2O_3 suspensions with Na^+ salt of polymethacrylic acid (PMAA- Na) and polyacrylic acid (PAA) polyelectrolytes was studied as a function of pH, solids loading, and molecular weight. Past work has found polyelectrolyte stabilized suspensions to be fairly pH independent at low (e.g., 20 v/o) solids loadings. However, we now show that the effective pH range to provide dispersed and fluid suspensions narrows as the concentration of solids increases. At high solids levels the presence of excess polymer in solution has detrimental effects on stability which increases with increasing molecular weight. Finally, with knowledge of the above concepts highly concentrated fluid suspensions of 60 v/o Al_2O_3 (> 85 w/o) with submicron size particles have been processed. Higher consolidated densities and reduced sintering temperatures are attained when compared to more conventional processing techniques.

* Presented at the 88th Annual Meeting of the American Ceramic Society, Chicago, IL, April 30, 1986 (#41-BP-86).

I. INTRODUCTION

Polyelectrolytes are widely used in industrial applications to prepare highly concentrated (> 50 v/o) ceramic suspensions which are subsequently fabricated into dense components by sintering. Although a variety of polyelectrolytes are commercially available and are used effectively in the preparation of suspensions, their role in colloidal stabilization has not been clearly understood.

In this paper, we aim to provide a clearer understanding of particle dispersion with adsorbed polyelectrolytes and relate it to the surface chemistries of the suspended particle surfaces and the polyelectrolyte. Aqueous oxide suspensions will be considered as a general example. The particular emphasis will be on the dispersion of α - Al_2O_3 suspensions with polymethacrylic acid (PMAA) and polyacrylic acid (PAA).

It is also an aim of this paper to describe the methodology of using polyelectrolyte stabilization for the processing of very highly concentrated (60 v/o) aqueous ceramic suspensions. This was studied with model experiments with submicron size alumina which determined the guidelines for the selection of a proper pH range and related rheological behavior to molecular weight. Finally, sintering behavior of compacts prepared by these techniques is compared to more conventional methods of processing.

II. BACKGROUND INFORMATION

For information concerning polyelectrolytes, surface charging of oxides, and related adsorption behavior of polyelectrolytes on oxides, the reader is referred to Ref. 1. The following discussion pertains to the particular aqueous system of aluminum oxide particles and polymethacrylic acid - Na^+ salt (PMAA-Na) and is a summary of the work described in Ref. 1. The structure of PMAA is shown in Fig. 1.

For PMAA alone, each molecule has many carboxylic acid sites or functional groups and depending on the solvent conditions (i.e., pH and ionic strength), the fraction of functional groups which are dissociated (i.e., COO^-) and those which are non-dissociated (i.e., COOH) will vary.

As the fraction dissociated (α) increases from ≈ 0 to ≈ 1.0 , the polymer surface charge varies from relatively neutral to highly negative. In general, for PMAA and other polyelectrolytes which have carboxylic acid groups as the functional groups, the dissociation and negative charge characteristics of the polymer increases with increasing pH.² For PMAA at pH values of ≥ 8.5 the molecules are effectively negative with $\alpha \approx 1$. In this condition, experimental evidence shows that the PMAA molecules are in the form of relatively large expanded random coils in solution.³ This results from electrostatic repulsion between the negatively charged surface sites. As pH is decreased, the number of negatively charged sites also continually decreases until the PMAA is effectively neutral near pH 3.4 and $\alpha \rightarrow 0$. In this condition the PMAA chains approach insolubility and form relatively small coils or clumps.³

In general, for oxides the relative charge density (σ) on the surface of the particles also varies with pH but in a different manner than the charging of anionic polyelectrolytes. For oxides, at every pH, there are large numbers of negative, neutral, and also positive surface sites. The value gives the overall net charge density. At low pH values positive sites are in the vast majority and therefore σ is positive. At high pH, negative sites are in the majority and σ is negative. At the zero point of charge (zpc), $\sigma = 0$ which occurs when the number of positive sites equals the number of negative sites. For α -Al₂O₃, the zpc is at approximately pH 8.7.

The comparison of the charging behavior of PMAA and Al₂O₃ with pH leads to an obvious conclusion that the saturation limit of PMAA adsorption on Al₂O₃ should be significantly affected by pH. Fig. 2 is a plot of the amount of PMAA adsorbed at the saturation levels versus pH. The amount of PMAA which must be adsorbed to achieve a stable suspension increases with decreasing pH. Regions above the solid curve are stable and dispersed. Regions below the curve are unstable and show an onset to flocculation. The regions below pH 4 are discussed in Ref. 1 and thus will not be discussed in this paper.

In order to expand the concepts for different solids concentrations, pH, and polyelectrolyte molecular weight, and to use these concepts for processing of these suspensions, more experiments were conducted using polyelectrolytes and colloidal α -Al₂O₃.

III. EXPERIMENTAL

1. Materials and Chemicals

The ceramics used in this study were of very high purity (>99.995%), submicron size, and relatively monodispersed (0.2-1.0 μm) $\alpha\text{-Al}_2\text{O}_3$ powders (AKP 20 and AKP 30).^{*} The average diameter measured by an x-ray adsorption/sedimentation technique[†] was 0.52 μm for AKP 20 and 0.41 μm for AKP 30. The average surface area as measured by standard B.E.T. N_2 adsorption[‡] was 4.5 m^2/g for AKP 20 and 6.8 m^2/g for AKP 30.

The polyelectrolytes used were the Na^+ salt of polymethacrylic acid (PMAA-Na) with an average molecular weight of 15,000 and polyacrylic acid (PAA) of various molecular weights (1800, 5000, and 50,000).[¶] These polyelectrolyte structures are shown in Fig. 1.

The water used was distilled and deionized. The pH was adjusted with standardized analytical grade HCl and NaOH solutions (1.0 and 0.1 N). Analytical grade NaCl was used to adjust the ionic strength as desired.

2. Experimental Methods

(A) **Viscosity Measurements:** Viscosity measurements were done with a rotary viscometer^{††} with a small sample chamber. To determine the relative magnitude of viscosity and whether the suspensions were flocculating or stabilized, the following rheological measurement method was used:

- (i) Each suspension was initially sheared at a relatively high shear rate of 93 sec^{-1} . This ensured that permanent particle clusters (if any) were dispersed;

*Sumitomo Chemical America, Inc., New York, NY.

†Micromeritics, Norcross, GA (Sedigraph 5000).

‡Quantachrome Company, Syosset, NY (Quantasorb)

¶Polysciences, Inc., Pittsburg, PA.

††Brookfield Engineering Laboratories, Inc., Stoughton, MA (Digital Viscometer, Model RVTD).

- (ii) The shear rate was then decreased every 30 seconds in 8 increments down to 0.46 sec^{-1} and the viscosities recorded;
- (iii) The suspensions were then allowed to sit at 0.46 sec^{-1} for 10 min. so that nucleation and growth of particle clusters could occur;
- (iv) The shear rate was then increased in 8 increments back up to 93 sec^{-1} and the viscosities recorded again.

Large differences between the initial rate sweep and the latter rate sweep were assumed to be due to flocculation (i.e., the nucleation and growth of particle clusters). The magnitude of the viscosities was taken as a relative measure of the fluidity of the suspensions as related to the particle interaction energy and the degree of particle clustering.

(B) Zeta Potential and Interparticle Repulsive Potential Calculations:

Zeta potential (ζ) was calculated by using the measured electrophoretic mobility* and Henry's equation⁵ with Overbeek's correction if necessary.⁶ This correction takes into account the value of κa , where κ is the inverse screening length and a is the particle diameter. In general, as the ionic strength of a suspension increases so does κa . For the purpose of this paper, the actual polymer chains were not included in the calculation of a ; however, their associated ions were included. These measurements can only be completed on very dilute suspensions. Therefore, it was very important that the suspensions were centrifuged and the supernatant carefully decanted into a beaker. Then a portion of the sediment was removed with the supernatant. Prior to taking the measurements, the new dilute suspensions were very briefly ultrasonicated and magnetically stirred to ensure that only singlet particles were measured. At least ten measurements were completed for each sample to ensure accuracy.

The calculations of interparticle repulsive potentials (V_r) were done according to Ref. 7. Since for any given powder the attractive potential is the same, it is only necessary to compare the values of V_r for qualitative arguments concerning interparticle potentials. Comparisons of V_r are made at a particle separation distance of 100 \AA .

*Rank Brothers, Bottisham, Cambridge, England (Micro-Particle Electrophoresis Apparatus Mark II).

(C) **Processing of Suspensions for Sintering:** Both the AKP 20 and AKP 30 α - Al_2O_3 powders were dry pressed, slip cast, and simply air cast (dried) in plastic molds. The dry pressed pellets were approximately 2.54 cm in diameter and pressed biaxially at 51.8 MPa. The slip cast samples were prepared from 50 v/o suspensions and cast between two slabs of plaster. The suspensions were prepared with a commercially available form of PAA-NH_4^+ (M.W. 5,000)* and the pH adjusted to 8.8 with small amounts of citric acid. The air cast samples were made by pouring 5 ml of very highly concentrated PAA-NH_4^+ stabilized Al_2O_3 suspensions (\approx 60 v/o) into plastic molds and allowing them to dry. All of the samples were then sintered in air. The samples were held at the maximum temperatures for one hour. The heating and cooling rates were $300^\circ\text{C}/\text{h}$. The sintered densities were measured by a standard alcohol immersion method.

IV. RESULTS AND DISCUSSION

1. Viscosity vs. pH

Fig. 3 shows the effect of pH on viscosity for stabilized suspensions at various solids loading. Using Fig. 2 for representation, all of these suspensions are in the stable region but still relatively close to the stability boundary.

In 20 v/o Al_2O_3 suspensions, all of the stabilized systems have very low viscosities and the difference between suspensions stabilized at pH 4.5 and 10 are minimal. As the v/o solids increase, the magnitude of viscosity also increases while the effective pH range gets smaller (Fig. 3). In all cases the minimum in viscosity occurs at approximately pH 8.8. The reason for the increase in viscosity at higher pH is because of the presence of excess polymer remaining in solution due to the adsorption behavior of the polyelectrolyte which is no longer high affinity type adsorption at high pH.¹ This leads to high viscosities in concentrated suspensions where the amount of water is small. Problems associated with excess polymer in solution will be discussed more fully in a following section. At lower pH,

*R. T. Vanderbilt Company, Norwalk, CT.

viscosity again increases because of two related phenomena. As the pH decreases, the amount of polyelectrolyte necessary to provide stabilization increases (Fig. 2) while at the same time the polyelectrolyte chains become less dissociated.¹ This leads to two problems. First, with less dissociation the negative charge characteristics of the polyelectrolyte decreases and the relative solubility of the polymer also decreases.¹ This leads to a situation where the adsorbed polyelectrolyte has less negatively charged functional groups extending into solution and therefore decreases the magnitude of the electrosteric repulsive barrier between particles.^{1,8} Secondly, as the amount of polyelectrolyte increases, the concentration of ions associated with the polyelectrolyte and ions due to pH adjustment also increases and therefore reduces the electrostatic portion of particle repulsion.

These effects become more appreciable at higher solids concentrations since the particle repulsion necessary to provide stability increases with increasing solids concentrations.⁹ For example, for a 20 v/o suspension at pH 5.5, the v/o solids is relatively low; and, under these conditions of polyelectrolyte dissociation and ionic strength, the binding energy between particles is low enough to prevent the nucleation and growth of particle clusters and the resultant viscosity remains low. In contrast, for a 40 v/o suspension at pH 5.5, the binding energy between particles is low enough to prevent permanent clusters but high enough to induce a large increase in viscosity. To have more fluid and stable suspensions at higher solids concentrations requires adjustment to a more optimum pH where the adsorbed polyelectrolyte is more fully dissociated and ionic strengths lowered so that a more effective electrosteric repulsion can exist between particles. These concepts will be revealed in more detail in the following section. It should be noted that for this system the optimum pH seems to be at pH ~ 8.8. This pH is where the minimum in viscosity occurs (Fig. 3) and coincides with the point at which the polyelectrolyte is fully charged and maintains maximum solubility while high affinity type adsorption still occurs and the ionic strength is relatively low. Under these conditions the amount of polyelectrolyte in solution is small and the binding energy between particles is low.

2. Relating Interparticle Forces to Rheological Behavior

Table I shows a summary of data relating interparticle forces to rheological behavior for 40 v/o AKP 30 suspensions stabilized with PMAA-Na⁺. The polymer ratio is a measure of the amount of polymer added in relation to that necessary for adsorption saturation according to Fig. 2. The value of k_a is a relative measure of the ionic strength of the solution. As k_a increases ionic strength increases and as a reference for this system, a k_a value of 425 is equivalent to a 0.1 M NaCl solution. The cV_r values are a relative measure of the repulsive potential between particles due solely to calculated electrostatic repulsion at a separation distance of 100 Å. The η_0 to η_{10} values are a measure of the change in viscosity over a period of 10 min at a shear rate of 9.3 s^{-1} , and the comments S, F, and SF are equalitative observations meaning stable, flocced, and slightly flocced, respectively.

The information in Table I can be used to provide some preliminary conclusions relating to interparticle forces. First of all, the most dominant cause for flocculation in polyelectrolyte stabilized suspensions is incomplete adsorption which provides a driving force for particles to cluster together in an effort to form saturated monolayers. This is clearly shown in Table I in that in all cases where the polymer ratio is <1.0, flocculation resulted even though the zeta potentials and electrostatic repulsive forces are relatively high. The best examples tabulated are at pH 9.5 for a polymer ratio of 0.55 and at pH 8.1 for a polymer ratio of 0.76. It may also be concluded that once enough polymer has been adsorbed there is a stabilization effect due solely to the polyelectrolyte even in the absence of repulsion due to electrostatics. This is especially apparent for samples at pH 8.1 w/NaCl and pH 6.5 where $V_r \approx 0$; but, stable fluid suspensions resulted. Further evidence for the stabilizing effects due to the polyelectrolyte is that for the same 40 v/o system in the absence of polymer an electrostatic value of $cV_r = 3$ is necessary to induce comparable levels of stability and viscosity as those found for PMAA stabilized suspensions at pH 8.8 with a cV_r value of 0.7.¹⁰

Another important aspect of polyelectrolyte stabilization is that the resulting zeta potential of stabilized suspensions tabulated in Table I can be directly correlated to the charge of the Al_2O_3 particles, amount of polyelectrolyte dissociation, and the amount of polyelectrolyte adsorbed on

the surface. This concept is represented in Fig. 4 which shows the zeta potential (ζ) and relative number of dissociated COO^- polymer sites (RNS) versus pH. The RNS was calculated by multiplying the amount of adsorbed PMAA (Fig. 2) times the percent of COOH groups dissociated (measured in Ref. 1). This quantity effectively represents the number of negative sites which are available to charge a particle surface. If there is no electrical interaction between the charged polymer and the particle surface, then ζ should ideally correspond directly with RNS. However, this system has electrical interactions with the particle surface; therefore, Fig. 4 shows that the combination of RNS and the influence of particle surface charge determine the resulting zeta potential. Fig. 4 was constructed so that RNS and ζ crossover at $\text{pH} \approx 8.8$ since this pH is very close to the zpc of the Al_2O_3 ; and, therefore, the overall net charge of the Al_2O_3 will have a minimal contribution to the observed ζ . As pH decreases to 8.1, RNS increases and ζ increases slightly as expected. However, at pH 6.5 RNS is at a maximum while ζ decreases appreciably. From this it may be concluded that below the zpc the excess positive surface sites on the Al_2O_3 begin to neutralize excess negative sites on the polyelectrolyte and the effective ζ is lower than expected. This behavior is shown to continue to lower pHs; however, it is expected that for $\text{pH} < 3$, the ζ will be determined only by the Al_2O_3 surface since ζ and RNS approach 0. However, for $\text{pH} < 3$, the ζ will probably still be lower than expected due to the physical presence of an adsorbed neutral polymer layer. At pHs above the zpc, the ζ is slightly larger than expected from the RNS values. This suggests that above the zpc the excess negative surface sites on the Al_2O_3 become additive to the excess negative sites on the polymer. A note that should be emphasized here is that for this system the ζ is a strong contributing factor to the overall suspension viscosity but not the sole determining factor. The maximum ζ is at pH 8.1; however, the best suspensions in terms of stability and viscosity are observed at pH 8.8-9.0. In general, the data from Table I and Fig. 4 show that for 40 v/o suspensions, ionic strength only slightly affects polyelectrolyte stabilized systems, but still a ζ of $> |20|$ mV is necessary for stabilization. The -20 mV gives an indication that the polyelectrolyte is still charged and has negative soluble functional groups extending into the solvent so that an enthalpic steric stabilization mechanism can be functional along with an

electrostatic stabilization mechanism.

3. Viscosity vs. Amount of Polyelectrolyte

Fig. 5 shows the viscosity of 50 v/o AKP 20 Al_2O_3 suspensions (pH 9) versus the amount of PAA added for various molecular weights. For each sample the viscosity was recorded at time = 0 and 10 min at a shear rate of 9.3 s^{-1} . Increases in viscosity (connected by tie lines) show that flocculation is occurring in the suspensions. For each molecular weight, there is a critical amount of polymer that must be added before stabilization and low viscosities result. This corresponds to the saturation adsorption limit of the polyelectrolytes on Al_2O_3 and is in agreement with the previous discussion concerning the stability map in Fig. 2.

Since the amount of polyelectrolyte necessary for stabilization increases as the molecular weight increases, this is an indication that the adsorbed layer thickness may also be increasing with molecular weight. This may have substantial effects for more highly concentrated suspensions.

Further additions of polymer, past the adsorption saturation limit, only serves to provide excess polymer in solution. As shown in Fig. 5, the rheological effects due to excess polymer are much more drastic as the molecular weight increases. This can be seen in two respects. First, the viscosity of polymer solutions is proportional to the size of the individual polymer coils squared.³ Therefore, as the molecular weight increases the viscosity of the aqueous solution part of the suspension drastically increases. Secondly, it is observed that as the molecular weight increases a more pronounced thixotropic effect occurs due to the excess polymer. This is the result of a destabilization mechanism called depletion flocculation.^{8,11} Basically depletion flocculation is the result of an osmotic pressure increase due to the polymer in solution. This effect increases with increasing molecular weight.

4. Processing of Polyelectrolyte Stabilized Suspensions

Using the concepts previously discussed, fluid Al_2O_3 suspensions with 60 v/o solids (> 85% by weight) were made with viscosities of $< 0.4 \text{ Pa}\cdot\text{s}$ at 100 s^{-1} . To show the advantage of increasing the solids concentration in suspension, some samples were cast in plastic molds from 40 to 60 v/o suspensions and then sintered at 1400°C for 45 min. Due to the reduced

volume fraction of solids and longer casting times for the 40 v/o suspensions, it is expected that long range particle segregation took place.¹² This resulted in slightly lower green densities for the 40 v/o suspensions by $\approx 2\%$. This also became apparent after sintering when all of the samples made from the 40 v/o suspensions consistently resulted in 3-6% lower sintered densities regardless of the powders used.

To more clearly show the possible benefits of processing with highly concentrated suspensions, two powder systems of high purity $\alpha\text{-Al}_2\text{O}_3$ were processed by pressing, slip casting 50 v/o suspensions, and casting ≈ 60 v/o suspensions in plastic molds. Then the sintering behaviors were compared; and, the results for AKP 30 Al_2O_3 are shown in Fig. 6. Figure 6 shows clearly that processing from highly concentrated polyelectrolyte stabilized suspensions leads to higher consolidated densities and that these benefits carry over in the form of reduced sintering temperatures. The samples processed from 60 v/o suspensions had a consolidated density of 65.8% theoretical and sintered to 99% theoretical at 1350°C. For an Al_2O_3 powder with a relatively low surface area of 6.8 m^2/g this is a very low sintering temperature. In contrast, filtration channels cause the development of excess voids in slip cast microstructures and higher sintering temperatures are required for the elimination of these voids.¹³ And as expected, the local density variations and inefficient particle packing caused by dry pressing require even higher temperatures for complete void elimination.

CONCLUSIONS

In highly (> 50 v/o) concentrated Al_2O_3 suspensions stabilized with PMAA, a viscosity minimum is observed at pH ≈ 8.8 . This coincides with the pH at which the polyelectrolyte is fully charged and maintains maximum solubility while high affinity type adsorption still occurs and the ionic strength is relatively low.

Below pH ≈ 8.8 , the viscosity increases because of a decrease in the negative charge characteristics of the adsorbed polyelectrolyte and a decrease in the electrosteric repulsive barrier between particles. Above

pH \approx 8.8, viscosity increases because high affinity type adsorption behavior is lost and excess polymer in solution becomes appreciable. Excess polymer can also lead to depletion flocculation and this effect becomes greater as molecular weight increases.

Polyelectrolyte stabilization can exist even in the absence of appreciable electrostatic repulsive forces due to conditions of relatively high ionic strength. However, even though polyelectrolyte stabilization can exist with low levels of electrostatic repulsion it is necessary that an appreciable zeta potential be present on the particles. The actual zeta potential built up on particles due to polyelectrolyte adsorption is a function of the amount of polyelectrolyte adsorbed, the fraction of polyelectrolyte dissociation, and the surface charge of the bare particle. For anionic PMAA and Al_2O_3 at pHs below the zpc of Al_2O_3 , the actual zeta potential is less than expected from the adsorbed PMAA due to the cancellation effect between the negative PMAA and positive Al_2O_3 surface. At pHs above the zpc there is an additive effect between the negative PMAA and the negative surface which yields a larger zeta potential than expected from the amount of PMAA adsorbed.

In general, by understanding the chemistries of the polyelectrolyte and particle surface, polyelectrolyte adsorption behavior, and polyelectrolyte rheological effects one may control the viscosity and rheology for all solids levels. If it is desired to work at low solids but still prevent problems due to segregation then the proper polyelectrolyte conditions can be tailored for a high viscosity thixotropic suspension. If full dispersion and high solids is desired then again the polyelectrolyte conditions can be tailored.

ACKNOWLEDGMENT

The work summarized in the Background Section of this paper was sponsored by the Air Force Office of Scientific Research (AFOSR) and the Advanced Research Projects Agency of the Department of Defense and was monitored by the AFOSR under Grant No. AFOSR083-0375. The work discussed in the main body of this paper was sponsored by the Oak Ridge National Laboratory under subcontract No. 19X-27458C.

REFERENCES

1. J. Cesarano III, I. A. Aksay, and A. Bleier, "Stability of Aqueous α - Al_2O_3 Suspensions with Polymethacrylic Acid (PMAA) Polyelectrolyte," submitted to J. Am. Ceram. Soc., March 1987.
2. P. Molyneux, Water-Soluble Synthetic Polymers: Properties and Behavior, Vol. II, CRC Press, Inc., 1984.
3. R. Arnold and J. Th. G. Overbeek, "The Dissociation and Specific Viscosity of Polymethacrylic Acid," *Recueil*, 69, 192 (1950).
4. J. Papenhuijzen, H. A. Van der Schee, and G. J. Fleer, "Polyelectrolyte Adsorption I. A New Lattice Theory," *J. Colloid Interface Sci.*, 104, 540 (1985).
5. D. C. Henry, "The Cataphoresis of Suspended Particles. Part I--The Equation of Cataphoresis," *Proc. Roy. Soc. (London)*, A133, 106 (1931).
6. P. H. Wiersema, A. L. Loeb and J. Th. G. Overbeek, *J. Colloid Interface Sci.*, 22, 78 (1966).
7. D. J. Shaw, *Introduction to Colloid and Surface Chemistry*, Third Edition, Butterworths, London 1980.
8. D. H. Napper, *Polymeric Stabilization of Colloidal Dispersions*, Academic Press, London 1983.
9. I. A. Aksay and R. Kikuchi, "Structures of Colloidal Solids," in *Science of Ceramic Chemical Processing*, L. L. Hench and D. R. Ulrich, eds., Wiley and Sons, New York, 1986, pp. 513-21.
10. J. Cesarano III and I. A. Aksay, unpublished data.
11. M. Yasrebi and I. A. Aksay, "Effect of Free Polyelectrolytes on

Colloidal Stability," to be submitted to J. Am. Ceram. Soc.

12. C. Han, I. A. Aksay, and O. J. Whittemore, "Characterization of Microstructural Evolution by Mercury Porosimetry," in *Advances in Materials Characterization II*, R. L. Snyder, R. A. Condrate, Sr., and P. F. Johnson, eds., Plenum Publishing Co., 1985, pp. 339-47.
13. I. A. Aksay and C. H. Schilling, "Colloidal Filtration Route to Uniform Microstructures," in *Ultrastructure Processing of Ceramics, Glasses, and Composites*, L. L. Hench and D. R. Ulrich, eds., Wiley Interscience, New York, 1984, pp. 483-91.

FIGURE CAPTIONS

- Figure 1: Schematic of PMAA and PAA polymer segments.
- Figure 2: A stability map showing the amount of adsorbed PMAA-Na required to form stable suspensions of 20 v/o AKP 30 α -Al₂O₃ as a function of pH.
- Figure 3: Viscosity at 9.3 s⁻¹ versus pH for PMAA-Na stabilized AKP 30 α -Al₂O₃ suspensions from 20 to 60 v/o solids concentrations.
- Figure 4: The relative number of COO⁻ polyelectrolyte sites and zeta potential versus pH for 40 v/o AKP 30 α -Al₂O₃ suspensions at pH 9.
- Figure 5: Viscosity versus the amount of PAA added for various molecular weights for 50 v/o AKP 20 α -Al₂O₃ suspensions at pH 9.
- Figure 6: The sintering behavior of AKP 30 α -Al₂O₃ for various processing techniques.

Joseph Cesarano III

Joseph Cesarano III is currently a graduate student at the University of Washington pursuing a Ph.D. in the Department of Materials Science and Engineering with interest in ceramic processing. In 1983 he received a B.S. in Ceramic Engineering at Alfred University and in 1985 a M.S. in Ceramic Engineering at the University of Washington. During the interim he has temporarily been with Sandia National Laboratories, Oak Ridge National Laboratory, and the Swedish Institute for Silicate Research.

Ilhan A. Aksay

Ilhan A. Aksay earned his B.Sc. degree (with honors) in Ceramic Engineering at the University of Washington, Seattle, in 1967. He received his M.Sc. degree in 1969 and Ph.D. in 1973, both in Materials Science and Engineering at the University of California, Berkeley. Upon completing a one year post doctoral appointment at the University of California, Berkeley, he joined Xerox, Webster Research Center in 1974. In 1975, he returned to his native country, Turkey, to accept a teaching position at the Middle East Technical University in Ankara where he stayed until 1981. In 1981, Dr. Aksay joined UCLA's Materials Science and Engineering Department as a visiting Associate Professor. In September 1983, he joined the faculty of the University of Washington, as an Associate Professor in the Department of Materials Science and Engineering and was promoted to Professor in 1985.

His research interests and teaching activities include the processing science of ceramics; thermodynamics and phase equilibria; diffusion and structural studies in ionic systems; and interfacial reactions and capillarity phenomena. His most recent research activities have been on the utilization of colloidal techniques to ceramic processing. In recognition of his contributions in this area, he has received the Richard M. Fulrath Award of the Society in 1987.

TABLE I. SUMMARY OF DATA RELATING INTERPARTICLE FORCES TO RHEOLOGICAL BEHAVIOR FOR 40 v/o Al_2O_3 SUSPENSIONS WITH PMAA-Na

pH	Poly. Ratio Actual/Needed	κa	ζ (mV)	Repulsion $cV_r c$ (ergs)	n_0 to n_{10} min. (cps)	Stability
8.1	0.76	278	-33	1.4	220-405	F
	0.95	303	-39	1.1	60-205	F
	1.2	327	-35	0.5	37-37	S
	1.9	396	-31	0.1	50-70	S
8.1 w/0.1 M NaCl	0.95	529	-26	0.0	415-645	F
	1.2	542	-27	0.0	55-82	SF
	1.4	558	-22	0.0	50-60	S
9.5	0.55	199	-29	7.6	55-115	F
	1.2	249	-30	1.4	85-87	S
	1.7	326	-31	0.4	205-215	S
9.0	1.3	287	-33	1.1	20-20	S
8.8	1.37	303	-31	0.7	20-20	S
6.5	1.2	426	-24	0.0	45-50	S
5.3	1.1	531	-17	0.0	205-230	SF
4.6	1.3	650	-13	0.0	1300-1700	F

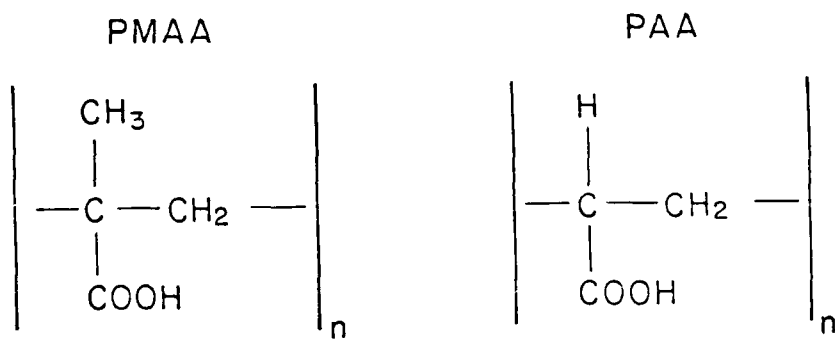


Figure 1

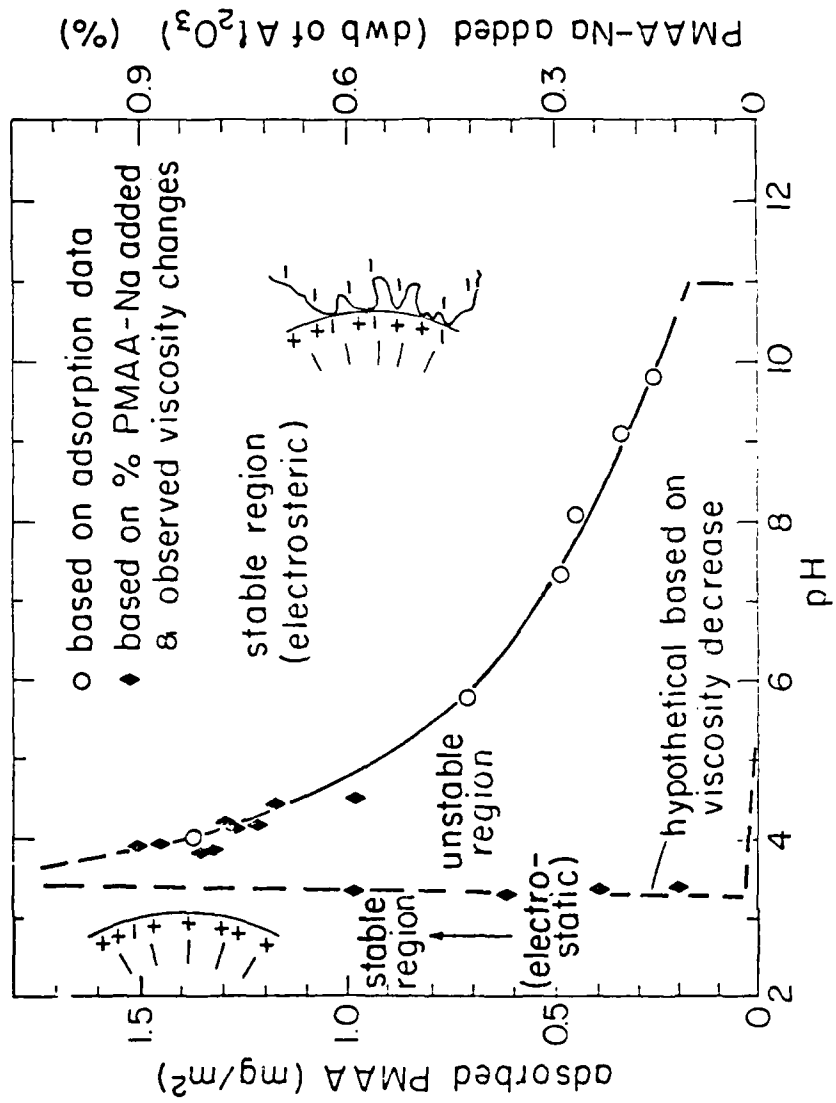


Figure 2

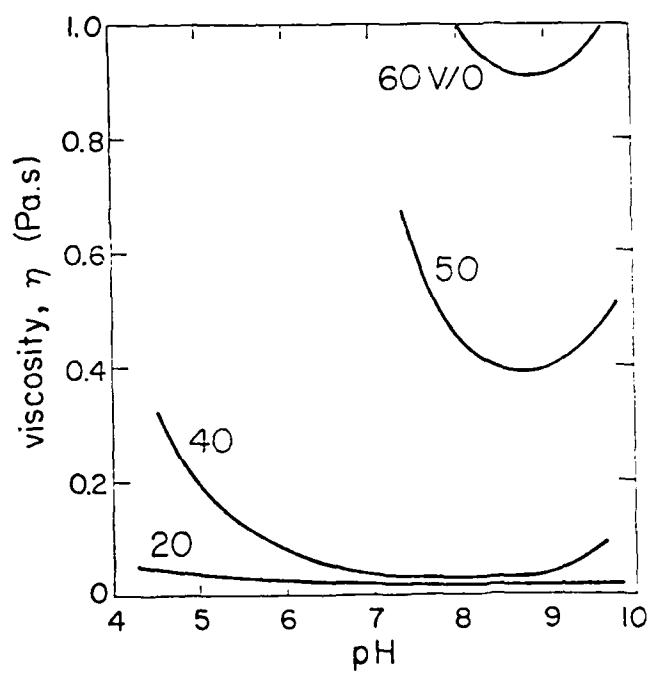


Figure 3

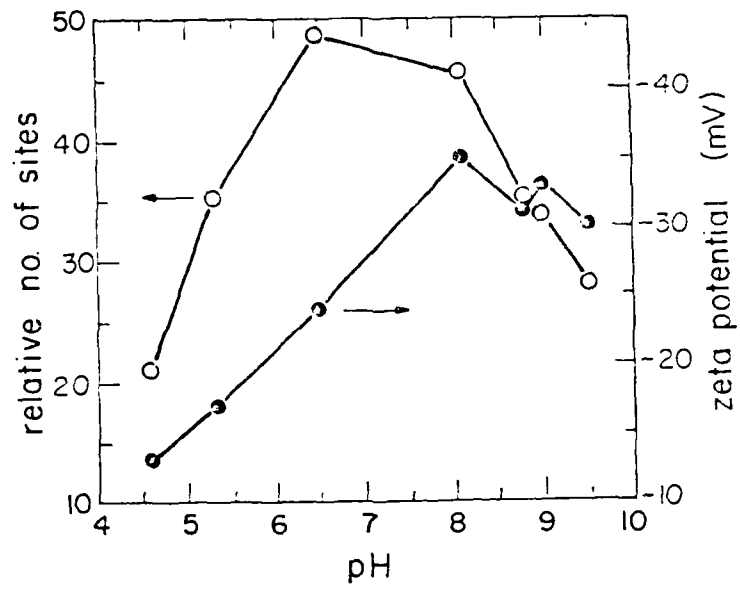


Figure 4

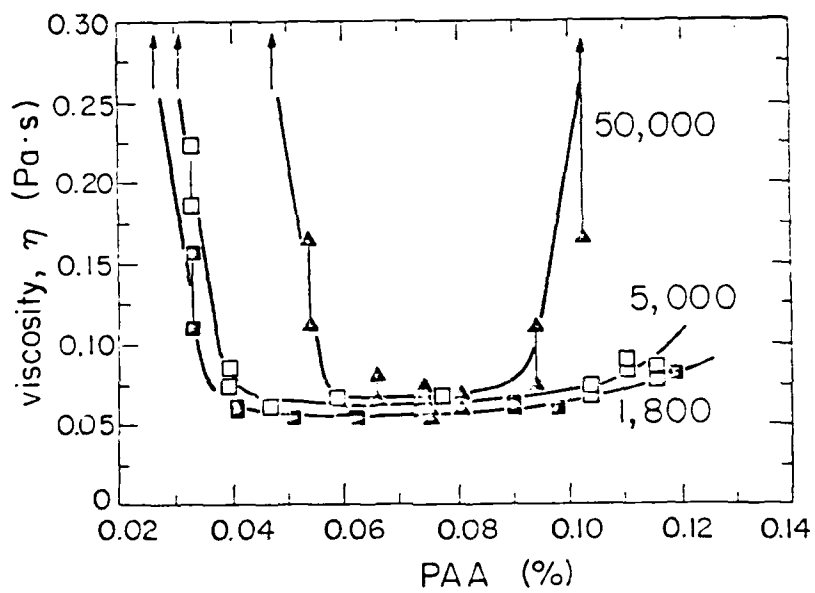


Figure 5

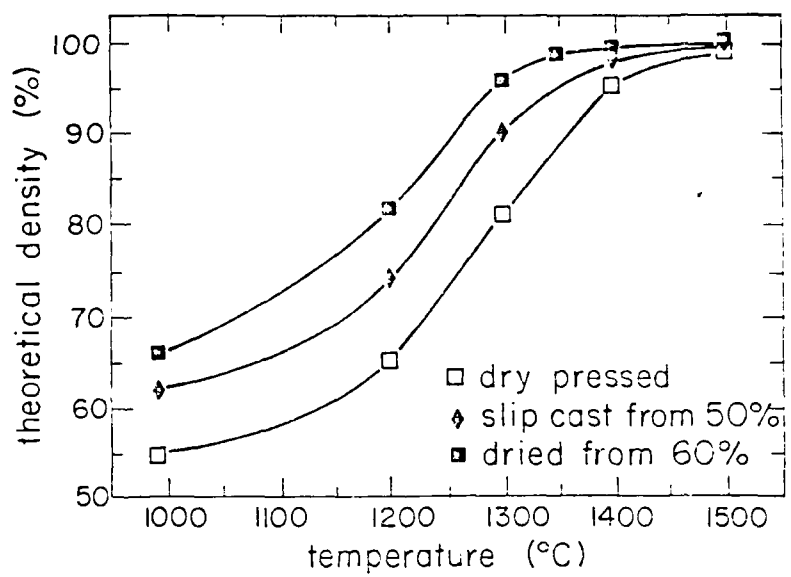


Figure 6

AD-A188 526

MICRODESIGNING OF LIGHTWEIGHT/HIGH STRENGTH CERAMIC
MATERIALS (D) WASHINGTON UNIV SEATTLE DEPT OF MATERIALS
SCIENCE AND ENGINEERING I A BRSAY 30 AUG 87

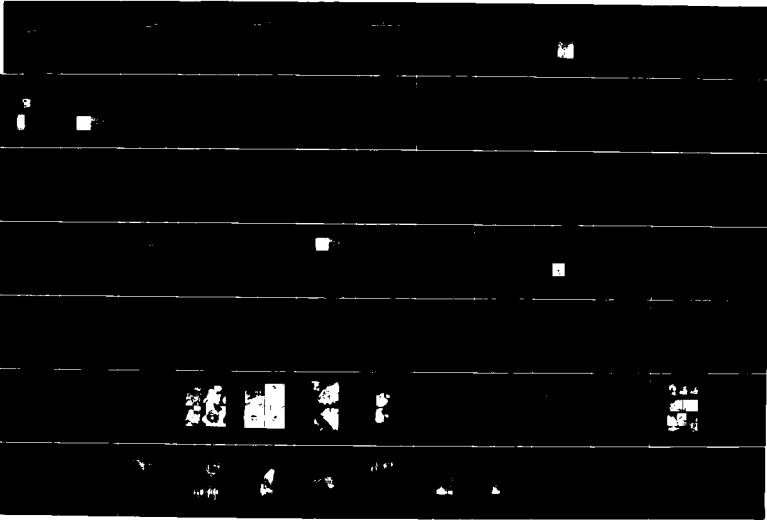
2/4

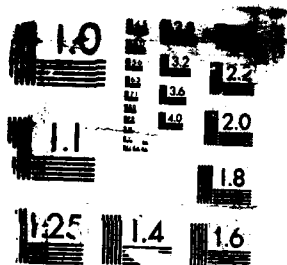
UNCLASSIFIED

AFOSR-TR-87-1595 AFOSR-83-0375

F/G 11/2

NL





RESOLUTION TEST CHART

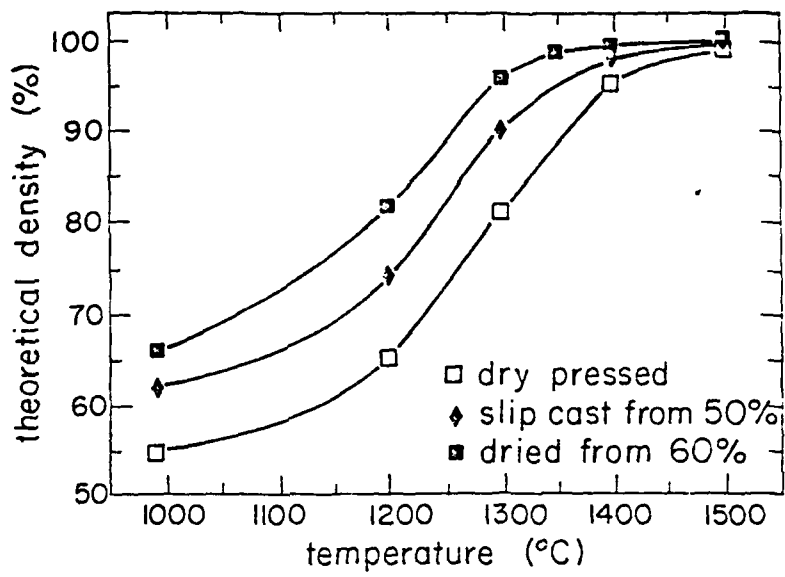


Figure 6

APPENDIX IV

**Effect of Free Polyelectrolytes on Stabilized Aqueous
Suspensions**

(Yasrebi, Aksay, and Cesarano 1987)

***EFFECT OF FREE POLYELECTROLYTES ON STABILIZED AQUEOUS
SUSPENSIONS***

M. Yasrebi, I.A. Aksay, and J. Cesarano

This paper will be submitted and published in the near future.

In this paper, we examine how the addition of a low concentration of free polymethacrylic acid (PMAA) and polyacrylic acid (PAA) effects the stability of α -alumina aqueous suspensions. The PAA we used in the experiments consisted of various molecular weights. Based on optical observations and sedimentation experiments, we have found that low concentrations of the above polyelectrolytes can flocculate the stable suspensions. Furthermore, our experimental evidence suggests depletion flocculation as the prime

APPENDIX V

Phase Stability and Structures in Colloidal Systems

(Yasrebi and Aksay 1987)

PHASE STABILITY AND STRUCTURES IN COLLOIDAL SYSTEMS

M. Yasrebi and I.A. Aksay

This paper will be submitted and published in the near future.

In this paper, we discuss the effect of zeta potential and particle concentration on the microstructure of colloidal suspensions. We studied these effects by making viscosity measurements in aqueous $\alpha\text{-Al}_2\text{O}_3$ suspensions. We show here that viscosity measurement is a suitable technique for studying structural formation in the suspension. In addition, we detected transition between different states of colloidal suspension and plotted a phase diagram. Finally, we discuss the correlation between the experimental data and the theoretical calculations of the colloidal phase diagram.

APPENDIX VI

**Fundamentals of Powder Consolidation in Colloidal
Systems**

(Aksay 1985)

FUNDAMENTALS OF POWDER CONSOLIDATION IN COLLOIDAL SYSTEMS¹

Ihan A. Aksay

Department of Materials Science and Engineering
University of Washington
Seattle, Washington 98195 U.S.A.

Abstract

Although colloidal dispersion techniques are useful in the elimination of unwanted particle clusters, during transitions from the dispersed to the consolidated state, particle clusters form again. We discuss these transitions with a phase diagram that outlines the stability regions of dispersed and consolidated states. The size and the packing arrangement of the particle clusters that form during consolidation can be controlled by the consolidation procedure followed. Due to the formation of these clustered structures, a narrow pore size distribution is not easily obtained. Advantages of using polydisperse particle size systems are illustrated.

1.0 INTRODUCTION

In ceramic processing, powder consolidation and sintering is generally preferred over other techniques (i.e., melt-solidification and vapor deposition) for either economic reasons and/or for its advantages in controlling the microstructure and thus the properties of polycrystalline and polyphase composite systems. In this endeavor for microstructural control through sintering, the most fundamental processing steps are (i) processing or selection of the raw materials in powder form, (ii) consolidation of powders either with the use of liquid suspensions or dry pressing techniques, and (iii) densification of powder compacts with the application of heat and/or pressure. The character of the final product is affected by all the steps of this processing chain (Fig. 1).¹ In a fundamental approach to processing, we must understand not only the role of the powder characteristics, but also the role of the consolidation technique and the sintering path on the final microstructure.

These issues are by no means new research topics. In the field of traditional clay-based ceramics, experience as well as research findings have long favored the use of colloidal suspension (slip) techniques to control not only microstructural uniformity but also to fabricate complex geometries that could not easily be processed by dry pressing techniques.² Further, the use of wide particle size distributions has traditionally been favored to achieve high packing densities and thus to lower sintering temperatures.³

¹Invited contribution to the seminar on "Ceramics: Today and Tomorrow," of the 20th Anniversary of the Basic Science Division of the Ceramic Society of Japan, Kobe, Japan, November 27, 1985.

PROCESSING BY POWDER CONSOLIDATION

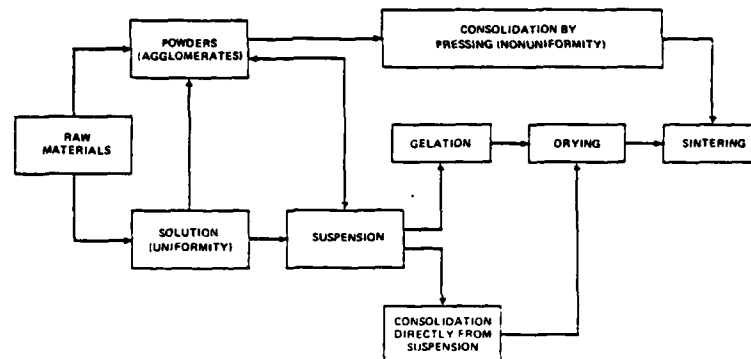


Fig. 1: Various processing paths followed in powder consolidation. Suspension route is used to eliminate unwanted particle clusters (agglomerates). Gelation route is for particles smaller than $\sim 75nm$.

In contrast, in the field of modern ceramics, the importance of using colloidal dispersion and consolidation techniques has not received wide recognition until recent years. Presently, various research laboratories throughout the world have active programs on the processing, colloidal dispersion and consolidation of submicrometer size powders.⁴ This renewed interest in the colloidal approach to processing is mainly a consequence of the realization that unwanted inhomogeneities introduced into a powder compact during the presintering stages generally remain in the finished product as defects.^{5,6}

As a result of this renewed interest in the colloidal processing approach, significant advances have already been made.^{7,8} In the following sections, we review the recent advances on the consolidation of powders by colloidal techniques and outline the guidelines that must be followed for the microdesigning of ceramics. Although these recent findings, in most part, are in agreement with our past experience on clay-based systems, we hope that the new interpretation of the colloidal consolidation processes presented here will establish the impetus for future developments.

Our discussion in Section 2 will start with the colloidal consolidation behavior of nearly monosize, spherical particles in the size range larger than $0.1\mu m$. In Section 3, we will illustrate that although monosize particles serve a useful role in model studies, as in the traditional approach, there are clear advantages to using polydisperse particle size systems when the goal is to complete densification at lower temperatures with minimum amount of grain growth. The directions that must be taken for future developments are outlined in Section 4.

2.0 COLLOIDAL PHASE TRANSITIONS

The use of powders in the submicron size range is preferred in order to increase the driving force for densification and also to form fine-grain microstructures. However, a key problem that arises with the use of submicron size powders is their tendency to form uncontrolled clusters due to van der Waals attractive interactions. Immediate consequences of uncontrolled clustering are that: (i) mixing of multiphase systems becomes difficult, and (ii) packing density variations associated with these clusters impede densification (Fig. 2).

The first stage of colloidal processing is the preparation of a stable suspension (*i.e.*, colloidal fluid or slip) by developing repulsive barriers between particles. The goal in the first stage is to break up or eliminate unwanted particle clusters. The goal in the second stage is to consolidate the particles to achieve a desired spatial distribution and packing density.

In the following sections, we will first outline the methodology of preparing dispersed suspensions by controlling particle interactions. Next, we will outline the transitions from dispersed to consolidated states with a phase diagram. Finally, we will illustrate that during transitions from the dispersed to the consolidated state, particle clusters will form again. However, unlike the particle clusters we wanted to eliminate in the first stage, the type of clusters formed during colloidal consolidation is now under our control.



Fig. 2: Scanning electron micrograph of an Al_2O_3, ZrO_2 composite. Although this composite was hot isostatically pressed at $1500^\circ C$ and 207 MPa for 1 hr. low density regions still remain.

2.1 Particle Interactions and Dispersed Colloidal State

Dispersion in a colloidal suspension is commonly accomplished either by generating an ionic cloud around the particles and/or by coating the particles with polymeric or macromolecular material. In the first case, electrostatic repulsion arises when ionic clouds overlap; and in the second case, steric repulsion is effective when the adsorbed polymer sheaths begin to fold back or interpenetrate. The fundamentals of electrostatic, steric, or the combined electrosteric repulsion mechanisms and the methodology of developing these barriers are discussed in various text books and review articles.^{9,10} The details will not be repeated here. For the purposes of our discussion, the important aspect is the role of repulsive interactions in counteracting the van der Waals repulsive interactions.

As illustrated with the case of electrostatic repulsion in Fig. 3, the combined form of the interaction potential between particles can be continuously varied by monitoring one or a combination of the parameters that affect the repulsive interaction. The case illustrated in Fig. 3

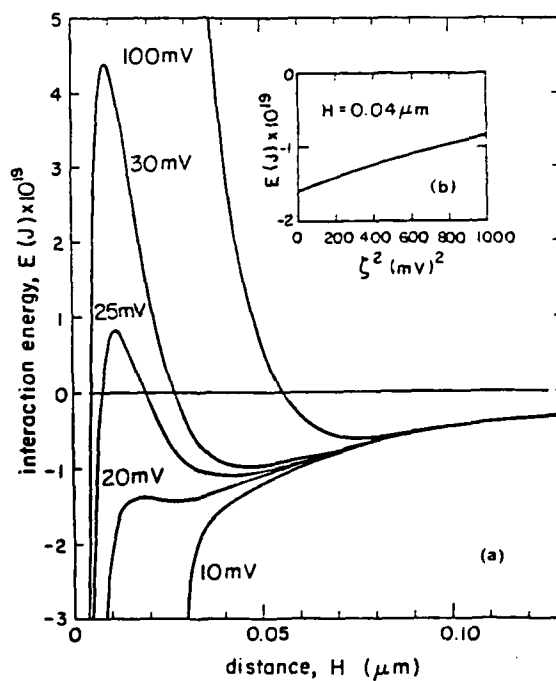


Fig. 3: (a) Variation in interparticle potential for electrostatically interacting $1.0 \mu\text{m}$ diameter particles at surface potentials ranging from 10 to 100mV . H is the surface to surface separation distance. Calculations were done for a double layer thickness of 10^{-6}cm and Hamaker constant of 10^{-19}J . (b) Interaction potential at a separation distance of $0.04 \mu\text{m}$ as a function of ζ^2

is the effect of surface potential (expressed as zeta potential, ζ)^[9] on pair potential. An important relation to note here is the approximate dependence of interparticle binding energy on ζ -potential by the following proportionality (Fig. 3(b)):

$$E \sim \zeta^{-2}. \quad (1)$$

Clearly, ζ -potential is not the only parameter that can be used to regulate the pair potential. In the case of steric stabilization, this goal is achieved by controlling the extent of polymer adsorption on the particle surface. In all cases, the first key requirement for the preparation of dispersed suspensions is to reduce E at the point of particle contact.^[11] By increasing ζ above a critical value (e.g., through *pH* regulation in aqueous systems), nucleation and growth of particle clusters can be prevented.^[12] However, maintaining a low E value alone is not the only requirement for the preparation of dispersed suspensions. As detailed in the next section, for a given E , the dispersed state will be retained only up to a critical particle concentration.

2.2 Phase Equilibria in Colloidal Systems

In the traditional sense, the onset of the cluster nucleation and growth process corresponds to the transition point from dispersed to the flocculated state. From a fundamental point of view, we will use the terms colloidal fluid and solid in analogy to the fluid and solid states in atomic systems. In this approach, the dynamics of particle clustering is the central issue. Transition from the embryo to the critical nucleus and growth stage is considered to be the main distinction between the fluid and solid states.^[13] In certain cases (e.g., injection molding) the structure of the fluid may be retained in the solid state by a process analogous to glassy phase formation in atomic systems.

The main advantage of viewing the process of particle clustering in colloidal systems as analogous to the nucleation and growth in atomic systems is that we can now outline the stability regions of colloidal fluid and solid states in the phase diagram forms familiar to us in the atomic systems. The theoretically calculated phase diagram for a one component colloidal system (i.e., monosize spherical particles with one type of pair potential) illustrated in Fig. 4 is our first attempt to achieve this goal.^[7,14] Here, the stability regions of colloidal fluid and solid states are outlined as a function of two intrinsic variables: (i) the reduced temperature, kT/E , where k is the Boltzmann constant, T is the thermodynamic temperature, and E is the binding energy between particles; and (ii) the particle number density, ρ , of the suspension. In the phase diagram, the temperature scale is normalized by the particle-particle interaction potential.^[14] Similarly, the density scale is normalized by the density of the first generation of particle clusters. In the case of dense packing of monosize spherical particles, the packing density of first generation particle clusters is 0.74.

The form of this phase diagram is not unique when we work with atomic systems. It is unique in colloidal systems in the interpretation of the reduced temperature scale. In atomic systems, the reduced temperature scale is only proportional to the thermodynamic temperature T since the pair potential in a given system is usually fixed. However, in colloidal systems, the

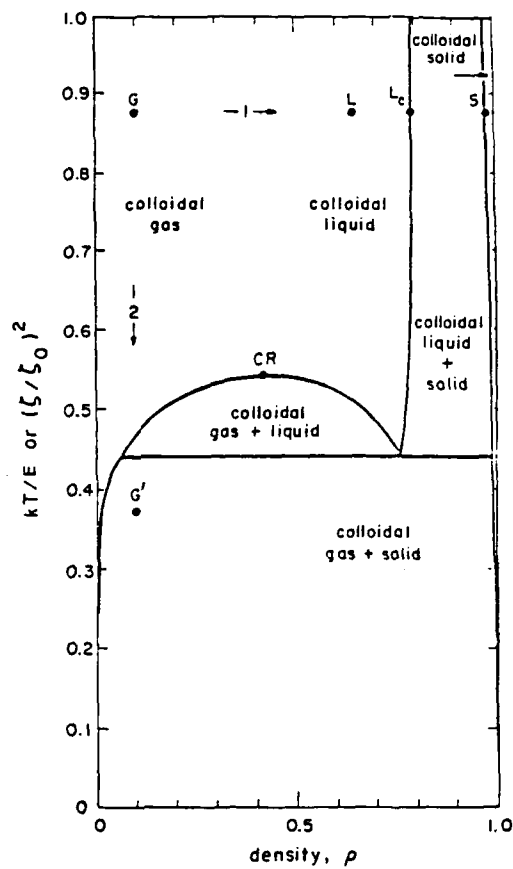


Fig. 4: Phase diagram for a one component colloidal system of mono-size spherical particles.¹⁴

interaction potential can be easily varied. As discussed above, in the case of electrostatically interacting systems, Eq. (1) can be used to express the reduced temperature as:

$$T_R = kT/E = (s/s_0)^2 \quad (2)$$

where s_0 is a normalization constant.

In the phase diagram, the colloidal fluid region above the critical point CR is labeled as colloidal gas when the suspension particle number density is low and as colloidal liquid when the density is high. In this range, the density change (e.g., along Path 1 from G to L) from the

colloidal gas to the liquid state is continuous and the change is not recognized as a first order transition. However, when the density of the liquid-like state exceeds a certain density L_c , a first order transition to a solid-like state starts with the nucleation and growth of particle clusters. When we work with monosize spherical particles, these first order transitions are referred to as disorder-order transitions.¹⁵ The ordered state is often recognized by its opalescent property.¹⁶ With polydisperse systems, the opalescent property can be lost; however, the transition can still be recognized through variations in other properties, e.g., rapid viscosity increase at a critical particle concentration.¹⁷

In contrast to the process along Path 1, if we follow Path 2 from G to G' (e.g., by changing ζ -potential as described above), first order transitions from gas- to liquid- and solid-like states are observed at much lower particle concentrations.^{14,18} In the traditional ceramics language, this colloidal fluid region above CR is where we prepare a slip or suspension at low viscosities and high solids loadings. However, below the critical point, the slip or colloidal fluid region narrows to low particle concentrations and thus is not suitable for the preparation of highly concentrated suspensions. When part of the suspending medium is eliminated, the slip is transformed to a consolidated state when the particle concentration exceeds the critical concentration line outlined in the phase diagram. Regardless of the path followed, the transition from a colloidal fluid to solid state is a nucleation and growth process of particle clusters; thus, we must next understand the structural variations associated with the multiple clustering of the first generation particle clusters.

2.3 Hierarchically Clustered Colloidal Solids

In Fig. 5(a), we plot the packing density of monosize (0.8 μ m) silica particles as a function of ζ^2 (i.e., kT/E) as determined by gravitational settling.¹⁴ Here, ζ_c is the ζ -potential at the critical point of the phase diagram presented in Fig. 4. A unique feature is the existence of two distinct density regimes with respect to this critical ζ -potential. In the supercritical regime ($\zeta > \zeta_c$), the packing density is $\sim 64\%$ of the total volume. In the subcritical regime ($\zeta < \zeta_c$), a continuous but significant decrease in the packing density down to 10% is noticed. As illustrated in the scanning electron micrograph of Fig. 5(b), this drastic decrease in the density is due to the formation of large voids between particle clusters. However, since this continuous density change as a function of the interparticle binding energy suggests a structural continuity in the particle clusters, we next examine the microstructural variations of the particle clusters as a function of E at a higher magnification.

In Fig. 6(a), we illustrate the continuously changing microstructural features of the particle clusters at three different ζ -potentials. The unifying feature of these microstructures is that a hierarchy of particle clustering is observed in all cases. The closely packed, smallest size particle clusters are identified as first generation particle clusters. The entire microstructure in each case represents the second generation of clusters. In Fig. 6(b), we illustrate the variations in the arrangement of the first generation particle clusters by highlighting the second generation voids as dark regions. Here, two features are noteworthy: (i) with increasing interparticle binding energy, first generation particle clusters become smaller, and (ii) parallel to this change, voids between these first generation particle clusters become larger.

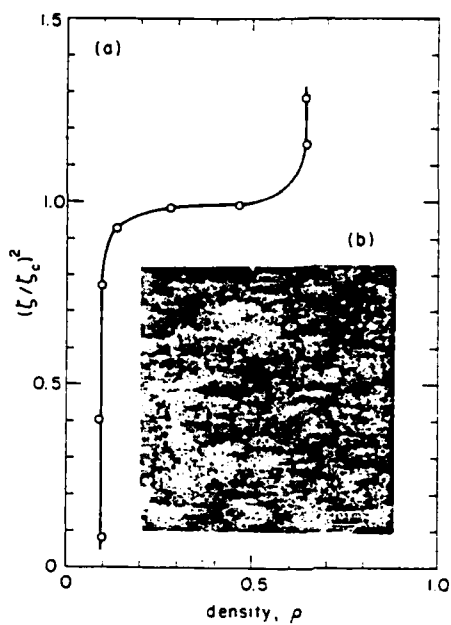


Fig 5: (a) Variations in the sedimentation density (relative to the total volume) of colloidal solids as a function of $(\zeta/\zeta_c)^2$ where ζ_c is the zeta potential at the critical point. (b) Scanning electron micrograph of particle clusters formed at low T_R values.¹⁴

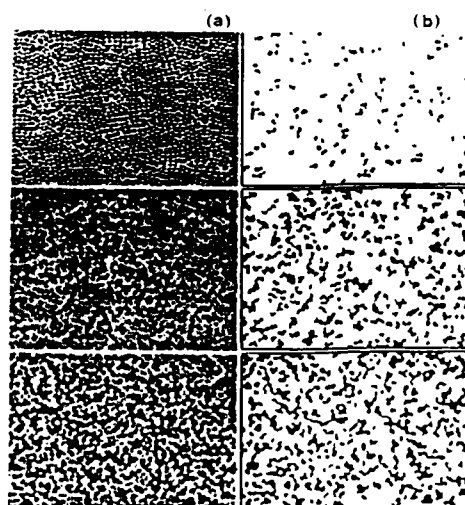


Fig. 6: (a) The arrangement of particle clusters formed by centrifugal sedimentation of SiO_2 microspheres (average diameter = $0.7\mu\text{m}$) in H_2O at $\zeta = 110\text{mV}$ (top), $\zeta = 68\text{mV}$ (middle), and $\zeta = 0\text{mV}$ (bottom). (b) Images where only the second generation voids are highlighted as dark regions in order to illustrate the continuous variations in clustering.¹⁴

Following this observation on the hierarchical clustering of particles, when we now reexamine the data of Fig. 5(a), the large voids that are responsible for the significant density decrease in the subcritical range are classified as third generation voids. In the supercritical range, third generation voids are not observed. In the subcritical range, as the clusters become stronger with increasing interparticle binding energy, third generation particle clusters also form. However, in most ceramic forming processes, these third generation clusters are easily collapsed.¹⁹ Thus, we have to be mainly concerned with the microstructural variations associated with the second generation particle clusters and the voids.

The most important implication of this hierarchical clustering during colloidal consolidation is that even the colloidal suspension routes cannot provide an easy solution to the problem of packing density inhomogeneities. Although colloidally consolidated microstructures are all uniform at a scale length larger than the size of the first generation particle clusters, a monosize porosity distribution is not necessarily obtained by using monosize particles. In fact, as will be illustrated in Section 3.0, polydisperse particle size systems have clear advantages over the monosize particle systems.

3.0 MICROSTRUCTURAL EVOLUTION

When colloidally consolidated microstructures are sintered, first generation particle clusters sinter faster and at significantly lower temperatures than the second generation void regions due to their higher packing density and smaller pore size.²⁰ As illustrated in Fig. 7, when we work with $0.8\mu\text{m}$ nearly monosize α -alumina (Sumitomo AKP-15) consolidated by colloidal filtration, the first generation particles are nearly fully dense at 1200°C in 1 hr.²¹ but, in order to densify the second generation void regions and to complete the densification of the entire system, it becomes necessary to work at temperatures as high as 1550°C .

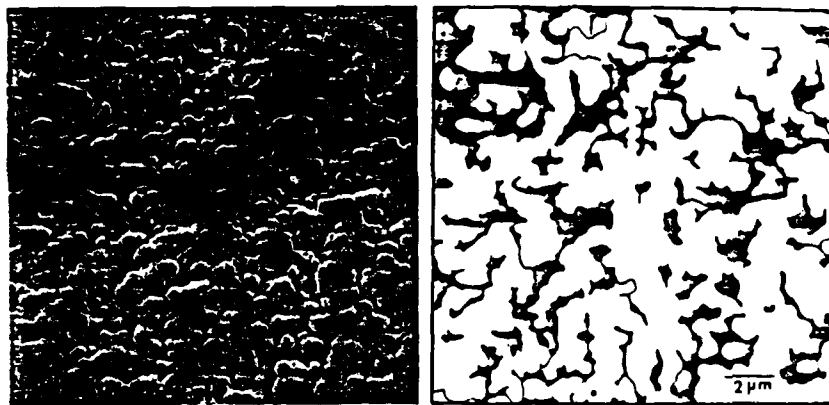


Fig. 7: Microstructure (SEM) of $0.78\mu\text{m}$ α -alumina powder compact after partial sintering at 1200°C for 1 hr. Inter-cluster regions are highlighted in the negative image.²¹

With this realization, we ask if it is ever possible to eliminate the multimodal nature of pore size distribution in colloiddally consolidated systems and pack the entire system as the first generation particle cluster itself. We envision three approaches to achieve this goal: (i) start the clustering process only from a single nucleus by a process similar to the growth of single crystals in atomic systems, (ii) minimize the size differences between the first and second generation voids by filling in the voids with smaller particles, and (iii) destroy the hierarchical clustering after its formation by shear deformation processes as in injection molding. The first approach is a difficult one especially in the processing of complex systems. The second and third approaches, definitely have the potential for success. In the following paragraph, we will illustrate the feasibility of the second approach.

In Fig. 8, we report the overall packing density of a bimodal particle size system consolidated by the same filtration technique used in the consolidation of the monosize particle size system of Fig. 7.²¹ In agreement with previous studies,^{22,23} the maximum packing density is achieved at a coarse to fine particle ratio of 3:1. The sintering behavior of the end members is compared with that of this 3:1 mixture in Fig. 9. Consistent with our analysis, the mixture sinters to a fully dense state at a 100°C lower temperature than the monosize coarse particle system. Further, when they reach the fully dense state, the mixture displays smaller grain size than the monosize coarse particle system.²⁴

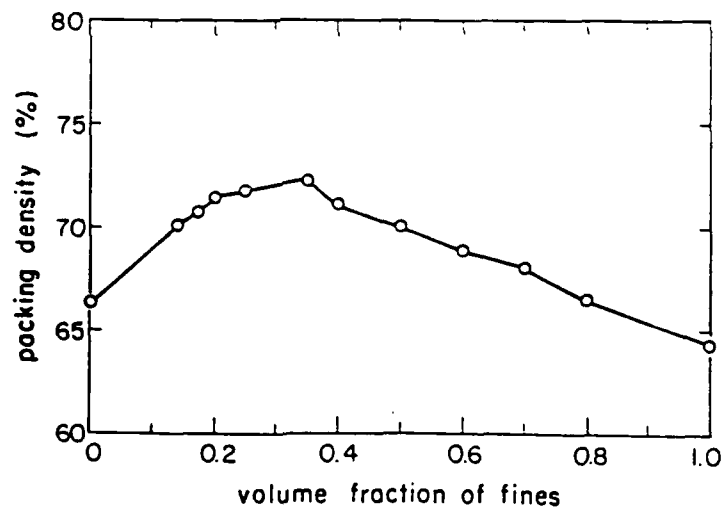


Fig. 8: Packing density variation in the bimodal systems with end members of 0.78 and 0.21 μm size particles.²¹

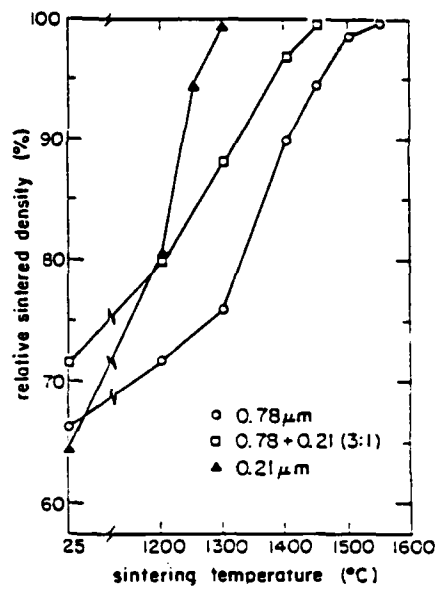


Fig. 9: Sintered density of monosize (0.78 and 0.21 μm) and bimodal systems.

4.0 CONCLUSIONS

The work presented in this review leads us to the following conclusions:

- (i) Colloidal dispersion techniques are needed to eliminate particle clusters that form uncontrollably due to van der Waals attractive interactions. This approach is especially useful when we work with multiphase particle systems in the 10^{-6} to $10^{-9}m$ range.
- (ii) Transitions from dispersed to consolidated state start as a nucleation and growth process of first generation particle clusters. These particle clusters form when either the interparticle binding energy, E , or the particle number density, ρ , in the suspension exceeds a critical value. We outline these transitions with a theoretically calculated E vs. ρ colloidal phase diagram.
- (iii) Hierarchically clustered microstructures form due to multiple clustering of particle clusters. Consequently, in such hierarchically clustered microstructures, the classification of the void space follows a similar trend as first, second, and third generation voids. Unlike the particle clusters that we wanted to eliminate in the dispersion stage, the size and the spatial arrangement of the particle clusters that form can be controlled by simply changing the colloidal consolidation path on the phase diagram.
- (iv) In most ceramic forming processes, voids that remain in a consolidated structure are only the first and second generation voids. In sintering these particle compacts, first generation particle clusters sinter faster and at significantly lower temperatures than the second generation void regions due to their higher packing density and smaller pore size.

We expect that the key future developments in powder consolidation by colloidal techniques will complement the findings reported in this paper in the following areas:

- (i) In order to achieve lower sintering temperatures, the goal must be to develop new techniques to consolidate the entire system as the first generation particle cluster itself (*i.e.*, a state approaching monosize pore distribution). An effective way to achieve this goal is to use polydisperse particle size systems. Suspensions of monosize particles can be no more than 64 v/o. This barrier of 64 v/o may be surpassed, in terms of space filling concepts, by using a multimodal or continuous distribution of particle sizes. Although we have already proven the validity of this concept with a bimodal distribution, we now need to determine the proper particle size distribution.
- (ii) Some traditional forming techniques (*i.e.*, slip casting or tape casting) are not suitable for the elimination of second generation voids due to the formation of flow channels during the process of filtration by capillary suction or drying. Advantages of shear deformation of polymer/ceramic composites (by extrusion and injection molding) should be exploited in an attempt to reduce and narrow the size distribution of the second generation voids.

- (iii) Presently, we mainly use organic polymers as binders and/or as dispersion media. The elimination of the organic polymers during the heat treatment stage is always a major problem. This problem can be avoided by using inorganic polymers that can be converted to ceramic phases during heat treatment. For this purpose, contributions of chemists should be encouraged in the synthesis of inorganic polymers.

Acknowledgements

This work was in part supported by the Advanced Research Projects Agency of the Department of Defense and was monitored by the Air Force Office of Scientific Research under Grant No. AFOSR-83-0375. The contributions of my colleagues, in particular R. Kikuchi and C. Han, to the work reported here are gratefully acknowledged.

REFERENCES

1. **Ceramic Processing**, Publication 1576, National Academy of Sciences. Washington, D.C., 1968.
2. F. H. Norton, **Elements of Ceramics**. 2nd Edition. Addison-Wesley. Reading, CA. 1974.
3. S. S. Kocatopcu, *J. Am. Ceram. Soc.*, **29** 41 (1946).
4. See research topics listed in the *Am. Ceram. Soc. Bull.*, **64** 3: 1082 (1985) and **64** 9: 1097 (1985).
5. W. D. Kingery, in **Ceramics Processing Before Firing**, G. Y. Onoda, Jr. and L. L. Hench, eds., Wiley-Interscience. New York, 1978, p. 291.
6. F. F. Lange, I. A. Aksay, and B. I. Davis, *J. Am. Ceram. Soc.*, **66** 6: 407 (1983).
7. **Ultrastructure Processing of Ceramics, Glasses, and Composites**. L. L. Hench and D. R. Ulrich, eds., John Wiley & Sons. New York. 1984.
8. **Better Ceramics Through Chemistry**. Materials Research Society Symposia Proceedings. Vol. 32. C. J. Brinker, D. E. Clark, and D. R. Ulrich, eds., North-Holland. Amsterdam. 1984.
9. R. J. Hunter, **Zeta Potential in Colloid Science, Principles and Applications**. Academic Press. London. 1981.
10. D. H. Napper, **Polymeric Stabilization of Colloidal Dispersions**. Academic Press. London. 1983.
11. J. Th. G. Overbeek, *J. Colloid Interface Sci.*, **58** 2: 408 (1977).
12. I. A. Aksay, F. F. Lange, B. I. David, *J. Am. Ceram. Soc.*, **66** [10] C-190-192 (1983).
13. G. Y. Onoda, Jr., *Phys. Rev. Lett.*, **55** 226 (1985).
14. I. A. Aksay and R. Kikuchi, "Structures of Colloidal Solids," to appear in **Ultrastructure Processing of Ceramics, Glasses, and Composites II**, L.L. Hench and D.R. Ulrich, eds., Wiley & Sons. New York, 1986.
15. I.F. Efremov, in **Surface and Colloid Science** E. Matijevic, ed., John Wiley & Sons, New York, 1976, Vol. 8, p. 85; and P. Pieranski, *Contemp. Phys.* **24** 25 (1983) provide extensive reviews on disorder-order transitions in colloidal systems.
16. T. Alfrey, Jr., E. B. Bradford, and J.W. Vanderhoff, *J. Opt. Soc. Amer.* **44** 603 (1954); A. Kose, M. Ozaki, K. Takano, Y. Kobayashi, and S. Hachisu, *J. Colloid Interface Sci.*, **44** 330 (1973).

17. J.W. Goodwin, T. Gregory, J.A. Miles and B.C.H. Warren. *J. Colloid Interface Sci.*, **97** 488 (1984).
18. J.A. Long, D.W.J. Osmond, and B. Vincent. *J. Colloid Interface Sci.*, **42** 545 (1973); and C. Cowell and B. Vincent. *ibid* **87** 518 (1982).
19. I.A. Aksay and C.H. Schilling, in **Ultrastructure Processing of Ceramics, Glasses, and Composites**, L.L. Hench and D.R. Ulrich, eds., John Wiley & Sons, New York, 1984. p. 439.
20. I.A. Aksay, in **Advances in Ceramics**, Vol. 9, J.A. Mangels and G. L. Messing, eds., Am. Ceram. Soc., Columbus, OH, 1984.
21. C. Han, I.A. Aksay, and O.J. Whittemore, in **Advances in Materials Characterization II**, R.L. Snyder, R.A. Condrate, Sr. and P. F. Johnson, eds., Plenum, New York, 1985. p. 339.
22. G. L. Messing and G.Y. Onoda, Jr., *J. Am. Ceram. Soc.*, **61** 1-2 1 (1978) and **61** 7-8 363 (1978).
23. J.P. Smith and G.L. Messing, *J. Am. Ceram. Soc.*, **67** 1 238 (1984).
24. C. Han. "Sintering of Bimodal Powder Compacts." M.Sc. Thesis, University of California, Los Angeles, CA, 1985.

APPENDIX VII
Sintering of Bimodal α -Al₂O₃ Compacts

(Han and Aksay 1987)

Sintering of Bimodal α -Al₂O₃ Compacts*

C. Han and I.A. Aksay

August 25, 1987

**Department of Materials Science and Engineering
University of Washington,
Seattle, Washington 98195**

*Presented at the 37th Annual Pacific Coast Regional Meeting of the American Ceramic Society, San Francisco, CA, Oct. 28-31, 1984.

Sintering of Bimodal α -Al₂O₃ Compacts*

ii

Abstract

In this paper, we compare the sintering behavior of colloidally prepared bimodal α - Al_2O_3 compacts to the behavior of a monosize coarse particle compact. In the range of up to 25 volume % fines, pore size and overall pore volume decrease continuously as the fine particle fraction increases. As a result, bimodal particle compacts sinter to full density at lower temperatures than does the coarse particle compact. Also, the grain sizes of nearly fully dense bimodal compacts are smaller than that of the monosize coarse particle compact.

I. Introduction

To a great extent, the sintering behavior of a powder compact is determined by the microstructure of the green compact, which in turn is controlled by the steps taken in the processing stages prior to sintering. Three conditions must be met in the green compact in order to successfully sinter at low temperatures: a small particle size, narrow size distribution of small pores, and uniform spatial distribution of pores. Herring (1) performed a theoretical comparison of sintering two different sized particle systems with identical packing geometry. He clearly showed that smaller particles sinter much faster because of their larger chemical potential. This potential is due to their smaller radius of curvature. By analogy, it can be seen that if the particle size is identical, a compact with smaller pores sinters faster than a compact with larger pores due to the higher chemical potential of vacancies in smaller pore. The pore structure in a particle compact is determined by both particle size and processing technique.

Recently, the trend has been to use colloidal processing techniques in order to obtain homogeneous particle compacts (2). However, the outcome of colloidal processing is always a hierarchical structure (3). In this structure, there are at least two types of pores; 1) smaller pores between primary particles in the first generation cluster (first generation pores whose size is determined solely by primary particle size), and 2) larger pores between the first generation clusters (second generation pores whose size is controlled by primary particle size and processing technique (4)). Upon heating, as described earlier, the smaller first generation pores sinter faster than the larger second generation pores.(4) Therefore, once the particle system and the processing technique are chosen, the sintering temperature of the resulting powder compact will be determined by the size of the larger second generation pores. In order to lower the sintering temperature, one must reduce the size of the second generation pores.

In homogeneous bimodal particle compacts, fine particles will occupy the void space between coarse particles. The space-filling concept suggests that the addition of fine particles in a coarse matrix results in the reduction of pore size and overall porosity. Although the effect of the addition of fine to coarse particles on the pore size reduction is not clarified experimentally, the effect of bimodal particle systems on packing density has been investigated theoretically (5) as well as experimentally.(6-8) In spite of the advantages of bimodal particle compacts, little attention (9-11) has been given to sintering them. Even the existing experimental results (9,11) do not clearly illustrate the advantage of bimodal systems due to deficiencies in the experimental procedures. In those experiments, samples were prepared by cold-pressing of

dried powder. In that process, although mixing of the two components may be proper, large pores are introduced due to the presence of large, inhomogeneous agglomerates in the dried state. These large pores would tend to offset the effect of fine particle addition.

This paper will provide data on the packing behavior of colloiddally consolidated bimodal compacts and will demonstrate that pore size decreases with the addition of fines to the coarse particle compacts. Also, data on the sintering behavior will demonstrate that as a result of the reduction of pore size, the bimodal compacts sinter to full density at lower temperatures than does the coarse particle compact.

II. Experimental Procedure

As used nearly monosize, pure α - Al_2O_3 powders (Sumitomo Chemical America, Inc., New York, NY (AKP-15 and AKP-50, Purity > 99.995%) with median particle diameters of 0.78 and 0.21 μm as the coarse and the fine particles, respectively. Bimodal mixtures were prepared at the fine particle fractions of 0.14, 0.17, 0.20, 0.25, 0.35, 0.40, 0.50, 0.60, 0.70, 0.80, and 0.90 (by volume, weight, or number?). All particle suspensions were dispersed electrostatically in distilled water at solids content of 50 volume % or greater in order to obtain homogeneous particle mixtures. Detailed information on the prevention of particle segregation at high solids content is given elsewhere.⁽¹²⁾ Proper dispersion of the α - Al_2O_3 powders in water was obtained by adjusting the pH (Fisher Scientific, Pittsburgh, PA (Accumet pH meter) of suspensions to 2.5 with HCl and by stirring the suspensions vigorously on a magnetic stirring plate. To facilitate the break-up of soft agglomerates, ultra sonic vibration (Fisher Scientific, Pittsburgh, PA (Sonic Dismembrator 300)) was applied occasionally.

Dispersed suspensions were cast into 5cm x 5cm x 1cm teflon frames placed on a plaster plate made at the consistency of 75. After approximately 3 hours, the cakes were removed from the plaster plates and dried at room temperature for 24 hours. All sides of the dried slabs were ground off in order to remove the inhomogeneities generated during filtration. These inhomogeneities included artifacts on the sides caused by the resistance from the teflon frame, contamination of the bottom from the plaster plate, and the skin on the top surface formed by sedimentation. From the ground slab, approximately 1cm x 1cm x 0.8cm samples were cut.

These were kept at 110°C in an air-circulating oven (Fisher Scientific, Pittsburgh, PA (Isotemp oven)) until they were needed for the measurements and sintering.

Samples containing 14, 17, 20 and 25 volume % fine particles were sintered in stagnant air at temperatures between 1000°C and 1550°C for 1 hour. The samples were loaded in the furnace (Lindberg, Watertown, WI) at room temperature and the furnace was heated up to the desired peak temperature in 30 minutes. After soaking for 1 hour at the peak temperature, the furnace was turned off automatically and was allowed to cool to room temperature.

Densities were measured (Mettler Instrument Corp., Highstown, NJ (Mettler AE160)) by a standard liquid displacement technique using distilled water for the sintered sample and kerosene for the unsintered powder compacts. We calculated closed as well as open porosities. Reported values are the mean of at least 9 measured samples. Pore neck size distributions of sintered as well as green powder compacts were measured by mercury porosimetry (American Instrument Co., Silver Spring, MD (Aminco porosimeter)). The maximum pressure applied was 15,000 psi. From the amount of mercury intrusion and applied pressure, the pore neck size was calculated by the Washburn equation (13) using 0.485 N/m and 140° as the surface tension of mercury and the contact angle of mercury on α -Al₂O₃ particles, respectively.

Microstructures of sintered samples were observed by scanning electron microscopy (Cambridge Instrument, Cambridge, England (Streoscan Mark II-A)). These SEM samples were polished with 1 μ m diamond paste on a nylon cloth. In order to reveal the grain boundaries for SEM observation, polished samples were thermally etched at 1200°C for 1 hour for samples sintered at 1300°C or below and at 1300°C for 1 hour for samples sintered at 1400°C or above. The heating schedule for thermal etching was identical to that for sintering.

III. Results and Discussion

The variation of packing densities in bimodal compacts are plotted as a function of volume fraction of fines in Figure 1. The results of the present study agree well with the previous experimental results (6,7) which show the deviation from the theoretical model.(6) This deviation from an ideal fine model was subsequently attributed to the particle size segregation that resulted from improper mixing.(14,15)

Bimodal mixtures in this study do not satisfy the size ratio (diameter of fines/diameters of coarse) assumed for the ideal model. Therefore, the results shown in figure 1 cannot be compared to the ideal model directly. However, close examination of figure 1 shows a non-linear increase in packing density in the coarse-rich region; that is, packing density increases with fines at a decreasing rate. In the present study, with the use of suspensions that contained > 50 volume % solid, size compositional inhomogeneities resulting from particle segregation during consolidation were prevented as confirmed through hydraulic resistance measurements.(12) In spite of this precaution, our density data still deviates from linearity. This suggests that the non-linearity results from another inhomogeneity _____ pore density fluctuation due to the presence of first generation clusters. The interpretation of this is that the addition of fines does not decrease the second generation porosity (between the first generation clusters) so effectively as it decreases the first generation porosity (within the first generation clusters).

As shown in figure 2, channel neck size decreases exponentially as the fraction of fines increases, indicating that the initial small fraction of fines is the most effective for the reduction of pore neck size. This behavior is consistent with the concept that in uniformly mixed bimodal compacts, fine particles act as space-filling units and thus the intrusion neck size decreases as fine particles occupy space between coarse particles. It is important to note that mercury intrusion provides information about the size of pore neck, not actual pore size (16). However, in the present study, a smaller neck size infers a smaller pore size as confirmed by the partially sintered microstructures shown in figure 6.

The sintering behaviors of compacts containing 0, 14, 25, and 100 volume % fine particles are shown in figure 3. It is reasonable to compare the sintering behavior of bimodal compacts to the pure coarse particle compact since the bimodal compacts contain at most 25 volume % fines. The coarse particle compact reaches full density at 1550°C, while the bimodal compacts containing 14% and 25% fines reach full density at 150°C and 1450°C, respectively. The pure fine particle compact reaches full density at 1300°C. However, the sintering of the fine particle compact will not be discussed further since the main purpose of this paper is to investigate how the addition of fines to the coarse particle compact affects the sintering behavior.

Close examination of the sintering curve reveals that the differences between sintered densities of coarse particle and bimodal compacts at each sintering temperature are always greater than the differences between their packing densities. This holds until they reach ap-

proximately 90% of theoretical density (TD). For example, the packing density difference between the coarse particle compact and the bimodal compact with 14% fines is only ~4%. However, the sintered density difference at 1300°C increases to ~9%. The above observation clearly demonstrates that the increase in the packing density of bimodal compacts is not the only cause for their improved sintering behavior. Another factor which contributes to this enhanced behavior is the reduction of pore size with the addition of fine particles (Figure 2).

In figure 4, the stability of pore channels is shown with a plot of the pore channel neck diameter as a function of the sintered density. In general, the pore channel neck diameters decrease as the sintered densities increase. Finally, at nearly full density, the pore size becomes zero, indicating that any pores left in the compacts are closed. The pore neck growth in bimodal compacts during the initial stage of sintering is not yet understood.

One important point to note in figure 4 is the cross-over of pore neck size. Initially, the neck size decreases with the increasing fine fraction at a given sintered density. However, at ~87% TD, the pore neck size inversion occurs between the two bimodal compacts. Also, another neck size inversion occurs between the bimodal compacts and the coarse particle compact at ~92% TD. As a result, above ~92% TD, the bimodal compact with 25% fines has the largest pore neck size, and the pure coarse particle compact has the smallest pore neck size. This neck size inversion indicates that the addition of fines improves the stability of pore channels, providing against the closure of pores and subsequent closed pore formation, although initially the addition of fines to the coarse particle compact decreased pore size. Due to the improved pore stability bimodal compacts, pores remain open until the compacts _____ to nearly full density.

Figure 5 shows decreasing open porosity in bimodal compacts during sintering. Data for compacts containing nothing but open pores would fall directly on the diagonal line. For the coarse particle compact all the data points are on this line up to ~95% sintered density where the density falls below the line, indicating the formation of closed pores. The position of the data point, midway between the diagonal line and the base line, indicates that about 50% of the total remaining porosity is closed pores. Bimodal compacts do not show any detectable deviation from the diagonal line throughout the entire sintering schedule. This result shows that the addition of fines improves the stability of pore channels against the formation of closed pores which hinders the sintering to full density.(17)

The microstructures of the coarse compact and of the bimodal particle compacts with 25% fines are shown in figure 6. Both compacts were sintered at 1150°C for 1 hour. These microstructures show the dramatic difference between the initial sintering behaviors of these compacts. At 1150°C, the coarse particle compact is barely sintered and individual particles are still seen, while the bimodal compact with 25% fines show large, fully sintered patches. However, large pores which are formed by the flow of water during colloidal filtration and which are between sintered patches (flow channels) remain unsintered. These microstructures show that the pores in a bimodal compact is generally smaller than in the coarse particle compact.

Figure 7 shows the microstructures of the coarse and the 25% fine compacts sintered to nearly full density (97% TD). In order to sinter these compacts to the same density at the same temperature, the coarse particle compact was held at 1400°C for 4 hours while the 25% fine compacts were held for 1 hour at that temperature. This treatment prevented very different grain growth kinetics which would result from sintering at different temperatures (17). It is evident that the coarse particle compact has a much larger grain size than the bimodal compact.

Grain growth during sintering initiates from regions which densify early. In powder compacts, densely packed clusters sinter much faster than the loose inter-cluster regions. While loosely packed inter-cluster regions are still densifying, fully dense clusters are suffering grain growth. When the pore size difference between intra-cluster pores (first generation pores) and inter-cluster pores (second generation pores) is large, more time is required to densify inter-cluster pores. This results in _____ grain growth. In Figure __ the coarse particle compact was sintered for 4 hours, while the bimodal compact was sintered for only 1 hour, showing that the grain size of the bimodal compact is smaller than that of the coarse particle compact.

IV. Conclusions

We investigated the effects of bimodality on packing and subsequent sintering.

The addition of fine particles results in 1) an increase of overall packing density, and 2) in the reduction of pore size. These two contributions enhance the sintering behavior of bimodal compacts. With the addition of 25% fines, the sintering temperature of the α -Al₂O₃ compact was reduced by 100°C. Due to the lower sintering temperature and/or shorter sintering

time for the bimodal particle compacts, their final grain size was smaller than that of the coarse particle compact. In addition, bimodal compacts are stable against the formation of closed pores. As a result, all pores remain open until full density is nearly attained.

V. References

1. C. Herring, "Effect of Change of Scale on Sintering Phenomena," *J. Appl. Phys.*, 21, 301-303 (1950).
2. Chapters in Part 4 of *Ultrastructure Processing of Ceramics, Glasses, and Composites*, Edited by L. L. Hench and D. R. Ulrich, John Wiley and Sons, New York, 1984.
3. R. M. Allman II, "Polycrystalline Colloids and Their Implications on Microstructural Evolution," M.S. Thesis, U.C.L.A. (1983).
4. I. A. Aksay, "Microstructure Control Through Colloidal Consolidation," pp 94-104, in *Advances in Ceramics, Vol. 9, Forming of Ceramics*. Edited by J. A. Mangels and G. L. Messing, The American Ceramic Society, 1984.
5. C. C. Furnas, "The Relations Between Specific Volume, Voids, and Size Composition in Systems of Broken Solids of Mixed Sizes," *U.S. Bur. Mines Rep. Invest.*, No. 2894, 1928.
6. A. E. R. Westman and H. R. Hugill, "The Packing of Particles," *J. Am. Ceram. Soc.*, 13(10) 767-79 (1930).
7. R. K. McGeary, "Mechanical Packing of Spherical Particles," *J. Am. Ceram. Soc.*, 44(10) 513-22 (1961).
8. F. N. Rhines, "Dynamic Particle Packing," pp 321-41 in *Ceramic Processing Before Firing*. Edited by G. Y. Onoda, Jr. and L. L. Hench, John Wiley and Sons, New York, 1978.

9. M. J. O'Hara and I. B. Cutler, " Sintering Kinetics of Binary Mixtures of Alumina Powders," Proc. Brit. Ceram. Soc., No. 12, pp. 145-54, 1969.
10. G. Y. Onoda, Jr., " Green Body Characteristics and Their Relationship to Finished Microstructure," pp 163-81 in Ceramic Microstructure '76. Edited by R. M. Fulrath and J. Pask. Westview Press, Boulder, CO, 1976.
11. J. P. Smith and G. L. Messing, " Sintering of Bimodally Distributed Alumina Powders," J. Am. Ceram. Soc., 67(4) 238-42 (1984).
12. C. Han, " Sintering of Bimodal Compact," M.S. Thesis, U.C.L.A. (1985).
13. E. W. Washburn, " Note on a Method of Determining the Distribution of Pore Sizes in a Porous Material," Proc. Nat. Acad. Sci., 7, 115-16 (1921).
14. G. L. Messing and G. Y. Onoda, Jr., " Inhomogeneity-Packing Density Relations in Binary Powders," J. Am. Ceram. Soc., 61(1-2) 1-5 (1978). "
15. G. L. Messing and G. Y. Onoda, Jr., " Inhomogeneity-Packing Density Relations in Binary Powders - Experimental Studies," J. Am. Ceram. Soc., 61(7-8) 363-366 (1978).
16. C. Schilling, " Microstructure Development by Colloidal Filtration," M.S. Thesis, U.C.L.A., (1983).
17. M. B. Waldron and B. L. Daniell, pp. 6-7 in Sintering, Edited by A. S. Goldberg. Heyden and Sons Ltd., Philadelphia, Pa., 1978.
18. M. F. Yan, " Microstructural Control in the Processing of Electronic Ceramics," Mat. Sci. Engr., 48, 53-72 (1981).

FIGURE CAPTIONS

Fig. 1: The variation of packing densities with the fraction of fines.

Fig. 2: The variation of channel neck sizes of green compacts with the fraction of fines.

Fig. 3: The sintered densities vs. temperatures of bimodal α - Al_2O_3 powder compacts.

Fig. 4:

Fig. 5: Open porosities vs. sintered densities of bimodal powder compacts.

Fig. 6: (a) 0% fine, (b) 25% fine sintered at 1150°C 1 hr.

Fig. 7: Microstructure at identical sintered density (97% TD). (a) 1400°C, 4 hrs, 0 % fine; (b) 1400°C, 1 hr, 25% fine.

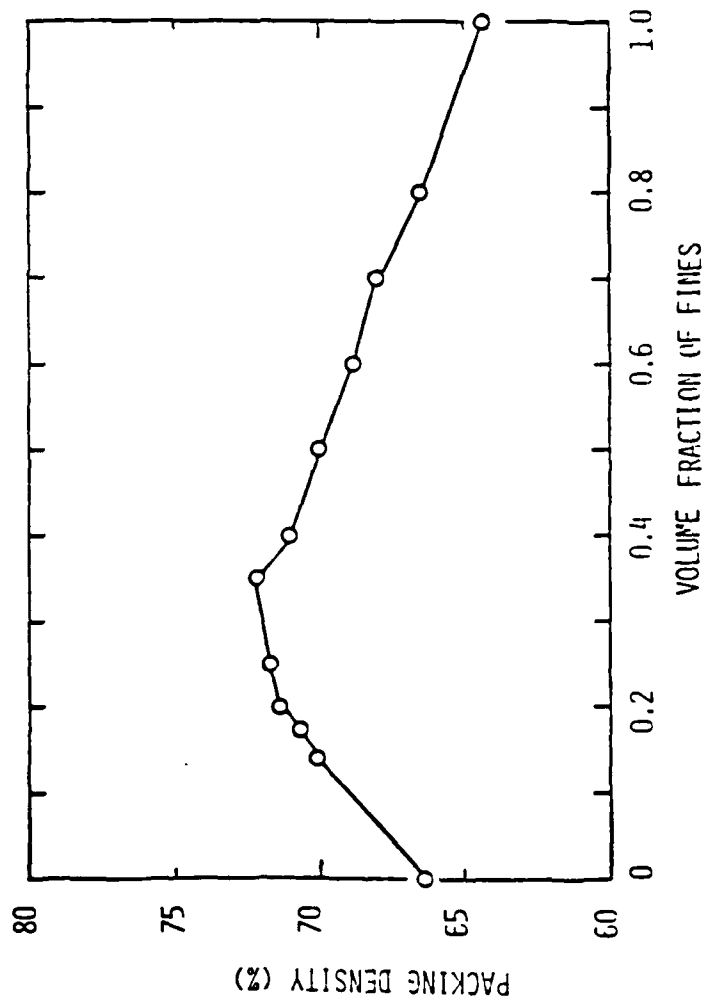


Figure 1 The variation of packing densities with the fraction of fines.

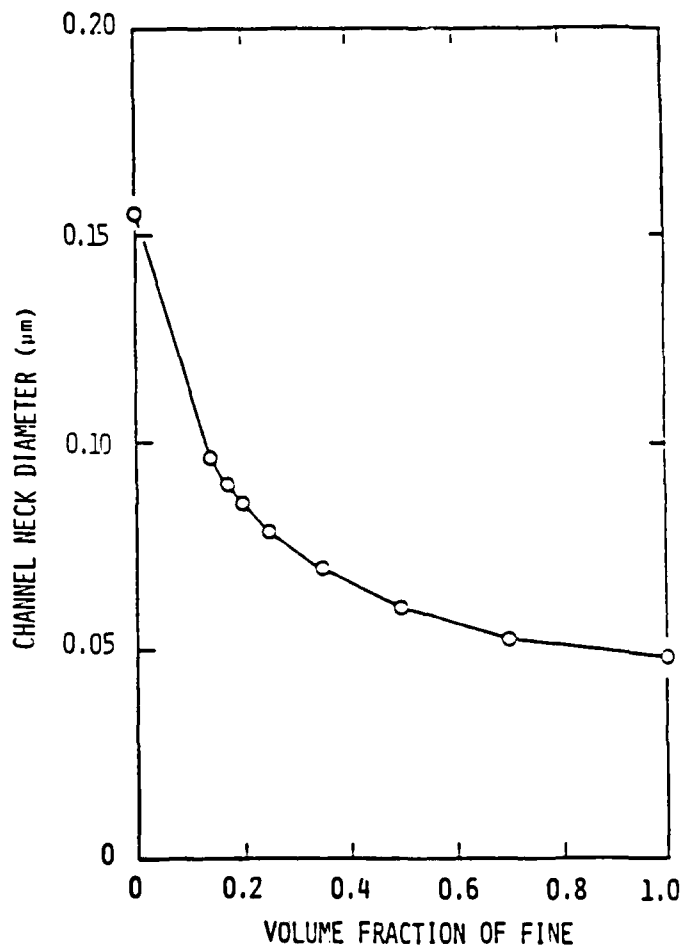


Figure 2: The variation of channel neck sizes of green compacts with the fraction of fines.

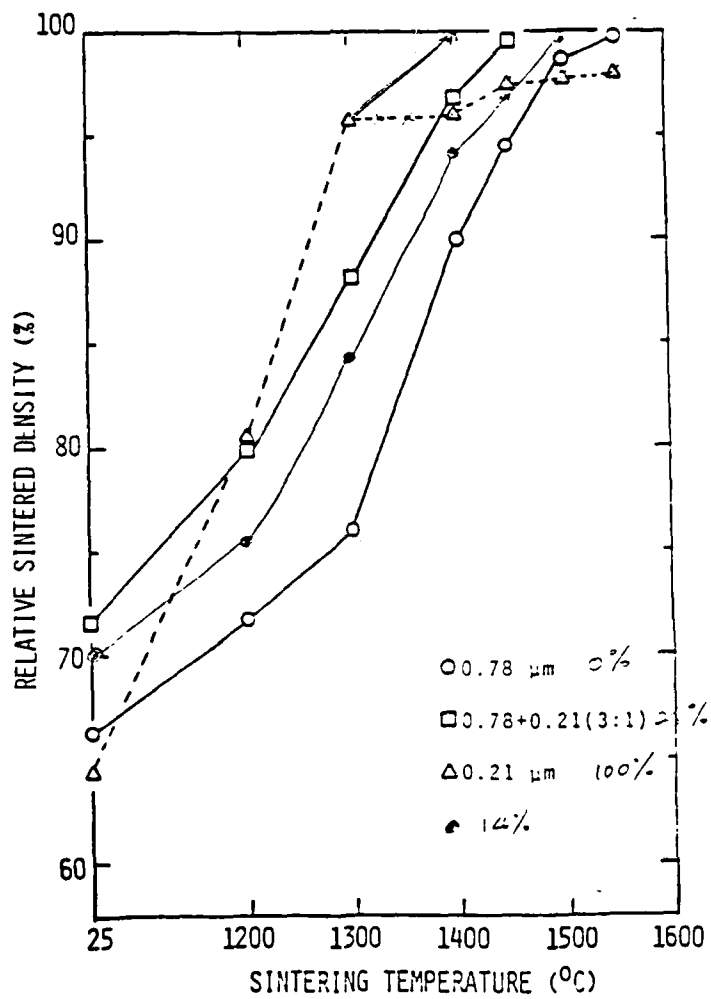


Figure 3. The sintered densities vs. temperatures of bimodal $\alpha\text{-Al}_2\text{O}_3$ powder compacts.

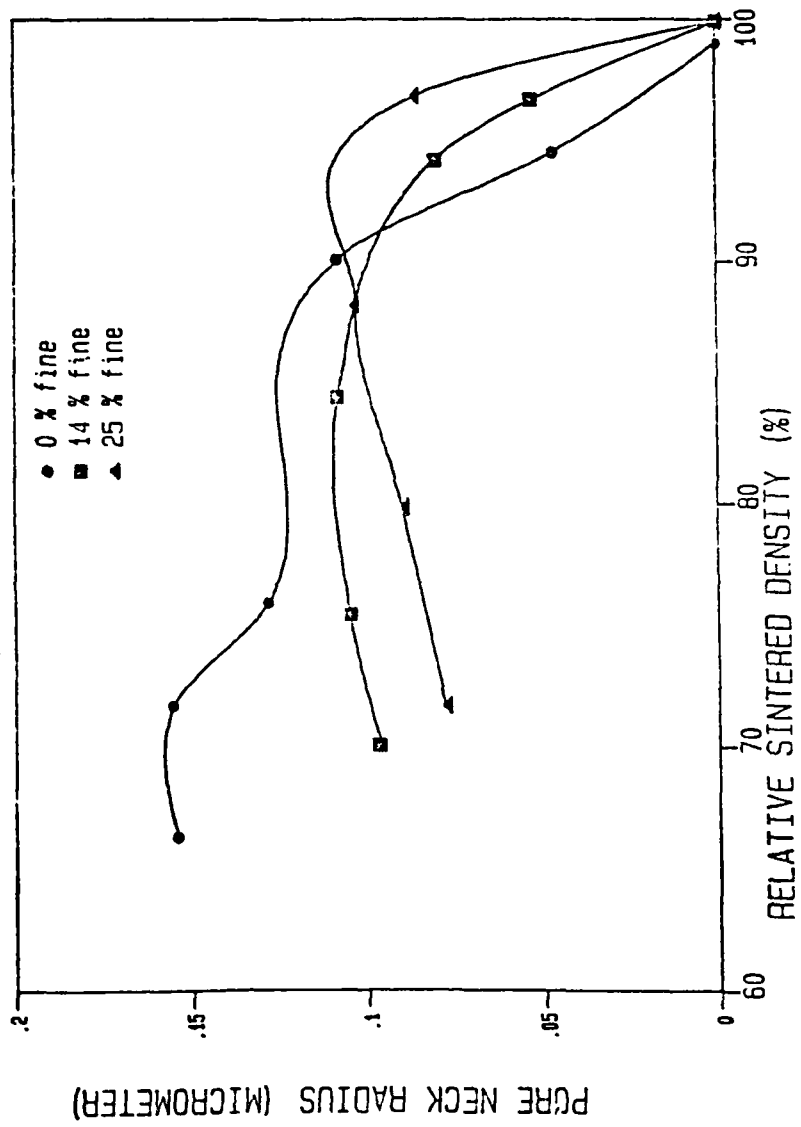


Figure 4.

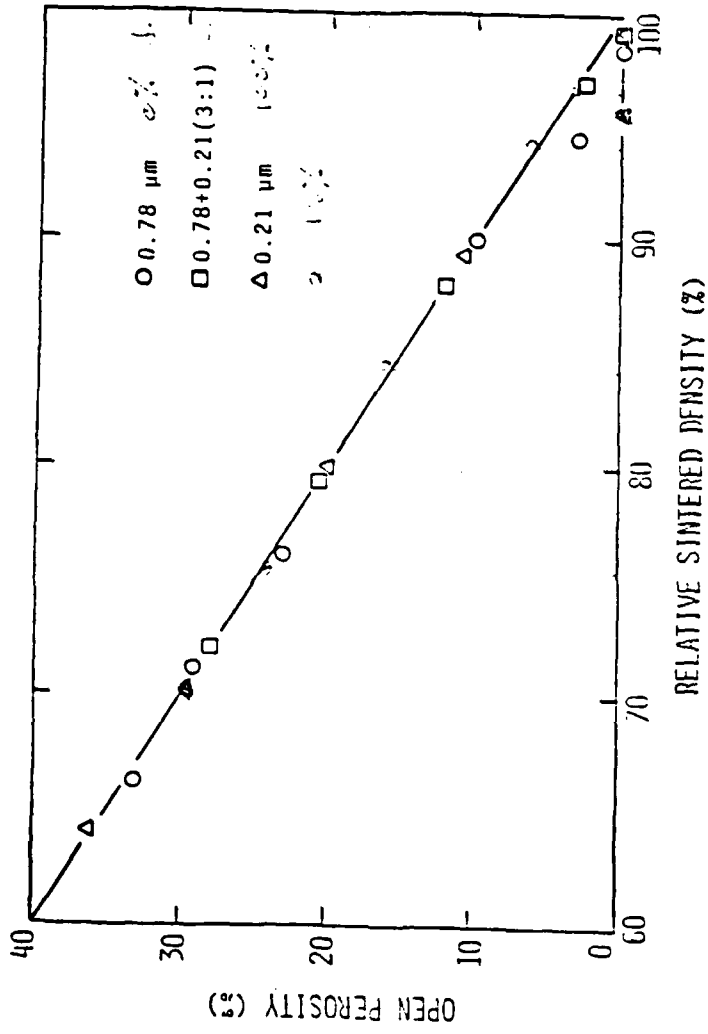


Figure 5 Open porosities vs. sintered densities of bimodal powder compacts.

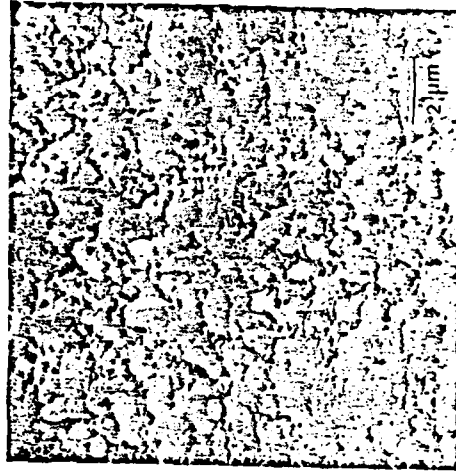


Fig. 6 (a) 0% fine, (b) 25% fine sintered at 1150°C 1 hour.

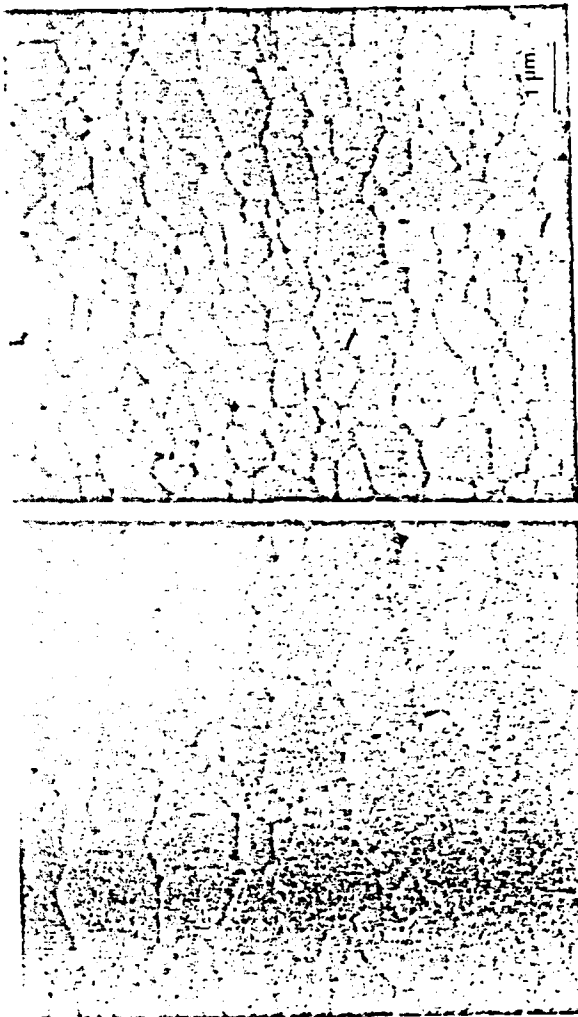


Fig. 7. Microstructure at identical sintered density (97% TD). (a) 1400°C, 4 hrs, 0% fine, (b) 1400°C, 1 hr, 25% fine.

APPENDIX VIII
Long Range Particle Segregation in Colloidal Filtration

(Hirata 1987)

LONG RANGE PARTICLE SEGREGATION IN COLLOIDAL FILTRATION

Y. Hirata

This paper will be submitted and published in the near future.

Powder consolidation mechanics in colloidal filtration of bimodal particle size system was analyzed theoretically and experimentally. Dominant consolidation process changes from filtration to sedimentation at the critical time t_s . Although the time t_s decreases with an increase in concentration of the suspension, the height of the layer consolidated through filtration by time t_s becomes higher at higher concentration. Long range particle segregation due to differential mass occurs after the time t_s . However, the particle segregation can be prevented by increasing the concentration. Packing density and homogeneity of microstructure of the consolidated layer increase with prevention of the particle segregation. These concepts on particle segregation in bimodal system were confirmed with the consolidation experiment in the bimodal system of $0.8\mu\text{m}$ (75 vol %) - $0.2\mu\text{m}$ (25 vol %) for Al_2O_3 .

B

C

C

C

APPENDIX IX

Characterization of Microstructural Evolution by Mercury Porosimetry

(Han, Aksay, and Whitemore 1985)

C

C

C

From: ADVANCES IN MATERIALS CHARACTERIZATION II
Edited by R.L. Snyder, R.A. Conrad, Sr.
and P.F. Johnson
(Plenum Publishing Corporation, 1985)

CHARACTERIZATION OF MICROSTRUCTURAL
EVOLUTION BY MERCURY POROSIMETRY

C. Han, I. A. Aksay, and O. J. Whittemore

Department of Materials Science and Engineering
College of Engineering
University of Washington, Seattle, WA 98195

ABSTRACT

Evolution of microstructure during the sintering of α -Al₂O₃ compacts formed by colloidal filtration was studied by mercury porosimetry. It is shown that the decay of the flow channels created during filtration plays an important role in the densification process. The retention of open channels until the final stages of sintering was essential in achieving high sintered densities.

INTRODUCTION

In the processing of ceramics by powder consolidation techniques, steps taken in the presintering stages play an important role in the densification behavior during sintering. For example, one essential requirement is to form the green compacts with uniform pore size distribution in order to minimize the variations in local densification rates during sintering. Experimental^{1,2} and theoretical^{6,7} studies have clearly demonstrated that nonuniformities in a green compact are often amplified during the subsequent sintering stages as a result of differential sintering rates.

A recent trend in ceramics processing, particularly when working with submicron size powders, has been the use of colloidal dispersion techniques to attain uniform microstructures.³ In colloidal techniques, submicron size powders that otherwise spontaneously agglomerate due to van der Waals attractive forces are

kept dispersed in a fluid medium by controlling the repulsive interparticle interactions.³ Once a uniform dispersion in the colloidal suspension stage is attained, the next goal is then to retain this uniformity while the fluid medium is being eliminated during consolidation.

Studies have shown that transitions from a dispersed colloidal suspension to a consolidated state resemble fluid to solid phase transitions observed in atomic systems.^{1,3} For a given interparticle interaction potential, this fluid to solid phase transition takes place at a critical particle concentration with the nucleation of densely packed particle clusters as a multiple site nucleation process. A direct outcome of this transition by a multiple site nucleation process is that the resultant microstructures always contain microagglomerates which we will refer to as domains hereafter. Due to the formation of these domains, at least two types of pores result: (1) small intra-domain pores, and (2) larger inter-domain pores. The most important implication of the domain formation is that even the colloidal suspension routes cannot provide an easy solution to the problem of packing density inhomogeneities. Furthermore, if the suspensions are consolidated by filtration, the inter-domain pores are modified by the flow of the dispersion medium which goes into the filter medium through the inter-domain voids, while the intra-domain voids remain unchanged.⁴ The bimodality of the pore size distribution then becomes more distinct.

In sintering of these compacts, domains sinter faster than the inter-domain regions due to their higher packing density and smaller pore size (Fig. 1). Because of this differential sintering rate, uniform sintering cannot be expected. In this paper we present data on the sintering behavior of α -Al₂O₃ compacts formed by colloidal filtration and illustrate that the pores associated with the inter-domain regions, i.e. filtration channels, control the densification behavior during the final stages of sintering. In addition, we provide data on the sintering behavior of monosize and bimodal particle size systems and illustrate that sintering rates can be enhanced with bimodal systems. Finally, we illustrate the importance of mercury porosimetry, especially in the characterization of the decay of filtration channels during sintering.

EXPERIMENTAL PROCEDURE

Nearly monosize α -Al₂O₃ powders* with median particle diameters of 0.78 and 0.21 μ m were used as the coarse and fine particle

*Sumitomo Chemical America, Inc., New York, NY, AKP-15 (0.78 μ m) and AKP-50 (0.21 μ m), with >99.99% purity.

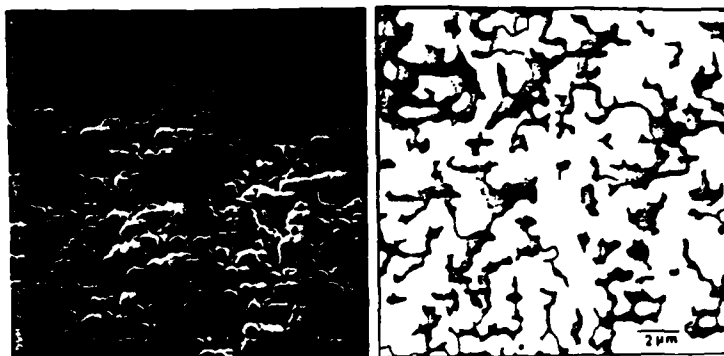


Fig. 1. Microstructure (SEM) of 0.78 μm powder compact after partial sintering at 1200°C for 1 hr. Inter-domain regions are highlighted in the negative image.

systems. In addition, these powders were used to prepare four binary mixtures at fine particle fractions of 0.14, 0.17, 0.20, and 0.25. Aqueous colloidal suspensions of the monosize and binary systems at particle concentrations of 55 % by volume were prepared at pH=2.5 with HCl additions. Ultrasonic vibration was applied occasionally to facilitate the breakup of the soft agglomerates. Suspensions were then cast on gypsum molds. Samples were prepared from the filtered cakes and sintered in air at temperatures between 1200°C and 1500°C for 1 hour. Mercury porosimetry and scanning electron microscopy were used for characterization.

RESULTS AND DISCUSSION

The variation of packing density with the fraction of fine particles is shown in Fig. 2. The packing densities of compacts initially increased with the addition of fine particles as expected based on previous theoretical and experimental studies.¹²⁻¹⁷ When fine particles are added to a system of much larger coarse particles, fine particles first fill the voids between the coarse particles. Therefore, until all the voids are filled, the partial molar volume of fine particles is zero, and the packing density of the mixture increases with the fraction of the fine particles. After all the voids are filled, additional fine particles expand the volume of the mixture compact, and then the packing density decreases with the fraction of fine particles.

A theoretical model on the variation of packing density in homogeneously packed bimodal systems was first developed by Furnas.¹² However, in subsequent experimental studies,^{13,14} it has

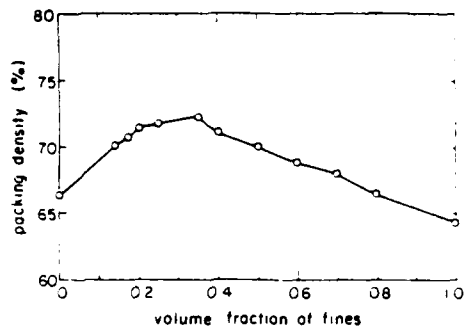


Fig. 2. Packing density variation in the bimodal system with end members of 0.78 and 0.21 μm size particles.

been shown that experimental data always displayed lower densities than the ones predicted by the model. Our data as presented in Fig. 2 similarly display deviation from Furnas' idealized model. In previous studies,^{15,17} inhomogeneities in the mixing of coarse and fine particles were proposed as the cause of this deviation. When the mixing of bimodal particles is not uniform, the partial molar volume of the fine particles does not follow the value predicted by the idealized model but deviates from ideality as the inhomogeneity of the mixing increases.

When working with colloidal systems, homogeneity in mixing can be achieved in the suspension stage prior to consolidation. However, problems in long-range particle segregation (on a dimensional scale larger than the particle domains) may arise during the consolidation stage due to differential sedimentation. In the present study, with the use of suspensions that contained >50 % by volume of particles, long-range segregation of particles during the consolidation stage was prevented as confirmed through electron microscopic examination and hydraulic resistance measurements.¹⁸ In spite of this precaution, the fact that our density data still

displayed deviation from Furnas' model would suggest short-range inhomogeneities. The implication is that, consistent with the formation of particle domains and the formation of filtration channels around these domains, fine particles do not decrease the inter-domain porosity as effectively as the intra-domain porosity.

Channel sizes as measured by mercury intrusion continuously decreased with increasing fraction of fine particles (Fig. 3). This behavior is consistent with the concept that, in uniformly mixed bimodal compacts, fine particles act as space filling units and thus the intrusion neck size decreases as fine particles occupy space between the coarse ones. However, it is important to note that, during the intrusion of mercury into pores with many openings, mercury penetrates into the pores through the largest opening, one which is still smaller than the largest dimension of the channels connected by the necks. Therefore, mercury intrusion data interpret pores as being cylindrical in shape with a diameter equal to the neck diameter. In fact, a comparison of the data presented in Fig. 3 with the microstructure of Fig. 1 reveals that, while the channel necks determined by porosimetry are all smaller than 0.2 μm , the microstructure clearly possesses many pores that are 10 times larger than the necks.

During sintering of powder compacts, smaller pores disappear faster than larger pores. Similarly, the channel necks decay faster than the main body of the channel and, at a certain stage of densification, this results in the formation of isolated pores. At this stage, whether these isolated pores will be in the shrinkage regime or not is determined by the number of grains surrounding a pore and the dihedral angle at the pore/grain boundary junctions.^{19,27} Therefore, it becomes necessary to control the size of the isolated pores and thus the number of grains surrounding a

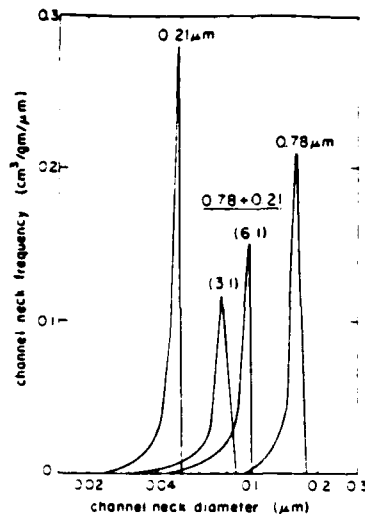


Fig. 3 Channel neck size frequency of monosize and bimodal compacts obtained by mercury intrusion.

pore through variations in channel morphology that in turn affects their decaying behavior.

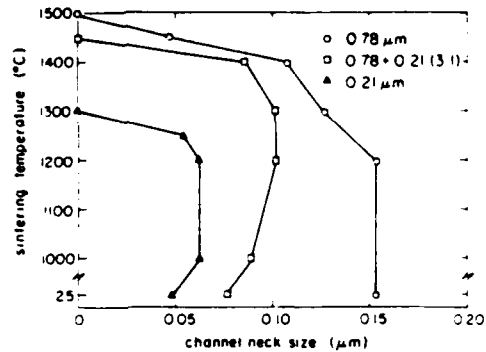


Fig. 4. Change of the largest neck size during the sintering of monosize (0.78 and 0.21 μm) and bimodal (3:1) systems.

Variations in the channel neck size during the densification of the fine, coarse, and bimodal systems are compared in Fig. 4. During the initial stage of sintering, channel neck growth was observed in the mixture and the fine particle compacts, whereas no neck growth was observed in the coarse particle compacts. On further sintering, necks shrank in all cases and eventually closed at approximately around the temperature of the last data point in each corresponding curve. The temperatures at which the neck closure occurred decreased with decreasing initial neck size. However, it is important to note that, at the point of neck closure, the compact with 100% fine particles still contained 5% porosity (now as closed pores) while both the binary mixture as well as the coarse particle compacts had less than 2% porosity.

The detrimental effect of this early neck closure upon the densification behavior of fine particle compacts in the final stage of sintering is illustrated in Figs. 5 and 6. Fine particle compacts initially displayed the fastest sintering up to 1300°C

(Fig. 5). At this point, due to the isolation of channels as closed pores that appear to be in the growth rather than the shrinkage regime, further densification practically stopped. On the other hand, coarse particle compacts and the mixtures showed lower densification rates initially; however, final sintered densities were higher than that of the fine particle compacts. In comparing the mixture compacts and the coarse particle compacts, it is apparent that the mixtures always sintered faster than the coarse particle compacts (Fig. 5).

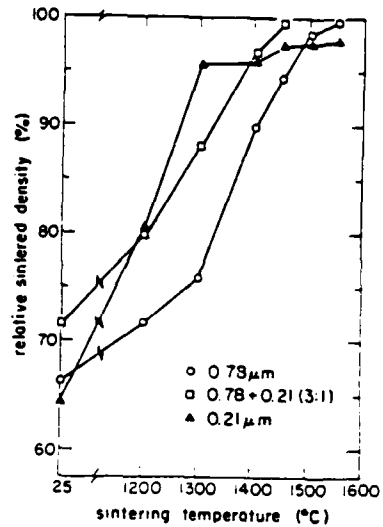


Fig. 5. Sintered density of mono-size (0.78 and 0.21 μm) and bimodal (3:1) systems.



Fig. 6. Microstructure (SEM) of 0.21 μm powder compact after reaching an end point density of 98.5 % TD at 1300°C for 3 hr.

CONCLUSIONS

In this study of microstructural evolution, where mercury porosimetry was used as the major characterization tool, the following conclusions can be made:

(1) In the densification of alumina compacts formed by colloidal filtration of submicron size particles, the decay of channels, which are formed during the filtration stage, affected the overall microstructural evolution. Channel closure at lower densities resulted in lower end-point densities.

(2) The addition of finer particles was shown not to be detrimental to sintering. On the contrary, the sintering temperature was reduced in bimodal mixture compacts.

ACKNOWLEDGEMENTS

This work was supported by the Advanced Research Projects Agency of the Department of Defense and was monitored by the Air Force Office of Scientific Research under Grant No. AFOSR-83-0375.

REFERENCES

1. K. D. Reeve, Am. Ceram. Soc. Bull., **42** [8] 452 (1963).
2. T. Vasilos and W. Rhodes, in "Ultrafine-Grain Ceramics," J. J. Burke, N. L. Reed, and V. Weiss, eds., Syracuse University Press, New York (1970), p. 137.
3. W. D. Kingery, in "Ceramic Processing Before Firing," G. Y. Onoda, Jr. and L. L. Hench, eds., John Wiley & Sons, New York (1978), p. 291.
4. F. F. Lange and M. Metcalf, J. Am. Ceram. Soc., **66** [6] 398 (1983).
5. F. F. Lange, B. I. Davis, and I. A. Aksay, J. Am. Ceram. Soc., **66** [6] 407 (1983).
6. A. G. Evans, J. Am. Ceram. Soc., **65** [10] 497 (1982).
7. R. Raj and R. K. Bordia, Acta Met., **32** [7] 1003 (1984).
8. Chapters in Part 4 of "Ultrastructure Processing of Ceramics, Glasses, and Composites," L. L. Hench and D. R. Ulrich, eds., John Wiley & Sons, New York (1984) provide reviews on recent developments in colloidal processing techniques.
9. J. Th. G. Overbeek, J. Colloid Interface Sci., **58** [2] 408 (1977).
10. I. A. Aksay, in "Advances in Ceramics," J. A. Mangels and G. L. Messing, eds., Am. Ceram. Soc., Columbus, OH, (1984), vol. 9, p.94.

11. I. A. Aksay and C. H. Schilling, in "Ultrastructure Processing of Ceramics, Glasses, and Composites," L. L. Hench and D. R. Ulrich, eds., John Wiley & Sons, New York (1984), p.439.
12. C. C. Furnas, Relations between specific volume, voids, and size composition in systems of broken solids of mixed sizes, U.S. Bur. of Mines Res. Invest., No. 2894 (1928).
13. A. E. R. Westman and H. R. Hugill, J. Am. Ceram. Soc., 13, [10] 767 (1930).
14. R. K. McGearry, J. Am. Ceram. Soc., 44 [10] 513 (1961).
15. F. N. Rhines, in "Ceramic Processing Before Firing," G. Y. Onoda, Jr. and L. L. Hench, eds., Wiley-Interscience, New York (1978), p.321.
16. G. L. Messing and G. Y. Onoda, Jr., J. Am. Ceram. Soc., 61 [1-2] 1 (1978) and 61 [7-8] 363 (1978).
17. J. P. Smith and G. L. Messing, J. Am. Ceram. Soc., 67 [4] 238 (1984).
18. C. Han, "Sintering of Bimodal Powder Compacts," M. Sc. Thesis, University of California, Los Angeles, CA (1985).
19. R. Cannon, in "Oxidation of Non-Oxide Ceramics," Case-Western Reserve University report to AFOSR, Contract #F49620-78-C-0053, June 1981.
20. F. F. Lange, J. Am. Ceram. Soc., 67, [2] 83 (1984).

APPENDIX X
High Strength Porous Ceramics: I. Processing

(Sonuparlak and Aksay 1987)

HIGH STRENGTH POROUS CERAMICS. I. PROCESSING

B. Sonuparlak and I.A. Aksay

This paper will be submitted and published in the near future.

In this paper, we outline the methodology of processing porous ceramics with controlled pore size, shape, and spatial distribution. In the generation of pores with controlled size and shape in an alumina matrix system, we used polystyrene microspheres that were processed by a two-stage polymerization and seeding technique. Alumina and polystyrene was codispersed either electrostatically or sterically in an aqueous medium. Specimens of porous alumina were fabricated either by homogeneous distribution of pores all around the sample or by keeping them inside the sample. Controlled decomposition of the organic microspheres was necessary to avoid cracking of the compacts during sintering. We also investigated flexural strength and its variability in these designs with controlled size, shape, and distribution of porosity.

APPENDIX XI

**Porous Al₂O₃ with Controlled Pores: II. The Effects
of Pores on Fracture Parameters**

(Sakai, Sonuparlak, and Aksay 1987)

POROUS Al_2O_3 WITH CONTROLLED PORES. II. THE EFFECTS OF PORES ON FRACTURE PARAMETERS

M. Sakai, B. Sonuparlak, and I.A. Aksay

This paper will be submitted and published in the near future.

The primary objective of the present work is to discuss the effect of pore size on the fracture parameters of polycrystalline aluminas with perfectly spherical pores as a fraction of porosity. The relationship between fracture strength, fracture toughness, modulus of elasticity and intrinsic flaw size was studied by measuring all four parameters for samples of a given porosity and diameter of spherical pores. Fracture strength, modulus of elasticity and fracture toughness were measured by the Knoop-indentation three-point bend method, compliance method, and chevron-notched three-point bend method, respectively. Experimental results are compared with various theories that have been developed for the mechanical properties materials comprising a continuous isotropic matrix and pores.

APPENDIX XII
**Spinel Phase Formation at the 980°C Exothermic
Reaction in the Kaolinite to Mullite Reaction Series**

(Sonuparlak, Sarikaya, and Aksay 1987)

SPINEL PHASE FORMATION AT THE 980°C EXOTHERMIC REACTION
IN THE KAOLINITE TO MULLITE REACTION SERIES*

B. Sonuparlak,[#] M. Sarikaya, and I. A. Aksay

Department of Materials Science and Engineering
College of Engineering
University of Washington
Seattle, Washington 98195

ABSTRACT

With the use of differential thermal analysis, x-ray diffraction, and transmission electron microscopic techniques, we showed that gamma-Al₂O₃ type spinel phase is solely responsible for the 980°C exotherm in the kaolinite to mullite reaction series. Transmission electron microscopic characterization indicated that the spinel formation is preceded by a phase separation in the amorphous dehydroxylated kaolinite matrix. Chemical analysis of the spinel phase by energy dispersive x-ray spectroscopy revealed a nearly pure Al₂O₃ composition.

October 1986

* Presented at the 37th Pacific Coast Regional Meeting of the American Ceramic Society, San Francisco, CA, October 30, 1984 (#55-B-84P).

[#] Now with Advanced Materials Division, Flow Industries, Inc., Kent, WA 98032

1.0 INTRODUCTION

The kaolinite ($\text{Al}_2\text{O}_3 \cdot 2\text{SiO}_2 \cdot 2\text{H}_2\text{O}$) to mullite ($3\text{Al}_2\text{O}_3 \cdot 2\text{SiO}_2$) reaction series has been the subject of various studies for nearly a century,¹ and still retains its active status as evidenced in most recent publications.²⁻⁷ However, these studies have not resolved the questions concerning the issue of which phase formation is responsible for the exothermic reaction commonly observed at around 980°C.

The first step in the reaction series is the formation of an amorphous dehydration product identified as metakaolinite ($\text{Al}_2\text{O}_3 \cdot 2\text{SiO}_2$) after an endothermic reaction at ~ 550°C. In the next step, the formation of crystalline product(s) from this amorphous intermediate phase results in a prominent exothermic reaction at ~ 980°C. In most studies³⁻¹⁷ dealing with this reaction series, the key issue has been the identification of the reaction product that results in this exothermic reaction.

The reaction mechanisms proposed for the 980°C exotherm can be classified into two general groups. In the first group, the common feature is the formation of a gamma- Al_2O_3 type spinel phase and its association to the exothermic reaction.^{3-5,8,9,13-17} The differences reported are mainly concerned with the composition of the spinel phase and whether the mullite phase (through a parallel reaction) also contributes to the exotherm.^{3,14,16} In contrast to these spinel-based models, the second group proposes the formation of mullite without any spinel phase.¹⁰⁻¹² In view of the convincing evidence presented in recent studies,^{3,14-16} the validity of this second mechanism can now be disputed.

With respect to the spinel-based mechanisms, however, two key problems still remain on the issues of (i) whether the spinel or the mullite phase is responsible for the exothermic reaction at 980°C, and (ii) how much silicon, if any, is present in the spinel phase. In this paper, we provide the answer to the first of these questions. We show that the spinel phase alone is responsible for the exothermic reaction. We also provide a partial solution to the second question, showing that this spinel contains less than 10 wt% silica and is probably very close to being pure alumina.

2.0 EXPERIMENTAL PROCEDURE

Well-crystallized kaolinite* was used in all our experiments. Based on chemical analysis and structural analysis by x-ray diffraction, 1.39 wt% TiO₂ was identified as the main impurity.¹⁷ Differential thermal analysis (DTA)[#] studies were performed in air, at a heating rate of 10°C/min, up to 1250°C. In addition, isothermal heating studies were performed at various temperatures below the exothermic peak temperature for up to 7 days in a resistance heated furnace. Phase characterization was performed by x-ray (Cu K_α) diffraction (XRD). Detailed description of the experimental conditions related to XRD and DTA are given elsewhere.¹⁷ In-situ beam induced heating experiments in a transmission electron microscope (TEM)[@] and high resolution electron microscopy (HREM)^{**} were performed in order to observe the phase changes directly. Chemical analyses of the phases were performed by utilizing energy dispersive x-ray spectroscopy (EDS)^{##}. Special powder samples were prepared by heat-treating the original kaolinite at temperatures below the 980°C exothermic reaction and by treating it with 10 wt% boiling NaOH solution at different periods of time up to 40 minutes. Amorphous silica-rich phase was dissolved during this NaOH treatment, allowing more accurate evaluation of the chemical composition of the spinel crystals which are not soluble under these conditions. The Cliff-Lorimer method¹⁸ was used to obtain quantitative analysis of the x-ray spectra. Kaolinite was used as a standard in the determination of k_{Al,Si}. All data for quantitative analysis were acquired by tilting specimens 30° towards the detector. Data were acquired in a multichannel scaler set at 10 kV range. Si_K (at 1.74 kV) and Al_K (at 1.48 kV) peaks were separated by using 250 eV energy windows. In all cases, powder samples for TEM characterization were suspended on a holly carbon film attached on a 75 mesh Cu grid.

* Georgia Kaolinite (KGa-1); Georgia Kaolin Company, Elizabeth, NJ

DuPont 900 Thermal Analyzer; E. I. Du Pont de Nemours & Co.,
Wilmington, DE

@ Philips 400 EM; Philips Electronics Inc., Mahwah, NJ

** JEOL 200CX; JEOL USA Inc., Peabody, MA

KEVEX 7000; KEVEX Co., Foster City, CA

3.0 RESULTS AND DISCUSSION

3.1 Formation of Spinel Phase:

XRD analysis of the DTA samples heated to or above the exothermic reaction temperature always indicated the formation of the spinel phase along with mullite. This concomitant existence of spinel with mullite led previous investigators^{3,14,16} to the conclusion that both of these phases may be responsible for the exothermic reaction. Therefore, in order to determine if the formation of these phases could be separated from each other, we isothermally heat-treated kaolinite at various temperatures lower than the exothermic peak temperature. In doing so, it was assumed that only one of the phases would be obtained at a given temperature and thus the contribution of this phase to the reaction would result in a decrease in the exothermic peak intensity in a subsequent run.

As expected, when kaolinite was subjected to heat-treatment at 850°C, the spinel phase formed before mullite. Figs. 1(a) and (c) show the XRD patterns obtained after heat-treatment for 1 and 7 days at 850°C, respectively. After a one-day heat-treatment, only the formation of pseudo-anatase, $2\text{Al}_2\text{O}_3 \cdot 2\text{TiO}_2 \cdot \text{SiO}_2$, (labeled p) and a large amount of an amorphous phase was observed (Fig. 1(a)). Our calculations indicated that the TiO_2 impurity may result in the formation of 2.46 wt% pseudoanatase. A large amount of an amorphous phase is also expected, because metakaolinite contains 51.61 wt% SiO_2 and as explained below most of this component segregates as a silica-rich phase during the heat-treatment process. Extended (7-day) heatings at 850°C resulted in the development of the spinel phase without any mullite Fig. 1(c). The DTA curves of these 1- and 7-day heat-treated samples are shown in Figs. 1(b) and (d), respectively. A significant difference is observed between the two samples. While the exothermic reaction is observed in the DTA curve for the 1-day heat-treated sample (Fig. 1(b)), it is completely eliminated in the second DTA trace (Fig. 1(d)). In spite of the differences in the DTA curves, upon further heating, mullite formation is observed to the same degree in both samples.

However, since mullite is formed through a diffusion controlled reaction in the second case, its formation is not easily observed in the DTA trace (Fig. 1(d)). This behavior and the information obtained from the XRD analyses clearly lead us to conclude that the spinel phase alone is responsible for the exothermic reaction.

Further evidence supporting this conclusion was obtained through beam-induced in-situ heating experiments performed in a TEM. Although in the in-situ experiments, the exact temperature of the samples could not be measured, approximate temperature ranges could be determined through comparison of the microstructures with those of ex-situ ones. Three different characteristic stages were observed (Fig. 2). The bright field (BF) image in Fig. 2(a) was taken after the dehydroxylation had started. The formation and growth of light-color patchy regions are interpreted to be associated with the loss of structural water. After the completion of this dehydroxylation process, the structure was determined to be amorphous by electron diffraction. The image in Fig. 2(b) was taken upon further heating, but to a temperature low enough so that crystallization would not occur. Careful inspection of this figure reveals a structure similar to that obtained in spinodally decomposed systems. Further heating to a higher temperature first resulted in the growth of these phase separated regions and then the formation of a crystalline phase took place. As revealed in the bright and dark field (DF) pairs of Figs. 2(c) and (d), respectively, the size of the crystalline regions was $\sim 5 - 8$ nm. Although we could not obtain isolated electron diffraction patterns, the analysis of the superimposed patterns indicated only the presence of a cubic spinel type phase but not mullite. This observation then also supports the view that spinel and mullite phases do not form in parallel reactions. Spinel formation takes place first, after a phase separation process in the metakaolinite.

In order to unambiguously determine that the crystalline phase formed at the 980°C reaction belongs to a spinel phase, we attempted to grow larger spinel crystals on which electron microdiffraction experiments would be performed to obtain isolated diffraction patterns. For this purpose, samples were externally heated at prolonged times (1 day) at temperatures

near but below the exothermic reaction. As illustrated in the TEM images of Fig. 3, we were successful in growing the spinel grains to sizes larger than 100 nm. The bright field (BF) image in Fig. 3(a) from a corner of a particle indicates variations in the structure resembling a contrast associated with a crystalline area. In fact, the corresponding dark field (DF) image in Fig. 3(b) clearly reveals the morphology of the crystalline region which is surrounded by an amorphous phase at the edge of the particle. Microdiffraction patterns were received from this region by using a 400 Å diameter electron beam. The microdiffraction pattern in Fig. 4(c) corresponds to a $\langle 114 \rangle_{\text{fcc}}$ zone axis orientation. The specimen was further tilted to another orientation, now near $\langle 122 \rangle_{\text{fcc}}$ to unambiguously confirm the fcc structure of the spinel phase. Similar experiments were also performed on another spinel crystal (FeZnO_3) which was used as a standard for comparison.

The growth pattern of the spinel phase was evidenced from the high resolution images taken at high enough magnifications to reveal the crystallographic planes of the spinel grains (Fig. 4). There are several image features worthwhile to describe here in studying the formation and the growth of the spinel phase at small scale. Firstly, in Fig. 4(a), two sets of Moiré fringes are revealed on the lower part of the micrograph indicating that there are two thin layers of crystals situated on top of each other possibly with an amorphous layer in between. This indicates that spinel phase grows in layers within an amorphous structure. There is only one layer, however, near the edge of the particle as indicated by CF and LF (corresponding to cross fringes and lattice fringes, respectively) where the thickness of the region in the electron beam direction should be considerably small. Another important image feature is the appearance of the very small regions, 1.5 to 4.0 nm in diameter (as indicated by black arrows), in Fig. 4(b). These small crystallites are forming in the amorphous matrix near the edge of the particle. They exhibit similar lattice spacing with the larger crystallites, such as the region on the lower left of the same micrograph, where the phase front (indicated by fat arrows) advances towards the small crystallites probably joining with them eventually and extending the spinel region all the way to the edge.

3.2 Composition of the Spinel Phase:

The observation of the spinel phase alone in an amorphous matrix, during in-situ heating experiments, led us to design another experiment to answer the second question associated with the composition of the spinel phase. In previous studies¹³⁻¹⁶ the composition of this phase was always determined through indirect analyses. However, direct compositional analysis is now possible by EDS in an analytical TEM if the spinel phase is physically isolated from the surrounding amorphous phase. For this purpose, the spinel containing samples, which were produced by extended heating (7 days) at 850°C, were treated with 10 wt% boiling NaOH. As a result, bulk of the amorphous phase was leached out, gradually leaving the spinel crystallites intact (Fig. 5). These figures are directly comparable with the images presented in Fig. 2(b) where the spinel phase was formed by beam heating. The original shape of the kaolinite crystals is still retained. Due to the leaching of the SiO₂-rich amorphous phase from the bulk of the platelets, the images exhibit a contrast resembling a porous structure.¹⁹ Direct microanalysis was performed by EDS on the clusters of crystallites after different leaching times to measure the amount of Al and Si from which the amounts of Al₂O₃ and SiO₂ would be calculated. Fig. 6 illustrates the results of the analysis where the amount of SiO₂ is plotted with respect to the leaching time. The analysis of this plot indicates that at extended leaching times (> 25 min.) the rate of leaching of SiO₂ approaches zero below 10 wt% SiO₂. It is important to point out that during the leaching process, the spinel crystals appeared to be unaffected visually. Their XRD patterns were also not different compared to the unleached and 40 minute-leached samples. This indicates that neither the particle size nor the composition of the spinel was changed through a possible reaction with the leachant. These direct microanalysis results clearly disprove the validity of the previously reported Al-Si spinel models with significantly higher (> 28 wt%) silica contents.^{13,16} On the other hand, these leaching experiments do not eliminate the possibility that the spinel phase might actually contain less than 10 wt% silica if the amount measured by EDS included some contribution from the surrounding (unleached) amorphous silica.

It should be emphasized that as the leaching time is extended the amount of SiO_2 left in the structure decreases, although less so as the leaching time is prolonged. The important question is whether this SiO_2 is in solution in the spinel phase or it is left between the spinel regions which are still intact. Assuming that treating with NaOH only affects the SiO_2 layer between the spinel grains but does not readily affect the layers trapped between the two spinel grains, we calculated the amount of silica, at a thickness of 0.25 nm, that may still be present between closely packed particles of 5 - 8 nm in size to be nearly 10 wt%. The close agreement between this calculated value and the amount determined by EDS analysis then supports the view that the actual amount of silica could be less than 10 wt%. This argument is also supported by the fact that by prolonged leaching treatment the amount of SiO_2 continuously decreases, although the rate is very small. In fact, as evidenced in some EDS experiments performed on occasional spinel particles suspended at the edge of the powders (similar to the ones shown in Figs. 4 and 5, but now in the leached sample), we obtained EDS spectra which displayed only Al peak, and a negligibly small Si peak, Fig. 7.

4.0 CONCLUSIONS

The main conclusion of this work is that the 980°C exotherm in the kaolinite to mullite reaction series is caused by the formation of a spinel phase but not by the parallel formation of spinel and mullite as reported in previous studies.^{3,14,16} It is also concluded that this spinel contains not more than 10 wt% silica (if any). It does not contain a large amount of silica as has been accepted previously.^{13,16}

ACKNOWLEDGEMENTS

This research was supported by the Defense Advanced Research Projects Agency of the Department of Defense and was monitored by the Air Force Office of Scientific Research under Grant No. AFOSR-83-0375. We are grateful to G. Thomas for the use of the TEM facilities at the University of California, Berkeley. Initial part of this work on the differential thermal analysis was performed at the Middle East technical University, Ankara, Turkey.

REFERENCES

1. H. LeChatelier "De L'Action de la Chaleur Sur les Argiles," Bull. Soc. Franc. Mineral., 10 204-211 (1887).
2. K. J. D. MacKenzie, I. W. M. Brown, R. H. Meinhold, and M. E. Bowden, "Outstanding Problems in the Kaolinite-Mullite Reaction Sequence Investigated by ^{29}Si and ^{27}Al Solid-State Nuclear Magnetic Resonance: I, Metakaolinite," J. Am. Ceram. Soc., 68 [6] 293-297 (1985).
3. I. W. M. Brown, K. J. D. MacKenzie, M. E. Bowden, and R. H. Meinhold, "Outstanding Problems in the Kaolinite-Mullite Reaction Sequence Investigated by ^{29}Si and ^{27}Al Solid-State Nuclear Magnetic Resonance: II, High Temperature Transformations of Metakaolinite," J. Am. Ceram. Soc., 68 [5] 298-301 (1985).
4. A. K. Chakravorty, D. K. Ghosh, and P. Kundu, "Comment on Structural Characterization of Spinel Phase in the Kaolin-Mullite Reaction Series through Lattice Energy," J. Am. Ceram. Soc., 69 [3] C200-201 (1986).
5. S. Mazumdar and B. Mukherjee, "Reply," J. Am. Ceram. Soc., 69 [8] C201 (1986).
6. A. K. Shakravorty and D. K. Ghosh, "Comment on Diphasic Xerogels, A New Class of Materials: Phases in the System $\text{Al}_2\text{O}_3\text{-SiO}_2$," J. Am. Ceram. Soc., 69 [8] C202-203 (1986).
7. S. Komarneni and R. Roy, "Reply," J. Am. Ceram. Soc., 69 [8] C204 (1986).
8. C. S. Ross and P. F. Kerr, "The Kaolin Mineral," U.S. Geol. Surv. Prog. Pap., 165E (1930).
9. H. Insley and R. H. Ewell, "Thermal Behavior of Kaolin Minerals," J. Research N.B.S., 14 [5] 615-627 (1935).

10. J. E. Comefore, R. B. Fischer, and W. F. Bradley, "Mullitization of Kaolinite," *J. Am. Ceram. Soc.*, 31 [9] 254-259 (1948).
11. W. F. Bradley and R. E. Grim, "High Temperature Thermal Effects of Clay and Related Minerals," *Am. Mineral*, 36 182-201 (1951).
12. R. Roy, D. M. Roy, and E. E. Francis, "New Data on Thermal Decomposition of Kaolinite and Halloysite," *J. Am. Ceram. Soc.*, 38 [6] 198-205 (1955).
13. G. W. Brindley and M. Nakanira, "The Kaolinite-Mullite Reaction Series: I-III," *J. Am. Ceram. Soc.*, 42 [7] 311-324 (1959).
14. H. J. Percival, J. F. Duncan, and P. K. Foster, "Interpretation of the Kaolinite-Mullite Reaction Sequence from Infrared Absorption Spectra," *J. Am. Ceram. Soc.* 57 [2] 57-61 (1974).
15. A. J. Leonard, "Structural Analysis of the Transition Phases in the Kaolinite to Mullite Thermal Sequence," *J. Am. Ceram. Soc.*, 60 [1-2] 37-43 (1977).
16. A. K. Chakraborty and D. K. Ghosh, "Re-examination of the Kaolinite to Mullite Reaction Series," *J. Am. Ceram. Soc.*, 61 [3-4] 170-173 (1978).
17. B. Sonuparlak, "Examination of Kaolinite to Mullite Reaction Series," Ph.D. Thesis, Middle East Technical University, Ankara, Turkey (1983).
18. G. Cliff and G. W. Lorimer, "The Quantitative Analysis of Thin Specimens," *J. Microscopy*, 103 203-207 (1975).
19. J. D. C. McConnell and S. G. Fleet, "Electron Optical Study of the Thermal Decomposition of Kaolinite," *Clay Minerals*, 8 279-290 (1970).

FIGURE CAPTIONS

Fig. 1: X-ray diffraction ((a) and (c)) and differential thermal analysis ((b) and (d)) patterns of kaolinite after an isothermal heat treatment at 850°C for 1 day ((a) and (b)) and 7 days ((c) and (d)). In the XRD patterns, pseudoanatase and spinel peaks are labeled as p and sp, respectively.

Fig. 2: Morphological changes that take place in kaolinite during electron beam induced in-situ heating experiments: (a) BF image revealing the microstructure during dehydroxylation; (b) Microstructure of metakaolinite before the 980°C exothermic reaction; (c) and (d) are the BF and DF images, respectively, which reveal the spinel crystallites in an amorphous matrix.

Fig. 3: Spinel phase grown at $\leq 980^\circ\text{C}$ for 1 day. (a) and (b) are BF and DF images, respectively, revealing the morphology. (c) and (d) are microdiffraction patterns near $\langle 114 \rangle_{\text{fcc}}$ and $\langle 122 \rangle_{\text{fcc}}$ zone axis orientations, respectively.

Fig. 4: High resolution images of a sample heated at $\leq 980^\circ\text{C}$ for 1 day. Images (a) and (b) were taken from region (1) and (2), respectively, of the crystal shown in the inset. In (a), two sets of Moire fringes (indicated by MF1 and MF2) are shown suggesting layers of crystals. In regions indicated by CF (cross fringes) and LF (lattice fringes), there is only one layer. In micrograph (b) beyond the phase front (between the spinel and the amorphous matrix), there are small crystallites (patchy regions with cross fringes indicated by the black arrows near the edge) forming in the amorphous phase.

Fig. 5: (a) and (b) are BF images of the sample heat treated at 850°C (1 week) and leached with NaOH to isolate the spinel phase. Images were taken under slightly underfocus condition to reveal small scale crystals (dark contrast) and pores (light contrast) left after the removal of the matrix SiO_2 phase.

Fig. 6: The amount of silica left in the spinel containing specimen as a function of leaching time. The wt% silica was calculated from the amount of Si measured by using EDS analysis in the TEM.

Fig. 7: An energy dispersive X-ray spectrum received from a spinel crystal formed in a sample heated in the vicinity of 980°C. Only the Al peak is observed, and almost no Si is present in the structure.

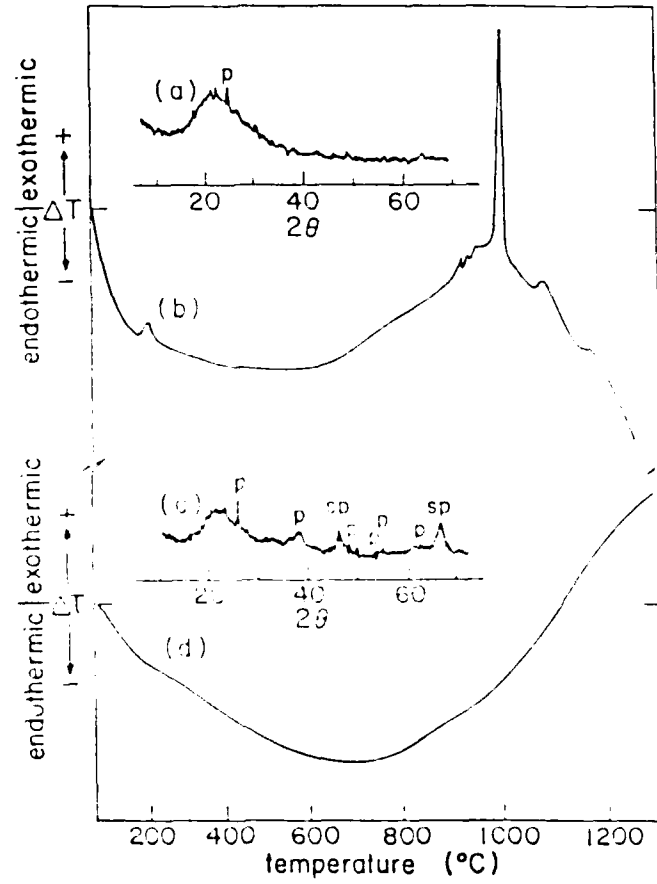


Figure 1

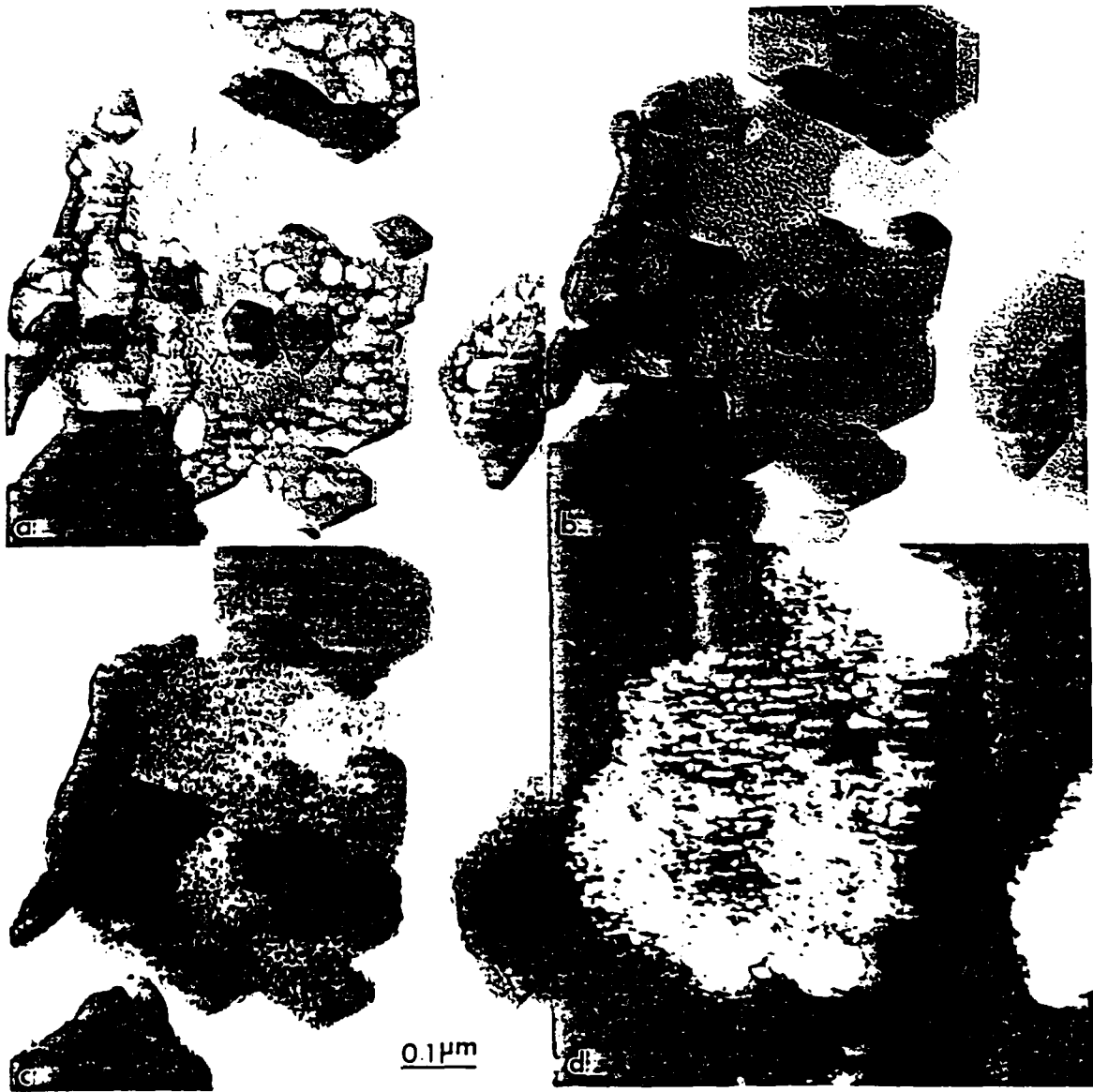


Fig. 2

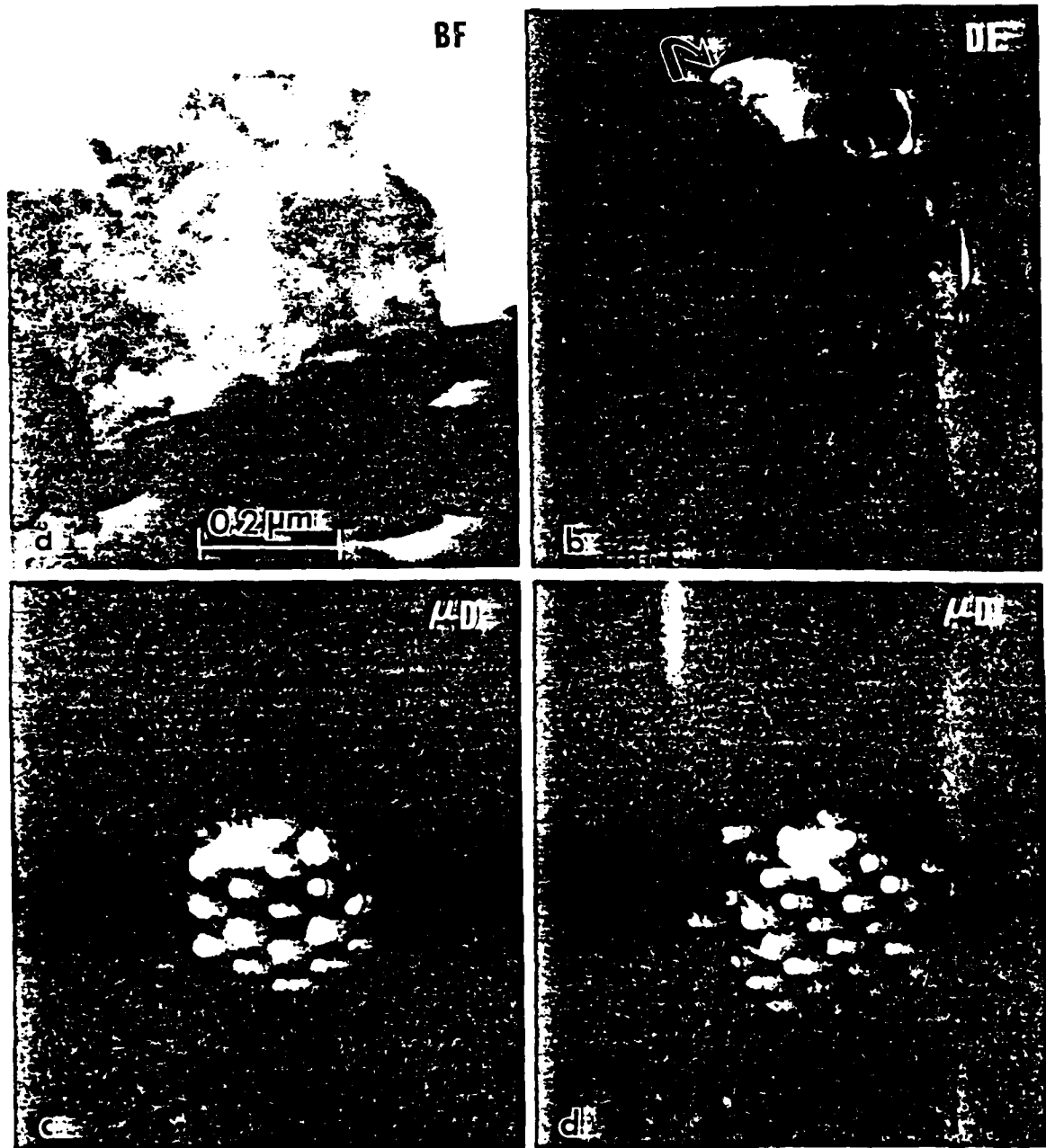


Fig. 3

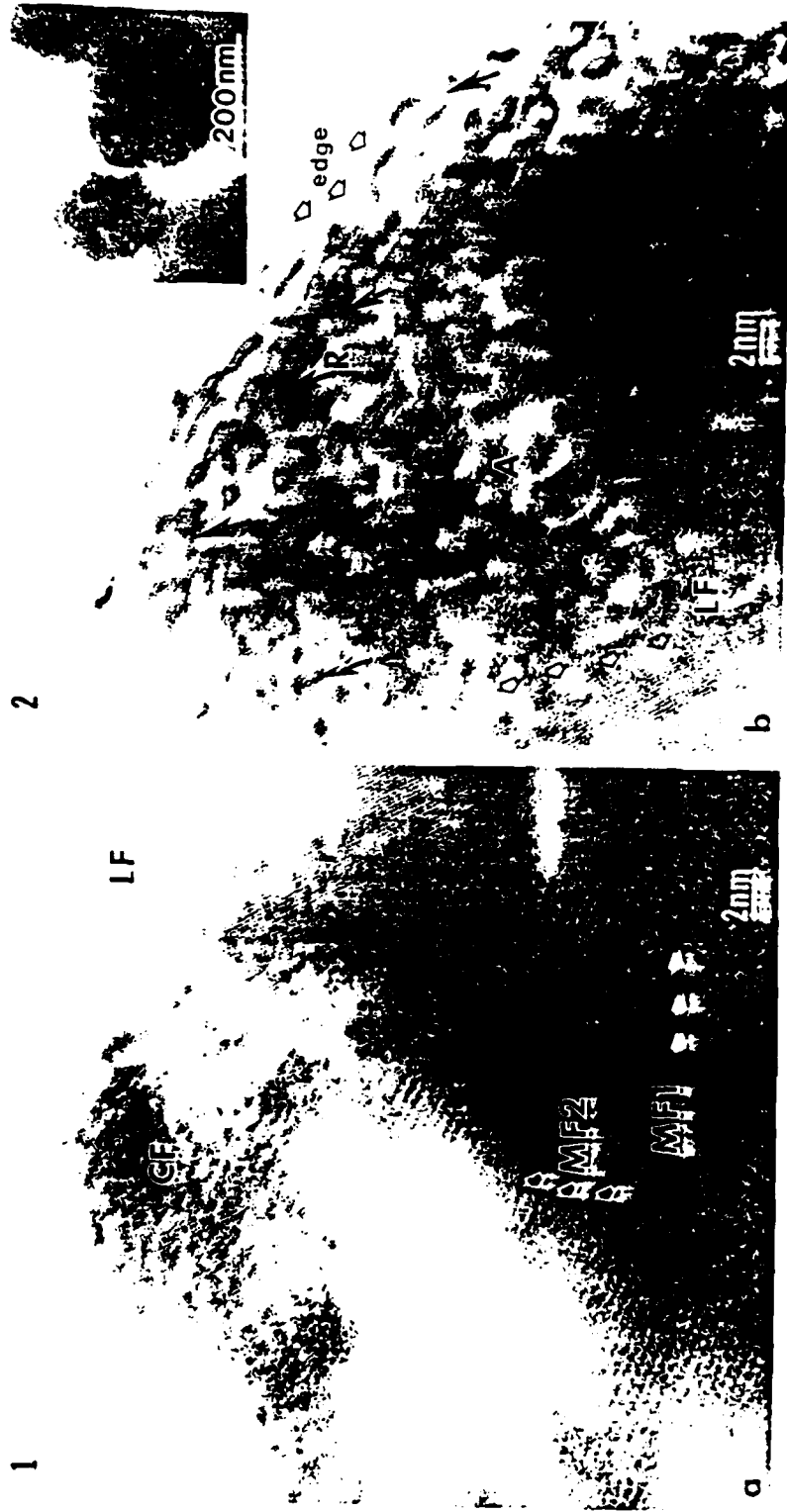


Fig. 4

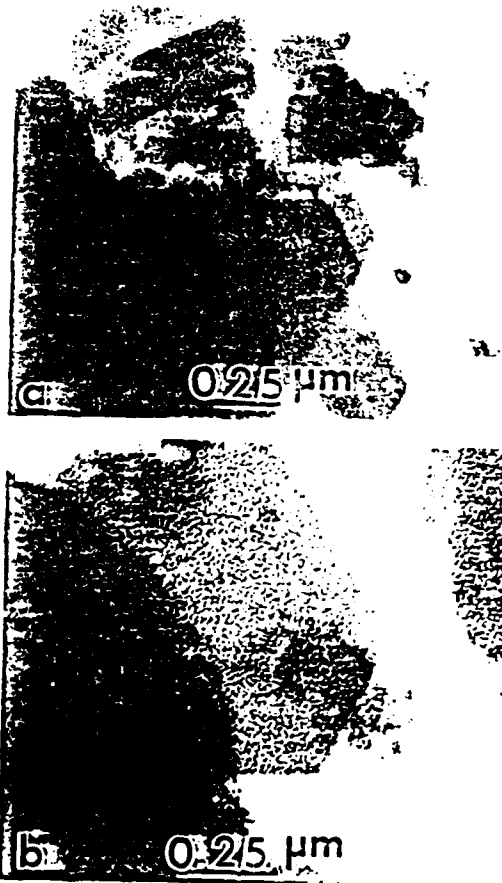


Fig. 5

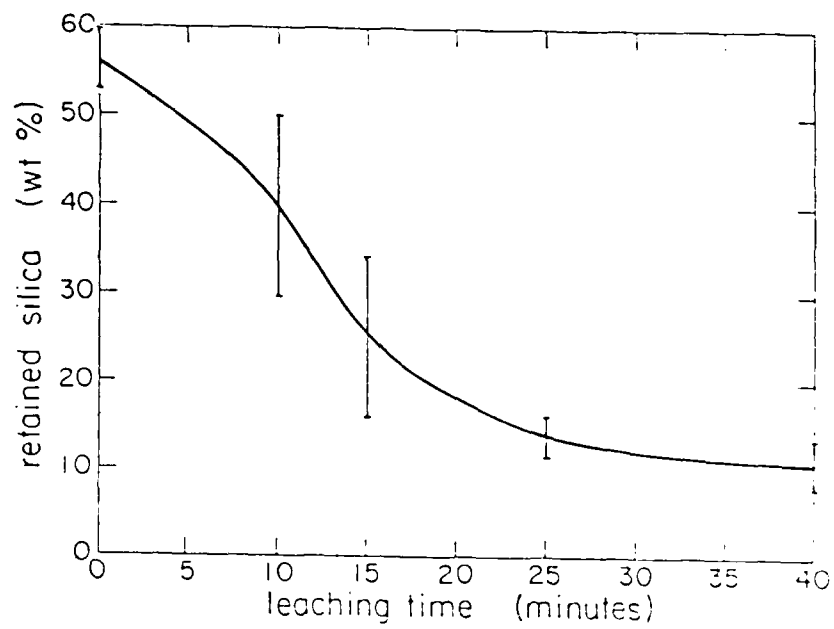


Figure 6

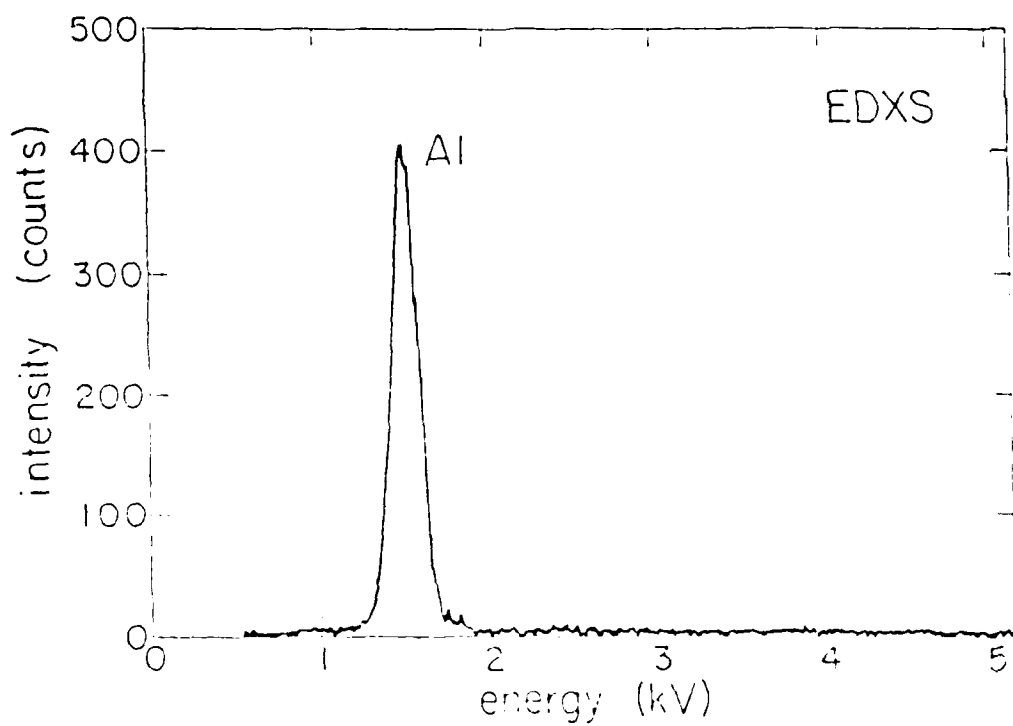


Figure 7

APPENDIX XIII

**High Resolution TEM Studies of Mullite Formation in
Metakaolinite**

(Sarikaya and Aksay 1986)

HIGH RESOLUTION TEM STUDIES OF MULLITE FORMATION IN METAKAOLINITE

Mehmet Sarikaya and Ilhan A. Aksay

Department of Materials Science and Engineering, University of Washington, Seattle, WA 98195

Studies on the compressive fracture strength (759 MPa at 1500°C)¹ and the flexural strength (700 MPa at 1300°C)² of polycrystalline mullite ($3\text{Al}_2\text{O}_3 \cdot 2\text{SiO}_2 - 2\text{Al}_2\text{O}_3 \cdot \text{SiO}_2$) illustrate its potential for high temperature applications. In the processing of these high strength mullites, molecularly mixed Al_2O_3 - SiO_2 precursors are used to enhance mullite formation rates and to achieve microstructural homogeneity in the submicrometer range.³ Reaction steps leading to the formation of mullite in molecularly mixed systems are not adequately understood.⁴ The prevailing problems center around (i) the composition of a spinel phase that forms at around a 980°C exothermic reaction, and (ii) the concurrent or subsequent formation and growth of mullite. Here, we report our high resolution TEM results on the formation of the spinel and mullite phases in a molecularly mixed precursor, metakaolinite ($\text{Al}_2\text{O}_3 \cdot 2\text{SiO}_2$).

Metakaolinite forms as the dehydration product of mineral kaolinite at 550°C. Although it retains the hexagonal morphology of the original kaolinite plates (Fig. 1), metakaolinite appears amorphous. In heat treatment of metakaolinite up to 1600°C, we observe three distinct reaction stages: (i) prior to the exothermic reaction at 980°C, density fluctuations which result in a texture similar to those observed in spinodally decomposed glass systems; (ii) at the exothermic reaction, the formation of a crystalline phase with spinel structure; and (iii) subsequent formation and growth of mullite. Here, we report our observations on the last two stages leading to the formation of liquid free mullite grain boundaries.

Fig. 2 shows the spinel particles that form in the amorphous metakaolinite matrix at the 980°C exothermic reaction. EDS and CBED analyses indicated that this spinel phase is nearly identical to pure γ - Al_2O_3 , both in composition and structure. Above 1000°C, while spinel particles disappear, the formation of elongated mullite crystals occurs due, most likely, to a reaction between the spinel phase and the amorphous matrix (Figs. 3(a) and (b)). The structure of mullite was confirmed by microdiffraction experiments. HREM images taken from these mullite crystals reveal structural details at atomic scale. Mullite crystals grow by the formation of ledges along their long edges (Fig. 3(c)) and the forward movement of these in the [001] direction. Metakaolinite alone cannot totally transform to mullite since it is deficient in Al_2O_3 . Therefore, we adjusted the overall composition to that of mullite through colloidal mixing of alumina with kaolinite. Mullites formed with these mixtures have grain boundaries mostly free from any amorphous film (Fig. 4). The formation of liquid free grain boundaries appears to be responsible for mullite's superior performance at elevated temperatures.

References

1. P. C. Dokko, J. A. Pask, and K. S. Mazdizyani, *J. Am. Ceram. Soc.*, 60 [3-4] 150 (1977).
2. S. Kanzaki, J. Asaumi, C. Mitate, O. Abe, H. Tabata, Proceedings of 24th Yogyo Kiso Toronkai, Sendai, Japan (1986).
3. K. S. Mazdizyani and L. M. Brown, *J. Am. Cer. Soc.*, 11 [11] 548 (1972).
4. I. W. M. Brown, K. J. D. MacKenzie, M. E. Bowden, and R. H. Meinhold, *J. Am. Ceram. Soc.*, 68 [6] 298 (1985).
5. This work was supported by the Advanced Research Projects Agency of the Department of Defense and was monitored by the Air Force Office of Scientific Research under Grant No. AFOSR-83-0375.

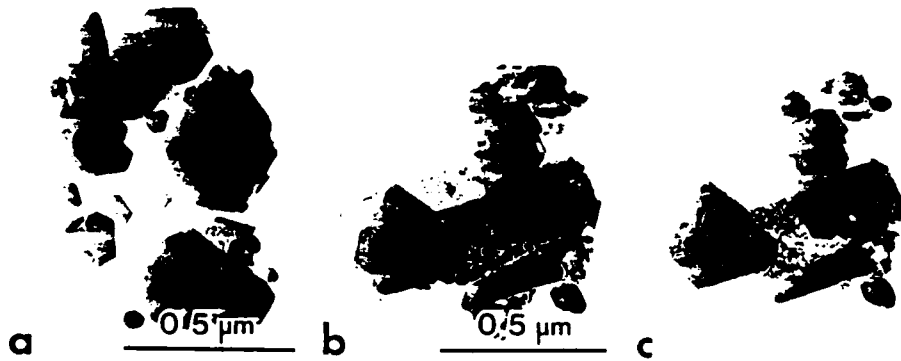


FIG. 1.--(a) BF image of as-received kaolinite particles (suspended on Holy-C film). BF images (b) kaolinite and (c) metakaolinite are seen before and after electron beam induced heating, respectively.

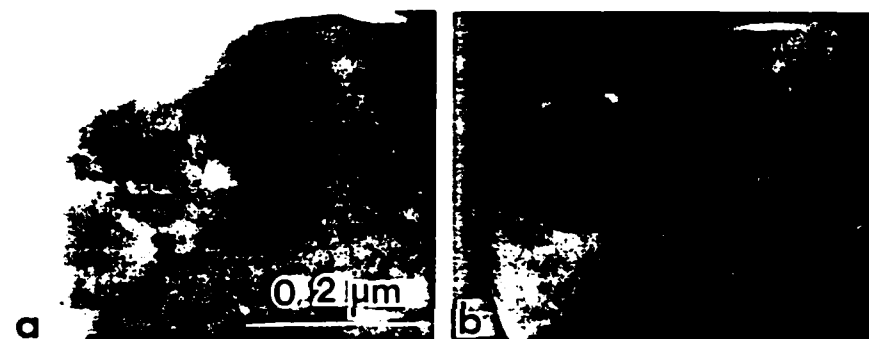


FIG. 2.--(a)BF and (b) DF images of spinel regions (1000°C).

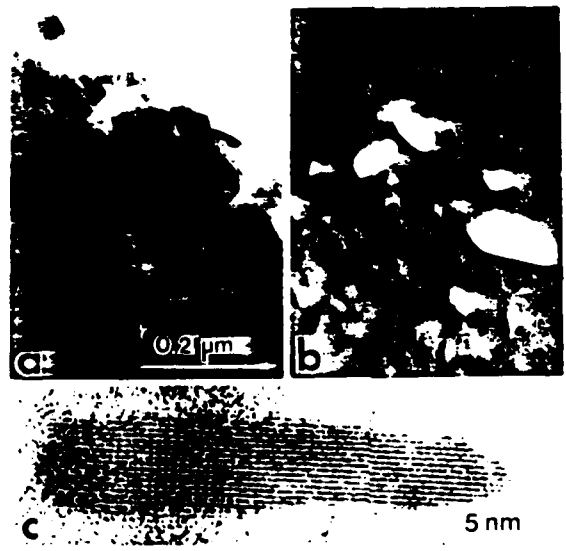


FIG. 3.--(a) BF and (b) DF images revealing mullite crystallites in an amorphous SiO₂ rich matrix. (c) HREM image of a mullite crystallite showing structural details (1034°C).

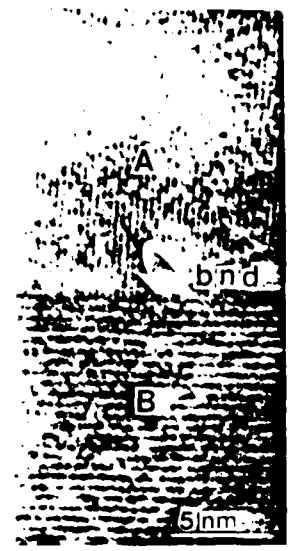


FIG. 4.--HREM image revealing a "clean" mullite-mullite grain boundary (1500°C).

APPENDIX XIV

**High Resolution Electron Microscope Characterization
of Interfaces in Ceramics**

(Sarikaya, Aksay, and Thomas 1985)

HIGH RESOLUTION ELECTRON MICROSCOPIC
CHARACTERIZATION OF INTERFACES IN CERAMICS

Mehmet Sarikaya, Ilhan A. Aksay, and Gareth Thomas*

Department of Materials Science and Engineering
University of Washington, Seattle, WA 98195

*Department of Materials Science and Mineral Engineering
University of California, Berkeley, and
National Center for Electron Microscopy
Lawrence Berkeley Laboratory, Berkeley, CA 94720

ABSTRACT

High resolution electron microscopy (HREM) is useful in bringing out the microstructural variations, such as structural details at grain boundaries, at very high resolutions, even at atomic levels. An important aspect is the examination of the surface irregularities at the boundary regions which provide information on the transformation characteristics of the phases. In this paper, we present data on the microstructural characteristics of some high temperature ceramics (silicon nitride, mullite, and aluminum nitride) with particular emphasis on the detection of grain boundary amorphous phases. Furthermore, the HREM technique is reevaluated with reference to other techniques.

INTRODUCTION

Interfaces are of great fundamental and technological importance in polycrystalline ceramics since their properties, such as electrical and mechanical, depend largely on the interfacial characteristics. In the characterization of interfaces in ceramic systems, electron microscopy provides a unique opportunity. In the conventional mode, bright-field (BF) imaging does not have sufficient resolution for interfacial details, especially in very thin regions of second phases which may be present at grain boundaries. However, high resolution electron microscopy (HREM) is an advanced imaging technique which can provide invaluable information on the

details of the interfaces, e.g., interfacial steps, and lattice arrangements at or near the interfaces at atomic levels.^{1,2} Especially important is the detection of thin film amorphous grain boundary second phases which usually occur in sintered ceramics.^{3,4}

The presence of amorphous grain boundary phases in ceramics is generally associated with additives that are used as processing aids. For instance, in the case of silicon nitride ceramics, as a result of reactions between the surface silica present on the matrix powder and the processing aids (such as alumina, yttria, and magnesia) a liquid phase, which wets the grains and acts as a densifying agent, is formed during sintering.³⁻⁷ A similar situation also arises during the sintering of aluminum nitride with (e.g., silica or calcia) additives.⁸ In the case of mullite, a metastable liquid phase may be present during the course of densification.⁹ In all cases, this amorphous grain boundary phase, with a low softening temperature, becomes responsible for the loss of strength at elevated temperatures.

The goal of this paper is two-fold. First, the technique of high resolution electron microscopy is discussed. Second, the use of HREM in the characterization of grain boundaries in ceramics is illustrated with case studies on silicon nitride, mullite, and aluminum nitride.

TECHNIQUE

An ideal condition for imaging an interface between two grains exists when the interface is parallel to the incident electron beam direction.^{3,4,10} In this way, the details of both surfaces on either side of the boundary will be clearly revealed. For example, such a configuration of the grain boundary with a thin amorphous film is schematically illustrated in Fig. 1. Here, the boundary is seen edge-on with respect to the incoming electron beam. In order to image the boundary,

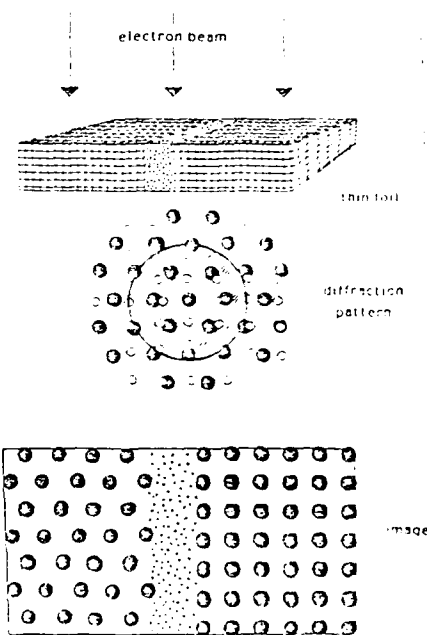


Figure 1. Schematic illustration of an edge-on configuration in imaging of an interface where the grains are in z.a. orientation.

an objective aperture is used which encompasses the diffraction spots due to both grains, as well as the diffuse ring (hatched) due to the inelastically scattered electrons from the amorphous region. Under favorable conditions consistent with the specimen-electron beam orientation discussed here and proper performance of all electron-optical alignments, a lattice image of the boundary region can be resolved in a sufficiently thin region of the foil. If both of the grains are in the zone axis (z.a.) orientation, then the atomic periodicities are resolved as schematically shown in Fig. 1, provided also that the correct defocus value has been set with an objective lens with sufficiently high resolving power ($\sim 0.2-0.3$ nm). The presence of an amorphous layer can then be discerned from the lack of any atomic periodicity right at the boundary, even if the layer is 1.0 nm thick. The sensitivity of this image also depends on the boundary tilt and the defocus value of the image.

Compared to other imaging techniques, such as diffuse dark-field imaging (DDF)¹⁰ in which the objective aperture is placed on the diffuse ring produced in the diffraction pattern due to the presence of an amorphous layer at the boundary, higher spatial resolution is achieved by the lattice imaging technique. In addition, an amorphous layer might be caused due to external effects, such as excessive carbon accumulation at the boundary groove which occurs during the carbon evaporation to the surface of the foil, a process used to prevent decharging during electron microscopy observation of insulators.

INTERFACE CHARACTERIZATION IN CERAMICS

Case I: Silicon Nitride

The silicon nitride compact used in this study was prepared with high purity powders of β - Si_3N_4 , α - Al_2O_3 , and Y_2O_3 with the use of an aqueous colloidal filtration route.¹² Densification was achieved by liquid phase sintering at 1750°C and 725 KPa nitrogen pressure.¹² The fully dense microstructures produced after this liquid phase sintering process displayed uniform distribution of β - Si_3N_4 grains (Fig. 2(c)). Two different second phases were determined within the microstructure: one crystalline and the other amorphous. Since there is no morphological difference between these two phases, geometrical effects in the crystallization behavior may be disregarded. However, a compositional analysis by energy dispersive x-ray spectroscopy (EDS) indicated a higher yttria content in the crystalline second phase than in the glassy regions, while electron energy loss spectroscopy (EELS) showed higher oxygen content in the glassy regions.¹³

The distribution of amorphous phase is homogeneous as revealed in the DDF micrograph of Fig. 2(b). Although the regions

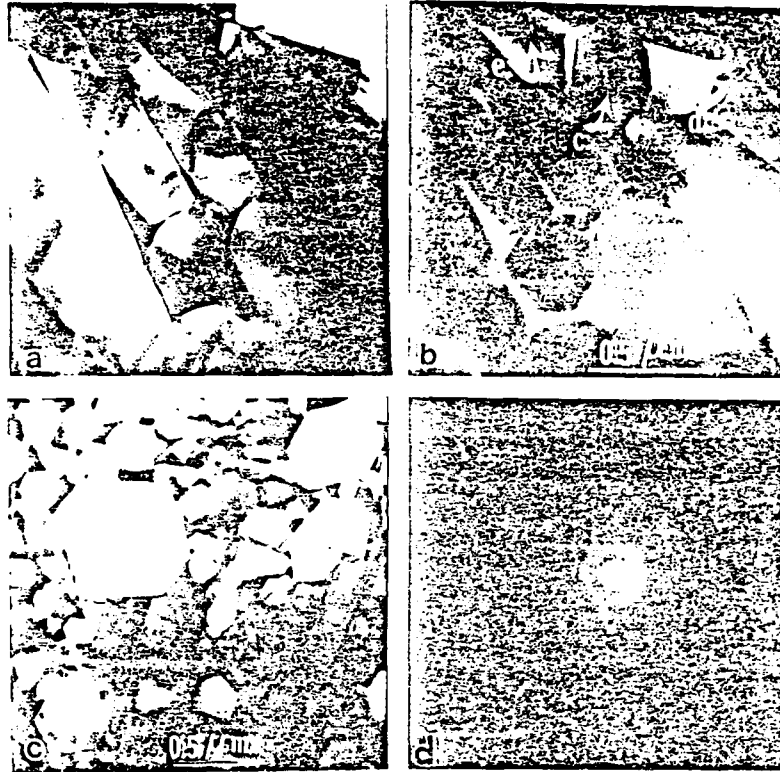


Figure 2. (a) BF and (b) DF images from a thin foil showing the distribution of glassy phase; (c) low magnification BF image showing the general microstructure; (d) microdiffraction pattern from glassy region revealing only diffuse scattering.

indicated as e and d produce similar contrast in the BF image of Fig. 2(a), only the region d changes contrast in the DDF image. In fact, microdiffraction from region e produces elastic scattering while diffuse scattering is produced from region d (Fig. 2(d)).

At low resolutions and magnifications (Fig. 2(c)), it is not possible to reveal whether or not grain boundaries are also covered with a thin (usually 2-10 nm thick) amorphous phase, which is usually the case in all liquid phase sintered silicon nitrides.^{5,6} Therefore, it becomes necessary to perform HREM. The example given

in Fig. 3 is of interest for several reasons: First, one of the grains is Si-Al-Y-oxynitride and the other is Si_3N_4 . Second, both of the grains are in the z.a. orientations. An amorphous phase is clearly seen in the lower portion as indicated by Am. However, as one follows this amorphous region towards the boundary, it is seen that several nanometers inside the boundary the amorphous phase ends. At this portion of the grain boundary, atomic periodicities in both grains continue right to the boundary and stop when they reach each other. The absence of any discontinuity at the boundary then indicates the absence of an amorphous phase. Fig. 4

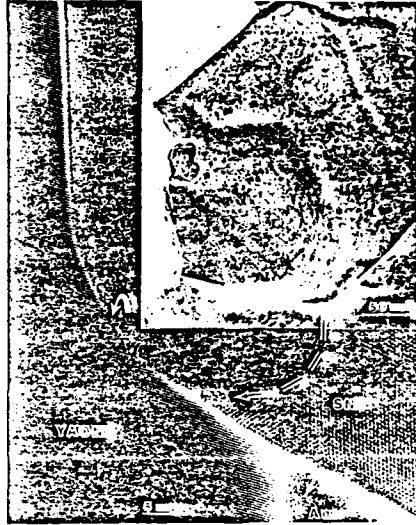


Figure 3. HREM image of an interface between a Y-Si-Al-oxynitride and silicon nitride grains.

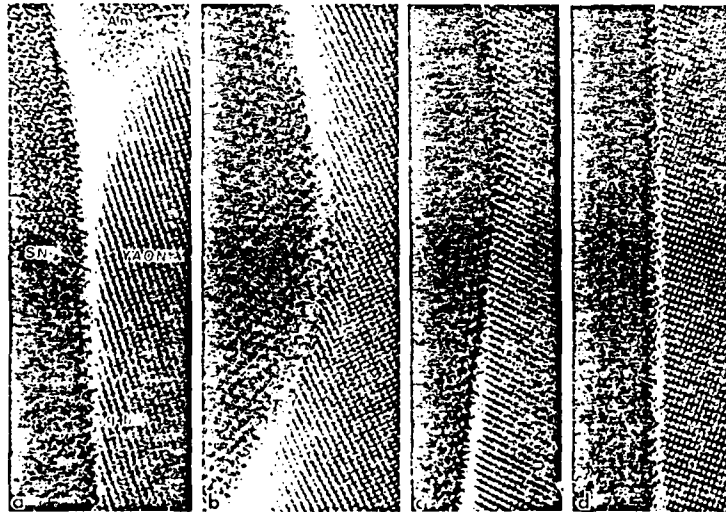


Figure 4. Details of the interface shown in Figure 3.

presents a series of images along the boundary revealing the details at very high magnifications. Again, the absence of any amorphous phase film is made obvious by the presence of rows of atoms in both grains at the points of contact.

One of the objectives in reducing the detrimental effects of the amorphous phase is to crystallize it during cooling. This crystallization can be achieved when the liquid phase, which is present at the sintering temperature, reaches a composition of one of the complex yttrium-aluminum-silicon oxynitride phases. Many factors can affect this process, such as compositional variations due to inhomogeneities in mixing, and the temperature and pressure of sintering. An example of such a case is shown in Fig. 5. At the triple junction of Fig. 5, where normally an amorphous phase would be present, lattice fringes are revealed which indicate that the amorphous phase has crystallized. However, upon a close examination of the boundary between this crystalline phase and the silicon nitride grains, one can still see a thin layer of amorphous film. Micrographs taken along the boundary region between the silicon nitride grains indicate that this film is discontinuous and the rest of the boundary is free from any amorphous layer.

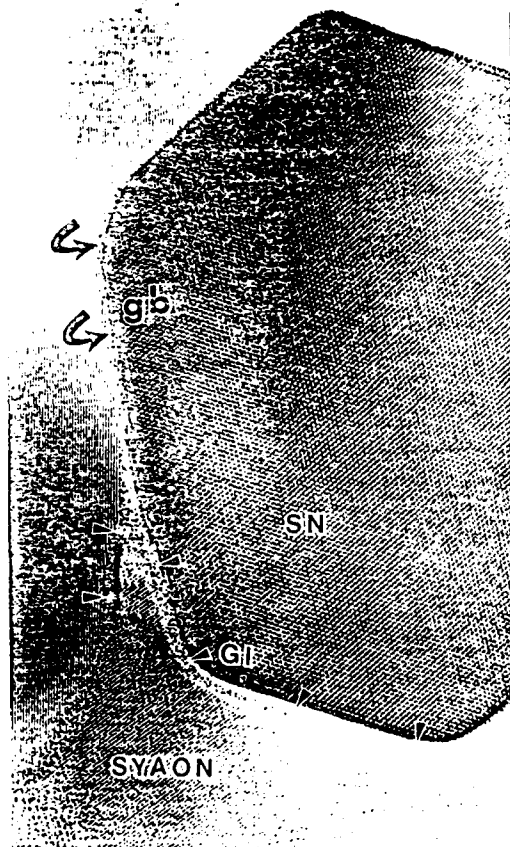


Figure 5. Low magnification HREM image revealing a crystalline phase, formed from the amorphous phase, at a three-grain junction.

Case II: Mullite

Mullite ($3\text{Al}_2\text{O}_3 \cdot 2\text{SiO}_2$) is the only stable intermediate compound in the silica-alumina binary system.¹⁴ Mullite's main importance as a structural material comes from the fact that it has favorable thermal shock resistance, low specific gravity, good corrosion resistance, and especially high creep resistance.¹⁵

In the processing of mullite, recent trends have favored the use of submicron size particles or molecularly mixed systems in order to enhance the mullitization process during densification.^{9,16} The mullite compact that was examined in this current study was similarly prepared by a colloidal filtration process of submicron size alumina and kaolinite ($\text{Al}_2\text{O}_3 \cdot 2\text{SiO}_2 \cdot 2\text{H}_2\text{O}$).¹⁷ The premise of the work was to show that if diffusion distances were shortened, diffusion controlled reactions could be completed at relatively low temperatures ($<1550^\circ\text{C}$) to form liquid free mullite. The results of the electron microscopy observations are as follows.

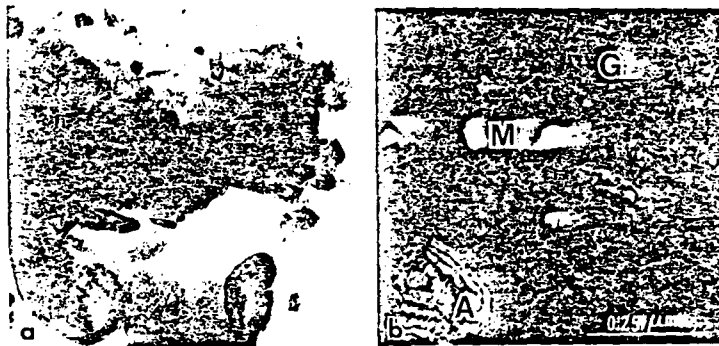


Figure 6. (a) BF and (b) DF micrographs from 1300°C sample. The amorphous phase, G, surrounding the crystals, M, are also revealed. Alumina crystals are still present as indicated by A.

In Fig. 6, the pair of TEM micrographs displays a characteristic region of a sample that was heat treated at 1300°C for 1 hr to achieve partial densification. In the BF image, small mullite crystals with well defined rectangular shapes are seen in various orientations. This is more clear in the dark-field (DF) micrograph (b), which was taken by using a superimposed reflection formed by the diffraction from those crystals which change contrast. The size of these crystals ranges from 10 to 100 nm. Mullite particles are embedded in an amorphous matrix which is mostly SiO_2 . (It should be noted here that because of experimental difficulties and uncertainties, quantitative chemical analysis by EDS method was not performed.) The distribution of this glassy phase is seen as a

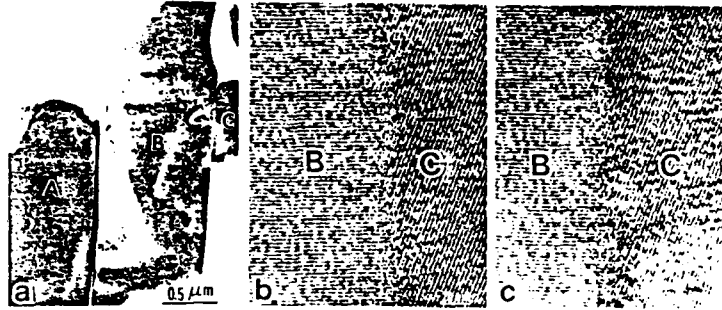


Figure 7. (a) BF image from 1500°C sample. (b) and (c) are HREM images taken along the boundary shown by arrow in (a) revealing the absence of any amorphous layer.

faint bright background in the DF image (due to diffuse scattering). The duration of sintering at this temperature was not sufficiently long enough to result in complete dissolution of the alumina grains within the amorphous matrix. Therefore, some alumina still remained in the compact (as indicated by letter A in the micrograph).

A portion of the microstructure evolved after a densification treatment at 1500°C, for 1 hr, is shown in Fig. 7(a). In comparison to the 1300°C treatment, considerable growth of mullite crystals has occurred at the expense of the surrounding matrix. Although an amorphous phase could still be detected in certain portions, the amount is reduced considerably and many mullite-mullite grain boundaries appear to be free of the amorphous phase. HREM is utilized to examine the mullite grain boundaries. A favorable configuration of imaging is presented in Fig. 7, where the boundary between grains B and C, each exhibiting one set of fringes, was examined. The fringes in grain C are continuous up to the interface where the fringes in grain B are also revealed. It was ascertained from this and other micrographs that many grain boundaries were free from an amorphous phase.

Case-III: Aluminum Nitride

AlN is a member of the SiAlON system and is used for high temperature applications.¹⁸ Only limited work has been reported on the Al rich corner of the SiO₂-Al₂O₃-Si₃N₄-AlN system.¹⁸⁻²⁰ Similar to the silicon nitride ceramics, AlN can be sintered with the aid of sintering additives such as silica and calcia. Small amounts of silica (5-10 %) produce alloys near the 2H phase field.⁹ The

samples in the present investigation (with 10% SiO₂ addition) were prepared by a two stage sintering process: First at 2000°C and then at 2100°C under 300 kg/cm² pressure in nitrogen atmosphere.⁸ In this research, our intent was to study the 2H to polytypoid transformation. HREM was utilized to examine the details of the 2H/polytypoid interface.

Conventional characterization of the microstructure revealed high amounts of different types of polytypoids, in addition to the original 2H structure.^{20,21} Polytypoids form because of the change in the stacking sequence. The reason for the local change in the hcp stacking sequence (ABABAB..) to cubic (ABCABC..) in AlN is because of the deviation of Al/N ratio from 1. As the Al/N ratio decreases, more N is taken into the structure. Together with N, Si and probably O are taken into the structure to keep the charge balance. In fact, a recent study with EELS indicated that oxygen is indeed incorporated into the polytypoid structure.²¹ There is also 5-10% Si in polytypoids as measured by EDS and no Si in the original grains.²¹

An example of the AlN microstructure examined in this study is shown in Fig. 8. In the low magnification BF micrograph (b), one can see a triangular projection of a three grain junction, which may be interpreted as a "glassy pocket" at this low magnification. However, the HREM micrograph in (a) reveals that this region is indeed crystalline and, interestingly enough, has an original 2H structure rather than



the polytypoid seen on the right of the micrograph, which repeats itself through the whole grain. Another interesting feature in micrograph (b) is the presence of several different polytypoids in a grain seen at the top of the picture, which are frequently observed in these samples. Therefore, in this grain, faulting is

Figure 8. (a) Lattice fringe image and (b) BF image taken from the AlN sample showing the details of a boundary region (arrow).

not a regular single type but is a combination of different types which repeat regularly throughout the structure.

It is often very useful to find grains which are half-transformed. Examination of the interfaces between the transformed and the untransformed regions reveals valuable information about the nature of the interfaces which could be related to the mechanism of transformation. Both straight boundaries and boundaries containing ledges were observed in an earlier study.²¹ Fig. 9 shows an example of the latter type. In the BF image of Fig. 9(a), the end part of the long grain is seen where, in either side of the grain, two small pockets of the original grain (shown by arrows) were left untransformed. The high resolution image in (b) reveals the details of the interface between the 2H and the polytypoid where the steps, or ledges, at the interface are clearly seen. It was hypothesized earlier²¹ that the growth of polytypoids occurs when the concentration of nitrogen reaches a critical value in the original structure. Under a positive nitrogen atmosphere and high temperature, nitrogen is taken into the structure at the boundary by forming ledges. The size of the ledges and, therefore, the type of the polytypoid is then determined by the local concentration of nitrogen in the structure which dictates the Al/N ratio.

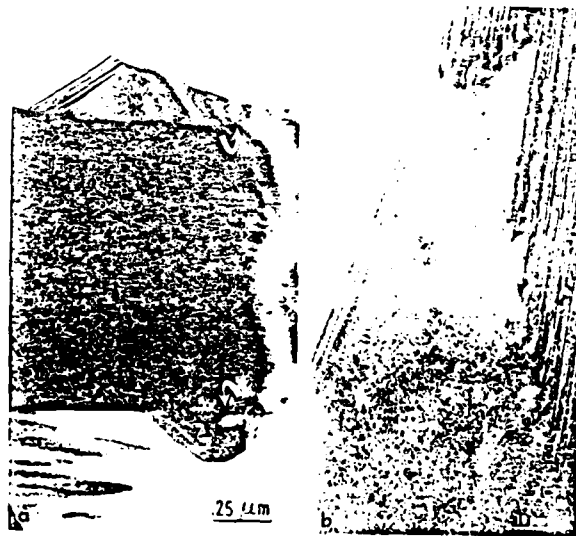


Figure 9. (a) BF image showing 2H/Polytypoid boundaries containing ledges, and (b) HREM image revealing the details of the boundary indicated by B in (a).

CONCLUSIONS

High resolution electron microscopy technique was used to reveal microstructural details in some ceramic systems. Lattice image analysis resulted in the following conclusions:

(1) At some grain boundaries of silicon nitride ceramics (fluxed with alumina and yttria) a glassy phase is absent and in some cases even a crystalline second phase is observed at three grain junctions.

(2) In mullite ceramics, mullite-mullite grain boundaries are shown to be glass-free provided that sufficient time is allowed during the densification stage to achieve an equilibrium phase structure.

(3) AlN doped with 10% silica does not contain a glassy phase but has polytypoids in which the Al/N ratio deviates from the value in the original, 2H, structure. Stepped, or ledged, interfaces as well as straight boundaries can be formed between polytypoids/2H grains depending on the transformation stage.

ACKNOWLEDGEMENTS

Financial support from NSF (DMR-83-1317239) for the work on silicon nitride and aluminum nitride and from AFOSR/ RPA (83-0375) for mullite work is greatly acknowledged. We thank K. Komeya for providing the AlN samples.

REFERENCES

1. J. C. Allpress and J. V. Sanders, J. Appl. Crystallogr., **6**, [pt.3] 165 (1972).
2. R. Gronsky, "High Resolution Electron Microscopy" in: "Experimental Methods in Materials Science", H. Herman, ed., Academic Press, New York (1982).
3. D. R. Clarke and G. Thomas, J. Am. Ceram. Soc., **60**, [11-12] 491 (1977).
4. L. K. Lou, T. E. Mitchell, and A. H. Heuer, J. Am. Ceram. Soc., **56**, [9-10] 392 (1978); and *ibid.*, p. 462.
5. F. F. Lange, Final Tech. Rep. No. 74-9D4-POWDR-R2, Westinghouse Corp., (1976).
6. G. E. Gazza, J. Am. Ceram. Soc., **56**, [12] 662 (1973).
7. O. L. Krivanek, T. M. Shaw, and G. Thomas, J. Am. Ceram. Soc., **62**, [11-12] 585 (1979).
8. K. Komeya and A. Tsuge, Yogyo-Kyokai-Shi, **89**, 515 (1983).
9. M. Sacks, Ph. D. Thesis, University of California, Berkeley, California, LBL Report # 10372, 1979.

10. O. L. Krivanek, T. M. Shaw, and G. Thomas, J. Appl. Phys., 50, [6] 4223 (1979).
11. D. R. Clarke and G. Thomas, J. Am. Ceram. Soc., 61, [3-4] 114 (1978).
12. I. A. Aksay and C. A. Ambarian, in: "Development of Homogeneity in Si₃N₄ Ceramics by Colloidal Filtration," Report submitted to Garrett Turbine Engine Co., Phoenix, AZ, 85010, 1984.
13. M. Sarikaya, P. Rez, and G. Thomas, paper to be submitted to J. Am. Ceram. Soc. (1985).
14. I. A. Aksay and J. A. Pask, J. Am. Ceram. Soc., 58, [11-12] 507 (1975).
15. R. F. Davis and J. A. Pask, in: "High Temperature Oxides", Part. IV, A. M. Alper, ed., Academic Press, New York (1972).
16. S. Prochazka and F. J. Klug, J. Am. Ceram. Soc., 66, [12] 874 (1983).
17. I. A. Aksay and M. Sarikaya, to be published.
18. K. H. Jack, J. Mat. Sci., 11, [10] 1611 (1983).
19. G. Van Tandeloo and G. Thomas, Acta. Met., 31, [10] 1611 (1983).
20. G. Van Tandeloo, K. T. Faber, and G. Thomas, J. Mater. Sci., 18, 525 (1983).
21. M. Sarikaya and G. Thomas, in: "Electron Microscopy", p.227, A. Csanady, P. Rohlich, and D. Szabo, eds., Proc. 8th EUREM, Budapest, Hungary, Aug. 13-18 (1984).

APPENDIX XV

**High Resolution Electron Microscopy Characterization
of Glass-Free Mullite**

(Sarıkaya and Aksay 1987)

**HIGH RESOLUTION ELECTRON MICROSCOPY CHARACTERIZATION OF
GLASS-FREE MULLITE**

M. Sarikaya and L.A. Aksay

This paper will be submitted and published in the near future.

A detailed characterization of interfaces of mullite, $3\text{Al}_2\text{O}_3 \cdot 2\text{SiO}_2$ was performed by using high resolution transmission electron microscopy imaging technique (HREM). The polycrystalline mullite was prepared by mixing kaolinite, $\text{Al}_2\text{O}_3 \cdot 2\text{SiO}_2 \cdot 2\text{H}_2\text{O}$, and fine $\alpha\text{-Al}_2\text{O}_3$ powders by colloidal techniques. Upon heating, mullite crystals started forming at temperatures as low as 1000°C and they gradually grew in $[001]$ preferential directions up to 1600°C , the temperature at which complete sintering takes place. It was found by HREM that mullite boundaries were free from intergranular amorphous films. This result is attributed to the success of the processing technique.

AD-A188 526

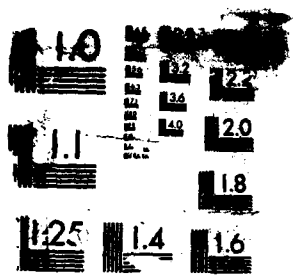
MICRODESIGNING OF LIGHTWEIGHT/HIGH STRENGTH CERAMIC
MATERIALS (U) WASHINGTON UNIV SEATTLE DEPT OF MATERIALS
SCIENCE AND ENGINEERING I A AFSAY 30 AUG 87
AFOSR-TR-87-1595 AFOSR-83-0375

3/4

UNCLASSIFIED

F/G 11/2

NL



MICROCOPY RESOLUTION TEST CHART

APPENDIX XVI

**Infrared Transparent Mullite Through Densification of
Monolithic Gels at 1250°C**

(Shinohara, Dabbs, and Aksay 1986)

Infrared transparent mullite through densification of monolithic gels at 1250°C

N. Shinohara, D. M. Dabbs, and I. A. Aksay

Department of Materials Science and Engineering, FB-10
College of Engineering
University of Washington
Seattle, Washington 98195

Abstract

Infrared transparent mullite ($3Al_2O_3 \cdot 2SiO_2$) was formed at 1250°C through densification of monolithic gels. The gels were prepared through colloidal mixing of boehmite (AlOOH, aluminum monohydroxide) and tetraethoxysilane (TEOS). After four hours at 1250°C, monolithic gels densified to 98% of the theoretical density (TD). Densification was promoted by viscous phase deformation of silica (SiO_2) during sintering. The extent of densification was found to be dependent upon the extent of agglomeration of boehmite powder in suspension. Transparency in the infrared region was obtained as a result of mullite formation in the sintered product. The microstructural evolution during densification and the concomitant spectral transmittances were characterized.

1.0 Introduction

Mullite is considered to be an important structural material for high temperature applications.¹ Recent advances in the manufacture of high purity, controlled microstructure mullite has also revealed its potential for optical and electronic uses.²⁻⁴ In this paper, we present data on the infrared transparency of high density mullite processed through densification of monolithic gels at 1250°C.

Mah and Mazdiyasn², Prochazka and Klug³ and Ohashi et al.⁵, have all reported on the infrared transparency of fully dense mullite. Each group found it necessary to either apply high pressure or high vacuum at temperatures above 1500°C in order to realize full densification. In contrast to these high temperature densification methods, various investigators attempted to densify mullite through lower temperature (<1300°C) densification of gels.⁶⁻⁸ Yoldas⁶ manufactured a transparent aluminosilicate at 1300°C using dried gels. Transparency was achieved through the formation of nanometer sized pores, resulting in lower relative densities and reduced strength. Wei et al.⁷ formed gels from colloidal boehmite (AlOOH) particles and tetraethoxysilane (TEOS) and sintered these at 1250°C to 93% of theoretical density (TD). Komarneni et al.⁸ have recently reported the formation of mullite from gels having 96% and 97% TD. These ceramics were sintered at 1200°C and 1300°C respectively. Fine grain (<1.0 μm) microstructure and translucency were observed. However, the transparency of the densified gels in the infrared region was not investigated in any of these studies.

The intent of the present study has been to investigate the formation of infrared transparent mullite through low temperature densification of monolithic gels. Unlike previous studies, we have successfully densified monolithic (>2.5 cm in dia.) gels to densities above 97% TD. The densified gels displayed infrared transparency at 1250°C upon formation of mullite. The synthesis and the infrared transmittance of these materials are discussed in the following sections.

2.0 Experimental

Monolithic gels were produced from colloidal boehmite powder suspensions and TEOS. Shinohara⁹ determined that boehmite agglomeration affected the sintering behavior of the gels. Fig. 1 shows the relationship between the bulk densities reached at different sintering temperatures and the agglomerate size in suspension. Thus, in the formation the gels for this study, the agglomerates larger than 0.3 μm were removed through classification by allowing the boehmite suspension to settle for over two weeks before using.

After classification, the boehmite suspension was mixed vigorously with partially hydrolyzed TEOS solution at pH 2.5 for approximately four days. The partial hydrolysis of TEOS solution in advance of mixing it with the boehmite suspension was necessary to prevent segregation of TEOS during gelation. For this partial hydrolysis, one mole of water was added for each mole of TEOS in an acidic solution (pH 2.0) at room temperature. At the completion of the mixing, the resultant mixture was dried at 60°C until the onset of gelation. The incipient gel was thereupon cast into a plastic dish and allowed to completely dry at room temperature for several days. The dried gels were subsequently sintered in air.

Samples of sintered gels were lapped and polished for use in infrared transmissivity measurements. Transmissivity of monolithic samples was measured on a Nicolet SDXB FTIR spectrometer. Crushed specimens, suspended in pressed KBr pellets, were used to gather chemical and phase information.

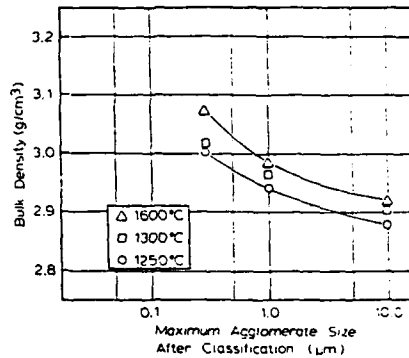


Figure 1. The classification of boehmite powder suspensions results in enhanced densification. After two weeks of undisturbed sedimentation, agglomerates larger than 0.3 µm were eliminated from the suspension. Higher densities were then achieved for the range of sintering temperatures shown. Further classification is expected to improve densification.

3.0 Results

3.1 Densification of gels:

Dried gels of two different compositions were sintered at several temperatures. Samples of type M were made from a mixture of boehmite and TEOS calculated to yield stoichiometric mullite, $3\text{Al}_2\text{O}_3 \cdot 2\text{SiO}_2$. The sample type M+1 was made from a mixture calculated to yield a final product containing one weight percent excess silica. Fig. 2 shows the effect of sintering temperature upon the density and porosity of stoichiometric (type M) samples. As shown, densification is rapid between 1200 and 1250°C. Similarly, in isothermal sintering at 1250°C, the most rapid densification was achieved within the first hour thereafter proceeding rather slowly (Fig. 3). This rapid densification is attributed to viscous phase deformation of silica before the onset of mullite formation at 1250°C (Fig. 4(A)).⁹ The higher densities achieved by the silica-rich M+1 samples also support this viscous phase densification mechanism (Fig. 3). The decrease in the apparent density above 1200°C (Fig. 2) is due to the entrapment of porosity associated with the boehmite agglomerates that were not totally eliminated in our colloidal processing.⁹

3.2 Infrared transmittance:

Three samples were used for infrared (IR) transparency measurements. Table 1 lists the sintering temperatures and densities of these samples. In both samples A and B, mullite was detected as the only crystalline phase; whereas, sample C showed theta-alumina as the crystalline phase but no mullite. The higher sintered density of sample A with respect to that of sample B at 1250°C is attributed to the presence of excess silica in sample A. This observation provides additional support for the mechanism suggested above on the enhanced densification due to viscous deformation of amorphous silica.

Table 1. Sintering data on the samples used for IR transparency measurements.

Sample	Type	Sintering Temperature, °C	ρ TD
A	M+1	1250	97.8
B	M	1250	95.2
C	M	1200	75.5

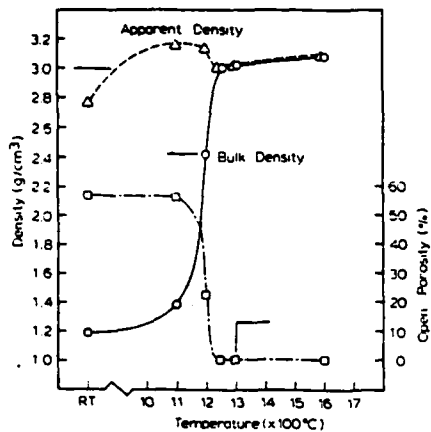


Figure 2. The densification of mullite forming gels with respect to temperature demonstrates the advantages of the sol-gel technique. The data shown was taken from densification studies on gels made from boehmite powder suspensions and TEOS, in amounts calculated to yield stoichiometric mullite ($3\text{Al}_2\text{O}_3 \cdot 2\text{SiO}_2$). The rapid densification between 1200 and 1250°C is attributed to viscous phase deformation before the formation of mullite. Once mullite has formed, densification shows appreciably (Figs. 3 and 4(A)). The decrease in apparent density above 1200°C is due to the entrapment of pores contained within agglomerates which were not eliminated by classification.

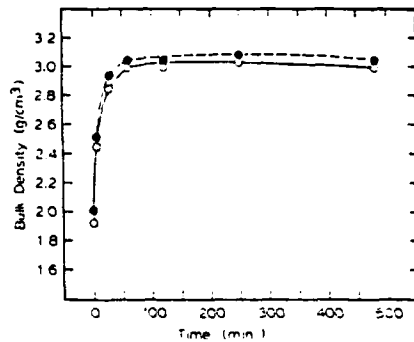


Figure 3. Isothermal sintering at 1250°C reveals the role of viscous phase deformation in densification. Two compositions are shown: the filled circles represent data taken from the densification of silica enriched gels (type M+1 samples in the text) and the open circles represent comparable data from gels which would yield stoichiometric mullite (type M samples in the text). The performance of the silica enriched gels indicates that an increase in the presence of a viscous phase (in this case, silica) results in better densification.

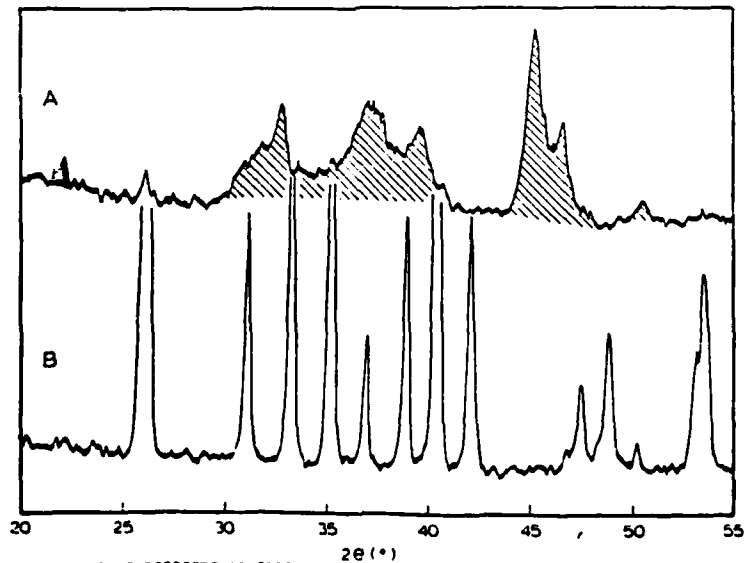


Figure 4. X-ray diffraction patterns of sintered gels made from stoichiometric amounts of boehmite and TEOS:

- A. Sintering a gel at 1200°C for two hours results only in the formation of theta-alumina (cross-hatched areas) and cristobalite (solid area).
- B. A gel which is sintered at 1250°C for two hours completely transforms to mullite.

C

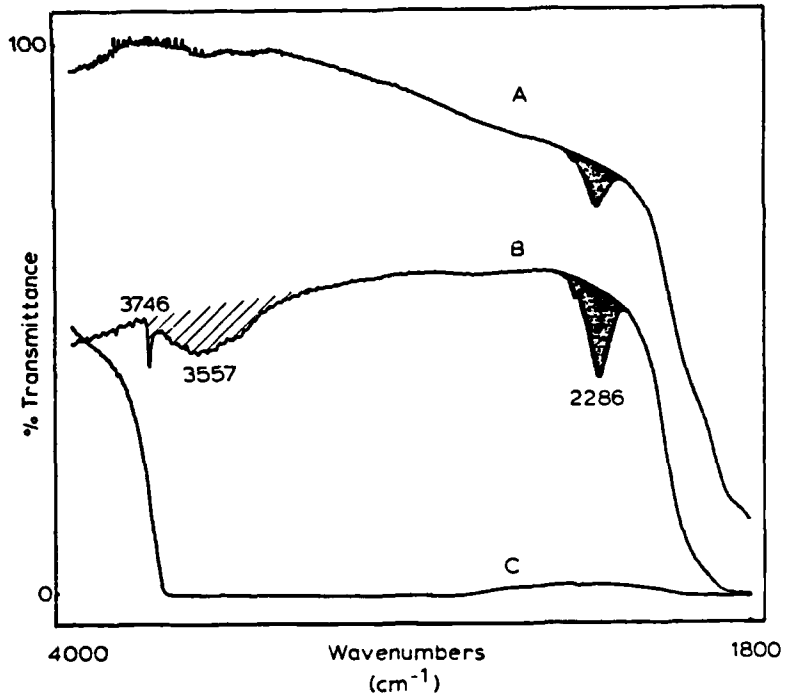


Figure 5. The infrared transmittance of three sintered gels was measured on monolithic samples (Table 2) within the region of 4000 to 1800 cm^{-1} (2.5 to 5.6 μm):
 A. A silica enriched sample (type M+1) sintered at 1250°C exhibited the best overall transmittancy. No extraneous bands were observed at the higher wavenumbers and the intensity of the 2286 cm^{-1} absorbance was reduced.
 B. A stoichiometric sample (type M) sintered at 1250°C had intermittent transmittancy. A stronger 2286 cm^{-1} absorbance and the presence of silanol bands (3746 and 3557 cm^{-1}) indicate the presence of a second phase, probably silica rich, which would explain the decrease in transmittancy.
 C. A stoichiometric sample (type M) sintered at 1200°C had no transmittancy within the region of interest. This opacity clearly shows the importance of mullite to the transparency observed in samples A and B.

Table 2. Data on the infrared transparency of sintered gels.

Sample	Thickness (mm)	\bar{T} TD	$\bar{\nu}_{\text{max}}$	$\bar{\nu}_{50}$	T (2435 cm^{-1})	T_{e} (2435 cm^{-1})
A	0.35	97.8	3785	2031	0.83	0.59
B	1.	95.2	2435	2086	0.54	0.54
C	1.	75.5	—	—	—	—

Fig. 5 contains the infrared transmittance spectra for samples A, B, and C within 1800 to 4000 cm^{-1} (5.56 to 2.50 μm). Table 2 reports the salient features of each sample's spectra.

Table 2 includes the wavenumber at maximum transmittance ($\bar{\nu}_{\text{max}}$), the wavenumber at 50% of maximum transmittance ($\bar{\nu}_{50}$), the measured transmittance at 2435 cm^{-1} (T_{2435}) and the transmittance at 2435 cm^{-1} normalized to a thickness of 1 mm. (T_{e}^{2435}).

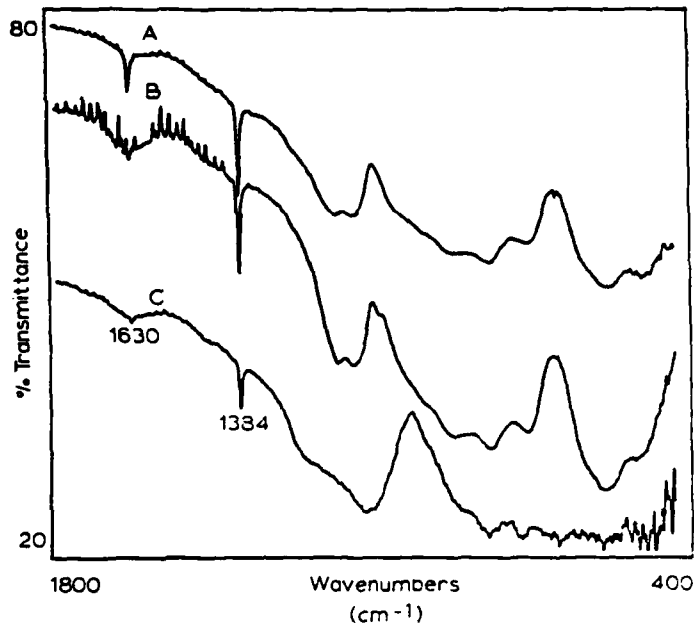


Figure 6. Samples of the sintered gels whose IR transmittancy is shown in Fig. 5 were taken for chemical analysis using FTIR. Chips were ground, mixed with KBr powder, and pressed into pellets for transmission analysis. The region 400 to 1800 cm^{-1} was chosen for the wealth of chemical information available for aluminosilicates there: Samples (A) and (B), silica-enriched and stoichiometric gels respectively, both sintered at 1250°C, exhibited much the same spectra in this region. Complete characterization has not been completed at the time of writing, but these two samples are quite obviously mullite.¹¹ Sample (C), a stoichiometric gel sintered at 1200°C, had a spectrum indicative of an aluminate, but one lacking the mullite structure. Peaks at 1630 and 1384 cm^{-1} are due to the presence of water in the KBr matrix and hydrocarbon residue within the gels, respectively.

The poor transmittance of sample C when compared to that of samples A and B demonstrates the importance of mullite to infrared transparency. As seen in the XRD pattern (Fig. 4), there was no detectable mullite phase in the samples sintered at 1200°C. Similarly, the fingerprint spectra shown in Fig. 6 show the characteristic absorption peaks for mullite in samples A and B but not in sample C.¹⁰

The band centered on 2286 cm^{-1} appears on the spectra of samples A and B. Prochazka and Klug³ indicated that this absorption increases in intensity with increasing silica content in the mullite solid solution. Our results are in contradiction with this explanation. It is obvious that the peak intensity is greater in the sample with less silica, sample B, than it is in the sample with the greater amount of silica, sample A. This observation suggests that the peak intensity is not simply associated with the amount of dissolved silica in mullite.

Sample B also exhibits bands at 3746 cm^{-1} (very sharp) and at 3557 cm^{-1} (broad). These bands have been shown to be associated with silanol (SiOH) groups within the silica network.¹⁰ The 3557 cm^{-1} band is due to hydrogen-bonded silanol groups, whilst the 3746 cm^{-1} band is due to unassociated silanol groups. The presence of silanol groups might also indicate the existence of a residual amorphous silica phase within sample B. If a second phase were found to be present in this sample, the lower transmissivity of sample B would be explained. XRD analysis of sample B gave a spectrum with very weak peaks which were thought to be due to silica, but presently this is uncertain. Transmission electron microscopy (TEM) might reveal a second phase if it exists, and such analysis is now being planned.

The spectra shown in Fig. 6 cover a region rich in information concerning the aluminosilicates.¹¹ Subtle differences exist between samples A and B, differences which have not as yet been satisfactorily explained. It is known that complex reaction sequences occur during the formation of mullite at high temperatures.¹³ The absorption spectra of these mullite ceramics probably result from slight variations in the reaction sequence. Further infrared characterization, coupled with other techniques, will be necessary to fully interpret this fingerprint region. However, with respect to processing-related problems, two bands common to samples A, B, and C should be noted. The sharp peak at 1384 cm^{-1} appears as a result of the presence of residual hydrocarbon within the sintered body from the ethoxy groups found on TEOS. Presently, a process to prevent hydrocarbon entrapment has not been determined. The band at 1630 cm^{-1} can arise from two contributing vibrations: first, water adsorbed into the KBr matrix, giving the broad band visible in samples B and C; and second, a SiO_2 network vibration, resulting in the sharp peak apparent in sample A.¹⁰ The presence of this band in sample A which lacks other characteristic silica peaks is not understood.

4.0 Conclusions

Infrared transparent mullite was sintered from monolithic gels at 1250°C to densities as high as 98% TD. The entrapment of porosity in the sintered gels was found to be associated with boehmite agglomeration. The transparency of sintered gels in the infrared region was dependent upon the formation of mullite at around 1250° . Infrared absorption analysis can detect small phase differences existing in samples of nearly equivalent composition.

Acknowledgement

This work was supported by the Defense Advanced Research Projects Agency of the Department of Defense and was monitored by the Air Force Office of Scientific Research under Grant No. AFOSR-83-0375.

References

1. P. C. Dokko, J. A. Pask, and K. S. Mazdidasni, *J. Am. Ceram. Soc.*, **60** [3-4] 150 (1977).
2. T. Mah and D. S. Mazdidasni, *J. Am. Ceram. Soc.*, **66** [10] 699-703 (1983).
3. S. Prochazka and F. J. Klug, *J. Am. Ceram. Soc.*, **66** [12] 874-880 (1983).
4. B. H. Mussler and M. W. Shafer, in Research Report, IBM Thomas J. Watson Research Center, RC 10033 (#4-590) Chemistry 6/22/83.
5. M. Ohashi, H. Tabata, S. Kanzaki, and S. Mithachi, *Proc. Annual Mtg. Jap. Cer. Soc.*, 245-246 (1986).
6. B. E. Yoldas, *Am. Ceram. Soc. Bull.*, **59** [4] 479-483 (1980).
7. W. C. Wei and J. W. Halloran, *Abstr. 88th Annual Mtg.*, 83 (1986).
8. S. Komarneni, Y. Suwa, and R. Roy, *J. Am. Ceram. Soc.*, **69** [7] C-155-6 (1986).
9. N. Shinohara, On-going Ph.D. Thesis study, University of Washington, Seattle, WA.
10. K. J. D. MacKenzie, *J. Am. Ceram. Soc.*, **55** [2] 68-71 (1972).
11. L. Wood, E. M. Rabinovich, D. W. Johnson, Jr., J. B. MacChesney, and E. M. Vogel, *J. Am. Ceram. Soc.*, **66** 693-699 (1983).
12. A. Bertoluzza, C. Fagnano, and M. A. Morelli, *J. Non-Cryst. Solids* **48** [1982] 117-128.
13. K. J. D. MacKenzie, *J. Am. Ceram. Soc.*, **68** [6] 298-301 (1985).

APPENDIX XVII

**Processing and Microstructural Characterization of
B₄C-Al Cermets**

(Halverson, Pyzik, and Aksay 1985)

Processing and Microstructural Characterization of B_4C -Al Cermets

DANNY C. HALVERSON

Lawrence Livermore National Laboratory
Livermore, CA 94550

ALEKSANDER J. PYZIK AND ILHAN A. AKSAY

Dept. of Materials Science and Engineering
University of Washington, Seattle, WA 98195

Reaction thermodynamics and wetting studies were employed to evaluate boron carbide-aluminum cermets. Wetting phenomenon and interfacial reactions are characterized using "macroscale" and "microscale" techniques. Macroscale evaluation involved aluminum sessile drop studies on boron carbide substrates. Microscale evaluation involved the fabrication of actual cermet microstructures and their characterization through SEM, X-ray diffraction, metallography, and electron microprobe. Contact-angle measurements and interfacial-reaction products are reported.

Introduction

The intent of this study is to apply thermodynamic fundamentals as a means of achieving lightweight boron carbide-aluminum (B_4C -Al) composites. To do this, we analyzed cermet systems based on chemical reactions and wetting phenomenon.

Aluminum is preferred for the development of B_4C -cermets because it is a terrestrially stable metal phase with a low specific gravity. It is also ductile, nontoxic, relatively inexpensive, easy to obtain, and available in corrosion-resistant forms. Boron carbide-aluminum cermets have the potential for offering a combination of high hardness and toughness in a lightweight structure.

Detailed selection criteria for other B_4C -metal cermet systems have been established.¹ Cermets can and have been made using nonreactive metal phases.^{2,3} Most nonreactive metals tend to be nonwetting⁴ and are not suitable for liquid phase sintering purposes. However, reactive systems usually meet the wetting requirement, and thus have considerably more to offer because they (1) may be consolidated by energy-saving-pressureless techniques, and (2) by nature of the chemical bond at the interface, can offer cermets with "tailorable" properties. B_4C -Al system is in this latter group.

Cermets are processed by powder metallurgical techniques. Such techniques have the advantage of permitting excellent control of the cermets' composition, size, and shape. Cermet powders are sometimes

formed into shapes by hot pressing, extrusion, slip casting, or dry pressing. In the processing of most cermets, the key objectives are (1) to obtain a pore free microstructure, where the ceramic grains are homogeneously distributed in the metal matrix, and (2) to ensure that a good adhesive bond is established at the ceramic-metal interface. Fully dense microstructures are usually achieved by sintering in the presence of a liquid phase.

Experimental Procedure

We performed experiments under macroscale and microscale conditions, then compared and integrated these results with those of the literature.

Macroscale experiments examine processing fundamentals that influence cermet microstructures through the use of large-size constituents. These experiments involve contact-angle studies of high-purity aluminum heated atop polished boron carbide substrates (1 μm finish). After heat treatment was completed, we measured contact angles to within one degree using a protractor grid and an optical 10X telemicroscope.

Microscale experiments were structured on the macroscale results and involved the evaluation of sintered compacts. Cermet powders were mixed in an alcohol slurry, ultrasonically treated, and then filtrated through a plaster-of-Paris mold. The powders were then cold pressed at 138 MPa, because higher pressures led to striations in the green body. Pressureless sintering was performed inside a resistance-heated vacuum furnace at pressures of 1.3×10^{-1} to 10^{-4} Pa. Some samples were sintered in flowing argon inside an Al_2O_3 tube furnace at atmospheric pressure. Some of the sintered compacts received hot-isostatic pressing at 750°-1000°C and 207 MPa for up to 1 h.

Cross sections of the cermet microstructures were polished to a 1 μm finish, then examined metallographically and with a scanning electron microscope. To determine the reaction products in the microstructures, we examined the samples by X-ray diffraction, energy dispersive spectroscopy, and electron microprobe analysis.

Thermodynamic Model

Reaction Thermodynamics

If sintering in the presence of a liquid phase is to occur, the cermet system must satisfy the reaction thermodynamic criterion that the solid ceramic phases be partially soluble in the liquid metal phases. This condition is termed "forward solubility."

Forward solubility is best illustrated by examining the WC-Co cermet system. This system can be successfully liquid-phase sintered using a low vol% metal phase between 1 and 30 vol%. The solubility of WC in cobalt under equilibrium conditions is 1 wt% at 800°C and 2 wt% at 1000°C. The solubility of cobalt in WC is negligible. Since this system satisfies the forward solubility condition required of all cermets, it is appropriate to model B_2C cermets similarly.

Figure 1 schematically represents the model along with the WC-Co system. This model demonstrates an important point with respect to the chemical stability of the cermet system. For any particular isotherm, the

ceramic phase (WC or B₄C) forms a composition band that connects to the pure metal (or alloy) phase located atop the diagram. However, since it is desired to produce a low vol% metal-phase cermet, this processing region is further restricted to the cross-hatched area below the broken line. Liquid phase densification requires that the systems within this cross-hatched area must be in a phase compatibility triangle which includes the liquid metal phase as an end member. Otherwise, the formation of reaction products may lead to the depletion of the liquid-metal phase during sintering. This depletion may occur if the solubility of the metal in the ceramic phase is high, or if an intermediate ternary compound forms as the reaction product. This undesirable condition is referred to as "reverse solubility." The WC-Co system does not suffer from the detrimental effects of reverse solubility and thus can be densified by liquid phase sintering. On the other hand, as will be illustrated, the B₄C-Al system falls into the reverse solubility category and must be densified by modified techniques.

Capillarity Thermodynamics

The mechanism of liquid-phase sintering is also very much dependent on the capillarity thermodynamic criteria of low contact angles and zero dihedral angles. Early thermodynamic treatments^{6,7} of wetting are based on the mechanistic approach of Young.⁸ Under these treatments, the solid-liquid-vapor systems is assumed to be at chemical equilibrium. In wetting studies at elevated temperatures, however, the phases of a solid-liquid-vapor system are often not at chemical equilibrium. Under chemical nonequilibrium conditions, the effect of chemical reactions on interfacial surface energies must be considered, because the phases of the solid-liquid-vapor system react with one another through the interface to achieve a state of chemical equilibrium. During these nonequilibrium dynamic conditions, the interfacial energies and the contact angle are continuously changing.⁴ Generally, wetting is achieved as a result of chemical reactions.⁴ Therefore, a nonwetting system can be transformed to a wetting state by taking advantage of chemical reactions.

Results and Discussion

Macroscale Conditions

Figure 2 shows the wetting behavior of liquid aluminum on boron carbide substrates. Results presented in this manner provide a very useful processing guide, because both temperature and processing time are considered. Unfortunately, most of the wetting data in the literature are presented with the contact angle shown as a function of temperature only, often without even mentioning the time of the experiment.

The micrographs of Fig. 3 illustrate the effectiveness of using wetting data for processing. These micrographs show different fracture surfaces for B₄C-Al (36.4 vol%) cermets processed at two of the isotherms in Fig. 2. After processing in vacuum for only 2 min at 1200°C, wetting conditions ($\theta < 90^\circ$) allow for strong interfacial bonding between boron carbide and aluminum. This is evident because the ceramic grain has cleaved, followed by ductile tearing of the surrounding aluminum matrix. Processing in vacuum at 900°C for 2 min shows a completely different fracture morphology. Under these processing conditions ($\theta > 90^\circ$), strong chemical

bond is not occurring at ceramic-metal interface due to the lack of wetting. This results in failure of the metal matrix alone, since the boron carbide grains can now be torn away from their sites.

Figure 2 indicates that the processing atmosphere also alters wetting behavior. For example, the same cermet processed at 1200°C in flowing argon exhibits fracture behavior similar to that of Fig. 3(B).

Metallographic investigation of sectioned contact-angle studies indicates that liquid aluminum becomes partially saturated with boron carbide, and that various interfacial reaction products form at the solid-liquid interface. Depending on the processing isotherm, a considerable amount of time may be required for the aluminum to completely react with boron carbide and other interfacial products. This implies that if full densification can be achieved prior to the possible depletion of aluminum, it should be possible to achieve stable room-temperature microstructures by "freezing in" nonequilibrium conditions during processing.

Microscale Conditions

Figure 4 shows the B-C-Al ternary with most of the possible compounds that can be formed. Not all of these compounds are present simultaneously and, as shown in Table I, results indicate that only eight have been observed in microstructures processed between 800°-1300°C. These compounds govern the composition of phases that occur in B₄C-Al cermets.

The compounds Al₂C₂, Al₃B₄C₂ (β-AlB₁₂), and the solid solution AlB_{1.3}C₄ are high-temperature forms that are not thermodynamically possible at the processing temperatures of this study. Other forms of boron carbide, e.g., B₂C, that exist outside the B-C homogeneity range (9 to 20 at % carbon) were not observed. The compounds AlB₁₀ and AlB_{2.4}C₄ are polymorphic and are not distinguishable by X-ray diffraction;⁹ however, previous investigations^{9,10} indicate that when carbon is present, the latter form generally occurs. This is consistent with the combined X-ray diffraction and electron microprobe results of this study.

The appearance of an aluminum-rich unidentified phase also occurs in B₄C-Al cermets and is located in the proximity of the shade region of Fig. 4. Attempts to identify phase X were unsuccessful because its X-ray diffraction pattern did not match any binary Al_xB_y, Al_xC_y, B_xC_y, ternary Al_xB_yC_z, binary or ternary oxide, oxycarbide, or XDRF patterns. Computer programs¹¹ were employed to identify its structure, but no prototype seems to exist.¹² Preliminary results indicate that phase X may be a new isotype.

Attempts to process B₄C-Al cermets (with metal content: form 15 to 48 vol%) to equilibrium conditions were unsuccessful. X-ray diffraction studies show that for any particular starting composition, the reaction products always result in the depletion of aluminum.

With this understanding, it is now possible to go back to the reaction thermodynamic model of Fig. 1 and determine how B₄C-Al cermets fit the established requirements. The model suggests that a low vol% metal phase be maintained in the final microstructure. In a nonreactive, yet wetting, B₄C-metal system, the initial amount of metal phase will generally remain constant unless it is removed by some external forces, e.g., extrusion from high applied pressure or by evaporation. The reactive

B_4C -Al system, on the other hand, can have starting compositions above the broken line if (1) reaction kinetics are sluggish enough to allow only local equilibrium between any three adjacent phases, and (2) the reaction products result in a microstructure with a low vol% metal phase.

Different microstructures were characterized using X-ray diffraction and electron microprobe. Table I presents the results for cermets processed at an initial temperature sufficiently high enough to allow for a rapid decrease in contact angle, and then subsequently heat treated at different isotherms. Table I shows the local equilibrium phases that are possible in these cermets, and it gives a qualitative analysis of the reaction kinetics. Using Table I and Fig. 4, the reaction thermodynamic criterion is now considered.

Figure 5 shows the microstructures of a "low-temperature" (800°C) processed cermet and a "high-temperature" (1300°C) processed cermet. As indicated in Table I, B_4C -Al cermets offer "tailorable" microstructures through process control. In the 800°C microstructure, phase X and AlB_2 are the major phases that form. Phase X is in local equilibrium with aluminum and AlB_2 , and with AlB_2 and $\alpha-AlB_{12}$. In the 1300°C microstructure, the tendency is for $AlB_{23}C_4$ to form as the major phase. Local equilibrium in the matrix occurs between phase X, aluminum, and Al_4C_7 . Phase X is a metastable phase that will begin to decrease only when all the aluminum is depleted from the system.

Table II suggests that controlled microstructures can lead to cermets with various mechanical properties. Since it is possible to achieve good interfacial bonding in cermets processed between 800°C and 1300°C by initially applying the appropriate capillarity thermodynamic conditions, further property enhancement must occur through heat treatment and applications of the reaction thermodynamics required to obtain a desired matrix.

In another publication, we present a more detailed account of the processing mechanisms that occur in B_4C -Al cermets.¹³ This publication discusses how reactive-liquid-sintering kinetics play a major role in the distribution of these phases. Without a uniformly dispersed starting composition, however, kinetics will not allow the system to reach full density. Future studies, therefore, will attempt to achieve homogeneous distributions in high-density green bodies through colloidal consolidation.¹⁴

Conclusions

Hard, yet potentially tough, lightweight B_4C -Al cermets have been manufactured by applying fundamental thermodynamic guidelines as processing principles.

In these cermets, sintering occurs through the formation of a reactive-liquid-metal phase when in contact with the solid-ceramic phase. Nonequilibrium wetting conditions occur due to chemical reactions at the boron carbide-aluminum interface. These reactions cause a dynamic state in the surface energies of the system, which lower the free energy and result in the spreading of the molten metal phase.

Interfacial bonding is required so the characteristics of individual phases contribute to the properties of the composite as a whole. Guidelines for cermet systems can be established based on contact angle data

that imply these interfacial reactions. Chemical reactions result in individual phases with unique properties that allow for "tailorable" microstructures. These reactions in turn control the evolving microstructure.

The unique properties associated with the individual phases occurring in B_4C -Al cermets illustrate that many "tailorable" microstructures are possible.

Acknowledgements

This work was supported in parts by the U.S. Department of Energy by the Lawrence Livermore National Laboratory under Contract No. W-7405-Eng-48 while the authors were at the Department of Materials Science of Engineering at UCLA, and also by the Advanced Research Projects Agency of the Department of Defense, and was monitored by the Air Force Office of Scientific Research under Grant No. AFOSR-83-0375 at the University of Washington.

References

- ¹D. C. Halverson, Development of Boron Carbide Aluminum Cermets, M.Sc. Thesis, University of California, Los Angeles (1983).
- ²M. L. Wilkins, C. F. Cline, and C. A. Honodel, Light Armor, Lawrence Livermore National Laboratory, Livermore, CA, UCRL-71817 (1969).
- ³J. E. Smugeresky, H. J. Rack, and G. B. Basell, Development of a Non-Volatile Boron Carbide Copper Cermet Neutron Shield for High Performance Shipping Casks, Sandia National Laboratories, Albuquerque, NM, U.S. D.O.E. Contract No. DE-AC04-76-DP00789 (1981).
- ⁴I. A. Aksay, C. E. Hoge, and J. A. Pask, "Wetting under Chemical Equilibrium and Nonequilibrium Conditions," *J. Phys. Chem.*, **78** (12) 1178-83 (1974).
- ⁵R. Kieffer, "Theoretical Aspects of Sintering of Carbides," pp. 282-88 in *Physics of Powder Metallurgy*, Ed. by W. E. Kingston, McGraw-Hill, New York, 1951.
- ⁶J. W. Gibbs, pp. 314 in *Scientific Papers of J. W. Gibbs*, Vol. 1, Dover Publications, New York, 1961.
- ⁷R. E. Johnson, Jr., "Conflicts Between Gibbsian Thermodynamics and Recent Treatments of Interfacial Energies in Solid-Liquid-Vapor Systems," *J. Phys. Chem.*, **63**, 1655 (1959).
- ⁸T. Young, *Phil. Trans. Roy. Soc. London*, **95**, 65 (1805).
- ⁹G. Will, "On the Existence of AlB_{10} , A Critical Review of the Crystal Structures of AlB_{10} and C_2AlB_{10} ," *Electron Technol.*, **3** (1-2) 119-26 (1970).
- ¹⁰V. I. Matkovich, J. Economy, and R. F. Giese, Jr., "Presence of Carbon in Aluminum Borides," *J. Am. Chem. Soc.*, **86** (12) 2377-40 (1964).
- ¹¹P. E. D. Morgan, Rockwell Science Center, Thousand Oaks, CA, unpublished computer program.
- ¹²J. D. H. Donnay and H. M. Ondik, *Crystal Data*, Vol. 2, Inorganic Compounds, 3rd ed., U.S. Dept. of Commerce National Bureau of Standards, 1973.
- ¹³D. C. Halverson, A. J. Pyzik, I. A. Aksay, and W. F. Snowden, "Processing of Boron Carbide-Aluminum Composites," to be submitted to the *J. Am. Ceram. Soc.*, 1985.
- ¹⁴Ongoing work at Lawrence Livermore National Laboratory under U.S. D.O.E. Contract No. W-7405-ENG-48.

Table I. Phase Behavior, after Capillarity Thermodynamic Criteria Have Been Met, for Subsequent Heat Treatment at Different Isotherms

Temp (°C)	800	900	1000	1100	1200	1300
Phase	Behavior with increasing time					
Al	always decrease					
B ₄ C	always decrease					
X	increase		con- stant		decrease	
AIB ₂	increase					
α-AIB ₁₂	constant					
Al ₄ C ₃	increase					
AIB ₁₂ C ₂	in- crease	constant			decrease	
AIB ₂₄ C ₄					increase	

Table II. Microhardness and Density Data for Phases Obtainable in B₄C-Al cermets. (From Various Sources in the Literature: Table is Meant to be Illustrative Only.)

Phase	Microhardness (kg/mm ²)	Density (g/cm ³)
B ₄ C	2750 - 4950	2.52
AIB ₂	980	3.16
α-AIB ₁₂	2600	2.56
AIB ₂₄ C ₄ (AIB ₁₀)	2530 - 2650	2.54
AIB ₁₂ C ₂	-	2.63
Al ₄ C ₃	-	2.93
Al	19	2.70
Al-C(1w/o)	47	2.70
Al-C(2w/o)	65	2.70
Al-C(3w/o)	91	2.70

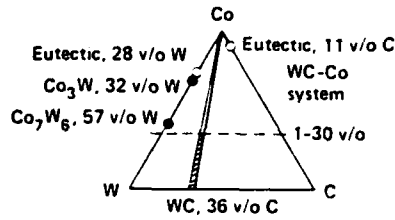


Fig. 1. The W-C-Co system.

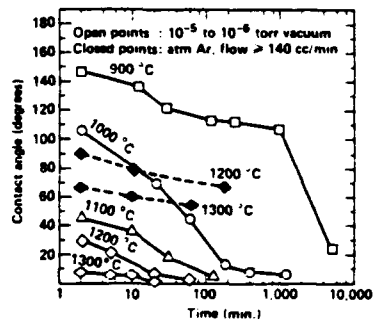


Fig. 2. Contact angle of molten Al on B_4C as a function of processing time for various isotherms and environments.

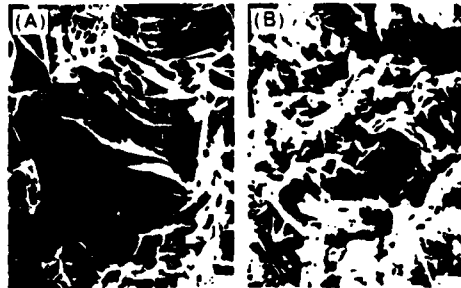


Fig. 3. B_4C -Al (36.4 vol%) cermet sintered in vacuum for 2 min at (A) 1200°C and (B) 900°C.

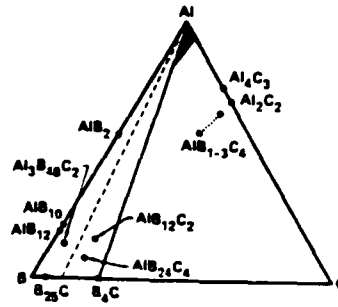


Fig. 4. B-C-Al ternary phase diagram showing most of the crystalline phases that can occur. The triangle formed by the dashed line and the B_4C -Al initial composition line corresponds to a hypothetical extension of the boron carbide solubility range.

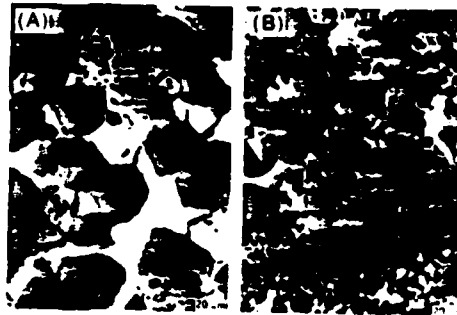


Fig. 5. B_4C -Al cermets showing different phases obtainable after vacuum heat treatment at (A) $800^\circ C$ for 24 h and (B) $1300^\circ C$ for 1 hr.

ANNALS OF THE ENTOMOLOGICAL SOCIETY OF AMERICA

VOLUME 58, PART 1, FEBRUARY 1967

NUMBER 1, FEBRUARY 1967

Processing of Boron Carbide-Aluminum Composites*

D. C. Halverson
Lawrence Livermore National Laboratory
University of California
Livermore, CA 94550

A. J. Pyzik and I. A. Aksay
Department of Materials Science and Engineering
University of Washington
Seattle, WA 98195

W. E. Snowden
Lawrence Livermore National Laboratory
University of California
Livermore, CA 94550

Abstract

The processing problems associated with boron carbide and the limitations of its mechanical properties can be significantly reduced when a metal phase (e.g., aluminum) is added. Lower densification temperatures and higher fracture toughness will result. Based on fundamental capillarity thermodynamics, reaction thermodynamics, and densification kinetics, we have established reliable criteria for fabricating B₄C-Al particulate composites. Because chemical reactions cannot be eliminated, it is necessary to process B₄C-Al by rapidly heating to near 1200°C (to ensure wetting) and then subsequently heat treating below 1200°C (for microstructural development).

Introduction

Boron carbide (B₄C)¹ is a very hard (9.5⁺ in Mohs scale),¹ low specific gravity (2.52), covalent ceramic that offers distinct advantages for applications involving neutron absorption, wear resistance, and impact resistance. The extreme sensitivity of boron carbide to brittle fracture ($K_{Ic} = 3.7 \text{ MPa m}^{1/2}$)² and the difficulties associated with fabricating fully dense microstructures are serious limitations, however. By using certain additives (e.g., graphite), B₄C sintered at high temperatures (>2000°C) can produce microstructures with a high density (~98.2% of theoretical density).³ Full density is usually achieved through costly hot-pressing techniques¹; however, even in a fully dense form, boron carbide's sensitivity to brittle fracture remains a major limitation.

Our experiments demonstrated that the processing problems and mechanical property limitations associated with B₄C ceramics can be significantly reduced by introducing a metal phase (i.e., by developing B₄C cermets). If the application is limited to low temperatures, then a low-melting-point metal phase (e.g., aluminum or aluminum alloys) can be introduced to obtain lower densification temperatures (<1200°C) and to increase fracture toughness many times that of B₄C. In addition, if the metal phase has a low specific gravity, then the resulting cermet can have improved mechanical properties with low weight.

High-strength (>1000 MPa) B-C-Al composites consisting of B₄C-coated boron fibers in an aluminum matrix (~50 vol% ceramic) have been fabricated.³ Particulate B₄C-metal composites currently manufactured include ma-

*B₄C herein refers to the complete homogeneous range of compositions for boron carbide.

*Work performed under the auspices of the U.S. Department of Energy by Lawrence Livermore National Laboratory under contract No. W-7504-ENG-48 and by the Air Force Office of Scientific Research under Grant No. AFOSR-83-0175 at the University of Washington.

materials consisting of dispersion-hardened metals (≤ 25 vol% B_4C),^{1,4} Boral (30–50 vol% B_4C),⁷ and B_4C -Cu cermets (~ 60 vol% B_4C).⁸ In these composites, processing temperatures are kept to a minimum ($< 1000^\circ C$) primarily to avoid chemical reactions between B_4C and the metal phase.

In our work with particulate B_4C -Al composites, which have a greater ceramic content (> 55 vol%), we employed processing temperatures above $1000^\circ C$ to promote wetting and to permit carefully controlled reactions in the system. Wetting is necessary to achieve strong interfacial bonding and to allow liquid rearrangement during sintering. If wetting does not occur, external pressure must be applied to improve consolidation; however, even pressure techniques are not satisfactory for densification of some high ceramic-containing (> 60 vol%) composites.⁹

We illustrate the importance of achieving a wetting condition in the processing of high ceramic-content (> 55 vol%) particulate-based B_4C -Al composites, the importance of understanding the phase equilibria in the B -C-Al system for the microstructural design of these cermets, and appropriate processing methods for producing cermets with negligible porosity.

Processing Experiments

Materials and Specimen Preparation

We used sessile drops formed from high-purity aluminum shot (99.999% pure), hot-pressed B_4C substrates made from commercial grade B_4C powders, and B_4C -Al compacts made from commercial grade B_4C and aluminum powders.

To prepare these compacts, we mixed B_4C powder (three particle-size distributions with median sizes of 4, 10, and 50 μm , ESK) and aluminum powder (-325 mesh, Alfa Products) in isopropyl alcohol, ultrasonically mixed the slurry to achieve homogeneity, and consolidated the solids by filtration in a plaster-of-Paris mold. These compacts were too weak for handling purposes; therefore, the composite powders were subsequently cold pressed at 138 MPa ($\sim 20,000$ psi). We found that higher pressures resulted in undesirable striations in the compacts.

Procedures

Our processing experiments included contact angle measurements, chemical reaction

studies, and densification studies in the molten aluminum + B_4C system.

In conducting our contact angles experiments, we placed aluminum sessile drops on hot-pressed B_4C substrates (polished to a 1- μm finish) and heated them in a tungsten-mesh resistance-heated vacuum furnace at pressures less than 5×10^{-3} Pa but greater than 10^{-4} Pa (typically between 10^{-3} and 10^{-6} Torr). After the specimens were vacuum cooled to room temperature and taken out of the furnace, we measured the contact angles to within 1° using a protractor grid and optical $10 \times$ telemicroscope.

To investigate the nature and extent of chemical reactions at the B_4C -Al interface, we examined polished (1- μm finish) cross sections of specimens from the wetting experiments using both optical and scanning electron microscopes. Further studies included x-ray diffraction, energy dispersive spectroscopy, and electron microprobe analyses to identify the reaction products in the microstructures of the sintered compacts.

In our densification kinetics studies, we subjected the B_4C -Al powder compacts to pressureless sintering, hot pressing, and hot-isostatic pressing (HIP). We sintered specimens in the tungsten-mesh resistance-heated vacuum furnace at the same pressures used in the sessile-drop experiments. Hot pressing and HIP were performed in accordance with the processing information in Tables 1 and 2. To determine the level of residual porosity, we made immersion density (Dow Corning 200, 2.0 centistokes) and bulk density measurements on each compact.

Results and Discussion

Wetting

An important point to be realized is that a nonwetting system can be transformed to a wetting system by taking advantage of chemical reactions.¹ Previous studies on the B_4C -Al system did not correctly recognize this fact, and as a result, both obtuse^{10,11} and acute^{11,14} contact angles were reported as equilibrium values. Previous works^{10,13} on B_4C -Al composites were discontinued when it was concluded that aluminum did not wet boron carbide.

Figure 1 shows the contact angle of aluminum on boron carbide as a function of temperature and time. Based on our contact angle data, processing of B_4C -Al composites below $1000^\circ C$ cannot be accomplished by

pressureless sintering techniques since acute contact angles are not obtained in reasonably short times. By increasing the temperature, low contact angles are obtained in reasonably short times; however, because the vapor pressure of aluminum also increases with increasing temperature, an upper processing temperature limit is also necessary to keep vaporation of the aluminum to a minimum.

The dynamic nature of the contact angle of aluminum on boron carbide is associated with the mass transfer across the solid-liquid interface as the system moves towards a state of chemical equilibrium. During this dynamic stage the contact angle cannot be expected to remain constant since the interfacial tensions between the solid, liquid, and vapor phases will be continuously changing as a result of compositional and structural variations across the interfaces. The nature of these reactions will be discussed in the next section.

Reaction Thermodynamics

At least 9 ternary phases have been reported for the B-C-Al system,¹⁶⁻²⁸ consequently, it is important to select processing conditions that will allow only certain reaction products to form so desired properties (negligible Al_3C_2) will be obtained. Previous attempts³ to fabricate B_4C -Al cermets were discontinued when it was concluded that the reaction products were detrimental to mechanical properties.

We investigated the reaction products that occur under different sets of wetting conditions. Figure 2 illustrates the results of our reaction thermodynamic studies from 800° to 1400°C and the reaction products that form when local equilibrium conditions are achieved. Under these conditions, sufficient aluminum is present to sustain the reactions shown. For any starting composition, the initial reaction products will always form at the expense of B_4C and aluminum.

Figure 3 shows some of the characteristic microstructures that can be obtained under conditions of local equilibrium. An unidentified phase, called Phase X, forms at all of the temperatures in this study. Phase X can coexist with B_4C . Initial attempts to identify Phase X were unsuccessful because its x-ray diffraction pattern did not match any binary Al_3B_2 , Al_3C_2 , B_4C , ternary $Al_3B_2C_2$, binary or ternary oxide, nitride, oxycarbide, oxynitride, or carbonitride

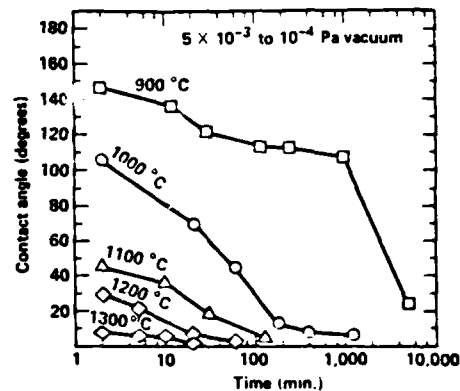


Figure 1. Contact angle of molten aluminum on boron carbide as a function of processing time for various isotherms at 5×10^{-3} to 10^{-4} Pa. Measurements were obtained after sessile drop was turned cooled to room temperature.

XRDF patterns.³⁰ Some of the characteristic x-ray diffraction lines for Phase X have been recently reported,³¹ and energy dispersive x-ray and electron microprobe analyses indicate that Phase X is largely aluminum with smaller amounts of boron and carbon.

In a recent study, Sarikaya and Aksav³² characterized the crystal structure and composition of Phase X by transmission electron microscopy techniques. Electron diffraction studies indicate that the crystal structure of Phase X is HCP with lattice parameters quite different from any of the other binary or ternary phases in the B-C-Al system. Their preliminary studies by electron energy loss spectroscopy indicate that the composition of Phase X corresponds to 75%Al-10%B-15%C.

Boron carbide and aluminum react to form Phase X. Under local equilibrium between 800° and 900°C, AlB_2 and Phase X are the major reaction products. Under these conditions Phase X is stable, and it will decompose only after all of the free aluminum is depleted from the system. Above 1100°C there is less Phase X because aluminum is rapidly being depleted through the formation of other more thermodynamically stable phases.

Figure 3(a) shows a typical microstructure in local equilibrium at the 800° to 900°C range. Small grains (1-5 μm) of B_4C are surrounded by

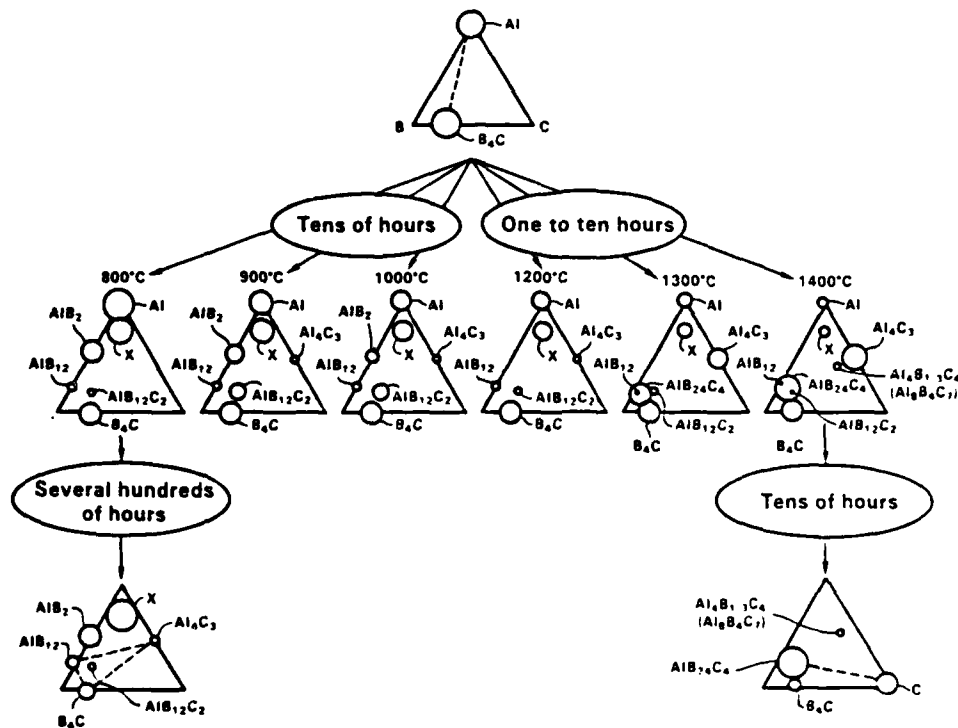


Figure 2. Thermodynamic-reaction-series map for B_2C -Al composites initially densified at $1180^\circ C$ and heat treated under various isothermal conditions between 800° and $1400^\circ C$.



Figure 3. Boron carbide-aluminum cermets showing different sintered microstructures obtained after initially heating to $1180^\circ C$ for 2 min, then subsequently heat treating at (a) $800^\circ C$ for 24 h (initial composition: 80vol% B_2C -20vol%Al); (b) $1000^\circ C$ for 1.5 h (initial composition: 70vol% B_2C -30vol%Al); and (c) $1300^\circ C$ for 1 h (initial composition: 30vol% B_2C -70vol%Al).

large, forming ceramic phases. After 24 h of heat treatment at 800°C [Fig. 3(a)], there is more Phase X and AlB_2 than B_4C (initial composition: 80vol% B_4C -20vol%Al). This microstructure reaches local equilibrium between Phase X, AlB_2 , and B_4C within tens of hours at 800°C. After 250 h some AlB_2 has decreased to form AlB_{12} ; after 500 h B_4C , Phase X, AlB_2 , AlB_{12} , $AlB_{12}C_2$, and Al_4C_3 are substantially present in the microstructure. Further heat treatment indicates a tendency to the rapid depletion of Phase X and an increase of AlB_{12} and Al_4C_3 .

The hypothetical compatibility triangle shown in the lower left-hand corner of Fig. 2 illustrates the tendency towards overall thermodynamic equilibrium. It is assumed that overall equilibrium is achieved when AlB_{12} , Al_4C_3 , and B_4C coexist as stable phases.

Above 900°C but below 1200°C the following microstructural differences occur: (1) $AlB_{12}C_2$ is thermodynamically favored over AlB_{12} between 900° and 1000°C, and (2) AlB_2 continues to form up to 1000°C, however, above 1000°C AlB_2 is only present when the microstructure is cooled. Figure 3(b) shows a microstructure resulting from these local equilibrium conditions after 15 h at 1000°C (initial composition: 70vol% B_4C -30vol%Al).

Between 1200° and 1400°C further changes in the microstructure occur: (1) Al_4C_3 is forming very quickly (this is associated with a decrease of the ternary Phase X), (2) $AlB_{12}C_4$ is now favored over $AlB_{12}C_2$ and becomes the major ternary phase, (3) above 1300°C x-ray diffraction patterns indicate the appearance of a phase previously reported as $Al_3B_{11}C_4$ ^{Ref. 17} but more recently reported as $Al_3B_4C_7$ ^{Ref. 28} and (4) at 1400°C Al_4C_3 begins to crystallize in the shape of short whiskers. Figure 3(c) shows a microstructure characteristic of the local equilibrium conditions after 1 h at 1300°C (initial composition: 30vol% B_4C -70vol%Al).

At temperatures above 1300°C overall equilibrium occurs only after all aluminum and Phase X are completely depleted from the system. This is followed by the decomposition of Al_4C_3 and the eventual coexistence of graphite, B_4C , and $AlB_{12}C_4$ as the remaining stable phases. The compatibility triangle in the lower right-hand corner of Fig. 2 illustrates this global equilibrium condition.

Our reaction thermodynamic study determined that local equilibrium conditions between 800° and 1200°C must be established so

that Phase X will evolve and consequently tie-up most of the free carbon required to form Al_4C_3 . Because of its hygroscopic nature and poor mechanical properties, Al_4C_3 is undesirable. Above 1200°C local equilibrium conditions do not suppress Al_4C_3 formation; however, composites with Al_4C_3 whiskers are more chemically stable because of a protective layer of Phase X around them. Therefore, to process B_4C -Al cermets it is necessary to rapidly heat the composition to near 1200°C to ensure that wetting occurs and then subsequently heat treat these compositions at temperatures below 1200°C if further microstructural development is desired.

Densification Kinetics

Fully dense states can be achieved prior to reaching desired thermodynamic conditions either by slowing down reaction kinetics or by speeding up densification kinetics. Favorable results can be obtained by employing small-size powders; however, in our study the larger B_4C powders (56 μm) were primarily used for two reasons. First, because appropriate colloidal processing techniques for codispersing boron carbide and aluminum powders had not yet been developed, the 4- and 10- μm B_4C powders resulted in large agglomerates (250 μm) which led to microstructural inhomogeneities during sintering. Secondly, we wanted to show that B_4C -Al composites could be fabricated without agglomeration problems and at the same time reduce the rate of chemical reactions by decreasing the B_4C -Al interfacial area.

Boron carbide-aluminum compacts will neither undergo pressureless nor pressure-assisted densification unless wetting occurs. Our pressureless sintered compacts always had residual porosity ranging from 28 vol% (for compacts containing 30-45 vol% aluminum) to as high as 44 vol% (for compacts containing 15-30 vol% aluminum). This occurred despite the fact that conditions for wetting were obtained; however, compacts with larger B_4C particles (56 μm) did achieve higher densities than compacts with smaller B_4C particles (4 and 10 μm). Even when pressure techniques (vacuum hot pressing and HIP) were applied to compacts containing between 15 vol% and 60 vol% aluminum, porosity was not completely eliminated, although it was significantly reduced.

High levels of porosity in the pressureless sintered compacts occurred because (1) at tem-

Table 1. Vacuum-hot pressed B₄C-Al densification results. All runs took 75 min to reach maximum temperature. Maximum temperature hold time was 6 min at the indicated pressure with pressure being applied after passing through 800°C. Processing environment was $\sim 5 \times 10^{-2}$ Pa (10^{-3} to 10^{-4} Torr). Samples were furnace cooled in vacuum under the indicated pressure. Porosity was determined by bulk density measurements.

Aluminum content (vol%)	B ₄ C grain size (μm)	Maximum temp (°C)	Indicated pressure (MPa)	Residual compact porosity (vol%)
30	<2	1180	15	24
50	<2	1160	15	8
50	<2	1050	20	14
50	<20	1150	15	22
60	<20	1100	15	13

peratures required for densification (wetting), chemical reaction rates are faster than the spreading rates for aluminum, and (2) at these temperatures the vapor pressure for aluminum is higher than that of the vacuum-processing environment employed. Both of these mechanisms result in the depletion of aluminum. The formation of new phases (reaction kinetics), however, has the most detrimental effect. When enough reaction products have formed, the microstructure becomes "locked up" prohibiting further rearrangement. This combined with the fact that there is an insufficient amount of molten aluminum to fill the remaining pores results in high-porosity final products.

Table 1 shows the results of the vacuum-hot-pressed compacts. These results indicate that increasing the aluminum content does reduce the amount of porosity in the cermet. Also, increasing the pressure (while lowering the hot-pressing temperature to slow down the depletion of aluminum) reduced but did not eliminate porosity completely.

Densification by hot pressing is inhibited by mechanisms other than just the competition between phase formation and the capillary flow of molten aluminum. Figure 4 shows regions where local densification is obtained by satisfying the capillarity-thermodynamic criterion of low contact angles, while grossly porous regions are sporadically located adjacent to these dense regions.

Axial forces applied to powders during vacuum-hot pressing in a graphite die result in radial forces on the compact. The magnitude of these radial forces is largely dependent on the plasticity of the powders, and always results in stress-concentration gradients within the compact.¹² When B₄C grains are forced to bridge or lock tightly in regions of high-stress concentra-

tions, liquid rearrangement by capillary action will be hindered. This will allow for local densification where rearrangement is possible (low-stress concentration areas within the compact) resulting in aluminum-depleted regions where bridging is the strongest.

Since we desired to achieve densification without depleting aluminum and also avoid the previously described mechanisms inhibiting uniform rearrangement, we hot-isostatically pressed presintered compacts. (The presintered compacts were sealed under vacuum in stainless steel cans.)

Table 2 shows the results of the hot-isostatically pressed compacts. Even with HIP, however, the results indicate that a minimum amount of aluminum is required to reduce porosity to negligible levels (≤ 1.0 vol%). Hot-isostatically pressed presintered compacts had connected porosities ≤ 3.5 vol% while nonpresintered (nonwetted) compacts had porosities in excess of 10 vol%. As aluminum content was increased above 30 vol%, connected porosities dropped to below 1 vol%. A hot-isostatically pressed microstructure is shown in Fig. 5. The microstructure confirms that the uniform application of pressure resulted in (1) accelerating the densification kinetics faster than the chemical reaction kinetics and (2) the elimination of stress-induced microstructural inhomogeneities.

Our study has shown that certain processing tradeoffs must be considered to produce B₄C-Al composites. Table 3 summarizes these tradeoffs.

Conclusion

Based on fundamental capillarity thermodynamics, reaction thermodynamics, and densification kinetics, definite processing criteria

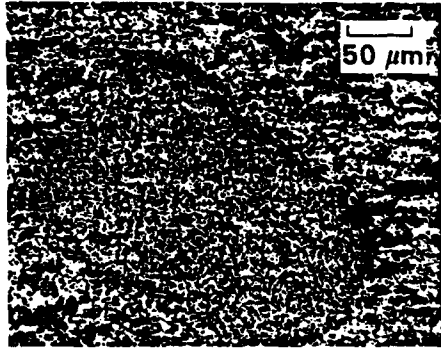


Figure 4. Boron carbide-aluminum (30 vol%) cermet hot pressed at 1180°C in vacuum (5×10^{-2} Pa) for 6 min at 15 MPa ($\sim 2,000$ psi) showing a region of local densification surrounded by porous regions.



Figure 5. Boron carbide-aluminum (30 vol%) cermet initially sintered at 1180°C for 2 min in vacuum (10^{-3} Pa), then subsequently hot-isostatically pressed at 1000°C for 30 min at 207 MPa ($\sim 30,000$ psi) argon. Note improvement in uniformity compared to Fig. 4.

Table 2. Hot-isostatic pressed B₄C-Al densification results. All samples were run at the maximum temperature with a 30-min hold at 207 MPa argon. Heating and cooling rates of 50°C/min were used at 207 MPa. Porosity was determined by immersion density measurements after 5 min.

Aluminum content (vol%)	B ₄ C av. grain size (μm)	Maximum temp (°C)	Sample presintered 1180°C/2 min/ $\sim 10^{-3}$ Pa	Residual connected porosity (vol%)
15	55	1000	Yes	3.50
30	55	1000	Yes	0.11
45	55	1000	Yes	0.04
30	4	750	No	>10

Table 3. Processing tradeoffs for B₄C-Al cermets.

Processing tradeoff	Parameters that control tradeoff	Effect of tradeoff on reactive-liquid sintering mechanism	Optimum processing
Wetting vs evaporation	High temp vs low temp	Depletion of liquid aluminum by evaporation	Use high temperatures for short times
Chemical reaction vs densification	Short time vs long time	Chemical reaction kinetics faster than densification kinetics results in inhibiting rearrangement and depletion of aluminum due to new phase formation	Speed up densification rate by applying pressure and/or slow down chemical reaction rate by increasing B ₄ C grain size
Axial pressure vs isostatic pressure	Hot pressing vs HIP	Stress gradients inhibit rearrangement	HIP presintered compacts

have been established for obtaining B_4C -Al composites. In these materials, chemical reactions occur between 800° and 1400°C. These interfacial reactions are the driving force for the wetting of boron carbide by molten aluminum. Because the chemical reactions cannot be eliminated, it is necessary to process B_4C -Al by rapidly heating to near 1200°C (to ensure wetting) and then subsequently heat treating below 1200°C (for microstructural development).

Densification is inhibited because chemical reactions occur faster than capillarity-induced liquid rearrangement. Therefore, it is necessary to apply pressure to accelerate densification faster than the kinetics of phase formation, which is the major hindrance to rearrangement during pressureless sintering. To ensure microstructural homogeneity, it is also necessary to apply this pressure in a uniform manner by hot-isostatic pressing presintered compacts.

References

1. A. Lipp, "Boron Carbide: Production, Properties, Applications," *Technische Rundschau* **14**, 28, 33 (1965); 7 (1966).
2. G. DeWith, "High-Temperature Fracture of Boron Carbide: Experiments and Simple Theoretical Models," *J. Mat. Sci.* **19**, 457-466 (1984).
3. S. Prochazka and S. L. Dole, *Development of Spacecraft Materials and Structures Fundamentals*, General Electric Company Corporate Research and Development, Schenectady, NY, Report No. SRD-85-021 (1985).
4. M. Beauvy and R. Angers, "Mechanisms of Hot Pressing of Boron Carbide Powders," in *Science of Ceramics*, Vol. 10, pp. 279-286 (1980).
5. J. A. Cornie, R. Suplinskas, and A. Hauze, "Boron-Aluminum Composites," *Proceedings of Advanced Fibers and Composites for Elevated Temperatures*, I. Ahmad, B. R. Noton, Eds. (The Metallurgical Society of AIME, Warrendale, PA, 1980), p. 28.
6. S. D. Karmarkar and A. P. Divecha, *Fabrication and Properties of Boron Carbide-Reinforced Aluminum Composites*, Naval Surface Weapons Center, Dahlgren, VA, NSWC TR 84-160.
7. P. R. Roy and C. Ganguly, "Dispersion Type Composites for Nuclear Reactors," in *Sintered Metal-Ceramic Composites*, G. S. Upadhaya, Ed. (Elsevier Science Publishers B. V., Amsterdam, 1984), pp. 159-179.
8. J. E. Smugeresky, H. J. Rack, and G. B. Brasell, *Development of a Non-Volatile Boron Carbide Copper Cermet Neutron Shield for High Performance Shipping Casks*, Sandia National Laboratories, Albuquerque, NM, SAND-80-0802C (1981).
9. I. A. Aksay, C. E. Hoge, and J. A. Pask, "Wetting under Chemical Equilibrium and Nonequilibrium Conditions," *J. Phys. Chem.* **78**, 1178-1183 (1974).
10. C. R. Manning and T. B. Gurganus, "Wetting of Binary Aluminum Alloys in Contact with B_4C , and Graphite," *J. Am. Ceram. Soc.* **52** [3], 115-118 (1969).
11. A. D. Panasyuk and T.V. Dubovik, "Wetting of Boron Carbide System Samples with Molten Metals," *Dielektriki (Dielektriki Polyprovodn)* **2**, 120-125 (in Russian) (1972).
12. G. A. Kolesnichenko, "Wettability of Refractory Covalent Crystals by Metallic Melts," *Smachivaemost i Poverkhnostnye Svoistva Rasplov Tverdykh Tel*, 71-74 (in Russian) (1972).
13. A. D. Panasyuk, V. D. Oreshkin, and V. R. Maslennikova, "Kinetics of the Reactions of Boron Carbide with Liquid Aluminum, Silicon, Nickel, and Iron," *Soviet Powder Metallurgy and Metal Ceramics*, **18** [7], 487-490 (1979).
14. A. D. Panasyuk, V. R. Maslennikova, and E. V. Marek, "Reactions of Materials of the B_4C -Cr System with Liquid Metals," *Soviet Powder Metallurgy and Metal Ceramics* **20** [10], 729-732 (1982).
15. M. W. Lindley and G. E. Gazza, *Some New Potential Ceramic-Metal Armor Materials Fabricated by Liquid Metal in Filtration*, Army Materials and Mechanics Research Center, Watertown, MA, AD-769742 (1973).
16. J. A. Kohn, G. Katz, and A. A. Giardini, " AlB_{10} , a New Phase, and a Critique on Aluminum Borides," *Z. Kristallogr.* **111**, 53-62 (1958).

17. V. I. Matkovich, J. Economy, and R. F. Giese, Jr., "Presence of Carbon in Aluminum Borides," *J. Am. Chem. Soc.* **86**, 2337-2340 (1964).
18. V. I. Matkovich, R. F. Giese, Jr., and J. Economy, "Phases and Twinning in $C_2Al_3B_{48}$ (beta AlB_{12})," *Z. Kristallogr.* **122**, 108-115 (1965).
19. A. Lipp and M. Röder, "Über ein aluminiumhaltiges Borcarbid," *Z. Anorg. Allg. Chem.* **343**, 1-5 (1966); trans. Leo Kanner Associates, Redwood City, CA (1971).
20. R. F. Giese, Jr., J. Economy, and V. I. Matkovich, "Topotactic Transition in C_4AlB_{24} ," *Acta Crystallogr.* **20**, 697-698 (1966).
21. G. Bliznakov, P. Peshev, and T. Niemyski, "On the Preparation of Crystalline Aluminum Borides by a Vapour Deposition Process," *J. Less-Common Metals* **12**, 405-410 (1967).
22. E. L. Muettterties, *The Chemistry of Boron and Its Compounds* (John Wiley & Sons, New York, 1967).
23. G. Will, "Die Kristallstruktur von C_4AlB_{24} ," *Acta Crystallogr.* **B25**, 1219-1222 (1969); trans. "The Crystal Structure of C_4AlB_{24} ," Lawrence Livermore National Laboratory, Livermore, CA, UCRL TRANS-11966 (1984).
24. A. J. Perrotta, W. D. Townes, and J. A. Potenza, "Crystal Structure of $C_4Al_2B_{51}$," *Acta Crystallogr.* **B25**, 1223-1229 (1969).
25. H. Neidhard, R. Mattes, and H. Becher, "Zur Darstellung und Struktur eines aluminiumhaltigen Borcarbids," *Acta Crystallogr.* **B26**, 315-317 (1970); trans. "The Production and Structure of a Boron Carbide Containing Aluminum," Lawrence Livermore National Laboratory, Livermore, CA, UCRL TRANS-11965 (1984).
26. G. Will, "On the Existence of AlB_{10} : A Critical Review of the Crystal Structures of AlB_{10} and C_4AlB_{24} ," *Elektron Technology* **3**, 119-126 (1970).
27. G. V. Samsonov, V. A. Neronov, and L. K. Lamikhov, "The Conditions, Structure, and Some Properties of Phases in the Al-B System," *J. Less-Common Metals* **67**, 291-296 (1979).
28. Z. Inouhe, H. Tanaka, and Y. Inomata, "Synthesis and X-ray Crystallography of Aluminum Boron Carbide, $Al_8B_4C_7$," *J. Mater. Sci.* **15**, 3036-3040 (1980).
29. M. L. Wilkins, C. F. Cline, and C. A. Honodel, *Light Armor*, Lawrence Livermore National Laboratory, Livermore, CA, UCRL-71817 (1969).
30. *Powder Diffraction File: Alphabetical Index Inorganic Phases*, (JCPDS International Centre for Diffraction Data, Swarthmore, PA, 1985).
31. D. C. Halverson, A. J. Pyzik, and I. A. Aksay, *Boron-Carbide-Aluminum and Boron-Carbide-Reactive Metal Cermets*, U. S. Patent 4,605,440 (Aug. 12, 1986).
32. M. Sarikaya and I. A. Aksay, University of Washington, Seattle, WA, private communication (1986).
33. R. A. Thompson, "Mechanics of Powder Pressing: I, II, and III," *Ceramics Bulletin* **60**, 237-251 (1981).

APPENDIX XIX

**Identification of a New Phase in the Al-C-B Ternary
by High Resolution Transmission Microscopy**

(Sarıkaya, Laoui, Milius, and Aksay 1987)

To appear in the Proceedings of the 45th Annual Meeting of
The Electron Microscopy Society of America, GW Bailey, ed.
San Francisco Press (1987).

IDENTIFICATION OF A NEW PHASE IN THE AL-C-B TERNARY BY HIGH RESOLUTION
TRANSMISSION ELECTRON MICROSCOPY

M. Sarikaya, T. Laoui, D. L. Milius, and I. A. Aksay

Department of Materials Science and Engineering, University of Washington,
Seattle, WA 98195

The purpose of this note is to report the identification of a ternary (X1) phase which has been observed as a reaction product during the processing of B₄C-Al composites.¹ These ceramic-metal composites (cermets) have the unique potential for structural applications because of their low density (> 2.6 g/cc) and a desirable combination of mechanical properties.² Guidelines for the processing of B₄C-Al have been successfully established; and now it is possible to produce tailored microstructures with varying amounts of constituent phases.^{1,2}

The samples for the analysis were prepared by the following procedure. First, it was necessary to heat the B₄C powder compacts in excess of 2000°C to attain an interconnected B₄C skeletal structure. Liquid aluminum was then infiltrated into this B₄C network at 1170°C. This procedure resulted in microstructures with a homogeneous distribution of B₄C and Al phases as depicted by the BF/DF pair in Figure 1. Second, a post-heat treatment in the temperature range of 800-1000°C for up to 100 hrs resulted in the formation of the reaction products that included the new ternary phase as well as the other binary (such as AlB₂ and Al₄C₃) and ternary (AlB₁₂C₂) phases which effectively alter the properties of the cermet.^{1,2} The morphological, crystallographical, and compositional identification of this new phase was performed by high resolution TEM imaging, diffraction, and spectroscopy techniques.

Figure 2 presents a BF/DF pair recorded from an area similar to that of Figure 1, in which the new phase has replaced the Al and B₄C regions. Interfaces between the new ternary phase and B₄C are coherent and fairly clean as depicted in the HREM image in Figure 3. The crystal structure was identified to be hexagonal by both electron and X-ray diffraction by using B₄C and Al as internal standards. The lattice parameters a_0 and c_0 were determined to be 3.520 Å and 5.820 Å, respectively ($c_0/a_0 = 1.65$). The compositional analysis was performed by using EELS. Quantitation was achieved both by calculations³ and by using standards, namely B₄C, AlB₂, and Al₄C₃, to calculate k_{B_4C} , k_{Al_2B} , and $k_{Al_4C_3}$, respectively. Figure 4 presents both the raw spectra and the thickness-deconvoluted and background-subtracted spectra. The analysis of EELS data yielded an approximate composition given by Al₄BC.

A combination of TEM techniques was used to determine the crystal structure and composition of a new ternary X1-phase in the Al-B-C ternary system. Studies are presently underway to determine the unit cell structure and the space group of the X1-phase by EELS and CBED techniques.

1. D. C. Halverson, A. J. Pyzik, and I. A. Aksay, *Ceram. Eng. Sci. Proc.*, 6 [7-8] 763 (1985).
2. A. J. Pyzik, I. A. Aksay, and M. Sarikaya, to appear in *Ceramic Microstructures, '86: Role of Interfaces*, J. A. Pask and A. G. Evans (eds.), Plenum, New York, 1988.
3. R. Egerton, *EELS in the Electron Microscope*, Plenum, New York, 1986.
4. This research was supported by the Air Force Office of Scientific Research (AFOSR) and DARPA and was monitored by AFOSR under Grant No. AFOSR-83-0375.

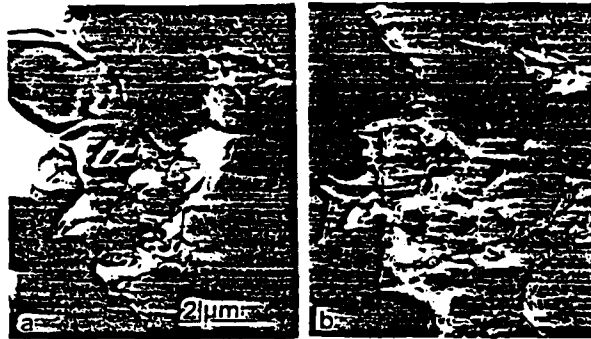


FIG. 1.--BF/DF pair revealing homogeneous distribution of B_4C particles in Al matrix. DF image was recorded by using an Al reflection.



FIG. 2.--BF/DF pair presenting a microstructure where the X1-phase has replaced Al. DF image was taken by using a X1-phase reflection.

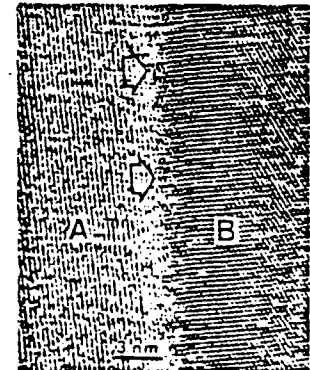


FIG. 3.--HREM image of a B_4C -X1-phase interface; A: X1-phase, and B: B_4C .

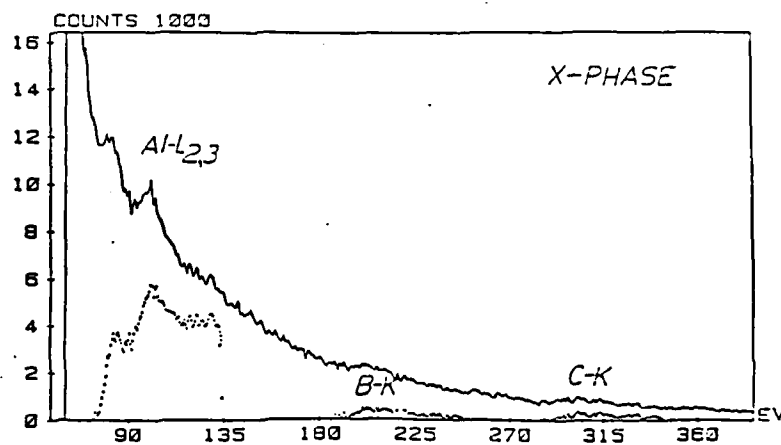


FIG. 4.--An EELS spectrum acquired from an X1-phase region revealing Al-L_{2,3}, B-K, and C-K edges. Deconvoluted and background subtracted spectrum is also shown. (Conditions: foil thickness = 0.73 m.f.p.; $d = 100$ nm; spectrometer entrance aperture = 2.0 mm; collection angle = 100 mrad; acquisition mode: TEM image; serial recording; $E_0 = 100$ kV)

IDENTIFICATION OF A NEW PHASE IN THE AL-C-B TERNARY BY HIGH RESOLUTION TRANSMISSION ELECTRON MICROSCOPY

M. Sarikaya, T. Laoui, D. L. Milius, and I. A. Aksay

Department of Materials Science and Engineering, University of Washington, Seattle, WA 98195

The purpose of this note is to report the identification of a ternary (X1) phase which has been observed as a reaction product during the processing of B₄C-Al composites.¹ These ceramic-metal composites (cermets) have the unique potential for structural applications because of their low density (> 2.6 g/cc) and a desirable combination of mechanical properties.² Guidelines for the processing of B₄C-Al have been successfully established; and now it is possible to produce tailored microstructures with varying amounts of constituent phases.^{1,2}

The samples for the analysis were prepared by the following procedure. First, it was necessary to heat the B₄C powder compacts in excess of 2000°C to attain an interconnected B₄C skeletal structure. Liquid aluminum was then infiltrated into this B₄C network at 1170°C. This procedure resulted in microstructures with a homogeneous distribution of B₄C and Al phases as depicted by the BF/DF pair in Figure 1. Second, a post-heat treatment in the temperature range of 800-1000°C for up to 100 hrs resulted in the formation of the reaction products that included the new ternary phase as well as the other binary (such as AlB₂ and Al₄C₃) and ternary (AlB₂C₂) phases which effectively alter the properties of the cermet.^{1,2} The morphological, crystallographical, and compositional identification of this new phase was performed by high resolution TEM imaging, diffraction, and spectroscopy techniques.

Figure 2 presents a BF/DF pair recorded from an area similar to that of Figure 1, in which the new phase has replaced the Al and B₄C regions. Interfaces between the new ternary phase and B₄C are coherent and fairly clean as depicted in the HREM image in Figure 3. The crystal structure was identified to be hexagonal by both electron and X-ray diffraction by using B₄C and Al as internal standards. The lattice parameters a₀ and c₀ were determined to be 3.520 Å and 5.820 Å, respectively (c₀/a₀ = 1.65). The compositional analysis was performed by using EELS. Quantitation was achieved both by calculations³ and by using standards, namely B₄C, AlB₂, and Al₄C₃, to calculate k_{B,C}, k_{Al,B}, and k_{Al,C}, respectively. Figure 4 presents both the raw spectra and the thickness-deconvoluted and background-subtracted spectra. The analysis of EELS data yielded an approximate composition given by Al₄BC.

A combination of TEM techniques was used to determine the crystal structure and composition of a new ternary X1-phase in the Al-B-C ternary system. Studies are presently underway to determine the unit cell structure and the space group of the X1-phase by EELS and CBED techniques.

1. D. C. Halverson, A. J. Pyzik, and I. A. Aksay, *Ceram. Eng. Sci. Proc.*, 6 [7-8] 763 (1985).
2. A. J. Pyzik, I. A. Aksay, and M. Sarikaya, to appear in *Ceramic Microstructures, '86: Role of Interfaces*, J. A. Pask and A. G. Evans (eds.), Plenum, New York, 1988.
3. R. Egerton, *EELS in the Electron Microscope*, Plenum, New York, 1986.
4. This research was supported by the Air Force Office of Scientific Research (AFOSR) and DARPA and was monitored by AFOSR under Grant No. AFOSR-83-0375.

APPENDIX XX

Microdesigning of Ceramic-Metal Composites

(Pynk, Aksay, and Sarikaya 1987)

MICRODESIGNING OF CERAMIC-METAL COMPOSITES

A. J. Pyzik, I. A. Aksay, and M. Sarikaya

Department of Materials Science and Engineering
College of Engineering
University of Washington, Seattle, WA 98195

ABSTRACT

Microdesigning of ceramic-metal composites is described in chemically compatible and incompatible systems. The problems associated with microstructural design are addressed with respect to capillarity and reaction thermodynamics. The B₄C-Al system is used to illustrate the formation of tailored microstructures which exhibited average fracture strength of 521 MPa and fracture toughness of 9.7 MPa·m^{1/2} at 36 v/o Al content.

INTRODUCTION

Ceramic-metal composites, when properly processed, combine the useful properties of ceramic and metal materials into one system. Perhaps the oldest example of a ceramic-metal composite is found in the Fe-C system, where pearlite combines bcc-iron and Fe₃C into a eutectoid microstructure. Formation of this composite structure takes place through solid state reactions below 723°C.

In contrast, the synthetically processed group of refractory carbide-metal composites have traditionally been processed by liquid phase sintering. Liquid phase sintering is an effective lower cost fabrication process;¹⁻⁴ however, its applicability to ceramic-metal composites has only been illustrated in thermodynamically compatible systems. The WC-Co and TiC-Ni systems are the best studied examples of these thermodynamically compatible systems. Most ceramic-metal composite systems of interest, however, are thermodynamically incompatible at elevated temperatures. Therefore, when the liquid phase sintering approach is attempted, chemical reactions may result in the depletion of either the metal or the ceramic phase prior to full densification. Consequently, a number of difficulties have been encountered in the development of many ceramic-metal composite systems.⁵⁻⁷ Low temperature, solid-state densification methods provide a solution to the phase depletion problems encountered at elevated temperatures. However, the main disadvantage of low temperature processing methods is that, in the absence of chemical reactions, wetting of the ceramic by the metal phase is not always achieved. In such cases, even with high pressure forming techniques porosity is not completely eliminated.

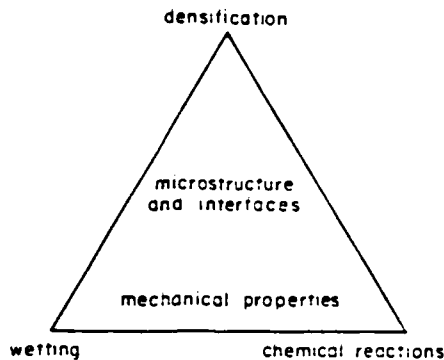


Fig. 1. The relationship between key processing factors that play a key role on microstructure development and mechanical properties.

In this paper, we illustrate a methodology to circumvent the problems encountered in the microdesigning of thermodynamically incompatible ceramic-metal composites in terms of the wetting characteristics of the ceramic phase by the metal, the rate of chemical reactions at the interfaces, the resultant microstructures, and mechanical properties (Fig. 1). The wetting requirement is satisfied by taking advantage of the chemical reactions between the metal and the ceramic phases. Since the retention of the metal phase in the final product is an essential requirement, we minimize the detrimental effect of the chemical reactions by using an infiltration technique to achieve fully dense composites prior to the depletion of the metal phase. Optimization of processing parameters and composite properties is illustrated with the case studies on B_4C -metal composites.

CAPILLARITY AND REACTION THERMODYNAMICS

In order to achieve intimately mixed multiphase combinations, the first requirement is to control the wetting characteristics of the solid phases by the liquid metal. At high temperatures, solid, liquid, and vapor phases are often under chemical nonequilibrium conditions. Under these conditions, chemical reactions at the interfaces result in a change in the interfacial free energies and thus the contact angle.⁸ In most cases, nonwetting systems can be transformed to wetting ones by taking advantage of these chemical reactions.⁸ However, mass transport across the interface that initially results in wetting may now result in the formation of new phases in excessive amounts. The formation of reaction products may then lead to the depletion of the liquid phase. Therefore, in most ceramic-metal systems, the control of chemical reactions is the first key processing factor that must be considered.

A typical example of a thermodynamically incompatible ceramic-metal system is the B_4C -Al composite which offers advantages in low density (< 2.7 g/cc) applications. In this system, wetting is not readily achieved below about 1100°C. However at temperatures above 1200°C, a contact angle of 20° is achieved within three minutes (Fig. 2). In this

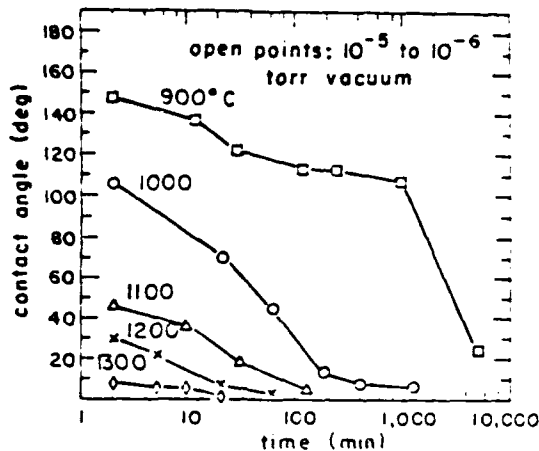


Fig. 2. Contact angle of molten Al on B_4C as a function of temperature and time.

case, the condition leading to wetting is associated with the rapid formation of new phases.⁹ As a result, liquid phase sintering of B_4C -Al composites under wetting conditions leads to a rapid decline in the metal content and to its eventual depletion prior to full densification. The formation of seven binary and ternary phases has been established between 680°C (the melting temperature of Al) and 1400°C.¹⁰ The major phases formed are AlB_2 and Al_2BC below 1000°C, $AlB_2Al_2C_3$ and Al_4BC between 1000° and 1200°C, and $AlB_2Al_4C_4$ and Al_4C_3 above 1200°C.

Most of the reaction products that form in the B_4C -Al system display high elastic moduli and hardnesses, and low densities. Thus, the formation of these reaction products can be beneficial in the tailoring of multiphase systems of a desired metal content when fully densified B_4C -Al composites are subjected to a post-heat treatment process. In order to achieve this goal, however, the reaction rates must be controlled precisely. As will be shown in the following sections, a pre-heat treatment of the commercial boron carbide powders (ESK 1500) above 1800°C in reducing conditions can be utilized to significantly reduce the reaction rates.¹¹ Change in the chemistry of B_4C creates the basis for the controlled densification of B_4C -Al composites.¹¹

In contrast to the B_4C -Al system, an example of a thermodynamically compatible system is the B_4C -Cu composite. Although this system offers the advantage of chemical compatibility, its main disadvantage is that the wetting angle of Cu on B_4C is higher than 90° at temperatures up to 1500°C. Cu may be forced between the B_4C grains by high pressure, e.g., hot isostatic pressing, techniques to achieve high densities;¹² however, the resultant composites exhibit very low fracture strength due to weak interfaces created between the metal and ceramic phases. We have illustrated that when Cu is alloyed with elements that are reactive with B_4C , e.g., Si, Mn, or Al, contact angles smaller than 90° can be achieved.¹³ This alloying approach then allows a processor an alternate approach to control the rate of chemical reaction(s) and, therefore, the kinetics of wetting at a given temperature (Fig. 3).

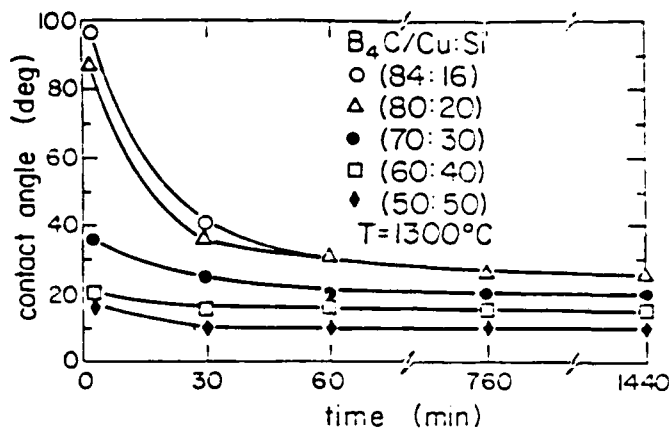


Fig. 3. Contact angle of molten Cu-Si alloys on B₄C as a function of composition and time.

DENSIFICATION THROUGH PHASE REARRANGEMENT

Our observations have shown that during the liquid phase sintering of ceramic-metal composites phase rearrangement becomes the major and often the only mechanism that affects the densification behavior of a compact. First, end-point densities lower than the theoretical densities may result due to the creation of large voids that form when the liquid metal rearranges through the porous composite. Second, the magnitude of shrinkage depends on the rearrangement of the solid particles under the capillary action of the liquid phase. The extent of phase rearrangement depends on the degree of packing density and chemical inhomogeneities that exist in a powder compact after the initial consolidation. Due to phase rearrangement, these inhomogeneities are amplified during sintering. As illustrated below, the way these rearrangement processes take place depends on the chemical compatibility of the system, wetting characteristics of the liquid, and the kinetics of liquid phase motion.

The formation of large voids due to the rearrangement of the liquid phase is of particular concern especially in chemically incompatible systems. As illustrated in Fig. 4, sintered, hot pressed, or hot isostatically pressed B₄C-Al composites all possess characteristic large voids surrounded by rigid ceramic shells. The steps that lead to the formation of these voids are as follows: (i) the liquid phase moves into the ceramic agglomerates due to capillary suction and thus the volume originally occupied by the metal powder remains as void; and (ii) dense B₄C-Al agglomerate regions support the formation of binary and ternary compounds as solid bridges between the B₄C grains and thus the densification process stops due to the formation of a solid skeleton.¹¹ Therefore, in order to obtain dense microstructures, either the kinetics of solid rearrangement needs to be accelerated and/or the kinetics of chemical reactions has to be slowed down. For instance, hot isostatic pressing can be used to enhance densification prior to the formation of a solid skeleton structure. However, even in the case of hot isostatic pressing, the presence of closed porosity is observed due to the formation of reaction products.¹⁰



Fig. 4. B₄C-Al composites showing large voids surrounded by ceramic shells.

Previous studies on the role of phase rearrangement during liquid phase sintering suggested that agglomerates that act as the suction media for the liquid phase can be disintegrated during sintering in systems with low wetting angles.^{13,14} Our studies also confirmed the validity of this disintegration mechanism but only in systems where reaction products do not result in the formation of a continuous skeleton between the particles. In the ceramic-metal systems reported here, we illustrate that the key factor to be considered in this disintegration is not the final equilibrium contact angle but the kinetics of wetting process itself (Fig. 3). In chemically reactive systems where a low contact angle is achieved rapidly (Fig. 3), the suction rate of the liquid phase into the agglomerates is high. In these cases, we observe that the agglomerate regions are infiltrated rapidly and become fully dense before any disintegration takes place (Fig. 5(a)). In the absence of disintegration, the densification process stops at a low end-point density.

On the other hand, the microstructural development in a composite with an initially high contact angle is different (Fig. 5(b)). More uniform microstructures and higher end-point densities are obtained due to the disintegration of agglomerates.¹⁵ The exact mechanism of this disintegration is not fully understood. However, its occurrence is very beneficial with respect to the minimization of density of inhomogeneities.

The problems associated with phase rearrangement during liquid phase sintering can be used to our advantage if the fabrication process is modified to infiltrate a monolithic porous ceramic with liquid metal in a manner similar to the densification of agglomerates discussed above. This approach allows us to process fully dense and uniform composites as

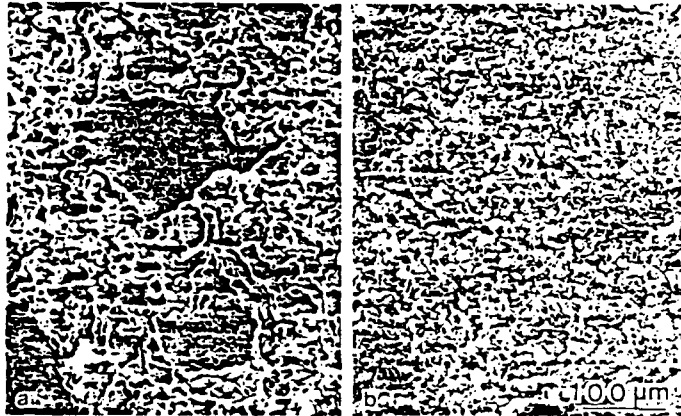


Fig. 5. B_4C -Cu-Si composite with high (a) and low (b) kinetics of wetting.

long as the hydraulic resistance and the thickness of the porous substrates are optimized to facilitate a rapid infiltration process. In the present work, porous B_4C compacts were prepared by a colloidal consolidation technique.¹¹ In order to modify the surface characteristics of the B_4C powder and also to obtain a high density B_4C skeleton, the compacts were first heat treated in a vacuum graphite furnace at a temperature range of 1800° to 2200°C. These porous B_4C compacts were then infiltrated with molten Al at 1200°C for 15 to 60 minutes. As a result, two major types of B_4C -Al composites were formed. In the first type, the metal is completely depleted to form a theoretically dense multi-ceramic microstructure. In the second type, a predetermined amount of Al is retained in the final product. As illustrated in the sections below, in these two cases, microstructures, interfaces, and mechanical properties all differ considerably.

MICROSTRUCTURES AND INTERFACE CHARACTERISTICS

In liquid phase sintering, the development of microstructure depends mainly on the sintering temperature and time. On the other hand, in the infiltration technique outlined above, microstructures can be altered in the following processing stages: (i) dispersion and consolidation, (ii) sintering, (iii) infiltration, and (iv) post-heat treatment. The primary advantage of the infiltration approach is that the distribution of both the solid and liquid phases can be controlled separately. Furthermore, agglomerated ceramic powders can also be used to form uniform composite microstructures by the infiltration technique.

Colloidal dispersion and consolidation of the B_4C powder provides the most effective approach to control the B_4C /metal ratio of the final product. In the preparation of high (> 70 v/o) B_4C content specimens, we use highly dispersed aqueous suspensions prepared in the pH range of 9-10.5. Conversely, for low B_4C contents, we work with flocculated aqueous suspensions prepared at pH 4. This adjustment in pH results in

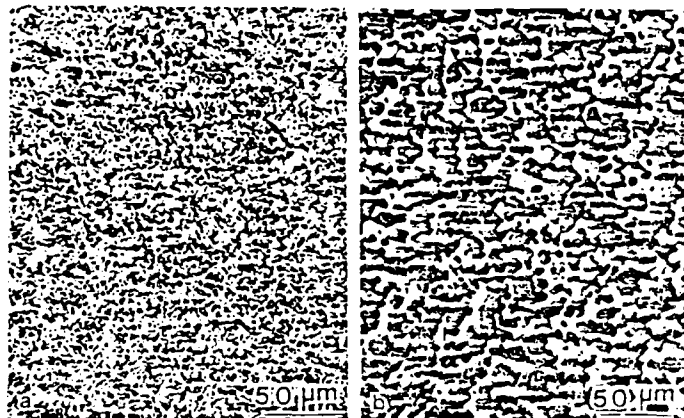


Fig. 6. B_4C -Al composite prepared by infiltration approach (A) Without B_4C heat treatment. (B) After B_4C heat treatment.

variations in the pore size and total volume of the B_4C substrates.¹¹ Subsequent sintering treatment in the temperature range of 1800° to 2200°C results in the formation of porous B_4C "sponges". The amount of total porosity, grain and channel connectivity, and the chemical composition of the substrate can be modified depending on the sintering conditions.¹¹ The composites formed after the infiltration display a bicontinuous microstructure of B_4C and Al phases (Fig. 6). When the infiltration time is limited to < 30 min, most of the B_4C /Al interfaces are atomically clean (Fig. 7a). However, binary and ternary compounds can be formed during the post-heat treatment step (Fig. 7b).

MECHANICAL PROPERTIES

Fracture strength (4-point bending) and fracture toughness (SENB) values for the B_4C -Al composites prepared by the infiltration approach are presented in Fig. 8. The data points on the solid lines are given with respect to the initial amount of Al used to form the composites. The best results were obtained at 36 v/o Al content, i.e., an average fracture strength of 621 MPa and a fracture toughness of 9.7 MPa $m^{1/2}$. However, the properties are controlled not necessarily by the total amount of the retained metal phase, but by the reaction products that form at the B_4C -Al interfaces. For instance, two specimens with different metal contents initially, e.g., 50 and 36 v/o, can be brought to the same retained metal content of 32 v/o after the post-heat treatment (Fig. 8). At this identical metal content, however, their properties differ considerably due to the difference in the amounts of chemical reaction products present in the microstructures. Strength measurements of porous B_4C (17 to 40 v/o porosity) indicate that the ceramic skeleton itself is not responsible for the deviation from the rule of mixture. The maxima on the fracture strength and K_{IC} data appear to be related to the continuity factor which is defined as the average number of connected grains.

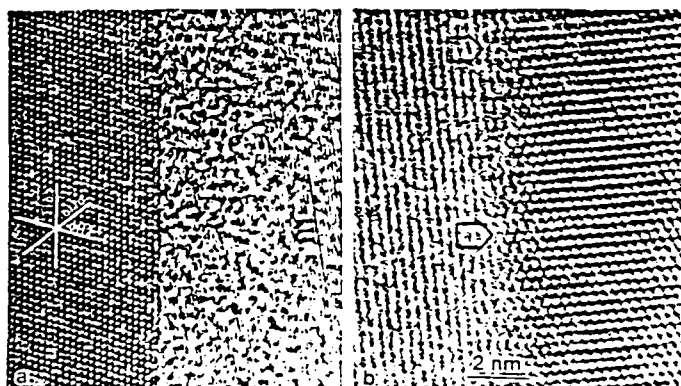


Fig. 7. High resolution transmission electron micrograph revealing the structural details of (a) B_4C -Al and (b) B_4C - $AlB_{12}C_3$ interfaces.

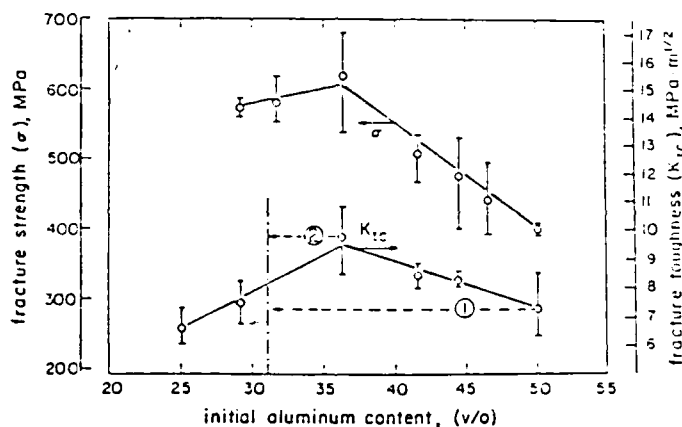


Fig. 8. Fracture toughness and fracture strength values for B_4C -Al composites as a function of initial Al content.

The interpretation of the relationships between mechanical properties and microstructure becomes even more complicated when, instead of the pure metal, its alloys are used. Heat treatment conditions and interactions of alloying elements with the ceramic phase(s) are more influential on the properties than the ceramic-to-metal ratio. The effect of alloying is illustrated in Fig. 9, where Knoop microhardness values for B_4C -Al, B_4C -2024-Al alloy, and B_4C -7075-Al alloy composites are plotted with respect to the initial metal content. The lack of variation in the microhardness for composites with high metal content is due to the tendency of alloying elements for segregation and precipitate formation at the B_4C grain boundaries. As a result, at high Al contents, bulk hardness remains similar to that of pure Al. Differences in

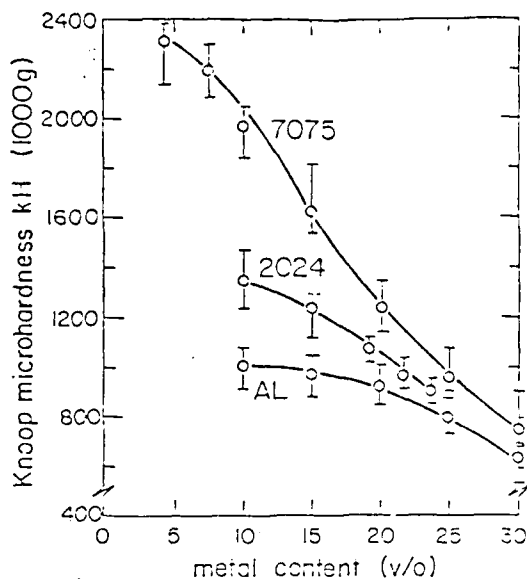


Fig. 9. Knoop microhardness of B_4C -Al, B_4C -2024 Al, B_4C -7075 Al alloys, as a function of final aluminum content.

hardness for composites with low metal content may be explained on the basis of: (i) the formation of hard phases due to chemical reactions between the alloying elements (e.g., Cr, Mn) and B_4C ; and (ii) high Cu and Mn activity as grain refiners in Al. However, to confirm this hypothesis, a detailed analysis of the microstructures and the interfaces has to be performed at high spatial resolutions.

CONCLUSIONS

In the microdesigning of ceramic-metal composites in the presence of liquid metal, the following main points have to be considered:

- (1) Phase rearrangement is the major densification mechanism. The magnitude of densification is related to the wetting kinetics and to the occurrence of chemical reactions. Liquid metal motion, if controlled, can be beneficial with respect to the uniformity of the final product.
- (2) The selection of a processing technique is directly related to the microstructure desired. The utilization of the infiltration approach provides an advantage in tailoring microstructures with precise ceramic-to-metal ratio, grain size, phase continuity, and the spatial distribution of the phases.
- (3) In chemically reactive systems, post-heat treatment can be used as an additional step to modify the microstructures through the formation of reaction products and thus lower the amount of the metal phase to any desired level.

ACKNOWLEDGEMENT

This research was supported by the Defense Advanced Research Projects Agency of the Department of Defense and was monitored by the Air Force Office of Scientific Research under Grant No. AFOSR-83-0375.

REFERENCES

1. W. D. Kingery, in "Ceramic Fabrication Processes," W. D. Kingery, ed., The MIT Press, Cambridge, MA (1958), pp. 131-43.
2. T. J. Whalen and M. Humenik, Jr., in: "Sintering and Related Phenomena," G. C. Kuczynski, N. A. Hooten, and C. F. Gibbons, eds., Gordon and Breach Sci. Pub., New York (1967), pp. 715-40.
3. V. N. Eremenko, Yu. V. Naidich, and I. A. Lavrinenko, "Liquid Phase Sintering," Consultants Bureau, New York (1970).
4. W. J. Huppmann, in: "Sintering and Catalysis," G. C. Kuczynski, ed., Plenum Press (1975), pp. 359-78.
5. M. L. Wilkins, C. F. Cline, and C. A. Honodel, "Light Armor," Lawrence Livermore National Laboratory, UCRL-71817 (1969).
6. G. G. Gnesin and Yu. V. Nadish, Poroshkovaya Metallurgiya, 74 [2] 57-63 (1969).
7. C. R. Manning Jr. and T. B. Gurganus, J. Am. Ceram. Soc., 52 [3] 115-18 (1969).
8. I. A. Aksay, C. E. Hoge, and J. A. Pask, J. Phys. Chem., 78 [12] 1178-83 (1974).
9. D. C. Halverson, A. J. Pyzik, and I. A. Aksay, Ceram. Engrg. and Sci. Proc. 6 [7-8] 736-44 (1985).
10. D. C. Halverson, W. E. Snowden, A. J. Pyzik, and I. A. Aksay, "Processing of Boron Carbide/Aluminum Composites," submitted to the Advanced Ceramic Materials, 1986.
11. A. J. Pyzik and I. A. Aksay, "Densification and Microstructure Evolution in Boron Carbide-Aluminum Composites," unpublished work.
12. J. E. Smugeresky, H. J. Rack, and G. B. Basell, "Development of a Non-Volatile Boron Carbide/Copper Cermet Neutron Shield for High Performance Shipping Casks," Sandia National Laboratories, Albuquerque, NM, U.S.D.O.E. Contract No. DE-ACC4-76-DPOC789 (1986).
13. W. J. Huppmann, S. Pejovnik, and S. M. Han, "Processing of Crystalline Ceramics," H. Palmour III, R. F. Davis, and T. M. Hare, eds., Plenum Press (1978), pp. 233-42.
14. S. Pejovnik, D. Kolar, W. J. Huppmann, and G. Petzow, "Sintering-New Developments," Proc. of the 4th Int. Conf., Dubrownik, Yu. (1979), pp. 285-92.
15. A. J. Pyzik and I. A. Aksay, "Phase Rearrangement During Liquid Phase Sintering," unpublished work

APPENDIX XXI
Structures of Colloidal Solids

(Aksay and Kikuchi 1986)

STRUCTURES OF COLLOIDAL SOLIDS

ILHAN A. AKSAY AND RYOICHI KIKUCHI

Department of Materials Science and Engineering
College of Engineering
University of Washington
Seattle, Washington

INTRODUCTION

Colloidal systems containing spherical particles have been shown to display disorder-order transitions.^{1,2} Since these transitions resemble the liquid to crystal transitions of atomic systems, many attempts have been made to outline the stability regions of the colloidal liquid and crystalline structures in phase diagram forms.³ The structural characterization of these phases has also been the subject of numerous studies.² In the crystalline form, these structures are often easily recognized by their bright iridescent colors. In the most commonly accepted theoretical treatments, the existence of highly repulsive interparticle interactions are considered to be the essential requirement for the formation of colloidal crystals.³

In contrast to this prevailing view, in this chapter we point out our observation on the formation of colloidal crystals through spontaneous gas to condensed phase transitions which can only be realized when net attractive interactions exist. Including our new interpretations, we now present an all-inclusive treatment of phase stability in colloidal systems combining gas, liquid, and crystal phases and transitions among them. Further, we provide experimental data on the unifying hierarchical features of the colloidal solids and their interpretations.

BASIC PHASE DIAGRAM OF THREE AGGREGATES

In discussing the phase diagram of colloidal systems the main requirement is that the interparticle potential must be known as a function of the system parameters. In our experimental studies we specifically worked with systems where the particles interacted electrostatically. Therefore, the discussion in this paper will be limited to such interaction.

In electrostatic systems, the repulsion energy between two colloidal particles can be expressed by the DLVO theory.⁴ The combination of this repulsive potential with the energy of attraction due to the van der Waals forces results in a pairwise potential that, in general, has a maximum (either in the repulsive or attractive range) separating two minima (both in the attractive range).⁴ A complete particle-particle contact is prevented at a cutoff point due to the presence of a semiincompressible fluid envelope surrounding the particles.^{4,5}

Therefore, for the phase transitions with which we are concerned, the particles do not come to the primary minimum which is at a much smaller interparticle separation distance than permitted by the fluid envelope. In this work, the key property of the potential energy curves is that the binding energy ϵ at the cutoff point is approximately proportional to ζ^{-2} where ζ is the zeta potential.⁴ When we use the lattice model in calculating the phase diagram of the system, as will be explained below, we can use the ϵ as the representative interaction potential, and then make an approximation that ϵ is proportional to ζ^{-2} :

$$\epsilon \propto \zeta^{-2} \quad (1)$$

It is not the purpose of this chapter to emphasize the functional dependence ζ^{-2} but to make use of the general qualitative dependence of ϵ on the inverse power of ζ .

In understanding experimental observations of phase transitions in colloidal systems, we distinguish the essential features and additional features. The essential features can be provided by equilibrium phase diagrams of atomic systems. Since we are interested in qualitative properties of the system, 2-D phase diagrams, rather than three, are sufficient for understanding the basic phase diagram properties. Further, in order to make the theoretical treatment of phase diagrams easier for a variety of cases, we work with lattice-gas model rather than with the more rigorous continuum space computation which is time consuming. An example of the 2-D lattice gas model calculations is that of Kikuchi and Cahn,⁶ which treated the grain boundary melting phenomenon, and is accepted as predicting essential features of the processes occurring in 3-D grain boundaries. In this chapter we also base our discussions on results due to the lattice gas model which was used in Ref.⁶

The method of formulation leading to the theoretical phase diagram of Fig. 54.1a is sketched here. The calculation was done using the cluster variation method (CVM). The system contains one kind of particles and vacancies and is described using the square lattice as the underlying structure Fig. 54.1b. The interparticle potentials are chosen in the same way as by Orban et al.⁷ When a particle exists at A , the nearest-, second-, and third-neighbor lattice points are excluded, and a second particle can approach A up to point B . In the treatment, we used two interaction potentials ϵ_{1B} and ϵ_{4C} . Particle pairs farther away are not considered as contributing to the potential energy. The equilibrium state is derived by writing the Helmholtz free-energy F and calculating the minimum of F as outlined in Ref. 6. In the phase diagram of Fig. 54.1a, the temperature scale is normalized by $\epsilon = |\epsilon_{4C}|$. Similarly, the density scale is normalized by the density of a fully occupied lattice structure. We use the phase diagram in Fig. 54.1 in *qualitatively* interpreting experimental observations. As many previous examples show, theoretical diagrams of 2-D systems can safely be used in interpreting experiments of three dimensions. Naturally we avoid accurate *numerical* comparison of 3-D experiments and 2-D theory. We can also use the phase diagrams which are calculated for equilibrium systems in interpreting nonequilibrium phenomena. In this case again, the equilibrium calculations are to be used as a qualitative guideline; when numerical comparison is to be attempted, special care is needed.

In atomic systems, the reduced temperature scale kT/ϵ of the phase diagram is only proportional to the thermodynamic temperature T since the pair potential in a given system is usually treated as fixed. However, when we work with colloidal systems, the interaction potential can be easily varied. Thus, in the case of electrostatically interacting particle systems, using the approximate property expressed in (1), we can work with a reduced temperature:

$$T_R = \frac{kT}{\epsilon} = \left(\frac{\zeta}{\zeta_0}\right)^2 \quad (2)$$

where ζ_0 is a normalization constant. The relation (2) is crucial in interpreting the phase diagram of colloidal systems as analogous to the three aggregate phases of atomic systems. At the high T_R end of the system, our treatment approaches that of repulsive interaction systems, while for the low T_R region the attractive interaction is appropriately taken into account. The essential point of our proposed interpretation (2) is that even when the thermodynamic temperature T is kept fixed, the reduced temperature T_R can be varied by changing the ζ -potential, and thus the "temperature" versus composition phase diagram can be used even for a constant T .

HIERARCHICAL STRUCTURE OF CLUSTERS

We can now use the phase diagram in Fig. 54.1 in interpreting experimental observations. In a dilute suspension, for example at the point G in Fig. 54.1a, colloidal systems display gaslike behavior. As the number density ρ of the colloidal particles is increased (along path 1), this gaslike state changes continuously to a liquidlike state at L . Finally, for ρ larger than a certain density L_c , the liquidlike state transforms to a solidlike state S through a first order transition.¹⁻³ In the phase diagram of Fig. 54.1a, the region where such transitions are observed is above the critical point, CR.

On the other hand, when this same suspension displaying gaslike behavior is shifted (along path 2) from its dispersed state G , to a new state G' of a lower kT/ϵ or ζ -potential value, we observe a distinct first order transition of gas to condensed phase. Our work with nearly monosize (0.7 μm) SiO_2 particle systems showed that, when a colloidal system is within the miscibility gap, some of the particles in the suspension start forming permanent multiparticle clusters, that is, colloidal solids.⁹ In the gravitational field, due to their higher effective mass, these clusters are separated from the remaining portion of the primary particles as a result of differential settling. The primary particles, which stay dispersed until they eventually sediment due to gravitational force, result in the formation of a cloudy supernate, that is, colloidal gas.

This phenomenon of cloudy supernate formation has long been observed by various researchers in flocculating, that is, condensing, systems.^{9,10} Experiments by Siano¹⁰ suggested the possibility of spinodal-decomposition like fluid-fluid phase segregation in colloidal systems. This interpretation is in agreement with the phase diagram presented here. Similarly, the work of Vincent and coworkers⁹ illustrated the coexistence of singlet particles as the gas phase with clusters of particles in weakly interacting particle systems in accordance with our interpretation. In recent theoretical treatments, the co-

existence of colloidal gas and liquid phases below a critical point has also been predicted.¹¹ Thus, in view of our experiments and supportive evidence in the literature, we propose that the stability regions of colloidal phases are outlined in the generalized phase diagram of Fig. 54.1*a*.

Our theoretical treatment of the phase diagram (Fig. 54.1) has been done for an idealizing condition that the colloidal solid can be assumed to form a single crystal and its structure approaches a perfect state (i.e., no vacancies) as kT/ϵ approaches zero. However, experiments are usually far from ideal and the formation of polycrystalline structures is the rule rather than the exception.^{12,13} Microstructural variations in these polycrystalline colloidal solids formed at three different ζ -potential levels of the phase diagram are illustrated in the scanning electron micrographs of Fig. 54.2. Particle clusters are formed during colloidal solidification. Note the special arrangement of these particle clusters. The first generation of clusters begin as domains and are formed by close packing of primary particles. The domain size decreases with increasing interparticle binding energy or decreasing T_R . The collection of a number of these domains results in the formation of second generation clusters. The structure of these second generation clusters displays continuous variations in the interdomain void space. At the high kT/ϵ end of the spectrum where the interparticle binding energy is low, tight domain interlocking results in polydomain structures which closely resemble polycrystalline atomic structures and are easily recognized as colloidal crystals due to their iridescent characteristics.^{1,2}

With increasing interparticle binding energies, domain interlocking efficiency decreases since domains become increasingly rigid and thus behave as hard sphere packing units themselves. The combined effect of the decreasing domain size and the increasing interdomain void space is the loss of the iridescent property of the colloidal solids. At the low T_R end, an additional contribution to the low packing efficiency may be the formation of third generation clusters and the associated void space with the grouping of second generation clusters, Fig. 54.3. The most important concept illustrated by our observations is that a hierarchy of microstructures can be obtained by varying the degree of interaction between particles as described by T_R .

This experimental evidence on the structure of colloidal solids suggests the modification needed in interpreting the theoretical phase diagram of Fig. 54.1*a* when compared with experiments. Remember that the density of the solid phase in the theory is only with respect to the intradomain regions. In Fig. 54.3*a*, we provide experimental data on the density of colloidal solids, obtained by sedimentation volume measurements, as a function of kT/ϵ . As the interparticle binding energy is increased (going to smaller kT/ϵ values), a significant decrease in the density of colloidal solids is observed below the critical point. The prime cause of this density decrease, in the subcritical region, is the retention of third generation void space in the colloidal solids formed by gravitational settling. However, when such a system is consolidated further by centrifugation, all the third generation voids can be eliminated completely and the density becomes greater than that shown in Fig. 54.3*a*.¹²

CONCLUSION

In colloidal systems the interparticle energy ϵ can be controlled through chemical adjustments to the fluid matrix surrounding the colloidal particles. An important implication of this property is that even when the thermodynamic temperature is kept fixed, changing the potential energy by other means than T has the same effect as changing T of phase diagrams for atomic systems. The stability regions of colloidal gas, liquid, and solid phases are outlined with a theoretically calculated kT/ϵ versus density phase diagram. In experiments, it is noted that the colloidal solids display (continuous) variations in the size and packing of particle clusters as a function of kT/ϵ . The first, second, and third generations of clusters and voids are clearly distinguished. This observation on the hierarchical nature of the colloidal solids plays a key role in our generalized treatment of the colloidal phase transitions.

The types of phase transitions discussed in this paper are of interest in diverse fields.² For instance, colloids play an important role in the processing of high-technology ceramics.¹⁴ Colloidal fluid-to-solid transitions have been widely observed in biological systems.² Furthermore, these colloids are ideal models for simulating atomic systems. Although the theoretical phase diagram presented here is based on idealized colloidal phase structures, it serves^{12,14,15} the purpose of outlining colloidal phase stability regions in a generalized form with sufficient accuracy when we accept the new hierarchical interpretation of clusters and voids observed in the solid structure.

ACKNOWLEDGMENTS

The major part of this work was sponsored by the Office of Naval Research under Contract No. N00014-82-K-0336 and in part by the Advanced Research Projects Agency of the Department of Defense and was monitored by the Air Force Office of Scientific Research under Grant No. AFOSR-83-0375.

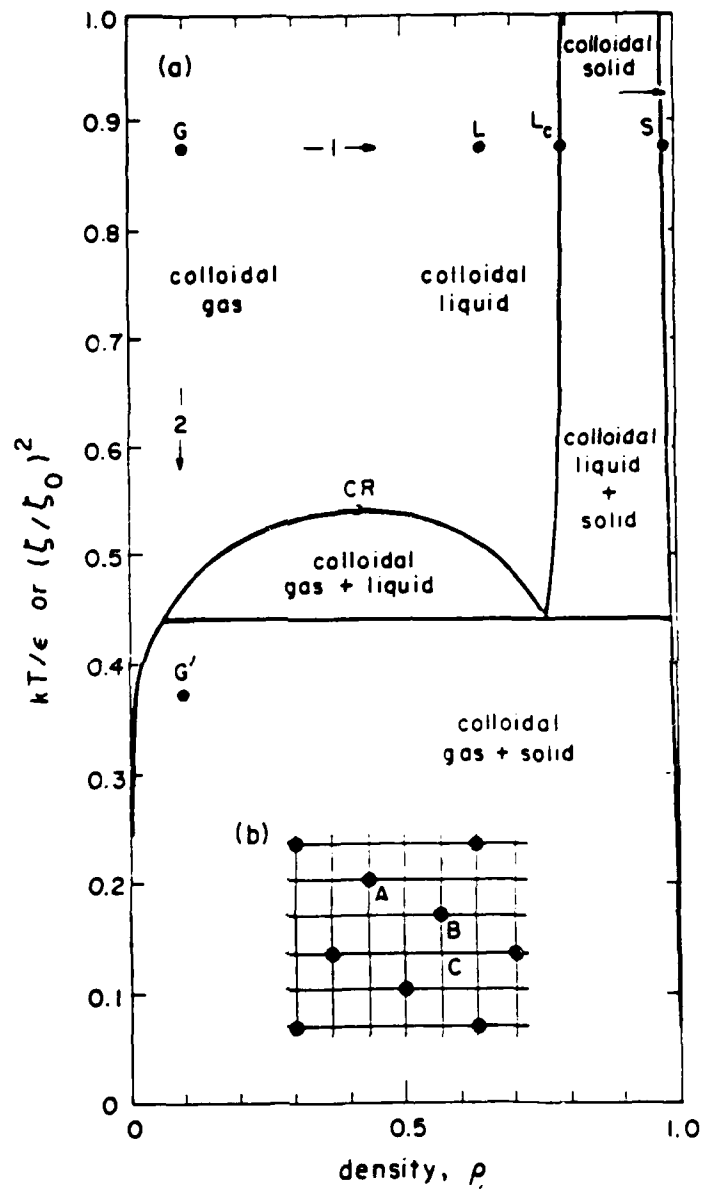
REFERENCES

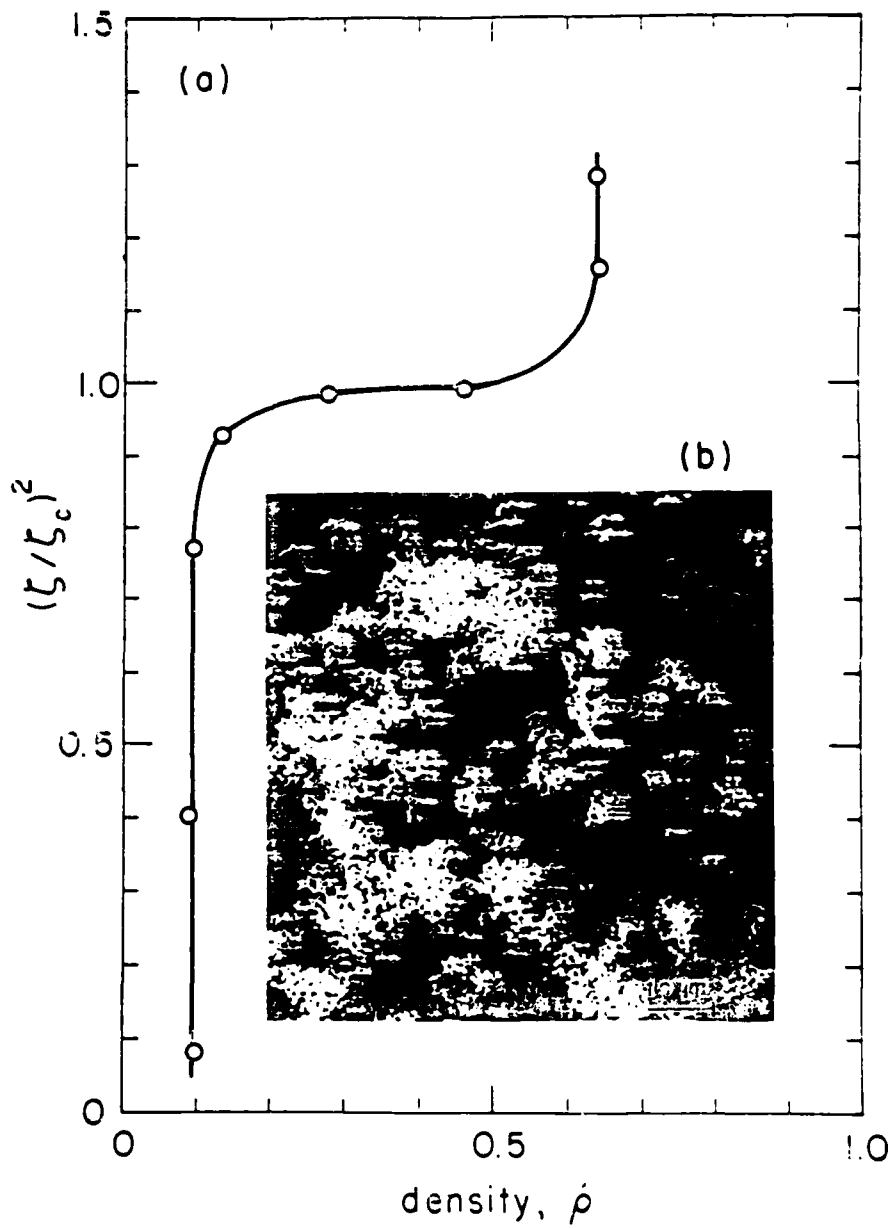
1. T. Alfrey, Jr., E. B. Bradford, and J. W. Vanderhoff, *J. Opt. Soc. Amer.* **44**, 603 (1954); W. Luck, M. Klier, and H. Wesslau, *Ber. Bunsenges. Phys. Chem.* **67**, 75, 84 (1963); P. A. Hiltner and I. M. Krieger, *J. Phys. Chem.* **73**, 2386 (1969); A. Kose, M. Ozaki, K. Takano, Y. Kobayashi, and S. Huchau, *J. Colloid Interface Sci.* **44**, 330 (1973).
2. I. F. Efremov, in *Surface and Colloid Science*, E. Matijević, Ed., Wiley, New York, 1976, Vol. 8, pp. 85-192; and P. Pieranski, *Contemp. Phys.* **24**, 25 (1983) provide extensive reviews on ordered colloidal systems.
3. J. A. Beunen and L. R. White, *Colloids and Surfaces* **3**, 371 (1981); P. M. Chaikin, P. Pincus, S. Alexander, and D. Hone, *J. Colloid Interface Sci.* **89**, 555 (1982), and references cited in these to earlier literature.
4. J. Th. G. Overbeek, *J. Colloid Interface Sci.* **50**, 408 (1977).
5. G. Frens and J. Th. G. Overbeek, *J. Colloid Interface Sci.* **38**, 376 (1972).
6. R. Kikuchi and J. W. Cahn, *Phys. Rev.* **B21**, 1893 (1980).
7. J. Orban, J. van Crean, and A. Bellmans, *J. Chem. Phys.* **49**, 1778 (1968).
8. A detailed account of this work which was performed with an X-ray absorption unit will be published elsewhere.
9. J. A. Long, D. W. J. Osmond, and B. Vincent, *J. Colloid Interface Sci.* **42**, 545 (1973), and C. Cowell and B. Vincent, *ibid.* **87**, 518 (1982).
10. D. B. Siano, *J. Colloid Interface Sci.* **68**, 111 (1979).
11. M. J. Grimson, *J. Chem. Soc., Faraday Trans. 2*, **79**, 817 (1983); and J. M. Victor and J. P. Hansen, *J. Phys. Lett.* **45**, L-307 (1984).
12. R. M. Allman, III and I. A. Aksay, to be published.
13. P. Pieranski, in *Physics of Defects*, R. Balian et al., Eds., North-Holland, Amsterdam, 1981, pp. 183-200.
14. I. A. Aksay, in *Advances in Ceramics*, J. A. Mangels and G. L. Messing, Eds., American Ceramic Society, Columbus, OH, 1984, Vol. 9, pp. 94-104.
15. M. Yasrebi, Kinetics of Flocculation in Aqueous Alpha Alumina Suspensions, M.Sc. Thesis, UCLA, 1984.

Figure 54.1 (a) Phase diagram for a one component colloidal system of monosize spherical particles calculated by the cluster variation method based on the two dimensional square lattice model of (b) Density scale is normalized with respect to a fully occupied lattice structure

Figure 54.2 (a) The arrangement of particle domains formed by centrifugal sedimentation of SiO₂ microspheres (average diameter = 0.7 μm) in H₂O at ζ = 110 mV (top), ζ = 68 mV (middle), and ζ = 0 mV (bottom);¹² (b) images where only the second generation voids are highlighted as dark regions in order to illustrate the continuous variations in the domain size with ζ-potential.

Figure 54.3 (a) Variations in the sedimentation density (relative to the total volume) of colloidal solids as a function of (ζ/ζ_c)² where ζ_c is the zeta potential at the critical point. (b) scanning electron micrograph of particle clusters formed at low I_g values.

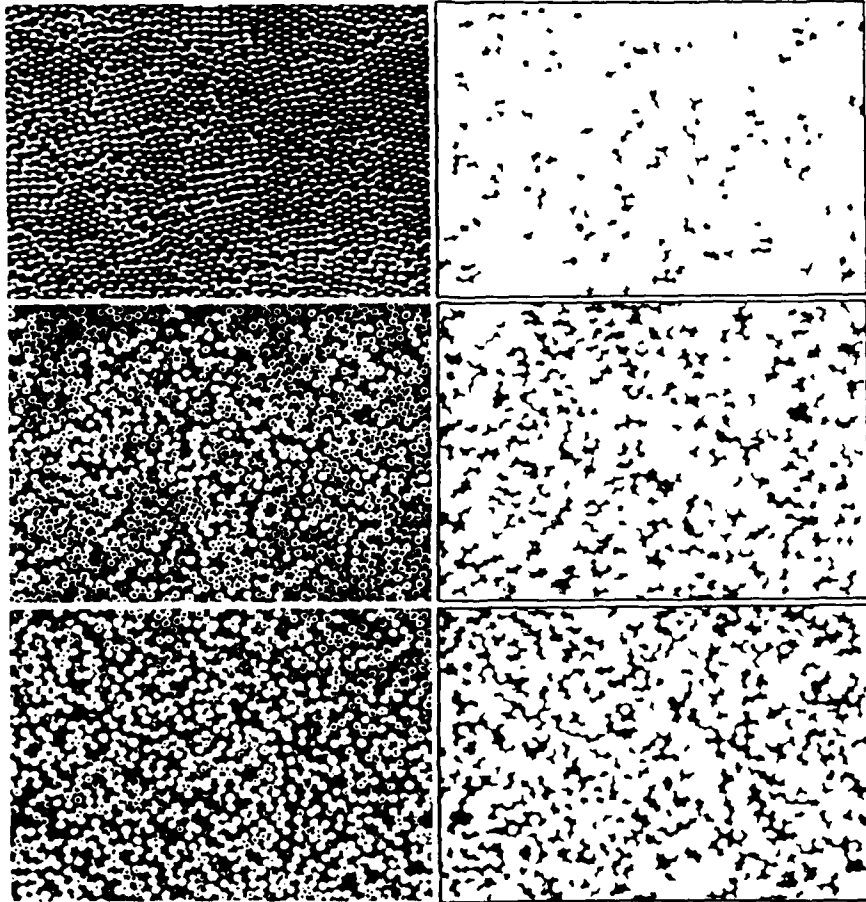




Akasu - Kikuchi
Fig. 3

(a)

(b)



Aksay - Kikuchi
Fig. 2

APPENDIX XXII
Phase Diagrams of Charged Colloidal Particles

(Shih, Aksay, and Kikuchi 1987a)

Phase diagrams of charged colloidal particles

Wan Y. Shih, İlhan A. Aksay, and Ryoichi Kikuchi

Department of Materials Science and Engineering, University of Washington, Seattle, Washington 98195

(Received 22 December 1986; accepted 26 January 1987)

We have calculated the phase diagrams of charged colloidal particles in the parameter space. The free energies of different phases, which were used to determine the phase boundaries, were calculated variationally. The Einstein oscillators and the hard sphere fluid were used as the reference systems for the solid phases and the liquid, respectively. The interparticle interactions were approximated to be the Debye-Hückel screened Coulomb potential with size correction. We show that the solid phases are stable at low salt concentrations: bcc is preferred only at high charges and at low densities while fcc is dominant at higher densities. The solid phases melt upon the addition of salt: bcc may or may not transform to fcc before melting, depending on the particle number densities. No reentrant transition is found upon the addition of salt. When the particles are extremely highly charged, the system may undergo fcc-bcc-fcc transitions at nonzero salt concentration when the particle number density is increased.

I. INTRODUCTION

The study of the colloidal suspensions of electrically charged particles such as polystyrene or silica spheres has received much attention.¹ These colloidal systems can be regarded as scaled-up atomic systems with charges, particle sizes, and length scales 10^2 - 10^3 times larger than the typical atomic species. The particles constitute "ions" and, in the case of aqueous systems, the interaction between them is classically screened by either H_2O^+ or OH^- . The monodisperse suspensions are observed to be disordered (the "liquid" phase) at low densities and crystalline when the density is high.¹⁻³ The average interparticle distance is often in the order of the visible light wave length; and, hence the crystalline phase can Bragg-diffract visible light and thus result in opalescence. Most often, the crystalline structure is found to be face-centered-cubic (fcc).²⁻⁴ In some dilute polystyrene suspensions where particles have high surface charges (in the order of 1000 electronic charges), body-centered-cubic (bcc) structure is found.⁴⁻⁹

Unlike their atomic counterparts, the interparticle interactions in colloids can be varied in a wide range by adjusting the parameters such as the salt concentration, the particle number densities, and the particle surface charge. It is therefore possible to talk about the phase diagram in the parameter space. So far, the calculated phase diagrams have either been based on an effective hard-sphere model¹ which is unable to produce a bcc phase, or based on solid-phase calculations¹⁰ which did not treat the liquid phase adequately. Shih and Stroud¹¹ have done a two-phase calculation for the freezing but they did not look into the stabilities of various solid phases.

It is the purpose of this paper to calculate a more complete phase diagram by treating all the phases at equal footing. That is, the phase diagram will be calculated by directly comparing the Helmholtz free energy of different phases (bcc, fcc, hcp, and liquid) at the same parameters. In principle, one should draw a common tangent between the Helmholtz free energies of two different phases in the free energy vs particle number density in order to determine the phase-coexistence regions in the phase diagram; but, the theory is

not accurate enough to allow this procedure. Our aim is then to get a correct qualitative account for the phase diagrams through our consistent way of treating different phases: the free energies of *all* phases are *calculated* via a variational principle based on the Gibbs-Bogolyubov inequality. Einstein oscillators are used as the reference systems for the crystalline phases and a hard-sphere fluid as that for the liquid. This procedure has been proven to give very good results for the polyvalent metallic systems.¹² We expect it to work well for the present case. The interparticle interaction is approximated to be the Debye-Hückel-screened Coulomb potential with size correction. The Debye-Hückel approximation is correct when the particle number density is low or the screening is weak, i.e., $qa_i \leq 1$, where q is the inverse screening length and a_i the average interparticle distance. Since our interest is to determine the phase boundaries in the part of the phase diagram where bcc is likely to appear, the Debye-Hückel-screened potential should then well represent the interparticle interactions in those regions where the particle number density is usually low.

We now turn to the body of the paper. Section II briefly describes the formalism. Section III gives the results and discussion. Some concluding remarks are given in Sec. IV.

II. FORMALISM

We consider an aqueous colloidal suspension of N spherical particles, each of radius a , in volume Ω , and at absolute temperature T . Each particle has an effective charge Z . The aqueous medium has a static dielectric constant. The NZ H_2O^+ or OH^- ions in the solution will neutralize the particles if no electrolyte is added to the solution. When the suspension is not too dense or the temperature is not too low, the interaction between particles can be adequately treated within the Debye-Hückel approximation. In MKSA units, the interaction takes the form

$$V(r) = \frac{Z^2 e^2}{4\pi\epsilon_0\epsilon} \frac{e^{-\kappa r}}{r}, \quad (2.1)$$

where ϵ_0 is the permittivity of free space, ϵ is the static dielectric constant of the aqueous medium, e is the electronic

charge, r is the distance between particles, and q is the inverse screening length which satisfies

$$q^2 = \frac{e^2}{\epsilon_0 \epsilon k_B T} \sum_i n_i Z_i^2, \quad (2.2)$$

where k_B is the Boltzmann constant, Z_i and n_i are the charge and the number density of the i th species of ions, respectively. In Eq. (2.1), the particles are assumed to be point-like. If the particles have a finite size, the interaction is modified as

$$V(r) = \frac{Z^2 e^2}{4\pi \epsilon_0 \epsilon} \left(\frac{e^{qa}}{1+qa} \right)^2 \frac{e^{-qr}}{r}, \quad (2.3)$$

where a is the radius of the particles. The factor $[e^{qa}/(1+qa)]^2$ takes into account the fact that the particles are not point-like and part of the volume in the solution is not available for screening because it is occupied by the particles. The size correction is important as is pointed out by Shih and Stroud¹¹ in order to avoid reentrant melting at high densities which is purely an artifact of the point-like interaction assumed in Eq. (2.1).

When the colloidal suspension is at equilibrium, its thermodynamic properties are determined by the Helmholtz free energy $F = E - TS$, where E is the internal energy and S the entropy. For a system of particles interacting via the potential (2.3), the free energy per particle F takes the following form:

$$F = \frac{1}{2N} \left(\frac{e^{qa}}{1+qa} \right)^2 \sum_{i,j} \frac{Z^2 e^2}{4\pi \epsilon_0 \epsilon} \left\langle \frac{1}{|r_i - r_j|} e^{-q|r_i - r_j|} \right\rangle + E_{\text{kin}} - TS, \quad (2.4)$$

where E_{kin} and S are the kinetic energy and the entropy per particle. $\langle \rangle$ denotes the thermal average over the canonical ensemble, and r_i is the position of particle i . Equation (2.4) includes only the terms of the free energy which depend on the arrangement of particles. These are the terms relevant in determining which structure (fcc, bcc, hcp, or liquid) is thermodynamically stable.

The free energy can be obtained from Eq. (2.4) by the use of a variational principle based on the Gibbs-Bogolyubov inequality¹³ which states as follows:

$$F \leq F_0 + \langle U - U_0 \rangle_0 \equiv F', \quad (2.5)$$

where F_0 is the free energy of the reference system and $\langle U - U_0 \rangle_0$ is the potential energy difference of the system of interest and the reference system, evaluated in the reference system. Since F is upper bounded by F' , we can then approximate F to be the minimum of F' with respect to the appropriate variables, that is, $F \approx F'(x_0)$ where

$$\left. \frac{\partial F'(x)}{\partial x} \right|_{x=x_0} = 0, \quad (2.6)$$

where x is the appropriate variational variable.

We will use the Einstein oscillators for the solid as the reference system, and the Einstein frequency is chosen as the variational parameter, while a hard-sphere fluid will be the reference system for the liquid and the packing fraction will be the variational parameter. This procedure has been previously shown to give very good results for polyvalent met-

als¹²; and, thus we expect that it should work well in the present case.

A. Solid

The Einstein oscillators are used as the reference system: each particle oscillates independently about a lattice point in a harmonic potential well with a frequency ω . The Einstein frequency is to be used as the variational parameter. In the actual calculations for the colloidal systems, $\hbar\omega/k_B T$ is in the order of 10^{-2} – 10^{-5} , much smaller than unity. Therefore, in terms of the Einstein temperature $\theta = \hbar\omega/k_B$, we may write

$$E_{\text{kin}} = \frac{3}{2} k_B T, \quad (2.7)$$

$$TS = 3k_B T [1 - \ln(\theta/T)], \quad (2.8)$$

and

$$\left\langle \frac{1}{|r_i - r_j|} e^{-q|r_i - r_j|} \right\rangle = f(|r_i - r_j|), \quad (2.9)$$

in which

$$f(r) = \frac{1}{2r} e^{uq^2} \left\{ e^{-qr} \left[1 - \text{erf} \left(\sqrt{u}q - \frac{r}{2\sqrt{u}} \right) \right] - e^{qr} \left[1 - \text{erf} \left(\sqrt{u}q + \frac{r}{2\sqrt{u}} \right) \right] \right\}, \quad (2.10)$$

where erf is the error function

$$\text{erf}(x) = \frac{2}{\sqrt{\pi}} \int_0^x e^{-y^2} dy, \quad (2.11)$$

and $3u$ is the mean square displacement which takes the following form:

$$u = \frac{\hbar^2 \coth(\theta/2T)}{2Mk_B \theta}, \quad (2.12)$$

in which M is the mass of the particles. Note that the anharmonic effect has been taken into account in Eq. (2.9). Combining Eq. (2.4) and Eq. (2.9), we get

$$F = \frac{1}{2} \left(\frac{e^{qa}}{1+qa} \right)^2 \sum_{\mathbf{R}} \frac{Z^2 e^2}{4\pi \epsilon_0 \epsilon} f(\mathbf{R}) + E_{\text{kin}} - TS, \quad (2.13)$$

where \mathbf{R} 's are the lattice vectors. In the actual calculations, $r/(2\sqrt{u}) \pm \sqrt{u}q$ is much larger than unity and Eq. (2.10) reduces to

$$f(r) \approx e^{uq^2} \frac{e^{-qr}}{r}. \quad (2.14)$$

B. Liquid

For the reference system, we use a fluid of particles interacting via the hard-sphere potential

$$U(r) = \infty, \quad r < \sigma, \text{ or} \\ = 0, \quad r > \sigma, \quad (2.15)$$

where σ , the hard-sphere diameter, is not, in general, equal to $2a$, the diameter of the actual particles. With this choice, the first term in Eq. (2.4) can be obtained analytically within the Percus-Yevick approximation, while the last term (the hard-sphere entropy) is available as an analytic fit to the

results of a Monte Carlo calculation. The liquid free energy thus takes the following form¹⁴:

$$F = \frac{Z^2 e^2}{4\pi\epsilon_0\epsilon} \left(\frac{e^{qa}}{1+qa} \right)^2 \frac{1}{r_0} [6\eta^{2/3} G(\lambda)] + \frac{3}{2} k_B T + \frac{k_B T \eta (4-3\eta)}{(1-\eta)^2} - TS_{ig}, \quad (2.16)$$

where $\frac{3}{2} k_B T$ is the kinetic energy per particle and r_0 is the Wigner-Seitz cell radius which satisfies

$$\frac{4\pi r_0^3}{3} = \frac{\Omega}{N}, \quad (2.17)$$

$\eta = (\pi/6)\sigma^3(N/\Omega)$ is the hard-sphere packing fraction, $\lambda \equiv 2\eta^{1/3} q r_0$, and

$$G(\lambda) = \lambda L(\lambda) / \{12\eta [L(\lambda) + \bar{S}(\lambda)e^{\lambda^2}]\},$$

$$L(\lambda) = 12\eta \left[\left(1 + \frac{\eta}{2}\right)\lambda + (1 - 2\eta) \right],$$

$$\bar{S}(\lambda) = (1 - \eta)^2 \lambda^3 + 6\eta(1 - \eta)\lambda^2 + 18\eta^2 \lambda - 12\eta(1 + 2\eta), \quad (2.18)$$

$$TS_{ig} = k_B T \ln \left[\frac{e\Omega}{N} \left(\frac{eMk_B T}{2\pi\hbar^2} \right)^{3/2} \right], \quad (2.19)$$

where $e \equiv$ natural number. The packing fraction η is the variational parameter for the liquid phase. It turns out that $\eta \approx 0.45$ at freezing, which is consistent with Ref. 11 and also consistent with other polyvalent metallic systems.¹²

III. RESULTS

We have carried out calculations for the solid phases (fcc as well as bcc) and the liquid phase at various values of the particle number densities $D = N/\Omega$, charges Z , and the salt concentrations ρ with the procedure described in the previous section. The temperature T for all calculations is kept fixed at the room temperature since most of the experiment were done at that temperature. The static dielectric constant of water is taken to be 80. The phase diagrams are determined by comparing the free energies of different phases at the same parameter (the stable phase has the lowest free energy) and the phase boundaries are taken at the crossover points of the free energies of different phases.

A. Effect of Z and ρ

In order to directly compare with experiments, we first plot the results in the D - ρ plane at different values of Z . Figure 1 shows the D - ρ phase diagram of particles with $Z = 400$ and different diameters. One can see that the colloidal suspension freezes when the particle number density is sufficiently high: The fcc phase is formed in most of the high-density region, whereas the bcc phase is stable only in a very narrow region of lower densities. The density range of the bcc phase shrinks as electrolytes are added to the solution, and the bcc phase completely disappears when the salt concentration is greater than about 2.5×10^{-8} M as seen in Fig. 1. Beside this, the addition of electrolytes will also make the crystalline phases become less favorable and eventually melt into liquid: The fcc phase always directly melts into liquid as

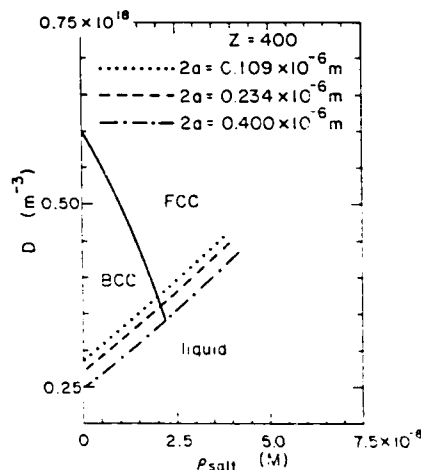
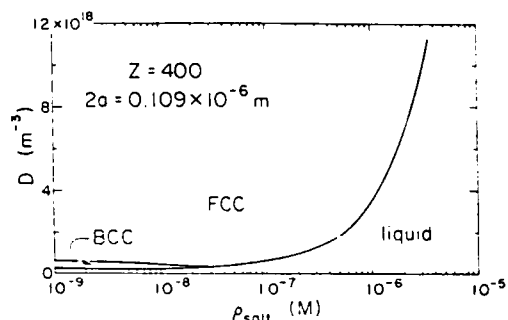


FIG. 1. D - ρ_{salt} phase diagram where D is the particle number density and ρ_{salt} is the added salt concentration in molar units; (a) for a particle diameter $2a = 0.109 \times 10^{-6}$ m and charge $Z = 400$; (b) in a different scale for $Z = 400$ and diameters $2a = 0.109 \times 10^{-6}$, 0.234×10^{-6} , and 0.400×10^{-6} m. The bcc-fcc phase boundaries are the same for the three cases while the liquid-solid phase boundaries are pushed to lower densities as the particle size is increased.

the salt concentration is increased, while the bcc phase can either transform into fcc before melting (at higher densities) or directly melts into the liquid phase (at lower densities). Note that there is no reentrant transition when the salt concentration is increased, and that the solid-liquid phase boundaries shift to higher densities when screening is increased by the addition of electrolytes.

In Fig. 2 we plot the D - ρ phase diagram for particles of the same size as Fig. 1(a) but with a smaller charge $Z = 200$. Note that the bcc region is now absent and the solid-liquid phase boundary is pushed to a higher density. (Note the scale difference in Figs. 1 and 2.) Other than that, the solid-liquid phase boundary behaves roughly the same as that in Fig. 1, i.e., the solid phase becomes unstable when screening is increased. Again, this is in agreement with experiments. The shape of the solid-liquid phase boundary resembles very much that of the gold colloids in Ref. 15. These results sug-

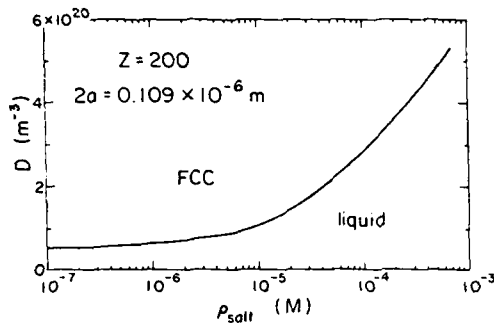


FIG. 2. D - ρ_{salt} phase diagram for particles with $Z = 200$ and $2a = 0.109 \times 10^{-6}$ m. Note that the bcc phase is missing when the particle charge is decreased. The definitions of D and ρ_{salt} are the same as in Fig. 1.

gest that the formation of a bcc crystalline phase in the colloidal suspension is a delicate matter: The bcc phase forms only when the electrolyte concentration is low and the particle charge is high, which is in agreement with experimental observations.^{3,9} To better illustrate this trend, we plot in Fig. 3, the density range of the three phases as a function of the particle charge Z at zero salt concentration. The bcc region becomes narrower and finally closes up when Z is decreased. Meanwhile, Fig. 3 also shows that a large charge can retain the crystalline phases to a lower density.

Since a high surface charge of particles enables the crystalline phases to persist at low densities, with increasing particle charge, at some point, the solid phases may exist at such low densities that some finite amount of electrolytes could provide enough screening to favor fcc phase at low densities and therefore, an fcc-bcc-fcc re-entrant transition at some nonzero salt concentration is possible as the particle number

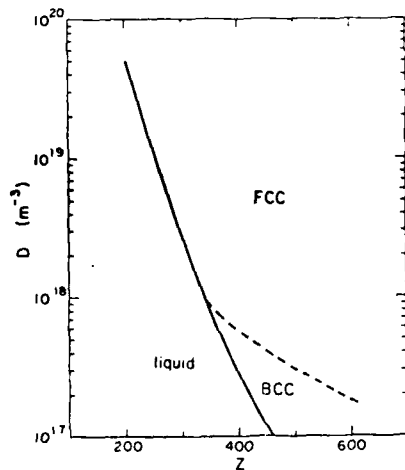


FIG. 3. The D - Z phase diagram for particles with diameter $2a = 0.109 \times 10^{-6}$ m and at zero salt concentration. bcc phase appears only when the charge Z is high and the particle number density D is low.

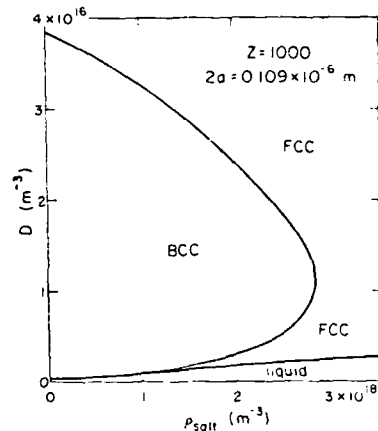


FIG. 4. The D - ρ_{salt} phase diagram for particles with diameter $2a = 0.109 \times 10^{-6}$ m and $Z = 1000$. Note that the system starts to undergo fcc-bcc-fcc transitions at fixed nonzero salt concentration when the particle number density is increased.

density is changed. Indeed, this can happen and is illustrated in Fig. 4 where particles of $0.109 \mu\text{m}$ diam with $Z = 1000$ undergo an fcc-bcc-fcc transition as the density is varied at fixed salt concentration $\rho \approx 1.3 \times 10^{18} \text{ m}^{-3}$. This can be explained as follows. At sufficiently low densities, the screening length does not vary much with the particle number density. (The major contribution to the inverse screening length comes from the added electrolyte concentration rather than the counter ions.) Under such conditions, the fcc phase is more stable at low densities because a given screening length would appear shorter when compared with the interparticle distance at low densities. We plot, as an example, in Fig. 5, the free energy difference between the fcc phase and the bcc phase as a function of the particle number density for particles of $1 \mu\text{m}$ diam and $Z = 4167$ when the inverse screening

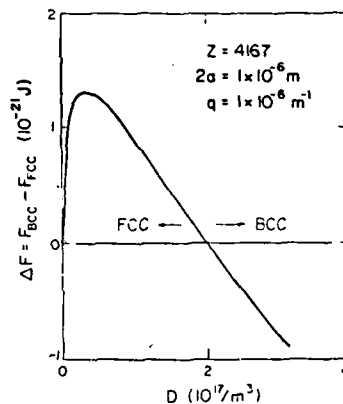


FIG. 5. Free energy difference between the fcc phase and the bcc phase as a function of the particle number density D .

length is fixed at $q = 1 \times 10^6 \text{ m}^{-1}$. As the particle number density increases, the contribution of the counter ions to the screening becomes important again. We then recover the situation where the fcc dominates at high densities. So far, we did not include the screening by the electrolytes from the water itself. This is perfectly all right when the particle number density is not too low. However, when the particle density is low, the electrolytes of pure water can contribute substantially to the screening. Thus, the reentrant transition discussed above may be washed out by the intrinsic electrolytes of pure water and it is very likely that we may not be able to see it experimentally.

B. \bar{T} - qa_s phase diagrams

If we define an effective temperature $\bar{T} = k_B T / (Z^2 e^2 / 4\pi\epsilon_0 \epsilon a_s)$ and measure the screening strength in terms of the dimensionless parameter qa_s , where $a_s = (\Omega/N)^{1/3}$ is the average nearest neighbor distance, the phase boundaries in Figs. 1-5 should then be all mapped onto the same curves on the \bar{T} - qa_s plane. The phase boundaries in the \bar{T} - qa_s plane are shown in Fig. 6. The liquid phase is stable at high \bar{T} and at large qa_s (i.e., small Z and high salt concentration). The bcc phase is preferred at small qa_s , and fcc at large qa_s . There is no reentrant transition in either the \bar{T} or the qa_s direction. The \bar{T} -independent bcc-fcc phase boundary is a result of the Debye-Hückel screened interparticle potential and can be explained as follows. First, within the physical range of \bar{T} , the internal energy difference between two crystalline phases will change sign at the same qa_s , as it does at $T = 0$. This can be seen from Eq. (2.14). The thermal vibration of the particles only magnifies the interparticle potential by a factor e^{uv} for all pairs and does not change the sign of the difference of the lattice sums of two crystalline phases which is the consequence of the Debye-Hückel screened potential. (The kinetic

energy which is $\frac{1}{2}k_B T$ for all phases is unimportant here.) For the entropy part, the Einstein frequency ω can be thought of as the average vibrational frequency of all modes and ω^2 is proportional to the average of the second derivatives of the interparticle potential at all particle sites which is $q^2 E_0$ within the Debye-Hückel approximation where E_0 is the $T = 0$ internal energy and q is the same for both phases at the same density. With the expression of TS in Eq. (2.8), one can readily see that the difference in $-TS$ between two crystalline phases has the same sign as that of the $T = 0$ internal energies and both change sign at the same qa_s . Therefore, the free energy difference between two crystalline phases always changes sign at the same qa_s , as the $T = 0$ internal energy difference. The bcc-fcc phase boundary is thus independent of \bar{T} .

C. Effect of particle size

We also plot phase boundaries of particles with $Z = 400$ but of different diameters in Fig. 1(b). First, one can see that a larger particle size moves the solid-liquid phase boundary to a lower density. The discrimination of the liquid phase by the size correction factor is precisely what prevents reentrant melting at high densities. The bcc-icc boundary is unaffected by the particle size. This size-independent bcc-icc boundary is again the consequence of the Debye-Hückel screened potential. The size correction $(e^{uv}/1 + qa_s)$ is only a multiplying factor of the lattice sum, which does not change the sign of the internal energy difference of the bcc and fcc structures and hence does not change the sign of the free energy difference is argued above.

D. Is hcp structure possible?

Finally, we check the possibility of the hcp structure at high densities since the hcp phase has the same packing frac-

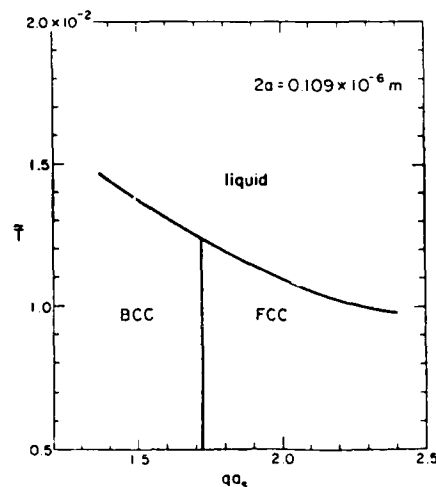


FIG. 6. The \bar{T} - qa_s phase diagram for particles with diameter $2a = 0.109 \times 10^{-6} \text{ m}$. Where \bar{T} , q , and a_s are as defined in the text.

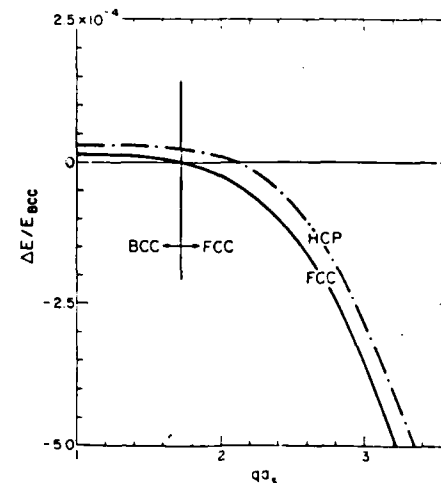


FIG. 7. The $T=0$ energy difference $\Delta E/E_{bcc}$ vs qa_s , where $\Delta E_{bcc/fcc} = E_{bcc/fcc} - E_{bcc}$.

tion as the fcc phase at close packing. It turns out that the hcp phase is not favored throughout the entire qa_s range. Since the free energy difference changes sign at the same qa_s , as the internal energy difference at $T=0$, we will show only the $T=0$ energy differences. In Fig. 7 we plot the $T=0$ internal energy difference of the hcp and bcc phases as well as of the fcc and bcc phases where $\Delta E_{\text{hcp(fcc)}} = E_{\text{hcp(fcc)}} - E_{\text{bcc}}$. One can see that at small qa_s , the bcc phase is the stable state. At large qa_s , the internal energy of the hcp is lower than that of the bcc but is still higher than that of fcc. Although, the overall packing fraction is the same for both the fcc and hcp, the difference in the arrangement of far neighbors results in the difference in energy. So far, experimentally, hcp structures have only been observed when the system is under a shear stress,⁵ which is obviously not an equilibrium state, in agreement with our results.

IV. CONCLUSIONS

We have determined the phase diagrams in the parameter space by directly comparing the Helmholtz free energies of different phases at the same parameters. The calculation of the free energies involves the use of a variational principle based on the Gibbs-Bogolyubov inequality and a Debye-Hückel-screened interparticle potential with size correction. We have shown that the colloidal suspensions can freeze into crystalline phases at higher densities. The fcc and bcc phases are the thermodynamically stable structures. The fcc phase is the dominant phase at higher densities while the bcc phase can exist at lower densities only when the particle charge is high and the salt concentration is low. Both crystalline phases will melt into liquid upon the addition of salt: fcc always melts into liquid directly, whereas bcc may transform into fcc before melting depending upon the particle number densities. No reentrant transition is found upon the addition of salt. However, highly charged particles can undergo an fcc-bcc-fcc reentrant transition at fixed nonzero salt con-

centrations when the particle number density is varied.

Our calculations have completely neglected the van der Waals attractions. This negligence is justified in the present case where the charges of the particles are in the order of 10^3 electronic charges and the densities are intermediate so that solid-liquid and bcc-fcc transitions can take place. Under such conditions, the interparticle interaction is dominated by the electrostatic potential. If the van der Waals attraction is taken into account, the phase boundaries should move to higher densities. Other than that, the phase diagram should remain qualitatively the same.

ACKNOWLEDGMENTS

The authors would like to thank W.-H. Shih for valuable discussions. This work was sponsored by the Defense Advanced Research Projects Agency of the Department of Defense and was monitored by the Air Force Office of Scientific Research under Grant No. AFOSR-83-0375.

- ¹For a review, see P. Pieranski, *Contemp. Phys.* **14**, 25 (1983).
²W. Luck, M. Klier, and H. Wesslau, *Ber. Bunsenges. Phys. Chem.* **57**, 75 (1963).
³P. A. Hiltner and I. M. Krieger, *J. Phys. Chem.* **73**, 2386 (1969).
⁴R. Williams and R. S. Crandall, *Phys. Lett. A* **48**, 225 (1974).
⁵B. J. Ackerson and N. A. Clark, *Phys. Rev. Lett.* **46**, 123 (1981).
⁶N. A. Clark, A. J. Hurd, and B. J. Ackerson, *Nature* **281**, 59 (1979).
⁷H. M. Lindsay and P. M. Chaikin, *J. Chem. Phys.* **76**, 3774 (1982).
⁸T. Yoshizawa, I. Sogami, and N. Ise, *Phys. Rev. Lett.* **53**, 2153 (1984).
⁹D. J. W. Aastuer, N. A. Clark, L. K. Cotter, and B. J. Ackerson, *Phys. Rev. Lett.* **57**, 1733 (1986).
¹⁰P. M. Chaikin, P. Pincus, and S. Alexander, *J. Colloid Interface Sci.* **89**, 555 (1982); D. Hone, S. Alexander, P. M. Chaikin, and P. Pincus, *J. Chem. Phys.* **79**, 1474 (1983).
¹¹W.-H. Shih and D. Stroud, *J. Chem. Phys.* **79**, 6254 (1983).
¹²Wan Y. Shih and D. Stroud, *Phys. Rev. B* **32**, 7779, 7785 (1985).
¹³See, for example, R. P. Feynman, *Statistical Mechanics* (Benjamin, New York, 1972); A. Ishara, *J. Phys. A* **1**, 539 (1968); D. J. Edwards and J. Jarezynski, *J. Phys. C* **5**, 1745 (1972).
¹⁴B. Firey and N. W. Ashcroft, *Phys. Rev. A* **15**, 2072 (1977).
¹⁵K. Takano and S. Hachisu, *J. Colloid Interface Sci.* **66**, 130 (1978).

APPENDIX XXIII
**A Reversible Growth Model: Cluster-Cluster
Aggregation with Finite Binding Energies**

(Shih, Aksay, and Kikuchi 1987b)

*A Reversible Growth Model: Cluster-Cluster Aggregation With
Finite Binding Energies*

Wan Y. Shih, Ilhan A. Aksay, and Ryoichi Kikuchi

Department of Materials Science and Engineering
University of Washington
Seattle, Washington 98195

Resubmitted August 3, 1987
Physical Review A

PACS numbers: 64.60.Cn, 05.40 + j, 68.70 + w, 82.70 Dd.

Abstract

A reversible growth model is built by modifying the cluster-cluster aggregation model with a finite interparticle attraction energy $-E$. When E is ∞ , the aggregation is described by the ordinary cluster-cluster aggregation model. Within our model, particles as well as clusters are performing Brownian motion according to the rate $1/\tau_D$, and the unbinding takes place according to $\frac{1}{\tau_R} e^{-\Delta E/T}$, where ΔE is the energy change due to the unbinding, T is the room temperature, and τ_R is the time constant associated with the unbinding. By changing E and τ_R/τ_D , we are able to change the aggregation behavior over a wide range from ramified clusters to compact ones. Moreover, due to a finite E , ramified aggregates may become compact at a later time. We show that the initially fractal aggregates can remain fractal objects during restructuring while the fractal dimension D increases with time. At large E , D can stay at some value that is larger than the value of the cluster-cluster aggregation model and can remain unchanged for a long time. At a given time, D increases drastically with decreasing E from the value of the cluster-cluster aggregation model when $E \leq 3 T$. The curve of the estimated sedimentation density vs. E resembles that of D vs. E and agrees with the experiments.

I Introduction

Under suitable conditions, fine colloidal particles ($\sim 50 \text{ \AA}$ -- $\sim 1 \mu\text{m}$ in diameter) can form aggregates of a fairly large size (up to several thousand particles). Extensive light, X-ray, and neutron scattering experiments¹⁻⁶ showed that these aggregates are fractal objects and that the fractal dimension D varies with the experimental condition: $D = 1.75$ [Refs. 2, 4, 6] when the clusters grow rapidly and $D = 2.02-2.12$ [Refs. 1, 3, 5] when the growth is slow. Furthermore, when light scattering measurements were taken repeatedly in a temporal sequence, it was found that aggregates with an initially lower D (1.75) can restructure to a higher D (2.08-2.1 [Ref. 4], 2.4 [Ref. 6]) at a later time. This signifies that the growth processes involve some reversibility. Some critical questions then arise: How do the structures of these aggregates change with time? Do these aggregates remain fractal objects during restructuring? If so, how does the fractal dimension D change with time?

The cluster-cluster aggregation (CCA) model^{7,8} which yields $D = 1.78(1.4)$ in $3(2)d$, where d is the Euclidean dimension, seems to agree with the colloidal aggregates of rapid growth. When the CCA model is modified with a sticking probability p and when p is approaching zero,⁹ it produces clusters of $D = 2.0(1.55)$ in $3(2)d$ and is often compared with the aggregates from slow processes. Although Ref. 9 gives a fractal dimension close to that of the colloidal aggregates by slow growth, it cannot account for the restructuring observed in the experiments because of its irreversible nature. Kolb et al.¹⁰ have considered a reversible growth model by modifying the CCA model with random bond breaking which yielded $D = 2.03(1.57)$ in $3(2)d$ at dynamic equilibrium; however, they did not observe the change of D with time.

The purpose of this study is (1) to construct a more realistic reversible growth model which involves the rearrangement of particles from energetic consideration rather than random bond breaking and (2) to investigate the restructuring of aggregates with computer simulations. The direct observations of the colloidal clustering under an optical microscope¹¹ showed that under weakly attractive conditions, a particle can join and leave a cluster repeatedly and that a particle with fewer bonds is more active than one with more bonds. Furthermore, the compaction of a colloidal sediment can occur upon the decrease of the interparticle attraction.¹² These observations plus other flocculation studies¹³ suggest that the interparticle attractions play an important role in aggregation.

II Model

Since the CCA model seems able to describe the colloidal clusters grown from the rapid processes, we build our model by combining the CCA model with a finite nearest-neighbor attraction energy $-E$. The unbinding process is simulated with the Monte Carlo method. For convenience, the calculations are performed in 2d. The procedure is as follows. Initially N particles are placed randomly in an $M \times M$ square lattice with periodic boundary conditions. The particles and the clusters are performing Brownian motion (random walk). After each time interval τ_D , all particles and clusters move one lattice constant. For simplicity, we assume all clusters to have the same mobility since this does not change the scaling properties.^{7,14} When two clusters collide, they stick together forming a larger cluster and then move on as a whole.

Moreover, because of its thermal motion a particle can unbind from its neighbors according to the rate $\frac{1}{\tau_R} e^{-\Delta E/T}$, where τ_R is the time constant associated with the unbinding process, T is the room temperature, and ΔE is the energy change due to the unbinding. We assume $\Delta E = nE$ where n is the number of neighbors of that particle, 1 to 3 in the case of a square lattice. Particles with four neighbors are not allowed to unbind in this case. In practice, the unbinding transition of every particle is examined after each time interval τ_R with a probability $e^{-nE/T}$. If $e^{-nE/T}$ is larger than a random number, the transition is accepted or otherwise rejected. When the unbinding is accepted, the particle moves one lattice constant in one of the rest of the $4 - n$ directions at random and the cluster is divided into segments. The resulting number of segments ranges from two to four depending on the number of neighbors bonded to that particle and on the configuration of the cluster before the break-up. For example, the break-off of a double-bonded particle in the neck portion of the cluster can result in as many as 3 segments, namely, one particle and two other parts. Each segment will then diffuse as an independent cluster and will stick to whatever it collides into later on. In our calculations, we do not allow particles or clusters to rotate. However, we do not expect the rotations to affect the scaling properties.¹⁵

By varying E and τ_R/τ_D , we are able to change the growth behavior over a wide range. The CCA model corresponds to a special case when $E = \infty$. The parameter τ_R is the inverse of the unbinding attempt frequency while τ_D is related to the diffusivity of the particles in the solution and is used in normalizing the time scale. A large τ_R/τ_D may be interpreted as a higher particle mobility relative to relaxation and is analogous to the quenching rate in the glass transition.

III Results

We show as examples in Figure 1 three different aggregation conditions initiated with the same number densities but with different values of E and τ_R/τ_D . Figure 1(a) is the case when $E = 1.5 T$ and $\tau_R/\tau_D = 0.2$ in which large aggregates can hardly be formed. Figure 1(b) shows the case when $E = 1.5 T$ and $\tau_R/\tau_D = 2$ where aggregates are formed but there are still quite a number of particles left in the fluid phase throughout the simulation. In Fig. 1(c), we show the case when $E = 3.5 T$ and $\tau_R/\tau_D = 2$ in which almost no free particles are left in the solution and the cluster looks more ramified. Figures 1(a), (b), and (c) together show the general trend that cluster size increases with increasing E and τ_R/τ_D .

At a given number density, as E decreases, the cluster size decreases and the fluid phase becomes more favored due to more efficient relaxation. In Fig. 2, we show the saturated cluster size as a function of E for three different cases. The fact that the logarithm of the cluster size is linear with E for all cases indicates that the cluster size decreases exponentially with E . This means that the actual aggregates cannot grow to an infinite size because of the finite coupling energy. Meanwhile, it is worth noting that the cluster size also increases with increasing τ_R/τ_D or particle concentration, both of which are similar to increasing quenching rate. However, we will show later that only E affects the restructuring behavior of clusters with respect to time.

To investigate the effect of restructuring we use two different procedures: (1) We start with clusters of various sizes N grown from the CCA model at the same number density and turn on the relaxation. To show the restructuring effect this way is mainly for the case of

comparison, although it may appear unnatural at the first sight (there seems to be a sudden change in E from $-\infty$ to some finite value at $t = 0$). What this procedure really represents are the cases where τ_R/τ_D is large enough, i.e., the aggregation is much faster than the relaxation so that initially the aggregates are not very different from those of the CCA model. (2) We have also studied the structural evolution of aggregates during growth. This can be achieved by choosing smaller values of τ_R/τ_D so that sufficient unbinding is taking place along with cluster growth. We will show later that the results of the two procedures are quite similar.

For each set of E and τ_R/τ_D , $\log N$ is plotted against $\log R_m$ in every $100 \tau_D$ where R_m is the maximum radius of a cluster and is defined as

$$R_m = \frac{1}{2} \max_{i,j} |\vec{r}_i - \vec{r}_j|. \quad (1)$$

In each N vs. R_m plot, we include 11-14 data points in the range $30 \leq N \leq 200-300$; each point is the result of averaging over ten samples. It turns out that the curves are linear throughout the simulation and the slope of the lines increases with time. An example done with procedure (1) is given in Fig. 3. Note that for a given N , the corresponding R_m is decreasing with time, indicating that the clusters are getting denser and denser. The $t = 500 \tau_D$ and the $t = 10000 \tau_D$ plots remain linear while the slope is increasing with time: 1.35 at $t = 0$, 1.46 at $t = 500 \tau_D$, and 1.63 at $t = 10000 \tau_D$. This suggests that the clusters remain fractal during restructuring but that the fractal dimension is increasing with time.

We then take as the fractal dimension the slope of the $\log N$ vs. $\log R_m$ lines by least square fit. The $t = 0$ plot which represents clusters grown from the CCA model thus has a

fractal dimension $D = 1.35 \pm 0.05$, in agreement with the values obtained in Refs. 7 and 8 within numerical errors. We have also plotted $\log N$ vs. $\log R_g$ (not shown) where R_g is the radius of gyration and is defined as

$$R_g = \frac{1}{2N^2} \sum_{\substack{i,j \\ (i \neq j)}}^N |\vec{r}_i - \vec{r}_j|. \quad (2)$$

Generally, the fractal dimension D obtained from the $\log N$ vs. $\log R_g$ plots are somewhat larger (by about 0.05 on the average) than that of the $\log N$ vs. $\log R_m$ plots; however, the difference is comparable with the numerical error bars. The values of D reported in this paper are all based on the N vs. R_m plots.

In Figure 4, we plot D vs. t for various values of E and τ_R/τ_D . In Fig. 4(a), we have chosen a small value of $\tau_R/\tau_D = 0.5$ and used procedure (2). Because of the small values of τ_R/τ_D and E , the unbinding is taking place sufficiently along with cluster growth. In fact, when we stopped monitoring, i.e., at $t = 1000 \tau_D$, the clusters were still growing. Thus, Fig. 4(a) can be regarded as the structural evolution of aggregates during growth and will be compared with Fig. 4(b) which is obtained by using the same value of E but a different value of τ_R/τ_D and procedure (1). In spite of different procedures used, the two curves look similar and the only difference is in the time units. Thus, varying τ_R/τ_D only changes the time scale but not the behavior of D vs. t . When E is increased, the change of D becomes slower, as is shown in Figs. 4(c)-(e), which are obtained by procedure (1). Note that Figs. 4(d) and (e) both have the same value of D which is 1.35 at $t = 0$ because we start with the same initial clusters for the purpose of comparison. In Figs. 4(d) and (e), D quickly increases from the CCA value

and then saturates at some value D' while D' decreases with increasing E : $D' = 1.5$ for $E = 2.5 T$, $D' = 1.42$ for $E = 3 T$. This indicates that under suitable conditions aggregates can have a fractal dimension D that is substantially larger than the CCA value and D remains unchanged over a long period of time, which has been observed experimentally.⁴

We plot in Fig. 5, D vs. E for $\tau_R/\tau_D = 5$ at $t = 5000 \tau_D$ and at $t = 10000 \tau_D$ to show the different restructuring rates at different E . It is clearly shown that the change of D with time is accelerated when E is decreased from $3 T$. Also note that for a given t , D remains close to the CCA value at large E but drastically increases from that at around $E \leq 3 T$. If we take D as a rough measurement of the densities of the agglomerated solids, we would expect a similarly drastic change in the density when the interaction energy is varied. Indeed, this has been observed in flocculated colloids.¹² We show the relation between the zeta potential of the particles and the sedimentation density in Fig. 6 which is taken from Ref. 12. In a charged colloidal system, the interparticle interaction is the sum of (1) the screened Coulomb repulsion and (2) the van der Waals attraction. The screened Coulomb repulsion can be varied over a wide range by adjusting the pH, the salt concentration, and so on, while van der Waals attraction remains more or less unchanged. Thus, under certain pH and salt concentrations, when the screened Coulomb repulsion is sufficiently reduced, a net interparticle attractive potential well can develop. The data points in Fig. 6 were taken under such conditions. The magnitude of the square of the zeta potential ζ^2 can serve as a rough measure of the screen Coulomb repulsion at a fixed salt concentration:¹² The higher the value of ζ^2 , the stronger the Coulomb repulsion. Therefore, in Fig. 6, a smaller value of ζ^2 represents a deeper attraction well. It is shown that at small values of ζ^2 (larger net attractions) the sedimentation density

is very low and that the sedimentation density increases at larger values of ζ^2 (smaller net attractions). Note that the sedimentation density does not change much until the zeta potential reaches some critical value ζ_{cr} around which the sedimentation density increases by many folds.

In order to estimate the sedimentation density from our calculations, we assume the sediments to be composed of blobs of some 175 particles and the sedimentation density is approximated to be $175/(\pi R_m^2)$ where R_m is taken from the calculations at $10000 \tau_D$. This is not unreasonable since the aggregates start to settle to the bottom when they reach a certain size. The results are plotted in Fig. 7. One can see that the estimation closely resembles the experimental curve in Fig. 6.

IV Summary

To summarize, we have built a reversible growth model in which nearest neighbors have a finite attraction energy $-E$ so that the rearrangement of particles is possible. By varying E , τ_R/τ_D , and the particle concentration, we are able to change the aggregation condition over a wide variety. The restructuring behavior is mainly affected by E . We show that the aggregates can remain fractal during restructuring while the fractal dimension D is increasing with time. When E is large, the change of D becomes so slow that D stays at some intermediate value D' and remains unchanged for a long time while D' decreases with E . In the D vs. E plot we show that D increases drastically from the CCA value at around $E \approx 3T$ and is getting closer

to d as E is decreased. We have also estimated the sedimentation densities from our calculations. The estimated sedimentation density vs. E closely resembles the experimental curve.

In principle, the results we have just shown should readily apply to a variety of systems, since our model is quite general. However, the colloids seem to be ideal to test our results. The reasons are the following: first, the interaction between the colloidal particles can be varied easily over a wide range by changing the particle surface potential (zeta potential), the salt concentration in the solvent, or the extent of steric interaction when they are coated with polymeric units. Secondly, the size of the colloidal particles can also be varied in a wide range, which is equivalent to changing the particle mobility and is somewhat related to the change of the parameter of τ_R/τ_D in our model.

Acknowledgments

The authors would like to thank Wei-Heng Shih for various discussions. This research was supported by the Air Force Office of Scientific Research (AFOSR) and the Defense Advanced Research Projects Agency (DARPA) of the Department of Defense and was monitored by the AFOSR under Grant No. AFOSR-83-0375.

References

1. D.A. Weitz, J.S. Huang, M.Y. Lin, and J. Sung, Phys. Rev. Lett. **54**, 1416 (1985).
2. D.A. Weitz and M. Olivera, Phys. Rev. Lett. **52**, 1433 (1984).
3. D.A. Schaefer, J.E. Martin, P. Wiltzius, and D.S. Cannell, Phys. Rev. Lett. **52**, 2371 (1984).
4. C. Aubert and D.S. Cannell, Phys. Rev. Lett. **56**, 738 (1986).
5. J.C. Rarity and P.M. Pusey, *On Growth and Form* (1986) Martinus Nijhoff, Dordrecht, p. 219.
6. P. Dimon, S.K. Sinhar, D.A. Weitz, C.R. Safinya, G. Smith, W.A. Varady and H.M. Lindsay, Phys. Rev. Lett. **57**, 595 (1986).
7. P. Meakin, Phys. Rev. Lett. **51**, 1119 (1983).
8. M. Kolb, R. Botet, and R. Jullien, Phys. Rev. Lett. **51**, 1123 (1983).
9. M. Kolb and R. Jullien, Phys. Lett. (Paris) **45**, L977 (1984).

10. M. Kolb, R. Botet, R. Jullien and H.J. Herrmann, **On Growth and Form** (1986, Martinus Nijhoff, Dordrecht), p. 222.
11. G.Y. Onoda, *Phys Rev. Lett.* **55**, 226 (1985).
12. I.A. Aksay and R. Kikuchi, **Science of Ceramic Chemical Processing**, (1986, John Wiley and Sons, New York), p. 513.
13. J.A. Long, D.W.J. Osmond, and B. Vincent, *J. Colloid Interface Sci.* **42**, 545 (1973); C. Cowell and B. Vincent, *ibid.*, 518 (1982).
14. P. Meakin, **On Growth and Form**. (1986, Martinus Nijhoff, Dordrecht), p. 111.
15. P. Meakin, *Phys. Rev. A* **27**, 604 (1983).

Figure Captions

Fig. 1. Temporal evolution of various aggregation conditions with 212 particles in a 50×50 square lattice (a) $E = 1.5 T$ and $\tau_R/\tau_D = 0.2$, (b) $E = 1.5 T$ and $\tau_R/\tau_D = 2$, (c) $E = 3.5 T$ and $\tau_R/\tau_D = 2$.

Fig. 2. N_m vs. E/T , where N_m denotes the largest cluster, (o) at $\rho = 0.051$, $\tau_R/\tau_D = 5$, (Δ) at $\rho = 0.125$, $\tau_R/\tau_D = 2$ and () at $\rho = 0.11$, $\tau_R/\tau_D = 2$ where ρ denotes the density.

Fig. 3. N vs. R_m where N is the cluster size and R_m is the maximum radius in units of the lattice constant as defined in the text.

Fig. 4. D vs. t for various cases where D is the fractal dimension and t is the time.

Fig. 5. D vs. E for $\tau_R/\tau_D = 5$, (o) at $t = 10000 \tau_D$ and (Δ) at $t = 5000 \tau_D$.

Fig. 6. The variation in the sedimentation density (relative to the total volume) of the colloidal solids as a function of $(\zeta/\zeta_{cr})^2$ where ζ_{cr} is the zeta potential at the critical point.¹²

The insert is the scanning electron micrograph of particle clusters formed at low ζ values.

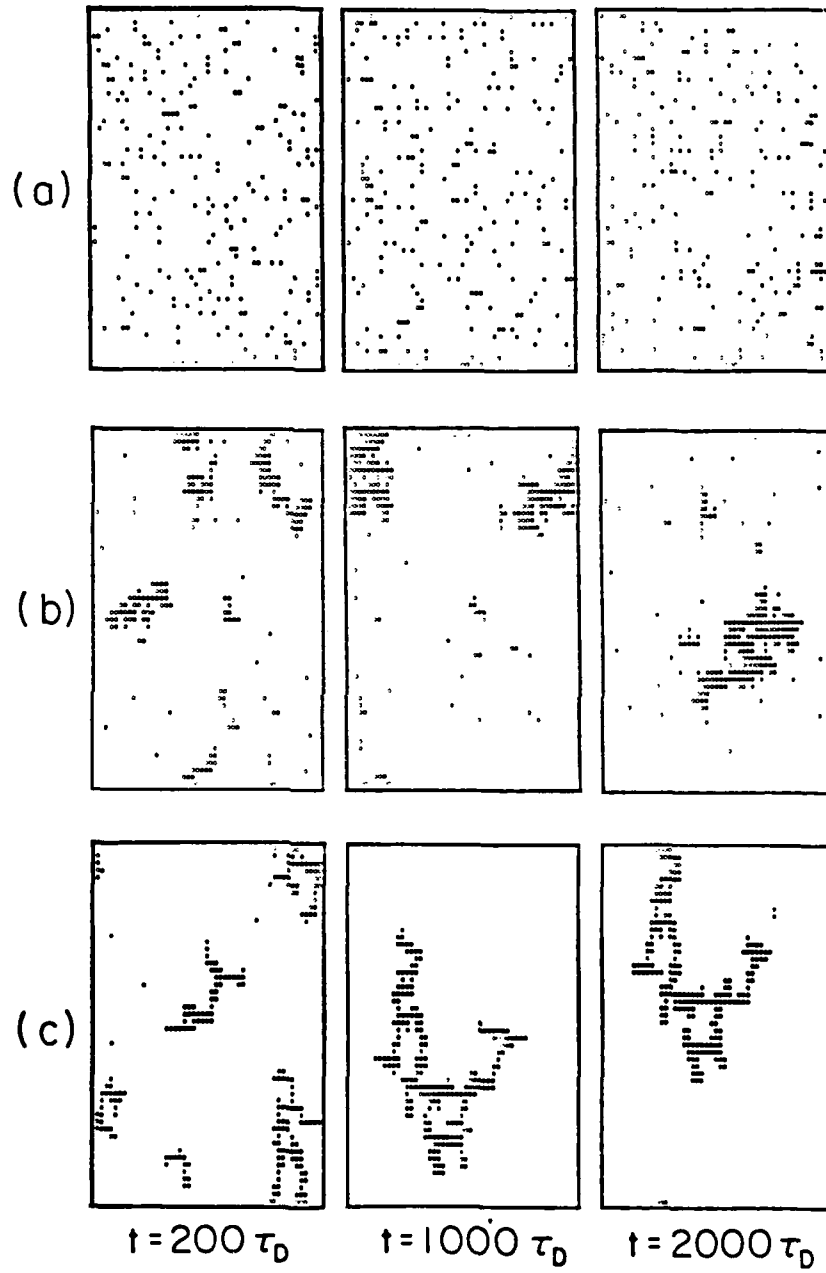


Figure 1

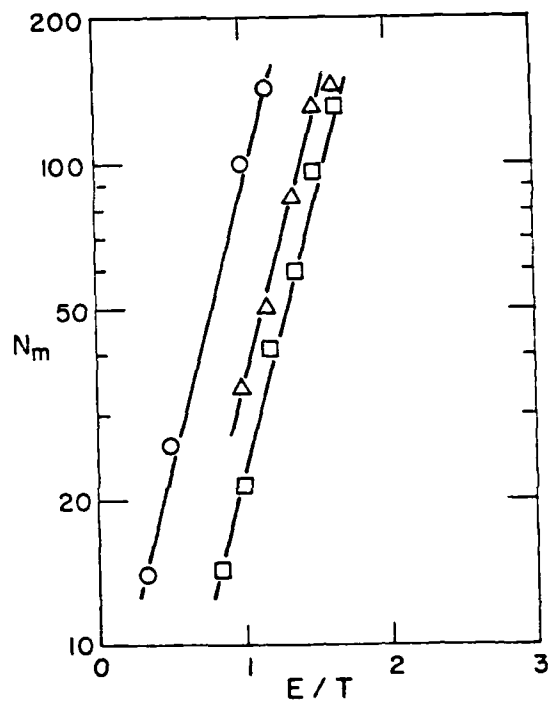


Figure 2

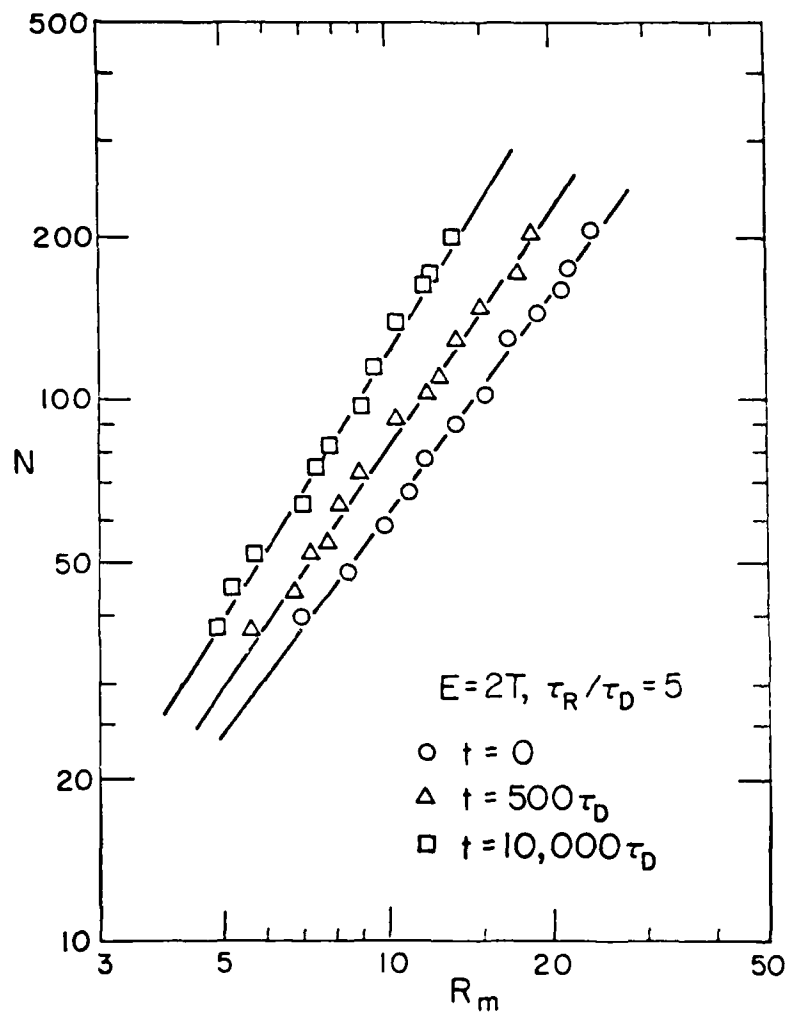


Figure 3

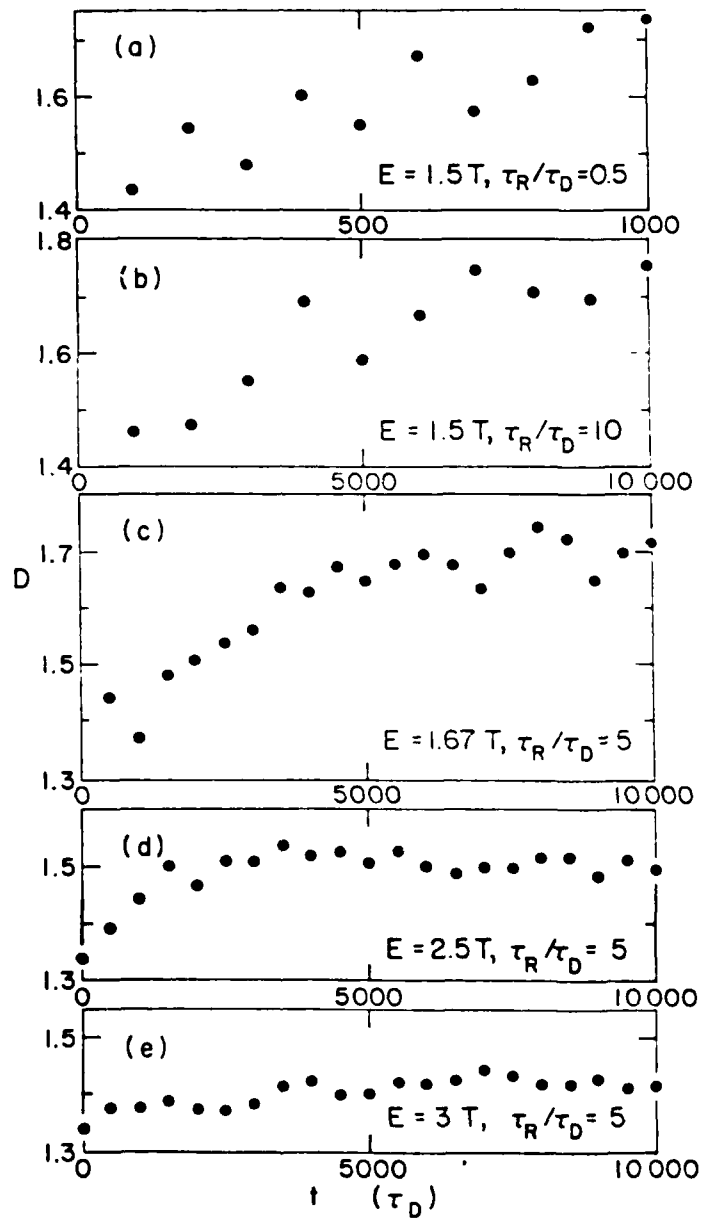


Figure 4

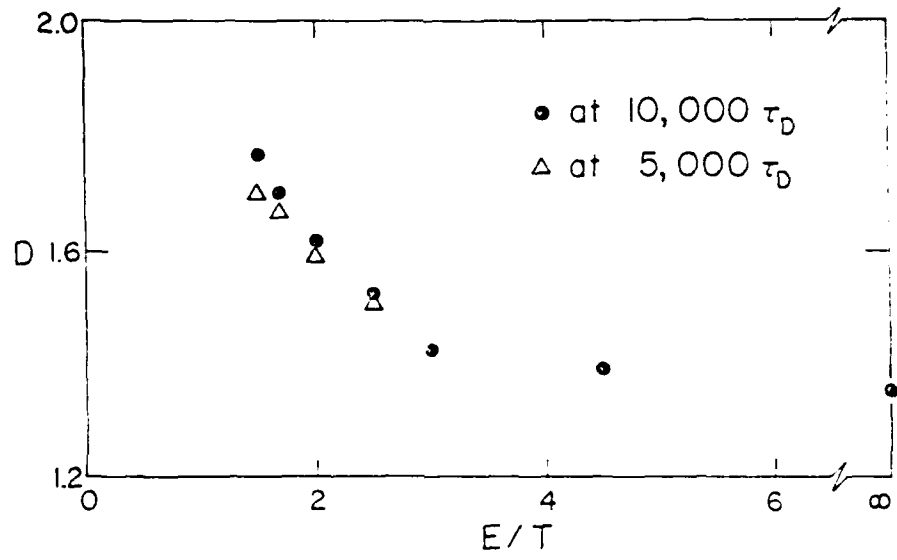
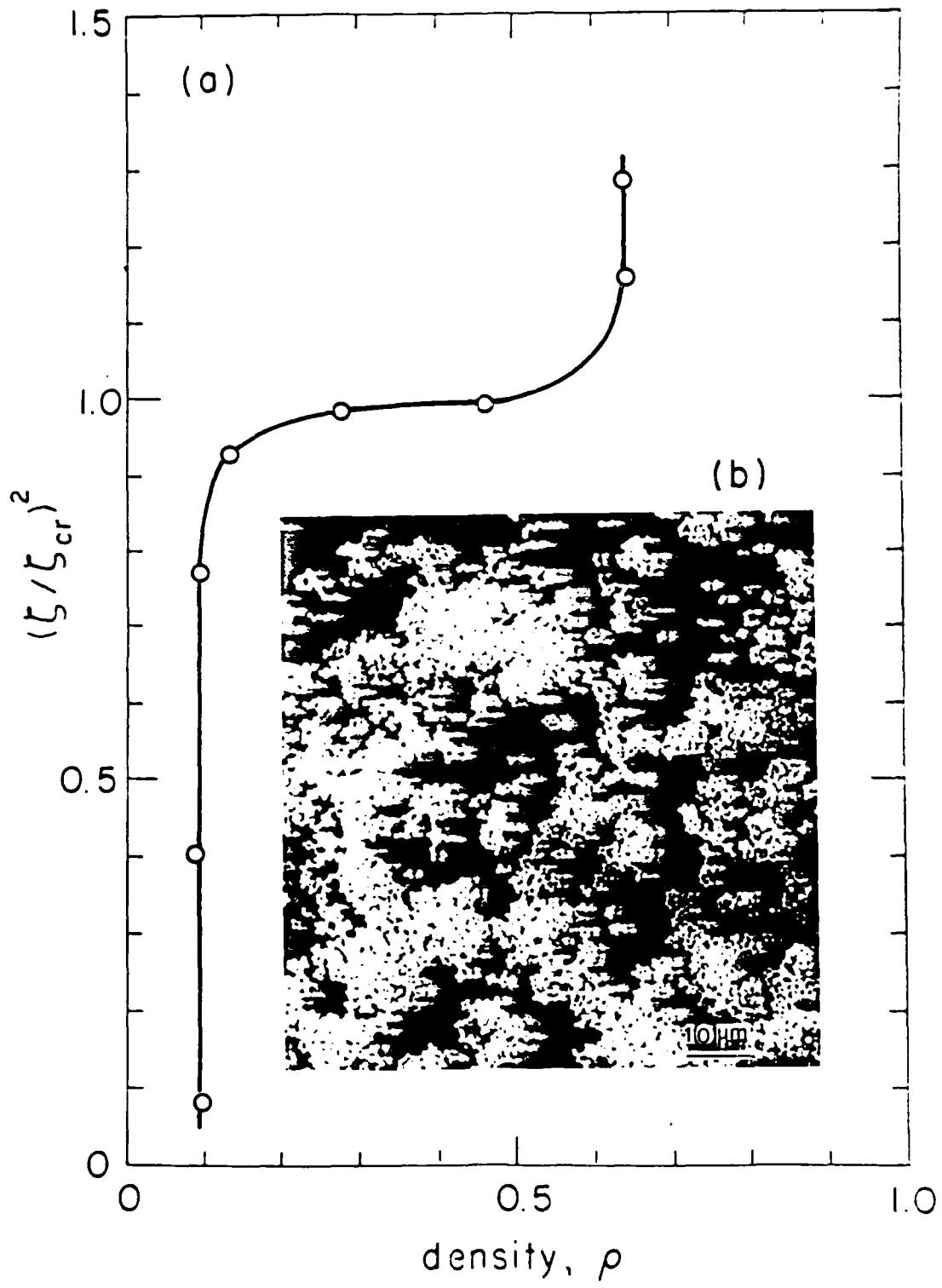


Figure 5

Figure 6



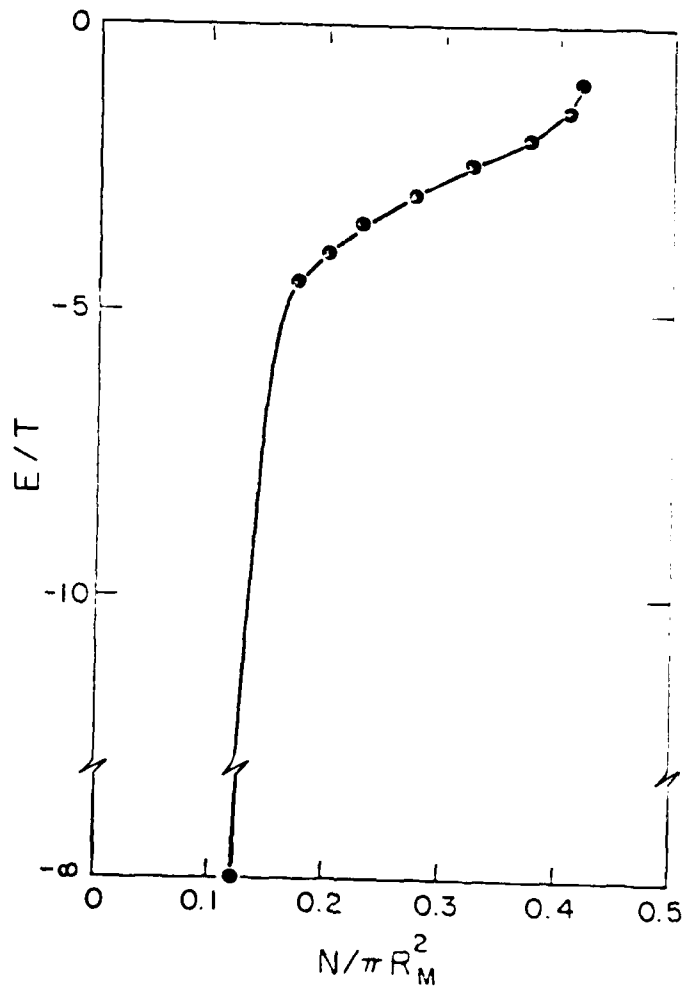


Figure 7

APPENDIX XXIV
Colloidal Processing of Ceramics

(Aksay, Shih, and Sarikaya 1987)

COLLOIDAL PROCESSING OF CERAMICS WITH ULTRAFINE PARTICLES

I. A. Aksay, W. Y. Shih, and M. Sarikaya

Department of Materials Science and Engineering
College of Engineering
University of Washington
Seattle, Washington 98195

Submitted to

Third International Conference
on Ultrastructure Processing
of Ceramics, Glasses, and Composites
San Diego, California
February 23-27, 1987

COLLOIDAL PROCESSING OF CERAMICS WITH ULTRAFINE PARTICLES

I. A. Aksay, W. Y. Shih, and M. Sarikaya

Department of Materials Science and Engineering
College of Engineering
University of Washington
Seattle, Washington

INTRODUCTION

Recent advances in the development of ceramic matrix composites have illustrated the importance of microdesigning increasingly complex systems for structural, electronic, magnetic, and optical applications. The trend is in the direction of tailoring composites that display spatial resolution in the submicrometer range.¹ In accordance with this trend, the work that we reported in the first two proceedings of this conference series on Ultrastructure Processing emphasized the role of colloidal dispersion and consolidation techniques in tailoring microstructural features of ceramic systems in the 10^{-4} to 10^{-7} m range.^{2,3} In these studies, we examined the process of colloidal consolidation from a fundamental point of view and introduced an equilibrium phase diagram that provided an all inclusive treatment of phase stability in colloidal systems.³ Further, we presented our experimental observations on the metastable hierarchical features of the colloiddally consolidated systems which played a key role in our generalized treatment of the colloidal phase transitions.

In this chapter, we expand the scale of our interest to the nanometer ($< 10^{-7}$ m) range to illustrate the unifying features of colloidal processing in the micrometer vs. nanometer range. Since the formation of hierarchically clustered structures in colloiddally consolidated systems appears to be a rule rather than an exception, we now more critically examine (i) the conditions that result in the formation of particle clusters and their networks, and (ii) the role that hierarchically clustered structures play in the processing of ceramic systems. First, we briefly summarize the implications of the equilibrium phase diagram. Next, we summarize the predictions of a reversible cluster growth model which accu-

rately accounts for the energetic and entropic effects leading to the formation of low density clusters and their restructuring. Last, we emphasize the practical aspects of ceramics processing by illustrating the role that hierarchical clustering plays in the evolution of nanostructural features. The $\text{SiO}_2\text{-Al}_2\text{O}_3$ system is used to illustrate the concepts.

PHASE STABILITY IN COLLOIDAL SYSTEMS

Our prior work illustrated that in colloidal systems of only one type of particles, one component equilibrium phase diagrams familiar to us in the atomic systems can be used to outline the onset of transitions from a stable suspension (colloidal fluid) to consolidated (colloidal solid) state in a generalized form as a function of two intrinsic variables: (i) the reduced temperature, kT/E , where k is the Boltzmann constant, T is the thermodynamic temperature, and E is the interaction potential between particles; and (ii) the particle number density, i.e., solids content, of the suspension (Fig. 1).³ Here, the colloidal fluid refers to the state of a dispersed suspension or "slip" that generally displays a low viscosity. The colloidal solid refers to the consolidated or "cast" state of a significantly higher viscosity that is subsequently transformed into a denser component through sintering.

Two aspects of this phase diagram are of practical importance in colloidal processing. The first one relates to the preparation of low viscosity suspensions, i.e., "slips"; and, the second one relates to the packing density of the consolidated structures, i.e., "casts". Both of these issues are of prime importance since in many processing applications it is advantageous (i) to work with suspensions that contain high solids contents (> 60 vol. %) but low viscosities (< 1 Pa-s), and (ii) to consolidate these suspensions into densely packed states. On the first issue, the model³ used in the calculation of the phase diagram in Fig. 1(a) predicts (and it is experimentally confirmed⁴⁻⁶) that dispersed suspensions of high solids loadings (> 50 v/o) can only exist above a critical interaction potential. Typically, these dispersed suspensions display low viscosities; thus, the supercritical range is highly preferred in the preparation of low viscosity and highly concentrated slips.⁷ In contrast, below the critical

point, particles readily cluster at significantly lower solids loadings (< 10 v/o), and these low density clustered (i.e., flocculated) networks generally display significantly higher viscosities than the dispersed suspensions. Therefore, the supercritical range is preferred for forming processes where the use of low viscosity suspensions with high solids loadings is required, and the subcritical range is avoided.

On the second issue, it is predicted that regardless of the interaction potential the formation of high packing density casts (Fig. 1(a)) is expected if a colloidal system can attain its equilibrium (i.e., the lowest free energy) state. However, these equilibrium packing densities are never attained experimentally (Fig. 1(b)).^{3,8} This discrepancy is due to the formation of metastable hierarchically clustered particle compacts during the transition from the dispersed to consolidated state.^{2,3} Consequently, in such hierarchically clustered structures, the classification of the void space follows a similar trend as first, second, third, and higher generation voids. In the supercritical range, the hierarchy is generally observed only to the second generation, and, typically, average packing densities of ~ 0.64 are obtained with monosize particles (Fig. 1(b)). In the subcritical range, however, the existence of third and higher generation voids results in significantly lower packing densities than those predicted by the equilibrium phase diagram of Fig. 1(a). These second and higher order voids become responsible for the higher sintering temperatures and shrinkages than are intrinsically possible if dense packing could be achieved.⁹⁻¹¹

Once again, in forming processes where high density packing and thus low temperature sintering is required, it becomes undesirable to work in the subcritical range, and this provides another justification for avoiding flocculated systems. Although flocculated systems have been avoided in the past, in the following sections we will show that it is difficult to totally avoid the subcritical range, especially in the nanometer range. In such cases, a solution must be found to the high viscosity and low packing density problems discussed above.

DENSIFICATION OF FRACTAL CLUSTERS AND NETWORKS

The formation of low density networks in the subcritical range has been the subject of numerous studies.¹² In particular, the most recent studies on the kinetics of particle clustering in colloidal systems have emphasized the fractal aspects of multiple clusters formed either by rapid or slow growth processes.¹³ Experiments showed that when the clusters grow rapidly the density is low with a fractal dimension $D = 1.75$;¹⁴ and when they grow slowly, the density is higher with $D = 2.02-2.12$,¹⁵ where $D = 3$ corresponds to the densest packed state in 3d.

It has also been shown that, under certain conditions, clusters that are initially at a low density state may densify with time to yield a higher fractal dimension (e.g., $D = 2.4$).¹⁴ This restructuring to a denser state suggests the possibility of attaining densely packed structures even in the subcritical region. Since the conditions that yield restructuring of fractal clusters and their networks to higher densities are not clearly understood, in a recent study we have simulated the process of restructuring with the Monte Carlo method in order to determine the parameters that play a key role in the densification process.¹⁶ As summarized below, the model accurately mimics the experimental results and predicts that in colloidal systems of weakly interacting particles it is possible to achieve high packing densities.

The model used in the Monte Carlo simulations¹⁶ is a modified form of the cluster-cluster (CL-CL) aggregation model.^{17,18} In order to facilitate unbinding and restructuring of clusters, we introduce a Boltzmann factor $e^{-nE/T}$ where n is the coordination number of an unbinding particle, $-E$ is the interparticle attraction energy, and T is the laboratory temperature (Fig. 2). The unbinding transition of each particle in a square lattice is examined after a time interval of τ_R with a probability $e^{-nE/T}$. If $e^{-nE/T}$ is larger than a random number, the transition is accepted, or otherwise it is rejected. If unbinding is accepted, the particle moves at random one lattice constant in one of the rest $4-n$ directions while the cluster is divided into one to four segments depending on the configuration. Each particle or segment then diffuses as an independent unit and may cluster with other units at a later collision. The particles or clusters alone perform Brownian motion with a time interval of τ_D . Thus, the parameter τ_R

is the inverse of the unbinding attempt frequency while τ_D is related to the diffusivity of the particles or clusters in the suspension and is also used to normalize the time scale. The dimensionless quantity τ_R/τ_D is analogous to the quenching rate of transitions from fluid to solid phase. A high τ_R/τ_D implies higher particle or cluster mobility that is relative to relaxation, i.e., a rapid quenching rate.

In Fig. 3, we plot the fractal dimension D (in 2d) vs. E determined through the computer simulation for $\tau_R/\tau_D = 5$ at $t = 5,000 \tau_D$ and at $t = 10,000 \tau_D$. Since D is a rough estimate of the cluster density, the relationship in Fig. 3 can also be viewed as a density vs. E profile. The striking similarity between this computer simulated density profile and the experimentally determined profile of Fig. 1(b) supports the appropriateness of the parameters and the procedure used in the simulation. We may now use this model to predict the behavior of colloids in general with respect to the parameters E and τ_R/τ_D . The binding energy E which appears in the Boltzmann factor is the key parameter that affects the extent of restructuring. When E is large, the probability of unbinding is small and restructuring is less significant. As a result, at large E ($> 3T$), D is low and remains close to the CL-CL value (Fig. 3). In contrast, with decreasing E , restructuring becomes more significant and D increases with time towards the dense packing value of 2 (in 2d).

The second parameter τ_R/τ_D mainly affects on the rate of restructuring. Fig. 4 shows that for a low E value a high density state is achieved in a shorter time when τ_R/τ_D is small (Fig. 4(a)). Thus, this simulation implies that if we retain both E and τ_R/τ_D at a low value, it is possible to achieve densely packed structures even with the flocculated networks of the subcritical regime.

We may now combine the results of this simulation with the equilibrium phase diagrams observed in highly repulsive systems to suggest the form of a nonequilibrium phase diagram of V/kT vs concentration as shown in Fig. 5 where V denotes the generalized interaction potential and $V = -E$ for attractive systems. The high V/kT region of this diagram outlines the equilibrium phase transitions observed in highly repulsive systems as detailed in Ref. 19. Here, with increasing V/kT , the onset of fluid to solid transition shifts to lower concentrations as the hydrodynamic radius of the particles increases with the development of an electrostatic or

steric repulsive barrier around the particles. The low V/kT region corresponds to the highly attractive systems that result in the formation of ramified structures as discussed above. In this case, although the hydrodynamic radius is small, the onset of fluid to solid transition again shifts to low solids loadings due to the formation of fractal clusters with low density. Either extreme must be avoided when high density packings are desired. The intermediate range is most suitable for the preparation of slips with high solids loadings and densely packed structures. In practical terms, this goal is accomplished when we work (i) with dispersed suspensions in the lower supercritical range (Fig. 1) where the hydrodynamic radius of the particles is minimized,⁷ or (ii) with weakly flocculated suspensions in the upper subcritical range that can readily restructure towards densely packed states. In the latter case, the use of surfactants as lubricating agents aids the process of restructuring to form higher densities.^{20,21} In effect, the use of surfactants as lubricating agents is equivalent to lowering both E and τ_R/τ_D in the Monte Carlo simulation discussed above, although presently we do not clearly understand the exact role of the surfactants separately on E and τ_R/τ_D . The important point is that the suggestion of using weakly flocculated systems to process densely packed casts is contrary to the conventional wisdom which suggests that only dispersed systems be used.²²

TAILORING OF NANOCOMPOSITES WITH ULTRAFINE PARTICLES

It has been customary to divide the field of ultrastructure processing into two distinct groups as (i) sol-gel and (ii) colloidal suspension processing.²³ As Iler appropriately pointed out,²⁴ this distinction relates mainly to the size of the particles used in a suspension. In the sol-gel group, the scale of interest is the nanometer range, whereas the colloidal suspension group is mainly concerned with processes that utilize suspensions of micrometer size particles. The model presented in the previous section may be used to explain the unifying features and the differences observed between these two groups. The unifying feature is that the nucleation of particle clusters and their networks as hierarchically clustered structures is expected in both groups. The extent of

hierarchy determines the overall packing density of the system. The first difference is predicted to be in the relaxation behavior of these hierarchically clustered structures as related to the parameter τ_R/τ_D . In the nanometer range, the formation of low density structures is favored even in weakly attractive systems as τ_R/τ_D is expected to increase due to higher particle mobility (i.e., small τ_D) and high reactivity (i.e., high τ_R).

The second difference relates to the hydrodynamic size of the particles which becomes a significant factor in limiting the effective particle concentration in a suspension. As a result of these differences, the fluid range of Fig. 5 becomes more narrow even in the intermediate range as the particle size decreases to the nanometer scale. Consequently, with nanometer size particles it is difficult to prepare concentrated suspensions and gels (Fig. 6), and the processing of monolithic components is often impossible due to excessive shrinkage and cracking during drying and sintering stages.

Presently, an easy solution to this excessive shrinkage problem is not available. An ultimate solution would be to establish a methodology for the preparation of highly concentrated suspensions in the nanometer range. Based on the model presented in the previous section, we again emphasize that two possible approaches are: (i) the minimization of the hydrodynamic radius, and (ii) enhanced restructuring of the clustered networks. In either case, the use of surfactants is expected to be essential.^{20,21} In spite of this excessive shrinkage problem, however, many successful applications of nanocomposite processing with ultrafine particles have been illustrated.²³ Below, we summarize the results of our work on the processing of monolithic mullite with ultrafine particles and outline the process requirements for the control of nanostructural features.

Recent studies have illustrated the potential of mullite ($3Al_2O_3 \cdot 2SiO_2$) as a matrix material for high temperature applications.²⁵ In most studies, it has been necessary to work at temperatures above 1500°C in order to achieve full densification (Fig. 7). Our studies on kaolinite ($Al_2O_3 \cdot 2SiO_2 \cdot 2H_2O$) - Al_2O_3 mixtures have illustrated that these high processing temperatures may not be necessary if amorphous and nanometer size particles are used to promote rapid densification by viscous deformation at temperatures as low as 1250°C.²⁶ Similar observations have been made by other investigators; but, fully dense and monolithic specimens could not be

obtained.²⁷ In our studies, we have been able to densify monolithic gels to 98% of the theoretical density at 1250°C within 4 h.²⁸ The essential requirement is to control the degree of particle and thus chemical segregation in the nanometer scale in order to delay the crystallization of mullite prior to total densification (Fig. 7). Particles of AlOOH (~15 nm) are used as alumina source, and the controlled hydrolysis of tetraethoxysilane (TEOS) around the AlOOH particles provides the silica component. Viscous deformation of silica before the onset of mullite formation at temperatures ~1250°C provides the mechanism for rapid densification. Subsequent crystallization to mullite results in the depletion of both alumina and silica provided that the degree of particle segregation is controlled to an optimum level. When particle segregation is not controlled and AlOOH particles aggregate into clusters > 50 nm, two types of defects result: (i) with the capillary suction of silica into the AlOOH particle clusters, intercluster pores form and thus result in low sintered densities (Fig. 8), and (ii) pockets of ~5-10 nm size amorphous silica are permanently trapped within mullite grains when mullite crystals sweep through the silica rich regions (Fig. 9). The atomic resolution image in Fig. 9, taken in [010] orientation, reveals an example of amorphous region (> 90% SiO₂) within a mullite grain.

CONCLUSIONS

The equilibrium phase diagram of colloidal systems predicts the formation of densely packed particle compacts regardless of the interaction potential between particles. However, in reality these equilibrium packing densities are never attained due to the formation of metastable hierarchically clustered particle compacts. The reversible particle clustering model summarized in this paper properly accounts for the formation of low density structures and their restructuring behavior towards the equilibrium state. In order to prepare highly concentrated suspensions and casts, two approaches are emphasized: (i) the minimization of the hydrodynamic radius, and (ii) enhanced restructuring of the clustered networks. The accomplishment of this goal, however, becomes increasingly more difficult as the particle size decreases to the nanometer range.

In spite of the low packing density problems of the nanometer range, processing with nanometer size particles or polymeric units offers advantages not only in the control of structural details down to the molecular dimensions but also in achieving lower sintering temperatures than are possible with micrometer size particles. The advantage of using amorphous particles to achieve rapid densification rates is illustrated with the case study on the $\text{SiO}_2\text{-Al}_2\text{O}_3$ system. It is also illustrated that a precise control of particle clustering is required to eliminate defects that are smaller than 5-10 nm.

ACKNOWLEDGEMENT

The research summarized here was sponsored by the Air Force Office of Scientific Research (AFOSR) and the Defense Advanced Research Projects Agency of the Department of Defense and was monitored by AFOSR under Grant No. AFOSR-83-0375.

REFERENCES

1. P. Chaudhari, "Electronic and magnetic materials," *Scientific American*, 255 [4] 137-44 (1986).
2. I. A. Aksay and C. H. Schilling, "Colloidal filtration route to uniform microstructures," in *Ultrastructure Processing of Ceramics, Glasses, and Composites*, L. L. Hench and D. R. Ulrich (eds.), John Wiley and Sons, New York, 1984, pp. 439-47.
3. I. A. Aksay and R. Kikuchi, "Structures of colloidal solids," in *Science of Ceramic Chemical Processing*, L. L. Hench and D. R. Ulrich (eds.), John Wiley and Sons, New York, 1986, pp. 513-21.
4. M. Yasrebi and I. A. Aksay, "Phase stability and structures in colloidal systems," to be submitted to the *J. Am. Ceram. Soc.*, 1987.
5. B. Vincent, "Phase separation in dispersions of weakly interacting particles," *Chem. Engrn. Science*, 42 [4] 779-86 (1987).
6. J. M. Victor and J. P. Hansen, "Liquid-Gas transitions in charged colloidal dispersions," *J. Phys. Lett. (Paris)*, 45, L307 (1984).

7. J. Cesarano III and I. A. Aksay, "Processing of α -Al₂O₃ with highly concentrated aqueous alumina suspensions," submitted to the Am. Ceram. Soc. Bulletin, 1987.
8. C. H. Schilling and I. A. Aksay, "Slip casting of advanced ceramics and composites," in Proc. of Third Canadian University-Industry Council on Advanced Ceramics, 1987.
9. F. F. Lange, "Sinterability of agglomerated powders," J. Am. Ceram. Soc., 67 [2] 83-89 (1984).
10. I. A. Aksay, "Microstructure control through colloidal consolidation," in Advances in Ceramics, Vol. 9, Forming of Ceramics, J. A. Mangels and G. L. Messing, (eds.), Am. Ceram. Soc., Columbus, Ohio, 1984, pp. 94-104.
11. C. Han, I. A. Aksay, and O. J. Whittemore, "Characterization of microstructural evolution by mercury porosimetry," in Advances in Materials Characterization II, R. L. Snyder, R. A. Condrate, Sr., and P. F. Johnson, (eds.), Plenum Publ. Co., New York, 1985, pp. 339-47.
12. R. Buscall and L. R. White, "The consolidation of concentrated suspensions," J. Chem. Soc., Faraday Trans. 1, 83, 873 (1987).
13. See articles in Kinetics of Aggregation and Gelation, F. Family and D. P. Landau (eds.), North-Holland, Amsterdam, 1984.
14. P. Dimon, S. K. Sinhar, D. A. Weitz, C. R. Safinya, G. Smith, W. A. Varady, and H. M. Lindsay, "Structure of aggregated gold colloids," Phys. Rev. Lett., 57, 595 (1986).
15. J. C. Rarity and P. N. Pusey, in On Growth and Form, Martinus Nijhoff, Dordrecht, 1986, p. 219.
16. W. Y. Shih, I. A. Aksay, and R. Kikuchi, "Restructuring of fractal clusters and networks," submitted to Phys. Rev. A, 1987.
17. P. Meakin, "Formation of fractal clusters and networks by irreversible diffusion limited aggregation," Phys. Rev. Lett., 51, 1119 (1983).
18. M. Kolb, R. Botet, and R. Julien, "Scaling of kinetically growing clusters," Phys. Rev. Lett., 51, 1123 (1983).
19. W. Y. Shih, I. A. Aksay, and R. Kikuchi, "Phase diagrams of charged colloidal particles," J. Chem. Phys., 86, 5127 (1987).

20. R. E. Johnson, Jr. and W. H. Morrison, Jr., "Ceramic powder dispersion in nonaqueous systems," in *Advances in Ceramics*, Vol. 21, Ceramic Powder Science, G. L. Messing, K. S. Mazdhyasni, J. W. McCauley, and R. A. Haber, (eds.), Am. Ceram. Soc., Westerville, Ohio, 1987, pp. 323-48.
21. D. Gallagher, D.-J. Rhee, and I. Aksay, "Compaction of flocculated suspensions with polymeric additives," to be submitted to the *J. Am. Ceram. Soc.*, 1987.
22. See articles of Section III in Reference 20.
23. See Parts 1, 2, and 5 in *Science of Ceramic Chemical Processing*, L. L. Hench and D. R. Ulrich (eds.), John Wiley and Sons, New York, 1986.
24. R. K. Iler, "Inorganic colloids for forming ultrastructures," *ibid.*, pp. 3-20.
25. S. Kanzaki, J. Asami, S. Mitachi, O. Abe, and H. Tabata, "Mechanical properties of SiC whisker/mullite composite," abstract in 24th Yogyo-Kiso-Toronkai (Meeting of Basic Science of Ceramics), Japan, 1986, p. 65.
26. N. Shinohara, On-going Ph.D. Thesis study, University of Washington, Seattle, WA.
27. S. Komarneni, Y. Suwa, and R. Roy, "Application of compositionally diphasic xerogels for enhanced densification: the system $Al_2O_3-SiO_2$," *J. Am. Ceram. Soc.*, 69 [7] C155-56 (1986).
28. N. Shinohara, D. M. Dabbs, and I. A. Aksay, "Infrared transparent mullite through densification of monolithic gels at 1250°C," *Proc. of SPIE*, 683, 19 (1986).

FIGURE CAPTIONS

- Figure 1: (a) Phase diagram (outlined with thin solid lines) for a colloidal system of only one type of particle.³ In electrostatically interacting systems, the reduced temperature scale is approximately proportional to $(\zeta/\zeta_0)^2$ where ζ is the surface potential and ζ_0 is a normalization constant. The maximum packing density is predicted as ~ 74%; (b) Sedimentation (thick solid line with open circles) and slip cast (thick broken line with open triangles) densities are lower than the predicted dense packing value.
- Figure 2: The model used in the Monte Carlo simulation of reversible clustering.¹⁶ Cluster (a) may go through configuration change with the unbinding of particles 1 through 3. Particle 4 cannot be removed. Unbinding takes place according to the removal rate $e^{-\Delta E/T}$ where ΔE is the energy change due to the unbinding and increases as the number of nearest neighbors increases. Possible configurations after unbinding are shown for each case.
- Figure 3: Fractal dimension D vs. E/T for $\tau_R/\tau_D = 5$. (●) at $t = 10,000 \tau_D$ and Δ at $t = 5,000 \tau_D$.
- Figure 4: Fractal dimension D vs. t at a fixed $E = 1.57$ and (a) for $\tau_R/\tau_D = 0.5$ and (b) $\tau_R/\tau_D = 10$.
- Figure 5: Schematic form of the nonequilibrium colloidal phase diagram. In the high V/kT region, the onset of fluid to solid transition shifts to lower concentrations due to increasing hydrodynamic radius.¹⁹
- Figure 6: The effect of particle size on the maximum particle concentration of electrostatically stabilized suspensions of $\alpha\text{-Al}_2\text{O}_3$ ($> 1 \mu\text{m}$) and AlOOH ($< 1 \mu\text{m}$) without exceeding a suspension viscosity of $< 1 \text{ Pa}\cdot\text{s}$. A significant densification is observed during drying in the nanometer range.
- Figure 7: Densification of mullite forming gels with respect to temperature. In contrast to the gel, a kaolinite + alumina mixture of mullite composition has to be heated to 1650°C in order to achieve a fully dense state.
- Figure 8: Schematic representation of the AlOOH (cross-hatch particles) + SiO_2 (dotted matrix) nanocomposites.

Figure 9: Atomic resolution image of mullite lattice. An amorphous entrapped region is seen with a "granular" contrast which contains 90% SiO₂ as determined by electron energy loss spectroscopy. Bright dots are projections of [010] atomic columns in the mullite lattice.

AD-A188 526

MICRODESIGNING OF LIGHTWEIGHT/HIGH STRENGTH CERAMIC
MATERIALS (U) WASHINGTON UNIV SEATTLE DEPT OF MATERIALS
SCIENCE AND ENGINEERING 1 8 ARSAY 30 AUG 87
AFOSR-TR-87-1593 AFOSR-83-0375

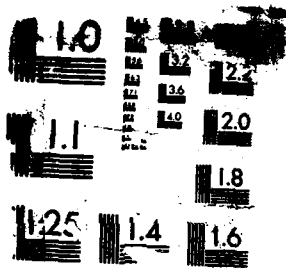
4/4

UNCLASSIFIED

F/G 11/2

ML





RESOLUTION TEST CHART

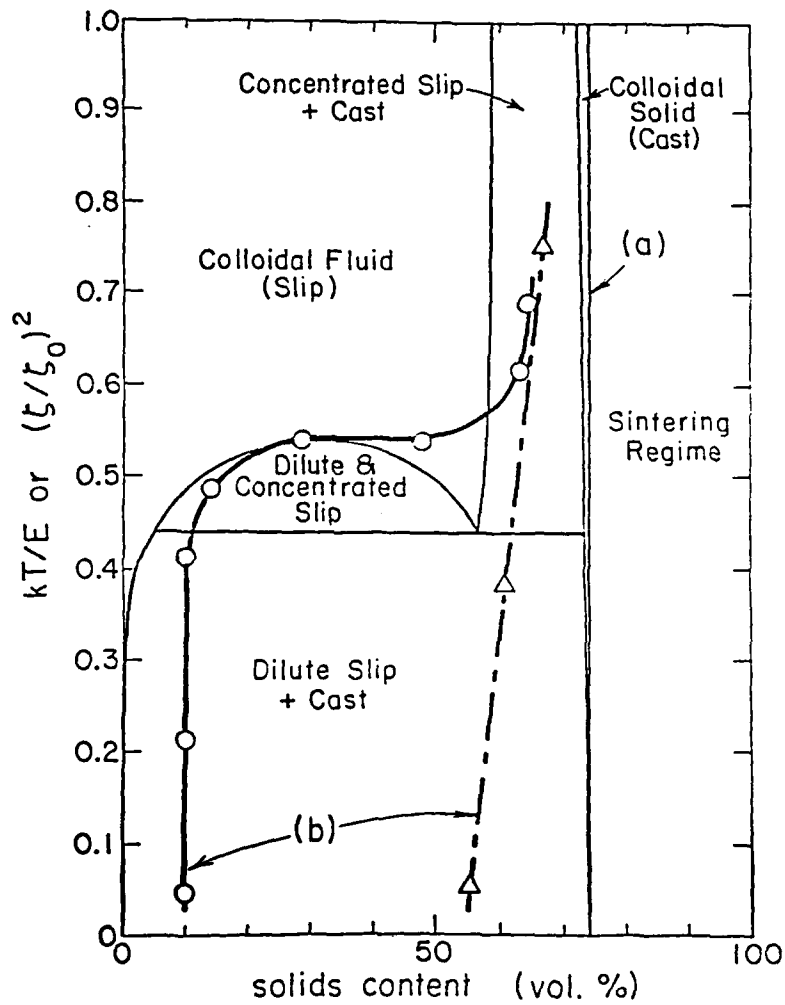
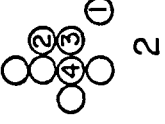
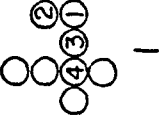
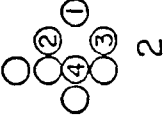
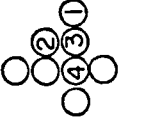


Figure 1

	removal rate	possible direction to move after removal	possible resulting configuration
①	$e^{-E/T}$	N, E, S	
②	$e^{-2E/T}$	N, S	
③	$e^{-3E/T}$	S	
④	can not be removed		

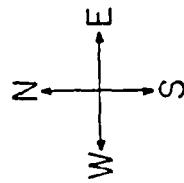


Figure 2

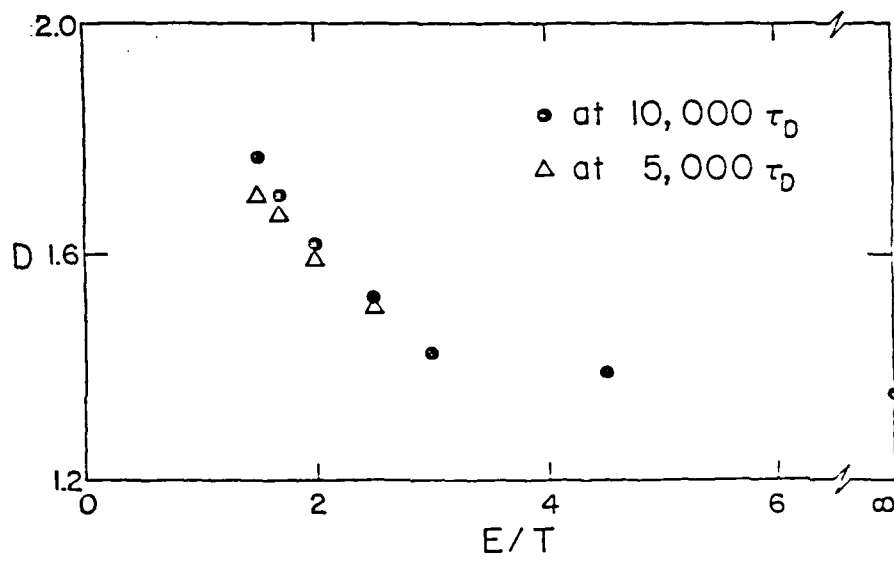


Figure 3

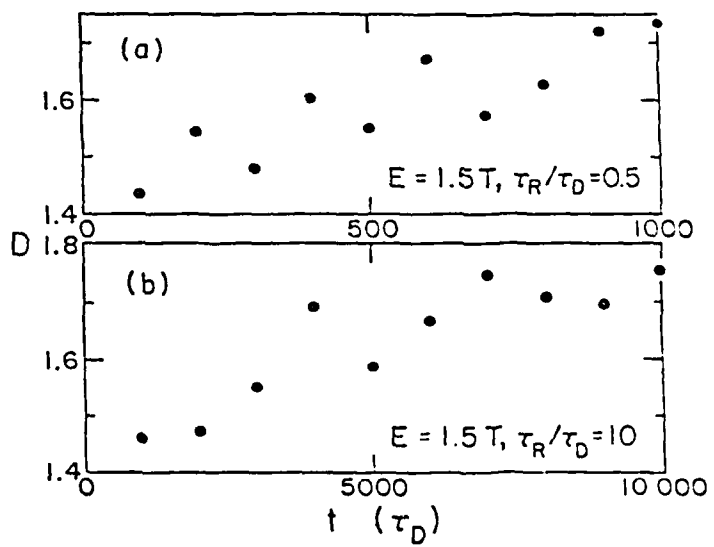


Figure 4

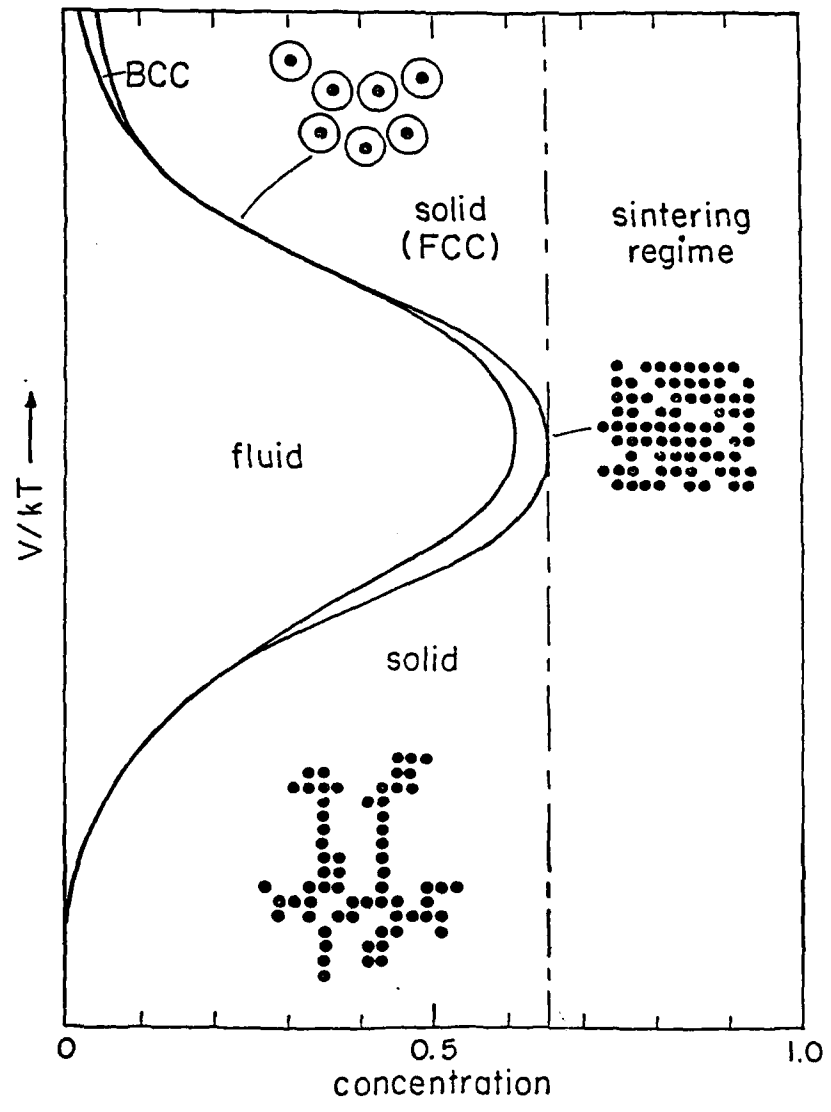


Figure 5

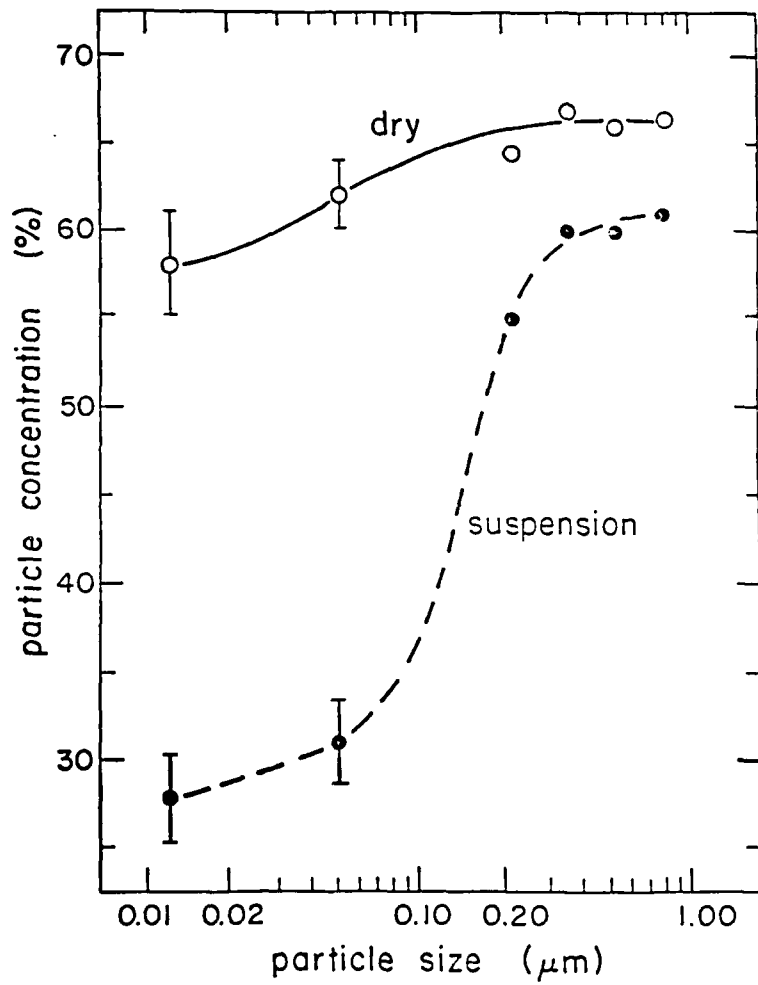


Figure 6

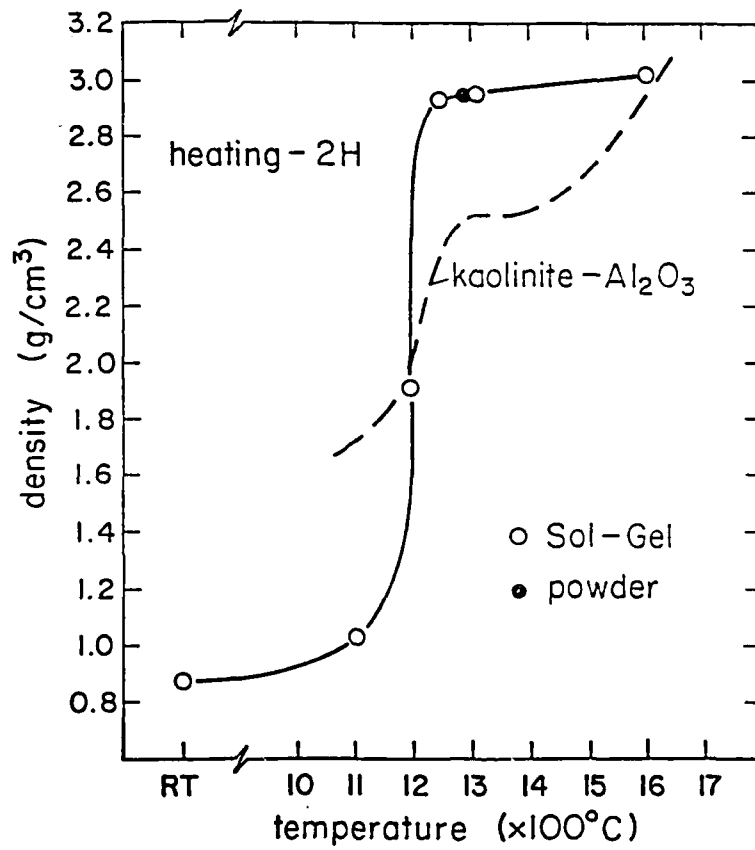


Figure 7

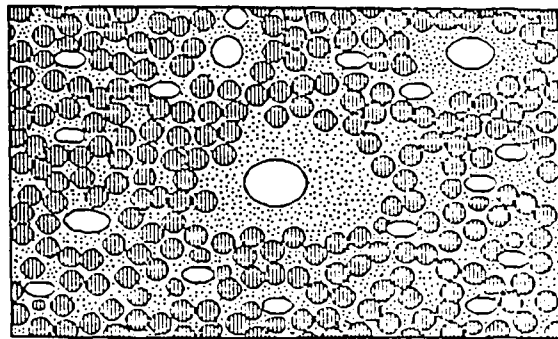
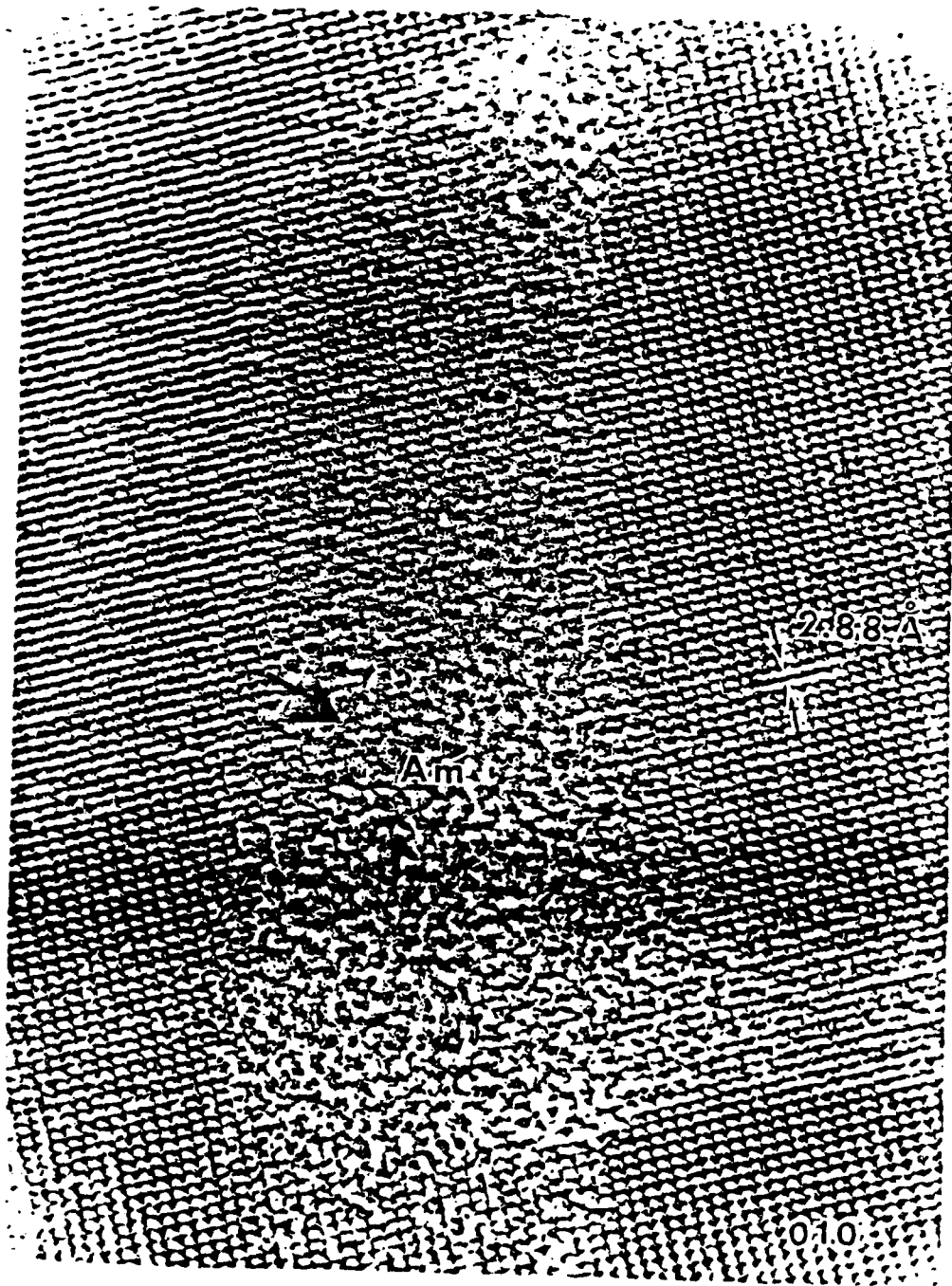


Figure 8

Figure 9



APPENDIX XXV

ABSTRACTS OF PAPERS IN PREPARATION

1. Shinohara, N., and Aksay, I.A., "Processing of Dense Al_2O_3 Through Gelation: I. Cracking Problem," *J. Am. Ceram. Soc.*, 1987a (manuscript in preparation).

Sol-gel processing has been widely investigated for the fabrication of ceramics and glasses because it has advantages for reducing the sintering temperature and for preparing the materials with high uniformity and purity compared to the conventional processing. In the present work, the drying behavior of α - Al_2O_3 -seeded boehmite gels and the influence of a heating rate on cracking were studied. Boehmite transforms to γ - Al_2O_3 by the reaction $2\text{AlOOH} \rightarrow \text{Al}_2\text{O}_3 + \text{H}_2\text{O}$. Since the weight of 15% is lost during the dehydration, it is estimated that the dehydration of boehmite causes cracking during heating of the gels. The gels were dried slowly at room temperature to prevent cracking.

The cracks in the samples were mainly attributed to the rapid dehydration of boehmite near 450°C , hence the heating rate had to be controlled below 1000°C to prevent the cracking. Fine, fibrous boehmite powder did not avoid the cracking because of the large shrinking anisotropy. The heating rate below 1000°C also affected the densification behavior of the samples.

2. Shinohara, N., and Aksay, I.A., "Processing of Dense Al_2O_3 Through Gelation: II. Densification Kinetics," *J. Am. Ceram. Soc.*, 1987b (manuscript in preparation).

Densification behavior of the α - Al_2O_3 seeded boehmite gels was investigated. Rapid densification occurred after the γ -to- α - Al_2O_3 phase transformation. Enhanced densification behavior of boehmite with α - Al_2O_3 seeds can be attributed to the (1) small neck size and the (2) small and uniform α - Al_2O_3 particles at the onset of the densification (after the completion of γ - to α - Al_2O_3 phase transformation). Seeding of α - Al_2O_3 particles into the boehmite matrix promoted the homogeneous nucleation and growth process of α - Al_2O_3 in the system in the low temperature region, resulting in the formation of small pores or cracks in the system. Decreasing the agglomerate size in the boehmite matrix led to a reduction in the sintering temperature.

3. Shinohara, N., Sarikaya, M., and Aksay, I.A., "Low Temperature Sintering of Mullite Through Sol-Gel Processing from Boehmite-TEOS," *J. Am. Ceram. Soc.*, 1987 (manuscript

in preparation).

Mullite ($3\text{Al}_2\text{O}_3 \cdot 2\text{SiO}_2$) is a sole stable phase in the $\text{SiO}_2\text{-Al}_2\text{O}_3$ binary system and is considered to be a candidate material for high temperature applications and for optical and electronic uses. Mullite powder has been synthesized by various approaches, such as powder synthesis from alkoxides or metal organic compounds, spray pyrolysis of the solution, heat-treatment of the gel, hydrothermal synthesis of alkoxy-derived precursor, and other methods. In this research, we investigated the densification behavior of mullite through sol-gel processing from boehmite and TEOS. The gels could be densified to 3.00 g/cm^3 at 1250°C by removing large agglomerates which were contained in the initial boehmite powder. Low densities of the gels with large agglomerates were attributed to the pore formation in the excess silica region. This was introduced by inhomogeneous mixing because of the agglomerates. Heating the gels caused mullite to form through sudden reaction in the $\gamma\text{-Al}_2\text{O}_3$ solid solutions and through the diffusion controlled process.

4. Pyzik, A.J. and Aksay, I.A., "Relation Between Microstructure and Some Mechanical Properties in the $\text{B}_4\text{C-Al}$ Composites," *J. Am. Ceram. Soc.*, 1987 (manuscript in preparation).

Fracture strength and fracture toughness of $\text{B}_4\text{C-Al}$ composites have been characterized with respect to type of microstructure. It was found that mechanical properties of this system depend on the amount of metal present, the type and distribution of the secondary phases that form and a continuity factor. Materials have been obtained with a combination of 645 MPa strength and $9.7 \text{ MPa m}^{1/2}$ toughness and 545 MPa strength and $14.4 \text{ MPa m}^{1/2}$ toughness.

5. Shih, W.Y. and Aksay, I.A., "Phase Diagrams of Bimodal Charged Colloidal Particles." *J. Chem. Phys.*, 1987 (submitted for publication).

The stability of the substitutional crystals of bimodal charged colloidal particles has been examined by comparing the free energies of the crystalline solids as well as of the liquid. The free energies are calculated variationally. The Einstein model and the hard-sphere fluid are respectively used as the reference system for the solid and for the liquid. The charge of a particle is assumed to be proportional to its diameter as is found experimentally. Let γ denote the ratio of the diameter of the small particles to that of the large particles. Our results show that only when γ is close to unity, say, 0.8, a substitutional

crystal can be formed while the crystalline phase is still less stable against the formation of the liquid phase in the intermediate concentrations than in the pure cases, i.e., the freezing density has a maximum at some finite concentration. When γ deviates more from unity, say, 0.5, the crystalline solid cannot be formed in most of the phase regions except those that are close to the pure cases.

6. Liu, J., Shih, W.Y., Kikuchi, R., and Aksay, I.A., "On the Clustering of Binary Colloidal Suspensions," *J. Colloid Interface Sci.*, 1987 (manuscript in preparation).

Recent experiments on binary colloidal suspensions have shown that particles of the first kind (e.g., alumina) can be induced to flocculate by the presence of particles of the second kind (e.g., polyacrylic acid particles), within a certain range of the density of the second species of particles. This is similar to the depletion flocculation and depletion stabilization of the polymer-colloidal systems. We have thoroughly examined the binary-particle systems with numerical simulations (Monte Carlo) as well as with analytical equilibrium calculations (CVM). The simulations show a peak in the flocculation rate as the density of the second-species particles is varied while the CVM calculations show a monotonic increase in cluster size. The discrepancy between the simulation and the CVM calculation suggests that the restabilization of particles at high density is due to kinetics. We further show from free energy calculations that the flocculated state is a metastable one whose underlying stable state is phase separation. Our calculations together with experiments on binary colloids may shed some light on the understanding of the polymer-colloidal systems.

7. Shih, W.Y., Liu, J., and Aksay, I.A., "Adsorption of Polymers and Polyelectrolytes on Colloidal Surfaces," *J. Colloid Interface Sci.*, 1987 (manuscript in preparation).

Polymer and polyelectrolyte adsorption on colloidal surfaces has been a useful technique for tailoring the properties of a colloidal system. Here we provide a lattice model in which a polymer can wiggle through the individual monomers' flipping, and can perform Brownian motion as a whole (random walk) as well. By assigning appropriate interactions between the individual monomers and between the monomers and the colloidal surfaces, one can study the *multi-chain* adsorption behavior of neutral polymers as well as polyelectrolytes. The processes involving the Brownian motion and the flipping are simulated with the Monte Carlo method. Details of the model and the preliminary results on adsorption and



the steric interaction between two adsorbed layers will be presented. Comparison with experiments will also be made.

APPENDIX XXVI
THESES ABSTRACTS

THESIS ABSTRACT

Sintering of Bimodal Compact

by

Chan Han

M.S. 1985

To achieve desirable sintering behavior of powder compacts resulting in a dense material at low temperatures, it is necessary to obtain green compacts with uniform pore size distribution. One current school of thought is that the uniform pore size distribution can be obtained through colloidal processing of monosize, spherical particles. However, it has been shown that colloidal processing always results in the formation of multi-particle clusters. As a result, additional pores are formed between them. Furthermore, these pores are modified by different consolidation methods. Therefore, uniform sintering cannot be expected, even though monosize, spherical particles are used.

In this study, it will be shown that the second generation pores play an important role in sintering of powder compacts: that of controlling the sintering behavior of the entire powder compact. Also, it will be shown that the addition of fine particles is not harmful to the sintering. Actually, it decreases the sintering temperature of powder compacts. As a result, finer grain size is obtained.

THESIS ABSTRACT

Polyelectrolyte Adsorption on α -Alumina and Aqueous Suspension Behavior

by

Joseph Cesarano III

M.S. 1985

The surface chemistry and charge of polymethacrylic acid- Na^+ salt (PMAA) and $\alpha\text{-Al}_2\text{O}_3$ in aqueous systems were determined using potentiometric titrations. The adsorption of PMAA on $\alpha\text{-Al}_2\text{O}_3$ was determined using first derivative plots of potentiometric titrations. It was determined that electrostatic attraction between the PMAA and $\alpha\text{-Al}_2\text{O}_3$ was the driving force for the adsorption and that after a complete monolayer of PMAA was adsorbed, electrosteric stabilization of the suspension resulted. Using this concept, a stability map relating the amount of PMAA necessary for stabilization vs. pH was formulated. It was also determined that electrosterically stabilized systems have advantages over electrostatically stabilized systems in that: (i) colloidal fluid suspensions of > 50 v/o are easily attained with monosize particles of $0.3 \mu\text{m}$, and (ii) problems related to aging are reduced.

THESIS ABSTRACT

Morphological and Crystallographic Characterization of B₄C-Al Composites

by

Tahar Laoui

M.S. 1986

Transmission electron microscopy imaging, diffraction and spectroscopic techniques have been utilized in characterizing the morphology and crystallography of B₄C-Al metal matrix composites with ceramic phase being the major component (> 70 v/o). Special emphasis has been given to the crystallographic and compositional identification of a new phase present in the composite. This new phase, called X-phase, is a major second phase besides boron carbide which forms during the processing of B₄C-Al ceramic-metal composite under controlled conditions, spatially depleting the Al phase and replacing it around the B₄C particulates. The X-phase has a hexagonal crystal structure with lattice parameters; $a_0 = 3.5202 \text{ \AA}$, and $c_0 = 5.8204 \text{ \AA}$, as determined by X-ray diffraction and convergent beam electron diffraction, and a composition given by the approximate formula Al₄BC as determined by quantitative electron energy loss spectroscopy by using B₄C, Al₄C₃, and AlB₂ standards.

THESIS ABSTRACT

The Sintering of Silicon Carbide with Liquid Aluminum

by

D.L. Milius

M.S. 1986

The purpose of this study was to investigate the feasibility of developing a lightweight, high fracture toughness, and high hardness silicon carbide aluminum composite material with greater than fifty volume percent particulates using conventional ceramic engineering techniques such as liquid phase sintering and infiltration. In order to use conventional pre-firing processing techniques, particulates were used in this study. Silicon carbide and aluminum were chosen as constituents because of their low densities, economic viability, and ready availability. In addition, prior success has been achieved with this system. Currently, encouraging results have been obtained using non-conventional techniques such as hot isostatic pressing and hot extrusion at low temperatures (less than 750°C) and high pressures (10 to 50 MPa).

THESIS ABSTRACT

Microstructural and Fractographic Characterization of B₄C-Al Alloy Composites

by

Gyeongho Kim

M.S., 1987

Microstructural and fractographic characterization were performed on B₄C-Al 7075 alloy cermets. The composites were prepared by an infiltration method where metal constituted up to 50% by volume. The distribution of the primary phases and the reaction products as well as their associated defects were analyzed to determine their effects on the fracture and strength properties. By profiling the cracks on the matching fracture surfaces, the presence of a residual stress was recorded. The response of the microstructure to fracture of B₄C-Al alloy cermets which were subjected to high strain rate was studied by fracture surface replica and by thin foil TEM techniques.

THESIS ABSTRACT

Pressureless Sintering of Short-Fiber Reinforced Mullite

by

Reiichi Yamada

M.S., 1987

Mullite precursor powder which can be sintered into translucent dense (98%) ceramic body at 1250°C in 2 hours, was used for the matrix of the composite material with short fibers. The sintered density of the mullite precursor powder compacts can be controlled by two processing factors. The pressureless sintering of the composite precursor powder with 7.2 volume % fibers resulted in 96% dense material after a 1250°C heat treatment. The densification rates of the composites were slower and the final densities of them were lower than the monolithic mullite. By relating the densification rate of the matrix of the composite to that of the matrix ceramics without fibers, the densification behavior of the composite system was numerically explained. The existing differential sintering models do not explain the experimental data. Besides the powder processing, the gel forming technique was attempted to prepare the composite with short fibers. However, microcracks were introduced during drying and the gel was not sinterable.

END

DATE

FILMED

8